HIGH TEMPERATURE CRACK GROWTH IN A CAST NICKEL BASE SUPERALLOY

by

David William Dean

A thesis submitted for the degree of
Doctor of Philosophy
of the
University of London
and for the
Diploma of Imperial College

February 1986

Department of Mechanical Engineering
Imperial College of Science and Technology
London SW7 2BX

ABSTRACT

Internally cooled aircraft engine blades are subjected to complex thermal and mechanical loadings which can cause cracks to initiate at casting defects within trailing edge sections. Propagation of these cracks may ultimately result in blade failure. Mar MOO2 is typical of the generation of cast nickel base superalloys used for internally cooled aircraft engine blading. The aim of this thesis is to study crack propagation in this alloy at elevated temperatures (750^{o}C and 950^{o}C). The specimen geometry, used throughout the experimental investigations, was of the single edge notch type, designed to give microstructural features and mechanical loadings representative of the trailing edge section of a cast Mar MOO2 turbine blade. All tests were carried out in laboratory air and experimental crack lengths were determined using the d.c. potential drop technique. Effects of R ratio, cyclic frequency, loading waveform and prior creep exposure on crack growth behaviour were examined.

Experimental crack growth data were correlated in terms of the fracture mechanics parameters K and C^*. C^* values, used to correlate crack growth data, were derived from experimentally measured displacement rates using an approximate method based on limit analysis. Comparison of experimental and theoretical estimates of C^* showed that significant discrepancies can exist, particularly when crack growth is accompanied by significant damage accumulation ahead of the crack tip. Time dependent crack growth in Mar MOO2 at temperatures of 750^{o}C and 950^{o}C was found to be creep dominated and crack growth rates correlated best in terms of C^*. A model has been developed which has been shown to give reasonable agreement with experimental data for time dependent crack growth at 950^{o}C.

However, the experiments have shown that the influence of cyclic processes, particularly evident at high loading frequencies and low R ratios can result in significantly higher crack growth rates than would be predicted by C^*

ACKNOWLEDGEMENTS

Financial support for this work was given by an SERC Case Award in conjunction with Rolls Royce Limited, Derby.

I would like to thank the following people for their assistance during the progress of this work

Dr G A Webster, for his guidance and supervision throughout

Mr D K Willis, for his help and advice throughout the experimental testing programme

Mr G Asquith and Dr A C Pickard (Rolls Royce Ltd), for providing test specimens and valuable advice on stress analysis aspects of the work

Mr C Howland and Dr N McLeod (Rolls Royce Limited), for providing valuable advice on experimental and metallurgical aspects of the work.

Mrs E Plumbly, for typing this thesis.

CONTENTS

		Page
Title Page		1
Abstract		2
Acknowledgements		4
Contents		5
Nomenclature		10
CHAPTER 1 :	GENERAL INTRODUCTION	14
CHAPTER 2 :	INTRODUCTION TO THE STRUCTURE AND PROPERTIES OF NICKEL BASE SUPERALLOYS	16
2.1	Development of Nickel Base Superalloys	16
2.2	Alloy Composition, Structure and Microstructure	17
2.3	Material Properties of Nickel Base Superalloys	19
Table	2.1	21
Figures	2.1 - 2.3	22
CHAPTER 3 :	MECHANISMS OF CRACK GROWTH AT HIGH TEMPERATURES IN NICKEL BASE SUPERALLOYS	24
3.1	Introduction	24
3.2	High Temperature Crack Growth under Static Loading	26
	3.2.1 Environmental Effects	28
	3.2.2 Temperature Effects	29
	3.2.3 Microstructural Effects	29
3.3	High Temperature Crack Growth under Cyclic Loading	31
	3.3.1 Environmental Effects	32
	3.3.2 Temperature Effects	32
	3.3.3 Frequency Effects	33
	3.3.4 R Ratio Effects	34
	3.3.5 Waveform Effects	35
	3.3.6 Hold time Effects	35
	3.3.7 Microstructural Effects	36
Figures	3.1 - 3.4	37
Appendix 3	Creep Failure Mechanisms in Nickel Base Superalloys	41
	A3.1 Phenomenon of Creep	41
	A3.2 Creep Mechanisms	42
Figure	A3.1	45

		Page
CHAPTER 4 :	CHARACTERISATION OF CRACK TIP STRESS AND STRAIN FIELDS IN MATERIALS AT HIGH TEMPERATURES	46
4.1	Introduction	46
4.2	Linear Elastic Material Behaviour	48
4.3	Elastic-Plastic Material Behaviour	51
4.4	Steady State Creep Material Behaviour	54
4.5	Generalised Material Behaviour	56
	4.5.1 Transition from small scale creep to extensive secondary creep	56
	4.5.2 Influence of primary creep	59
4.6	Stress and Strain Fields Near the Tip of a Growing Crack	61
Figures	4.1 - 4.10	63
CHAPTER 5 :	MODELLING HIGH TEMPERATURE CRACK GROWTH BEHAVIOUR	73
5.1	Introduction	73
5.2	Creep Crack Growth Models	75
	5.2.1 Continuum models	75
	5.2.2 Micromechanistic models	79
5.3	Fatigue Crack Growth Models	84
Tables	5.1 - 5.2	93
Figures	5.1 - 5.9	95
Appendix 5	Models of Creep Failure	104
Figures	A5.1 - A5.4	107
CHAPTER 6 :	CORRELATION OF HIGH TEMPERATURE CRACK GROWTH DATA	111
6.1	Introduction	111
6.2	Correlation of High Temperature Creep Crack Growth Data	113
6.3	Correlation of High Temperature Fatigue Crack Growth Data	115
6.4	Evaluation of Fracture Mechanics Parameters used to Correlate High Temperature Crack Growth Data	118

CHAPTER 6 Continued

		Page
	6.4.1 Evaluation of K	118
	6.4.2 Evaluation of C^*	119
	6.4.2.1 Experimental data reduction method	119
	6.4.2.2 Approximate methods	120
	6.4.2.3 Numerical methods	125
Figures	6.1 - 6.3	129
Appendix 6	Common Test Piece Geometries	132
CHAPTER 7 :	EXPERIMENTAL PROGRAMME	134
7.1	Introduction	134
7.2	Material : Composition and Heat Treatment	135
7.3	*TCP* Specimen Geometry	137
7.4	Experimental Equipment	138
	7.4.1 Cyclic loading equipment	138
	7.4.2 Static loading equipment	139
7.5	Measurement Methods	141
	7.5.1 Temperature, Displacement and Load Calibration	141
	7.5.2 Crack Length Measurement	142
	7.5.3 Data Acquisition	145
7.6	Experimental procedure	146
	7.6.1 Cyclic Loading Tests	146
	7.6.2 Static Loading Tests	148
7.7	Test programme	150
	7.7.1 Crack Growth Under Cyclic Loading	151
	7.7.1.1 Crack growth at 750°C	151
	7.7.1.2 Crack growth at 950°C	152
	7.7.2 Crack growth under static loading	155
	7.7.2.1 Crack growth at 750°C	155
	7.7.2.2 Crack growth at 950°C	155
Tables	7.1 - 7.3	156
Figures	7.1 - 7.7	159
Appendix 7	Preliminary Crack Propagation Tests	166

		Page
CHAPTER 8 :	THEORETICAL Pd, K AND C^* CALIBRATION FOR THE CRACK PROPAGATION SPECIMEN	168
8.1	Introduction	168
8.2	Pd Calibration	169
8.2.1	Location of Reference Pd Leads	170
8.2.2	Location of Crack Pd Leads	170
8.2.3	Theoretical Pd Calibration	170
8.3	K Calibration	175
8.4	C^* Calibration	177
8.4.1	Theoretical C^* Calibration for 750°C	181
8.4.2	Theoretical C^* Calibration for 950°C	182
Figures	8.1 - 8.21	184
CHAPTER 9 :	EXPERIMENTAL RESULTS	205
9.1	Introduction	205
9.2	Calculation of Crack Growth Rates and Displacement Rates	206
9.3	Calculation of Fracture Mechanics Parameters K and C^*	208
9.3.1	Calculation of K	208
9.3.2	Calculation of C^*	208
9.3.2.1	Experimental C^* values	208
9.3.2.2	Theoretical C^* values	211
9.3.2.3	Comparison of C^*_{exp}, C^*_{mod} and C^*_{th}	211
9.4	Results of the Experimental Test Programme	213
9.4.1	Preliminary Crack Growth Tests	214
9.4.2	Crack Growth at 750°C	214
9.4.2.1	Crack growth in the threshold region	214
9.4.2.2	Effect of R ratio	215
9.4.2.3	Changing the R ratio during a test	216
9.4.2.4	Effect of frequency	218
9.4.3	Crack Growth at 950°C	220
9.4.3.1	Crack growth in the threshold region	220
9.4.3.2	Effect of R ratio	221
9.4.3.3	Changing the R ratio during a test	222
9.4.3.4	Effect of frequency	223

CHAPTER 9 Continued

		Page
	9.4.3.5 Effect of waveform	224
	9.4.3.6 Effect of prior creep damage	225
Figures	9.1 - 9.65	226
CHAPTER 10 :	DISCUSSION	291
10.1	Crack Growth at 750°C	291
	10.1.1 Crack growth in the threshold region	291
	10.1.2 Effect of R ratio	292
	10.1.3 Effect of frequency	294
10.2	Crack Growth at 950°C	297
	10.2.1 Crack growth in the threshold region	297
	10.2.2 Effect of R ratio	298
	10.2,3 Effect of waveform	301
	10.2.4 Effect of prior creep damage	302
10.3	Comparison of Crack Growth Behaviour of Mar M002 at Temperatures of 750°C and 950°C	305
10.4	Crack Growth Modelling	308
Figures	10.1 - 10.14	312
CONCLUSIONS		326
RECOMMENDATIONS FOR FURTHER WORK		334
REFERENCES		335

NOMENCLATURE

English Symbols

a	current crack length
a_i	initial crack length
$\dot{a}$	crack growth rate
B	specimen thickness
C	specimen compliance
C_n	specimen compliance under secondary creep conditions
C^*	energy rate line integral
C^*_{dam}	value of C^* in a creep damaged material
C^*_{exp}	experimentally measured C^* value
C^*_{mod}	modified experimental value of C^*
C^*_{th}	theoretical C^* value
$CTOD$	crack tip opening displacement
$CTOD_c$	cyclic crack tip opening displacement
d	material grain size
E	Young's modulus
f	cyclic loading frequency
G	energy release rate
J	energy line integral
K	stress intensity factor
K_{max}	maximum value of K under cyclic loading
K_{min}	minimum value of K under cyclic loading
ΔK	stress intensity factor range

n	creep exponent
N	number of fatigue cycles
P	applied load
P_L	limit load for uncracked body
P_{LC}	limit load for cracked body
P_{max}	maximum load for cyclic loading
P_{min}	minimum load for cyclic loading
r	radial distance (polar co-ordinates)
r_p	monotonic plastic zone size
Δr_p	cyclic or reversed plastic zone size
R	ratio of minimum to maximum cyclic stresses
t	time
t_h	hold time
t_R	time to rupture
T	temperature
T_M	melting temperature
U	stored strain energy density
U^*	stored strain energy rate density
V	voltage
V_c	voltage across crack
V_{ref}	reference voltage
V_{tr}	transducer output voltage
W	specimen width
W_s	strain energy density
W_s^*	strain energy rate density

x)) y)) z)	Cartesian co-ordinates

Greek Symbols

$\dot{\Delta}$	displacement rate
$\dot{\Delta}_c$	displacement rate due to the crack alone
$\dot{\Delta}_o$	displacement rate of an equivalent uncracked body
$\dot{\Delta}_T$	total displacement rate
ε	strain
ε_f	failure strain
ε_y	strain at yield
$\dot{\varepsilon}$	strain or creep rate
$\dot{\varepsilon}_A$	average creep rate
$\dot{\varepsilon}_{min}$	minimum or secondary creep rate
η	creep damage parameter
$\dot{\eta}$	rate of accumulation of creep damage
θ	angular rotation (polar co-ordinates)
ν	Poisson's ratio
σ	applied stress
σ_e	equivalent stress
σ_{ij}	stress tensor
σ^1_{ij}	deviatoric stress tensor

σ_{max}	maximum applied cyclic stress
σ_{min}	minimum applied cyclic stress
σ_{net}	net section stress
σ_{ref}	reference stress
σ_{y}	yield stress
σ_{∞}	remote applied stress
ψ	creep continuity parameter
ω	radial frequency

The above notation has been adopted throughout the text. The use of any other symbols is accompanied by a full explanation in the text.

CHAPTER 1

GENERAL INTRODUCTION

Performance and efficiency requirements for modern aircraft engines have necessitated the development of turbine blade materials, capable of operating under increasingly severe service conditions. The development of nickel base superalloys has been responsible, to a large extent, for allowing improvements in engine design to be implemented in practice. Further improvements in performance were achieved by the use of internally cooled cast blades. However, the presence of internal cooling holes within a blade introduce regions of high stress concentration and severe temperature gradients. The complex thermal and mechanical loadings, applied to blades, often cause cracks to initiate at casting defects within the trailing edge section. Propagation of these cracks may ultimately lead to blade failure.

Mar MOO2 is a typical cast nickel base superalloy used for internally cooled aircraft engine blading. The aim of this thesis is to study the factors affecting the rate of crack propagation in this alloy at elevated temperatures. The specimen geometry, used throughout the experimental investigations, was designed to give microstructural features and mechanical loadings representative of the trailing edge section of a cast Mar MOO2 turbine blade. All tests were carried out in laboratory air. Two temperatures, 750°C and 950°C, were considered, and the effects of loading ratio, cyclic frequency, loading waveform and prior creep exposure were examined. Crack lengths were determined using the *d.c.* potential drop technique.

Correlation and prediction of high temperature experimental crack growth data requires suitable parameters to characterise the crack growth rates. Under predominantly elastic conditions, the stress intensity factor, K, characterises the stress field in the vicinity of the crack tip and appears a logical parameter for correlating crack growth rates. When creep deformation is significant, a parameter called C^* has been found to be more relevant.

Essentially, the thesis is divided into six main areas of study. Chapters 2 and 3 review the properties of nickel base superalloys and micromechanisms responsible for crack growth at high temperatures. Chapters 4 and 5 consider characterisation of crack tip stresses and theoretical modelling of the crack growth process. Chapter 6 introduces fracture mechanics parameters used to correlate high temperature crack growth data and discusses the evaluation of parameters relevant to the present work. The experimental programme is reported in Chapter 7, while Chapter 8 describes methods used in determining theoretical potential drop, K and C^* calibrations. Finally, Chapters 9 and 10 present experimental results and discussion.

CHAPTER 2

INTRODUCTION TO THE STRUCTURE AND PROPERTIES OF NICKEL BASE SUPERALLOYS

2.1 Development of Nickel Base Superalloys

Over the past 40 years, aircraft gas turbine blading requirements have necessitated the development of alloy systems capable of operating under increasingly severe service conditions. From circa 1940 to 1965 the properties given the most attention for aircraft engine blades were high temperature tensile strength, short time rupture strength and oxidation resistance. With the advent of engines requiring materials for longer periods of service under increasingly severe conditions, further property requirements emerged. Long time rupture strength, fatigue resistance, thermal fatigue resistance, low thermal expansion, high modulus and low density are all properties desirable in modern aircraft engine blading materials.

Improvements in aircraft engine reliability and performance have coincided with the development of nickel base superalloys. Although nickel base superalloys have been used in aircraft engine blading for some 40 years, it is only relatively recently that a thorough scientific approach to the problems of alloy design has emerged. Although the physical metallurgy of nickel base superalloys is extremely complex, the relationship of properties to structures in these systems is the most well known of all materials for use in the high temperature range (650 - 1100°C). The following chapter introduces microstructural features and properties typical of the type of nickel base superalloy used in aircraft engine blading applications.

2.2 Alloy Composition, Structure and Microstructure

The nickel base superalloy Mar M002 used in the present work is typical of the type of conventionally cast alloy employed in aircraft engine blading applications. The nominal chemical composition of Mar M002 is given in Table 2.1. A nickel base superalloy generally comprises three major phases:

1. Alloy matrix (γ)

The continuous matrix is a face centred cubic (FCC) nickel base austenitic phase, which is usually strengthened by a high percentage of solid solution elements such as cobalt, chromium, molybdenum, tungsten, iron and vanadium.

2. Gamma prime (γ')

The major precipitate phase, which invariably precipitates coherently with the austenitic matrix. Aluminium, titanium and tantalum combine with nickel to form the precipitate $Ni_3(Al,Ti,Ta)$.

3. Carbides

Carbon added at levels of about 0.05 - 0.2% tends to react with reactive and refractory elements to form primary MC carbides, which usually occur as large blocky particles or in "script" form. During heat treatment and in service primary carbides decompose and generate lower carbides such as $M_{23}C_6$ and M_6C, which populate the grain boundaries. Elements which commonly form carbides include chromium, hafnium, molybdenum, tungsten, vanadium, titanium and tantalum.

Chromium and aluminium are also useful as oxide forming elements, forming an adherent oxide scale, which protects nickel base superalloys from environmental attack. In addition to carbon, other elements which tend to segregate to grain boundaries include boron and zirconium.

Over the years increasing strength requirements have necessitated changes in alloy design and microstructure. These changes in microstructure, shown schematically in figure 2.1(1), have occurred as a result of changes in alloy design, which are summarised below.

1. Volume fraction of γ' has increased.
2. Size of γ' at first increased and then remained constant at about 1μm.
3. γ' has become more cubic.
4. γ-γ' eutectic nodules have appeared in the structure.
5. A secondary precipitate of finely divided 'cooling γ'' has been introduced.

Having introduced the basic compositional and microstructural features common to the majority of nickel base superalloys, the following section will relate these features to the mechanical properties of these alloys.

2.3 Material Properties of Nickel Base Superalloys

Throughout the development of nickel base superalloys, the emphasis has been placed on producing alloys which possess excellent high temperature creep and tensile properties coupled with good oxidation resistance.

The volume fraction and size of the γ' precipitate plays an important role in alloy strengthening. The strength of the austenitic matrix, γ, (measured in terms of 0.2% flow stress) decreases steadily over the temperature range 0 - 1000°C, while the γ' precipitate exhibits an increase of strength with temperature, reaching a peak at about 900°C (figure 2.2). The effect on the flow stress of increasing the volume fraction of γ' is shown in figure 2.3(2) for a *Ni-Cr-Al* alloy. For a given volume fraction of γ', the average precipitate size for maximum strengthening is that which will cause moving dislocations to shear the precipitates rather than bow round them. A typical cast nickel base superalloy contains a distribution of fine secondary γ' precipitates interspersed with larger primary γ' particles. Prolonged high temperature exposure causes 'coarsening' or growth of the larger primary γ' precipitates while the secondary γ' precipitates shrink. This process increases the average precipitate size and causes progressive softening of the alloy.

At temperatures above about $0.6T_M$, where T_M is the absolute melting temperature of the alloy, grain boundaries become areas of weakness in polycrystalline materials. Grain boundary sliding can cause initiation and growth of grain boundary voids and microcracks, which lead eventually to an intergranular mode of failure. The resistance of an alloy

to intergranular cracking may be improved by inhibiting grain boundary sliding. Grain boundary carbides tend to inhibit grain boundary sliding by 'keying' the grains together (3,4). Serrated (or wavy) grain boundaries may also reduce sliding and thereby improve an alloy's resistance to intergranular fracture (3,5,6,7).

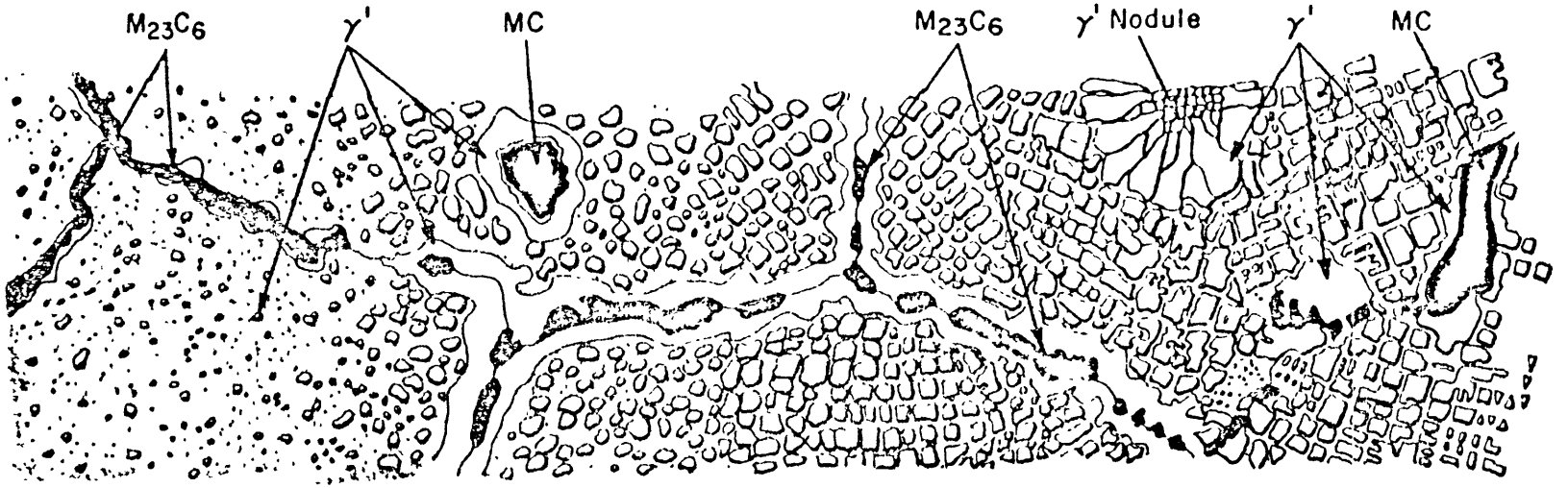
Further improvements in the high temperature mechanical properties of a nickel base superalloy may be achieved by minimising the harmful effects of oxygen from the environment. The addition of small amounts of the elements boron and zirconium (8) and hafnium (9) can significantly reduce the susceptibility of an alloy to oxygen damage. Despite these additions and the intrinsic oxidation resistance of nickel base superalloys, due to the protective oxide scales formed by chromium and aluminium, increasingly severe service conditions have necessitated the use of oxidation resistant coatings to protect modern aircraft engine blading.

Design of alloys for aircraft engine blading applications is further complicated by the fact that certain microstructural features, which enhance creep properties may be detrimental to fatigue strength (10). For instance, brittle minor phases such as carbides, which enhance creep rupture properties, can act as initiation sites for fatigue cracks. A compromise in properties may therefore be required in order to produce an alloy which possesses satisfactory properties under both creep and fatigue loading.

Table 2.1 Chemical Composition of Mar M002

Composition (wt.%)																	
C	Si	Mn	S	Al	B	Co	Cr	Cu	Fe	Hf	Mg	Mo	Ta	Ti	V	W	Zr
.150	.100	.100	.005	5.50	.015	10.00	9.00	.050	.250	1.50	.002	.250	2.50	1.50	.050	10.00	.055

Remainder Ni.



γ'-Formers →	2.5 Ti, 1.3 Al	2.9 Ti, 2.9 Al	3.5 Ti, 4.3 Al	4.7 Ti, 5 5 Al	1.5 Ti, 5.5 Al, 1.5 Ta
Carbide Formers →	20 Cr, 2.5 Ti	19 Cr, 4 Mo, 2.9 Ti	15 Cr, 5.2 Mo, 3.5 Ti	10 Cr, 3 Mo, 4.7 Ti, 1 V	9 Cr, 2.5 Mo, 10 W, 1.5 Ta
Examples →	Nimonic 80A	U-500	N-115/U-700/R-77	IN-100/R-100	Mar-M246

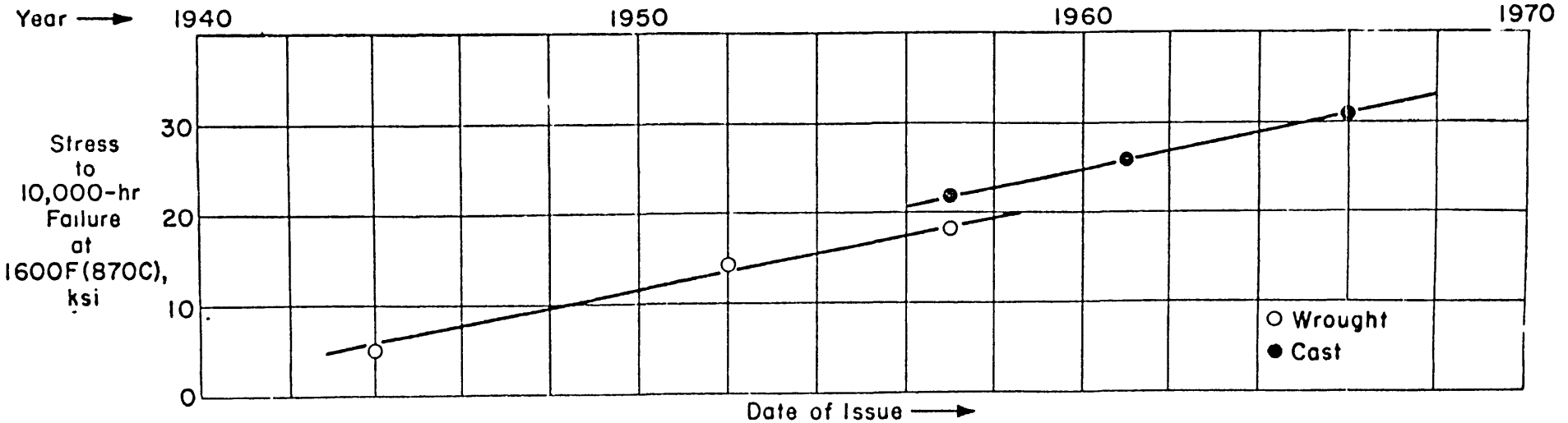


Fig. 2.1 Changes in nickel base superalloy design (1)

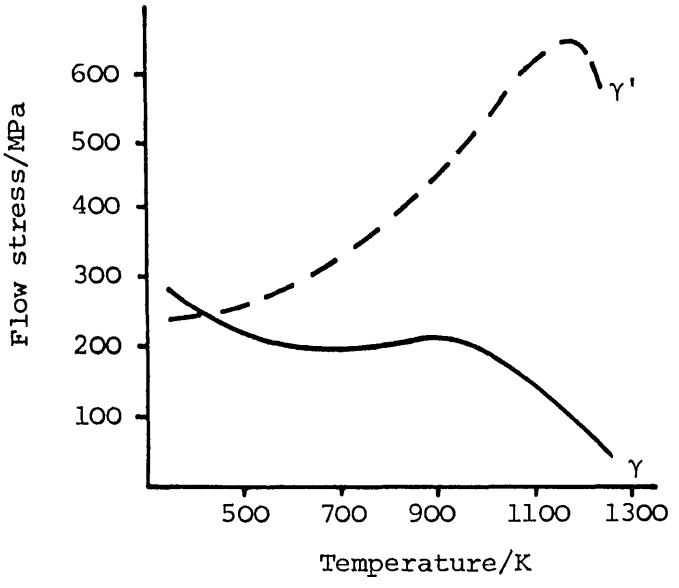


Fig. 2.2 Variation of γ matrix and γ' precipitate flow stresses with temperature

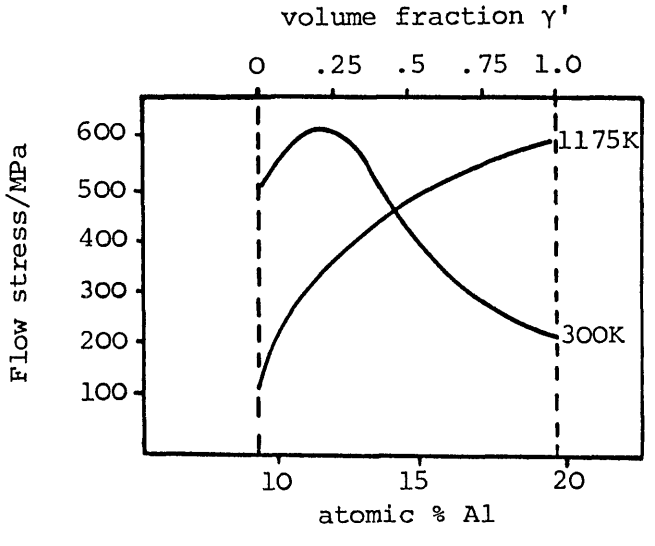


Fig. 2.3 Effect of increasing the volume fraction of γ' on flow stress

CHAPTER 3

MECHANISMS OF CRACK GROWTH AT HIGH TEMPERATURES IN NICKEL BASE SUPPERALLOYS

3.1 Introduction

Failure of components operating at elevated temperatures can occur by either the propagation of diffuse damage, with cavities nucleating and growing throughout the material, or by the propagation of localised damage in the form of a main crack. The present work is concerned with the latter failure mechanism, which has been frequently observed to cause failure of cast aircraft gas turbine blading. Internal cooling holes in the trailing edge section of the blades provide a stress concentration, which causes damage accumulation to be localised, leading to subsequent failure by the propagation of a main crack. In this chapter discussion is restricted to mechanisms responsible for crack growth at elevated temperatures. Creep failure, involving the propagation of diffuse damage, is discussed briefly in Appendix 3.

Cast nickel base superalloy components invariably contain inherent casting defects such as microporosity or shrinkage cracks. During service, these defects can act as stress raisers, thereby causing premature crack initiation. Crack initiation from internal casting defects has been observed during high cycle fatigue testing of the cast nickel base superalloy IN939 at 850^{o}C (11). Under these circumstances initiation occurs very rapidly and crack propagation occupies the majority of component life.

Crack propagation data are generally obtained from laboratory tests which are designed to simulate service loading conditions. Reliable

extrapolation of the laboratory data to service conditions requires a detailed knowledge of the underlying mechanisms responsible for crack growth under both laboratory and service conditions. Crack growth can occur as a result of static (creep) or cyclic (fatigue) loading. High temperature crack growth under creep loading invariably occurs by an intergranular mode, while crack growth under fatigue loading may be predominantly transgranular or intergranular depending on alloy structure and loading conditions. The mechanisms responsible for transgranular fatigue crack growth at high temperatures are similar to those which operate at ambient temperatures. Intergranular fatigue crack growth, however, involves different cracking mechanisms, which often bear a close resemblance to the mechanisms responsible for crack growth under static loading.

The following chapter describes the underlying mechanisms responsible for both transgranular and intergranular crack propagation. The effects of loading conditions, environment and alloy microstructure on the cracking mechanism are also considered.

3.2 High Temperature Crack Growth under Static Loading

Creep crack growth in nickel base superalloys at high temperatures ($T > 0.5T_M$) generally occurs by an intergranular mode. The majority of studies (3,12,13) reveal that the growth of a creep crack is related to the build-up of cavitation damage in the plastic zone ahead of the crack tip. However, Sadananda (14) has suggested that a different growth mechanism may operate in the wrought nickel base superalloy Inconel 718 in the temperature range 540 - 650°C. Based on experimental observations (15), he proposed a mechanism for crack growth involving grain boundary diffusion of vacancies to the crack tip. Further discussion will be restricted to micromechanisms of creep crack growth involving damage accumulation ahead of the crack tip.

Sadananda and Shahinian (16) have illustrated schematically the types of damage which can occur ahead of a crack subjected to high temperature static loading (figure 3.1).

(a) Crack tip blunting due to rapid deformation

(b) Wedge type or triple point crack growth.

(c) Round 'r' type cavity growth.

Crack propagation only occurs as a result of the latter two processes and involves linking of the damage with the main crack.

Factors which influence the grack growth rate are the relative rates of matrix deformation and grain boundary sliding, which, in turn, are determined by the chemical and metallurgical structure of the alloy and the testing temperature. Crack growth is also influenced by grain boundary precipitate morphology and the sensitivity of the alloy to environmental interactions. Environmental and microstructural effects on creep crack growth are discussed in Sections 3.2.1 and 3.2.3.

Analysis of creep damage mechanisms has indicated that grain boundary sliding provides the most effective means of cavity or crack initiation. Min (17) has shown that there is a range of applied strain rate, for which grain boundary sliding can cause sufficient stress concentration at triple point junctions to form wedge cracks. If the strain rate is too high, grain boundary sliding will not occur and fracture can occur by transgranular crack propagation or ductile rupture. If the strain rate is too low to nucleate wedge cracks, or if grain boundary sliding is restricted by grain boundary precipitates, discrete 'π' type cavities can nucleate at the precipitates. Restriction of grain boundary sliding by grain boundary precipitates (usually carbides) can cause sufficient local stress concentration to allow easy cavity nucleation at the precipitates. When sliding rates are small, stress concentrations at the precipitates may relax by creep and allow cavities to nucleate by clustering of vacancies. Once nucleated, these discrete 'π' type cavities grow by one of the following mechanisms:

1. Diffusion; modelled by Hull and Rimmer (18), Chuang and Rice (19) and Raj and Ashby (20).

2. Coupled diffusion and power law creep; modelled by Needleman and Rice (21).

3. Power law creep; modelled by Pavinich and Raj (22).

Wedge crack formation is generally observed at intermediate temperatures for high strain rates, while higher temperatures and lower strain rates favour 'π' type cavity formation. Discrete 'π' type cavities grow by a power law creep mechanism at higher temperatures and stresses, while growth by diffusion occurs at relatively lower

temperatures and stresses. At sufficiently low stresses, the rate of cavity growth is constrained by creep deformation of the surrounding grains, although the local void growth mechanism is diffusive.

Experimental observations on a wide variety of materials have indicated that creep crack growth is highly sensitive to the environment, temperature and microstructure. The following sections examine the effects of environment, temperature and microstructure on creep crack growth in nickel base superalloys.

3.2.1 Environmental Effects

Several authors have observed higher creep crack growth rates for alloys tested in air compared with those obtained in inert environments such as helium or a vacuum (3,16,23). The presence of oxygen has been identified as the principal cause of this acceleration in crack growth.

Diffusion of oxygen along grain boundaries can provide an additional driving force for the nucleation and growth of grain boundary cavities (24,25). Alternatively, diffusion of oxygen along grain boundaries can cause embrittlement contributing to debonding and brittle decohesion of the grains (26). Environmental effects generally tend to be more pronounced in smaller grained wrought alloys than in larger grained cast materials. However, environmental sensitivity can vary significantly between one wrought alloy and another, depending on the micro mechanisms responsible for crack growth. The wrought nickel base superalloys Inconel 718 and Inconel X-750 both exhibit significant environmental sensitivity at intermediate temperatures, where creep crack growth occurs in a brittle intergranular manner with no observable

microcracking ahead of the main crack (27). However, much lower environmental sensitivity was observed for the wrought alloys Udimet 700 and Nimonic PE16, in which creep crack growth is accompanied by a build-up of cavitation damage ahead of the crack tip (27,28).

In general, the extent of any environmental interaction depends on several factors, including the crack growth mechanism, temperature and alloy microstructure. Environmental sensitivity tends to be lowest in cast alloys tested at very high temperatures, where crack growth occurs by a deformation controlled process, involving growth of cavities ahead of the main crack by power law creep.

3.2.2 Temperature Effects

Testing temperature is important in determining both the crack growth mechanism and the extent of any environmental interaction. Higher temperatures generally favour the nucleation of 'η' type cavities ahead of the main crack, which can grow by either a diffusional mechanism, a deformation controlled mechanism or a combination of the two. The operative crack growth mechanism is also influenced by other factors, such as stress level, strain rate, environment and alloy microstructure. Higher temperatures also favour increased environmental interaction, although the sensitivity of the crack growth mechanism to the environmental effect may be reduced.

3.2.3 Microstructural Effects

Increases in grain size generally improve the creep crack growth resistance and reduce the environmental sensitivity of nickel base superalloys (5,6,12,29). Wavy, or serrated, grain boundaries are beneficial as they restrict grain boundary sliding and increase the

path for grain boundary diffusion (3,5,6,7,30). Sadananda and Shahinian (31) suggested that creep crack growth was more sensitive to the presence of grain boundary precipitates than to the alloy grain size. Grain boundary carbide morphology is certainly important (3,4), although Floreen (3) has shown that the optimum carbide microstructure depends on the test environment. Grain boundary carbides obstruct grain boundary sliding, but they can also provide sites for easy cavity nucleation.

Gamma prime, γ', morphology is also important. Coarsening the γ' precipitates can increase slip homogeneity and yield improvements in creep crack growth resistance (3,6,23). However, coarsening of the γ' can lead to a loss of creep strength, so that the optimum size of the γ' precipitates reflects a compromise between achievement of adequate crack growth resistance and creep strength (6).

Microstructural changes can effect the environmental sensitivity of an alloy. Environmental sensitivity is generally maximised in small grained materials. Pedron and Pineau (29) discovered that the environmental sensitivity of the wrought alloy Inconel 718 could be altered by changing the grain boundary microstructure. Small additions of the elements boron, zirconium and hafnium have been shown to dramatically reduce the environmental sensitivity of nickel base superalloys (8,9).

3.3 High Temperature Crack Growth under Cyclic Loading

High temperature fatigue crack growth is a complex problem because it involves additional factors, which do not influence behaviour at lower temperatures. Creep and environmental effects become increasingly significant at higher temperatures. Cyclic frequency (or strain rate), R ratio (ratio of minimum to maximum cyclic stresses), waveform, hold times, temperature, microstructure and environment all have strong influences on fatigue crack growth behaviour.

At high frequencies and low R ratios, in the absence of hold times, creep and environmental effects are minimised and crack growth can occur by a transgranular mode (as at ambient temperatures). Lower stress intensities favour crystallographic Stage I cracking, while at higher stress intensities cracks extend by Stage II growth, which occurs perpendicular to the applied stress and is generally non-crystallographic. Figure 3.2 shows, schematically, the differences between Stage I and II growth. The striation mechanism for Stage II growth is the most widely observed mechanism for crack growth in ductile materials at medium to high stress intensity factor ranges (ΔK). At lower values of ΔK, near the threshold, slip is restricted, favouring Stage I growth (31). Alloys which show planar slip behaviour, such as Udimet 700, can exhibit crystallographic cracking over a wider range of ΔK (33,34).

Decreasing the cyclic frequency, increasing the temperature or the R ratio, or imposing tensile hold periods can all cause increasing amounts of intergranular fracture, similar to that described in Section 3.2 for static loading. The following sections examine the effects of environment, temperature, frequency, R ratio, waveform, hold times and

microstructure on fatigue crack propagation in nickel base superalloys at elevated temperatures.

3.3.1 Environmental Effects

The presence of an air environment can lead to increases in the cyclic crack growth rate without any change in the crack growth mechanism (26,35). Fatigue processes enhance environmental effects at the crack tip by favouring oxygen transport ahead of the crack. In the case of transgranular crack growth, oxygen can diffuse along persistent slip bands to enhance Stage I cracking or ahead of the crack tip to enhance Stage II growth. Environmental effects tend to be more pronounced in the threshold region due to the increased time available for the diffusion of oxygen.

Diffusion of oxygen along grain boundaries, particularly in small grained wrought alloys (36), can increase the likelihood of intergranular fracture. Environmental effects can promote a transition to intergranular crack growth, particularly in alloys which show appreciable environmental sensitivity. Environmental effects on intergranular cracking are discussed in section 3.2.1.

3.3.2 Temperature Effects

The effect of increasing temperature on the fatigue crack growth rate in air is, generally, to cause an increase at a given frequency, R ratio and ΔK. Shahinian (37) plotted cyclic crack growth rate as a function of temperature for several nickel base superalloys (figure 3.3) tested at high frequencies where creep effects were assumed to be small. Several authors (34, 38) have attributed increases in cyclic crack growth rate with temperature to environmental effects at the crack tip.

Lloyd (39) has shown that the temperature dependence of fatigue crack growth rate in type 316 stainless steel, which is relatively environmentally insensitive, can be adequately explained in terms of changes in yield or flow stress.

Increasing temperature increases the likelihood of intergranular fracture, which involves consequent changes in the mechanisms responsible for crack growth.

3.3.3 Frequency Effects

Many authors (11,23,26,29,40,41,42) have observed an increase in cracking rate with a reduction in cyclic loading frequency for nickel base superalloys tested at elevated temperatures in an air environment. Three theories have been proposed to account for these experimental observations. Increases in crack growth rate with decreasing frequency are attributed to:

1. Creep Effects

   At lower frequencies time is available for creep damage to accumulate ahead of the crack.

2. Environmental Effects

   Oxygen in the air is an aggressive species, and lower frequencies allow significant penetration of oxygen ahead of the crack.

3. Strain Rate Sensitivity

   Changes in strain rate as the loading frequency is decreased may change the deformation and crack growth mechanisms.

Increases in the cyclic crack growth rate are invariably accompanied by increases in the amount of intergranular fracture (11,23,26,40,42,43,44).

Figure 3.4 shows, schematically, the variation of cyclic crack growth rate with frequency for an alloy tested in both air and an inert environment (or vacuum). Diffusion of oxygen along grain boundaries promotes intergranular cracking at higher frequencies in air than in an inert environment. Build up of creep cavitation damage ahead of the crack tip also favours a transition to intergranular fracture. Sensitivity of intergranular cracking mechanisms to strain rate is discussed in section 3.2. Briefly, the strain rate must be below a certain value for intergranular fracture to occur. Intergranular crack growth mechanisms are therefore favoured by lower cyclic loading frequencies (and strain rates).

3.3.4 R Ratio Effects

At high temperatures, where creep and environmental interactions may operate, increases in cyclic crack growth rate (for a given ΔK) have been observed with increases in R ratio (11,45). Hoffelner and Speidel (11) found increases in crack growth rates with increases in R ratio for a cast nickel base superalloy in both air and vacuum. As cast alloys tend to be relatively insensitive to environment, the observed R ratio effects were attributed to creep effects causing a transition from transgranular to intergranular cracking. Crack growth rates have been found to be more sensitive to changes in R ratio for higher R values (45).

For crack growth in the threshold region, crack closure effects can be significant at low R ratios (46). Surface roughness induced non-closure effects are particularly apparent in coarse grained alloys at longer crack lengths.

3.3.5 Waveform Effects

The loading waveform can influence the transition frequency from transgranular to intergranular crack growth (7). In particular, slow/fast cycling can promote intergranular cavitation and oxidation damage. Min and Raj (47) have shown that slow/fast cycling can lead to an intergranular failure mode involving wedge crack formation ahead of the main crack.

Waveforms, which include tensile hold times (such as trapezoidal or square waveforms) can also favour intergranular crack propagation.

3.3.6 Hold Time Effects

Increases in crack growth rates have been observed (13,29,36,45, 48,49) when tensile hold times are included in the loading cycle. This acceleration in crack growth is often associated with the occurrence of intergranular cracking. Increases in crack growth rate have been attributed to:

1. Creep Effects
2. Environmental Effects

The relative contribution from the two effects depends on several factors, including alloy composition and microstructure, test temperature, hold time and load level. Creep damage can accumulate ahead of the crack tip during the hold time, while time is also available for diffusion of oxygen ahead of the crack tip. Both of these processes can influence cracking behaviour. In general, environmental effects tend to be more significant at intermediate temperatures, while creep effects dominate at higher temperatures.

3.3.7 Microstructural Effects

Transgranular fatigue crack growth can occur by either a structure sensitive Stage I mechanism or by a structure insensitive Stage II mechanism (figure 3.2). Microstructure and yield stress have relatively little effect on Stage II growth, but crystallographic Stage I growth is highly sensitive to changes in microstructure. Transition from Stage I to Stage II cracking has frequently been observed when the cyclic plastic zone size becomes equal to the material grain size (7,36,50). This explains why large grained cast alloys tend to show extensive Stage I cracking.

Optimising component life at high temperatures can often be achieved by retarding the onset of intergranular cracking. Larger grained cast alloys often show rapid initiation, so that the majority of component life is spent in crack propagation. The onset of intergranular cracking can be retarded if grain boundaries are wavy (or serrated) (5). Increasing the grain size improves the resistance of alloys to high temperature fatigue crack growth (6,29,36), particularly when crack propagation occurs by an intergranular mode. Coarsening the γ' precipitate can yield improvements in intergranular crack growth resistance (3,6,23) but may also lead to a loss of creep strength. A compromise in properties may be required in this case. Grain size and grain boundary precipitate morphology are also crucial in determining the extent of any environmental effect on intergranular crack growth. The effects of the environment on intergranular cracking are discussed in section 3.2.1.

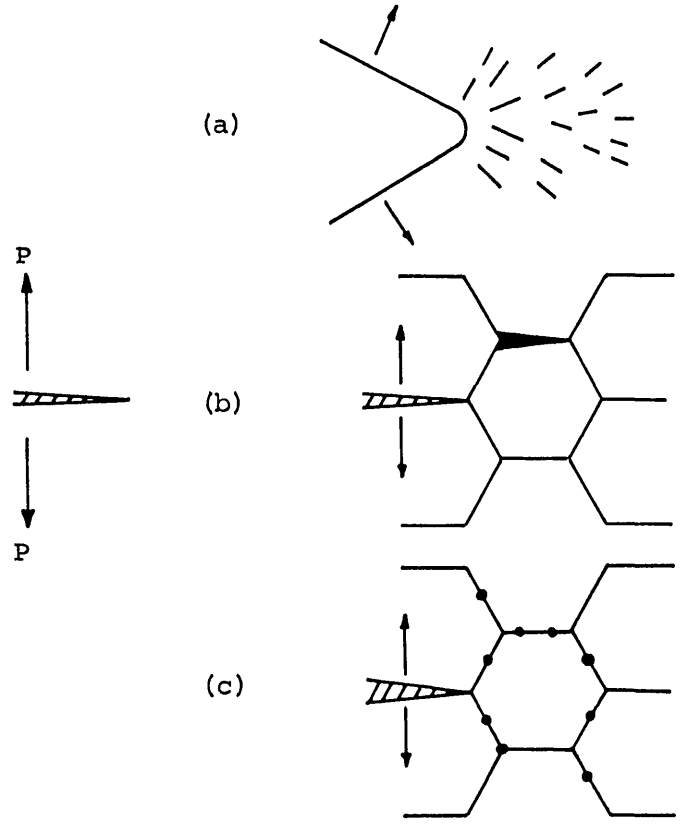
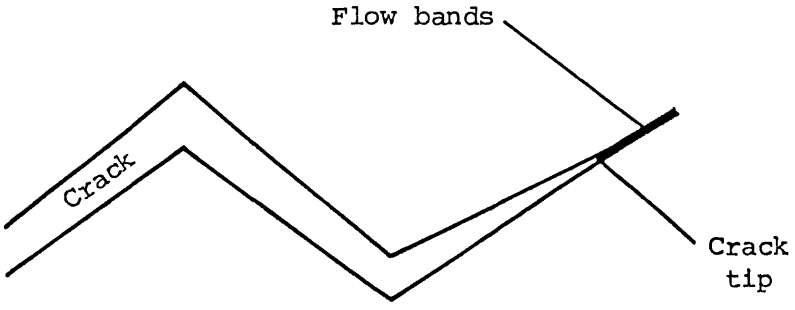
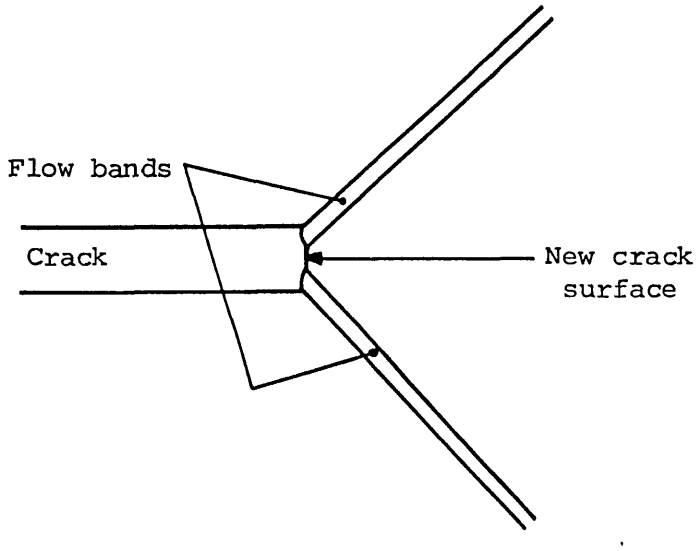


Fig. 3.1 Types of damage which can occur ahead of a crack subjected to high temperature static loading (a) crack tip blunting due to rapid deformation and formation of fissures ahead of the crack tip, (b) grain boundary sliding leading to nucleation and growth of wedge cracks, and (c) formation of cavities at grain boundaries and growth by plastic deformation (16)



(a) Stage I fatigue crack growth



(b) Stage II fatigue crack growth

Fig. 3.2 Schematic diagram showing the differences between Stage I and Stage II fatigue crack growth

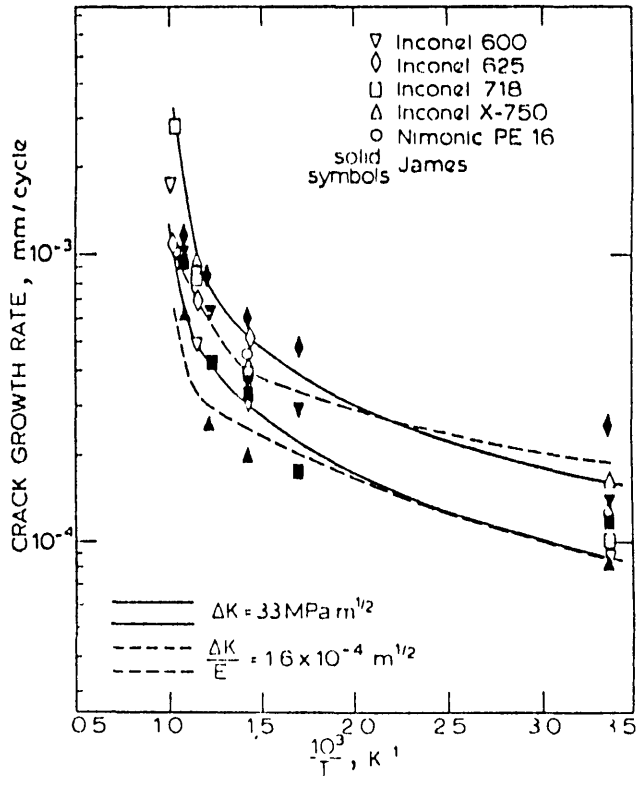


Fig. 3.3 Variation of crack growth per cycle with temperature for a range of nickel base superalloys (37)

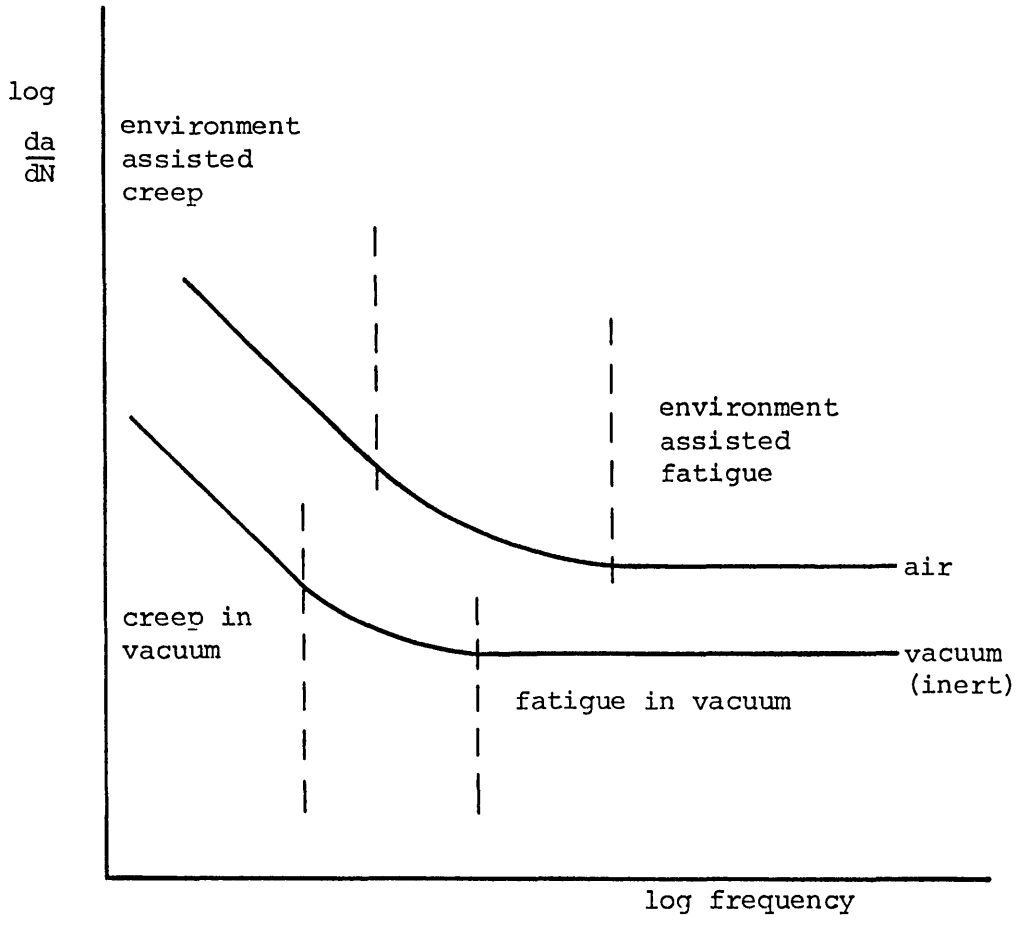


Fig. 3.4 Typical variation of cyclic crack growth rate with frequency for an alloy tested in air and an inert environment

APPENDIX 3

CREEP FAILURE MECHANISMS IN NICKEL BASE SUPERALLOYS

A3.1 Phenomenon of Creep

At elevated temperatures, metals under load often exhibit mechanical behaviour which is non-linear and time dependent. This high temperature behaviour is termed creep. Creep data is frequently obtained from tensile creep tests, in which a uniaxial specimen is subjected to a constant stress (although creep tests are also carried out under constant load conditions) at a constant temperature. The response of the specimen to the applied stress is represented by a strain versus time characteristic, known as a creep curve. The actual form of this curve depends on several factors, including material, environment, test temperature and stress level.

A schematic illustration of the form of a typical creep curve is shown in figure A3.1. Although not representative of all metal behaviour, this curve may be used to highlight the areas of interest. On loading, the initial response of the uniaxial specimen will be either elastic or elastic/plastic depending on the stress level. As time passes, the deformation appears to exhibit three regions of behaviour. Region I, known as primary creep, is associated with a gradual decrease in strain rate which, physically, may represent a period of work hardening in the material. Secondary or steady-state creep which occurs in region II can be thought of as a balance between softening and hardening processes. In this region, the material exhibits a constant strain rate. Finally, region III, known as tertiary creep, is associated with an acceleration in creep rate up to the point of failure.

A3.2 Creep Mechanisms

Creep behaviour occurs as a result of two competing processes, which cause material hardening and softening. Steady state creep occurs when a kinetic balance is reached between the two processes. The hardening mechanism can be attributed to a decrease in the rate at which dislocations cross their obstacles (in the case of nickel base superalloys γ' precipitates act as obstacles to dislocation movement). The softening mechanism can be attributed to dislocation glide at low temperatures and to dislocation climb or grain boundary sliding at higher temperatures. At high stresses, dislocations can bow round or cut through the γ' precipitate particles, while at lower stresses this is not possible. At higher temperatures, increased mobility allows dislocations to climb while grain boundary zones become areas of weakness in the material. At lower stresses, when dislocations are unable to bow round or cut through the particles, either the dislocations surmount the particles by climb, or alternatively, deformation occurs predominantly in grain boundary zones (ie by grain boundary sliding and deformation of the grains in regions adjacent to the grain boundaries). Two theories have been proposed to account for the acceleration of the creep rate observed at the onset of the tertiary stage for tests conducted under conditions of constant stress. The acceleration of creep rate has been attributed to either

1. Development of cavities and cracks large enough to affect the deformation process.

2. Microstructural instability.

Creep fracture at elevated temperature occurs due to the nucleation and growth of cavities or cracks within the material, which eventually coalesce and cause failure. The failure mechanism which operates in a given situation is dependent on the applied stress, temperature and environment. Fracture mechanism maps, constructed by Ashby (51), may be used to predict the likely failure mechanism for a range of metals from a knowledge of temperature and stress level.

Creep failure at elevated temperatures can occur by a variety of mechanisms. In general, high stresses favour a relatively ductile failure mode with cavities nucleating and growing within the grains until they coalesce to give a transgranular fracture path. Lower stresses tend to favour a more brittle intergranular failure mode. Grain boundaries slide and wedge cracks or cavities grow on grain boundaries lying roughly normal to the tensile axis. The growth can occur by diffusion alone (18,19,20), by power law creep alone (22), or by a coupling of diffusion and power law creep (21). Eventually the cracks or cavities coalesce to give an intergranular fracture path.

Creep failure mechanisms can be significantly affected by the environment, particuarly in situations where failure occurs by an intergranular mode. In inert environments, failure often occurs due to the accumulation of cavitation damage on internal grain boundaries (30,52). These cavities grow and finally link up to cause failure. This mechanism can also be responsible for creep failures in air (52), although in many cases failure occurs by the formation of oxidised surface cracks, which initiate and grow from grain boundaries intersecting the specimen surface (30,53,54). Both air strengthening, manifested by lower creep rates and longer rupture lives for specimens

tested in air compared to those tested in an inert environment, and air weakening are possible. (30,55).

Microstructural features can be very important in determining the creep behaviour of nickel base superalloys. Matrix γ' precipitates hinder dislocation movement within the grains and are important in determining the strain rate during secondary creep, known as the minimum creep rate. The magnitude of the minimum creep rate for a given temperature and stress level depends, to a significant degree, on the volume fraction and size of the γ' precipitates (4). Rupture lives have been shown to be sensitive to grain size (and shape) and grain boundary precipitate morphology (4,30,55). Environmental attack is minimised in large grained alloys due to the lack of transverse grain boundaries intersecting the specimen surface. Cavity nucleation can be retarded by reducing the amount of grain boundary sliding. Large grains, wavy (serrated) grain boundaries and grain boundary carbide precipitates are all used to inhibit grain boundary sliding in nickel base superalloys.

The behaviour of a nickel base superalloy under creep conditions is complex and is influenced by several factors including environment, temperature, stress level and alloy microstructure. Mathematical representation of creep behaviour is discussed in Appendix 5.

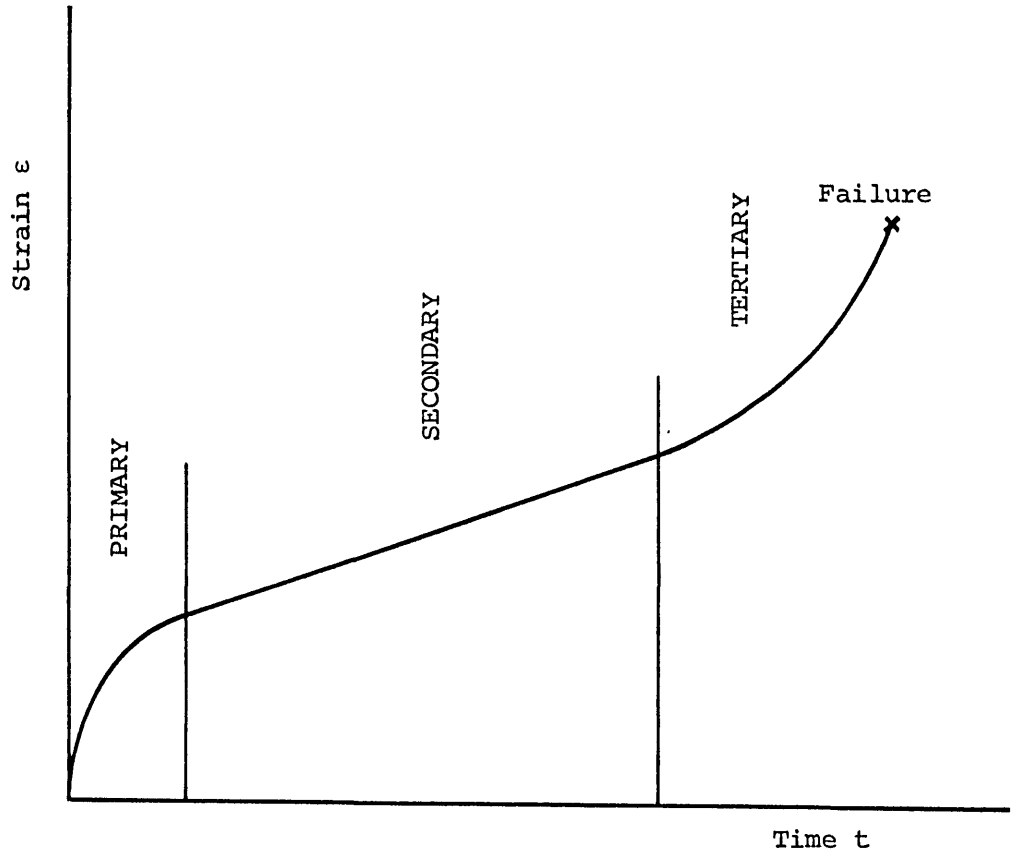


Fig. A3.1 Typical creep curve

CHAPTER 4

CHARACTERISATION OF CRACK TIP STRESS AND STRAIN FIELDS IN MATERIALS AT HIGH TEMPERATURES

4.1 Introduction

Correlating or predicting crack growth at high temperatures relies on a knowledge of the stress and strain fields operating at the crack tip. Under linear elastic conditions, the stress distribution at the tip of a stationary crack can be characterised by the stress intensity factor, K. However, at higher temperatures, plasticity and creep effects may become significant due to

1. A decrease in yield stress with increasing temperature tending to promote increased plasticity in the crack tip region.

2. Creep effects becoming increasingly significant at higher temperatures, and especially for $T > 0.5T_M$.

When the extent of crack tip plasticity becomes significant, crack tip fields may be characterised by a parameter known as J-Integral, while if the material is deforming by secondary creep, crack tip stresses and strains are characterised by a parameter C^* (also known as $\dot{J}$ and J^*). Parameters K, J and C^* characterise the stress and strain fields at a stationary crack tip under steady state conditions. Under non-steady conditions, other time dependent parameters may be required to characterise the crack tip fields.

Although K, J and C^* only strictly characterise the stress and strain fields at the tips of stationary cracks, these parameters have been used, with considerable success, to correlate high temperature

crack growth rates.

This chapter introduces parameters which characterise the stress and strain fields at the tips of stationary cracks in materials deforming under steady state conditions. Several constitutive relationships are considered. Finally, the stress and strain fields, which develop at a crack tip under non-steady conditions, are discussed.

4.2 Linear Elastic Material Behaviour

Irwin (56) determined the elastic stress distribution ahead of a stationary crack, which takes the form

$$\sigma_{ij} = \frac{K}{\sqrt{2\pi r}} \delta_{ij}(\theta) \tag{4.1}$$

where $\delta_{ij}(\theta)$ is an angular function given by Irwin, and stress intensity factor, K, is a measure of the intensity of the crack tip stress singularity.

Stress intensity factor, K, is related to the energy release rate, G, in the following manner

$$K = \sqrt{EG} \qquad \text{for plane stress} \tag{4.2}$$

$$K = \sqrt{\frac{EG}{(1-\nu^2)}} \qquad \text{for plane strain} \tag{4.3}$$

where G may be derived from energy considerations (figures 4.1 and (4.2)

$$G = -\frac{1}{B}\frac{dU}{da} \tag{4.4}$$

Material behaviour may be idealised as linear elastic if both the plastic zone, r_p, and the creep zone, r_c, ahead of the crack tip are small compared to crack length, a, and remaining ligament (figure 4.3). The size of the plastic zone can be estimated in terms of the stress intensity factor, K, and yield stress, σ_y (57).

$$r_p = \frac{1}{2\pi}\left[\frac{K}{\sigma_y}\right]^2 \qquad \text{for plane stress} \tag{4.5}$$

$$r_p = \frac{1}{6\pi}\left[\frac{K}{\sigma_y}\right]^2 \qquad \text{for plane strain} \tag{4.6}$$

The above expressions represent lower estimates of the extent of crack

tip plasticity as no account is taken of the stress redistribution caused by the plasticity. Although the plastic zone is approximated as circular, it is in fact 'dumb-bell' shaped.

Stress intensity factor, K, may also be used to define the extent of crack tip opening, known as the crack tip opening displacement (CTOD), where

$$\text{CTOD} = \beta \frac{K^2}{E\sigma_y} \qquad \text{for plane stress} \qquad (4.7)$$

$$\text{CTOD} = \beta \frac{K^2(1-\nu^2)}{E\sigma_y} \qquad \text{for plane strain} \qquad (4.8)$$

and the value of β varies according to the assumptions made. Quasi elastic-plastic approaches give values of $\beta = 1$ and $4/\pi$, while measurements of the CTOD tend to give $\beta \simeq 1$. Despite these observations, the plane strain estimate most frequently used is $\beta = 0.44$ from Rice (58)

Under cyclic loading, the stress intensity factors associated with maximum and minimum loads, P_{max} and P_{min} (figure 4.4) are designated K_{max} and K_{min}. The cyclic loading ratio, R, is defined as

$$R = K_{min}/K_{max} \qquad (4.9)$$

and the stress intensity factor range

$$\Delta K = K_{max} - K_{min} = K_{max}(1-R) \qquad (4.10)$$

The size of the plastic zone operating under fatigue conditions, the reversed plastic zone size Δr_p, can be deduced (57) by assuming the local crack tip flow stress is approximately twice the monotonic flow stress σ_y.

Thus,

$$\Delta r_p = \frac{1}{8\pi}\left[\frac{K}{\sigma_y}\right]^2 \qquad \text{for plane stress} \qquad (4.11)$$

$$\Delta r_p = \frac{1}{24\pi}\left[\frac{K}{\sigma_y}\right]^2 \qquad \text{for plane strain} \qquad (4.12)$$

A diagrammatic idealisation of the reversed plastic zone, Δr_p, is shown in figure 4.5, following a plastic superposition argument advanced by Rice (59).

Similarly, the cyclic crack tip opening displacement, $CTOD_c$, may be derived by again assuming that the local crack tip flow stress is approximately $2\sigma_y$. Then,

$$CTOD_c = \beta \frac{K_{max}^2}{2\sigma_y E} \qquad \text{for plane stress} \qquad (4.13)$$

$$CTOD_c = \beta \frac{K_{max}^2(1-\nu^2)}{2\sigma_y E} \qquad \text{for plane strain} \qquad (4.14)$$

where typical values of β were given following equations 4.7 and 4.8.

4.3 Elastic-Plastic Material Behaviour

When substantial plastic deformation occurs, the plastic zone size, r_p (figure 4.3), will no longer be small compared to the crack length and remaining ligament, and the stress intensity factor, K, will cease to characterise the stress and strain distribution in the region of the crack tip. A corresponding non-linear parameter is required to characterise the crack tip stress and strain fields under these conditions.

Figure 4.6 shows an arbitrary contour surrounding a crack tip in a two dimensional body of uniform thickness, subjected to a remote tensile load. Rice (60) has defined a line integral, J, such that

$$J = \int_{\Gamma} W_s dy - T_i \frac{\partial u_i}{\partial x} \cdot ds \qquad (4.15)$$

where W_s is the strain energy density, given by

$$W_s = \int \sigma_{ij} \, d\varepsilon_{ij} \qquad (4.16)$$

and T_i and u_i are the components of the traction and displacement vectors respectively, x and y are co-ordinates and s is the arc length along Γ. Path independence of the J integral has been demonstrated for elastic and deformation type elastic-plastic material behaviour. Numerical results from incremental plasticity have been shown to agree fairly well with deformation type results.

Rice (60) has also shown that an alternative derivation of the J integral is possible from energy considerations (figures 4.1 and 4.7).

$$J = -\frac{1}{B} \frac{dU}{da} \qquad (4.17)$$

For the special case where material behaviour is linear elastic $J = G$.

Rice and Rosengren (61) and Hutchinson (62, 63) have shown that the J integral is a measure of the strength of the stress and strain singularities at a stationary crack tip in a power law hardening material. For a constitutive relation of the form

$$\frac{\varepsilon}{\varepsilon_y} = \left[\frac{\sigma}{\sigma_y}\right]^N \tag{4.18}$$

in simple tension, the equivalent relation for a multiaxial stress state is given by

$$\frac{\varepsilon_{ij}}{\varepsilon_y} = 3/2 \left[\frac{\sigma_e}{\sigma_y}\right]^{N-1} \frac{\sigma^1_{ij}}{\sigma_y} \tag{4.19}$$

where the equivalent stress, σ_e, determined using the Maxwell-Mises criterion, is given by

$$\sigma_e^2 = 3/2 \ \sigma^1_{ij} \ \sigma^1_{ij} \tag{4.20}$$

and the deviatoric stress tensor, σ^1_{ij}, is defined as

$$\sigma^1_{ij} = \sigma_{ij} - 1/3 \ \sigma_{kk} \ \delta_{ik} \tag{4.21}$$

where $\delta_{ik} = 1$ if $i = k$ and $\delta_{ik} = 0$ if $i \neq k$.

The stress and strain fields near a stationary crack tip in a power law hardening material are given by

$$\frac{\sigma_{ij}}{\sigma_y} = \left[\frac{J}{I_N \ \sigma_y \ \varepsilon_y \ r}\right]^{1/N+1} \tilde{\sigma}_{ij}(\theta, N) \tag{4.22}$$

$$\frac{\varepsilon_{ij}}{\varepsilon_y} = \left[\frac{J}{I_N \sigma_y \varepsilon_y r}\right]^{N/N+1} \tilde{\varepsilon}_{ij}(\theta, N) \qquad (4.23)$$

where $\tilde{\sigma}_{ij}$ and $\tilde{\varepsilon}_{ij}$ are dimensionless angular functions, given graphically by Hutchinson (62, 63). The factor I_N, tabulated by Hutchinson (62, 63) varies from 2.87 for $N = 13$, to 3.86 for $N = 3$, for plane stress conditions. For plane strain conditions, the following approximate expression for I_N has been derived by McClintock (64)

$$I_N = 10.3 \left\{0.13 + \frac{1}{N}\right\}^{\frac{1}{2}} - \frac{4.8}{N} \qquad (4.24)$$

Stress and strain singularities of the type

$$\sigma_{ij} \alpha \left\{\frac{1}{r}\right\}^{1/N+1} \qquad (4.25)$$

$$\varepsilon_{ij} \alpha \left\{\frac{1}{r}\right\}^{N/N+1} \qquad (4.26)$$

as in equations 4.22 and 4.23 are commonly termed HRR singularities after Hutchinson, Rice and Rosengren (61- 63).

4.4 Steady State Creep Material Behaviour

Goldman and Hutchinson (65) have shown that with a slightly different interpretation, the J integral proposed by Rice (60) could be applied to a cracked body deforming by steady state or secondary creep according to the Norton uniaxial law

$$\frac{\dot{\varepsilon}}{\dot{\varepsilon}_0} = \left[\frac{\sigma}{\sigma_0}\right]^n \tag{4.27}$$

which may be generalised for a multiaxial stress state by

$$\frac{\dot{\varepsilon}_{ij}}{\dot{\varepsilon}_0} = 3/2 \left[\frac{\sigma_e}{\sigma_0}\right]^{n-1} \frac{\sigma^1_{ij}}{\sigma_0} \tag{4.28}$$

where σ_e is the equivalent stress, defined in equation 4.20, and σ^1_{ij} is the deviatoric stress tensor, defined in equation 4.21. The relationships developed in Section 4.3 for power law hardening behaviour continue to hold if strain like quantities are replaced by their respective rates. Using the analogy suggested by Goldman and Hutchinson (65), Landes and Begley (66) and Nikbin et al (67) have proposed a contour integral, C^* (also known as $\dot{J}$ or J^*), which characterises the crack tip stress and strain rate fields for a material deforming by secondary creep.

Figure 4.6 shows an arbitrary contour surrounding a crack tip in a two dimensional body of uniform thickness subjected to a remote tensile load. If the body is deforming by secondary creep, C* can be defined as

$$C^* = \int_\Gamma W_s^* dy - T_i \frac{\partial \dot{u}_i}{\partial x} \cdot ds \tag{4.29}$$

where W_s^* is the strain energy rate density, given by

$$W_s^* = \int \sigma_{ij} \, d\dot{\varepsilon}_{ij} \tag{4.30}$$

and T_i and $\dot{u}_i$ are the components of the traction and displacement rate vectors, respectively, x and y are co-ordinates and s is the arc length along Γ.

By analogy with the J integral, C^* may be evaluated from energy rate considerations (figures 4.1 and 4.8)

$$C^* = -\frac{1}{B}\frac{dU^*}{da} \tag{4.31}$$

C^* may also be used to characterise the stress and strain rate fields around a stationary crack tip in a material deforming by secondary creep. Stress and strain rate fields near the crack tip are given by

$$\frac{\sigma_{ij}}{\sigma_o} = \left[\frac{C^*}{I_n \sigma_o \dot{\varepsilon}_o r}\right]^{1/n+1} \tilde{\sigma}_{ij}(\theta, n) \tag{4.32}$$

$$\frac{\dot{\varepsilon}_{ij}}{\dot{\varepsilon}_o} = \left[\frac{C^*}{I_n \sigma_o \dot{\varepsilon}_o r}\right]^{n/n+1} \tilde{\dot{\varepsilon}}_{ij}(\theta, n) \tag{4.33}$$

where non-dimensional angular functions $\tilde{\sigma}_{ij}$ and $\tilde{\dot{\varepsilon}}_{ij}$ can be obtained from Hutchinson (62, 63) by substituting $n = N$. By analogy, the factor I_n varies with n as I_N varies with N. I_n varies from 2.87, for $n = 13$, to 3.86, for $n = 3$, for plane stress conditions (62, 63). For plane strain conditions, the following approximate expression has been derived by McClintock (64)

$$I_n = 10.3(0.13 + \frac{1}{n})^{\frac{1}{2}} - \frac{4.8}{n} \tag{4.34}$$

4.5 Generalised Material Behaviour

Analysis of crack tip stress and strain fields has, thus far, been confined to situations in which the material obeys one of the following simplified uniaxial constitutive relations

1. $\varepsilon = \sigma/E$ — Linear Elastic

2. $\varepsilon/\varepsilon_y = (\sigma/\sigma_y)^N$ — Power Law Hardening

3. $\dot{\varepsilon}/\dot{\varepsilon}_0 = (\sigma/\sigma_0)^n$ — Secondary Creep

In general, when a cracked body is loaded at elevated temperature, the initial stress field surrounding the crack tip will be either elastic or elastic-plastic depending on the load level. The instantaneous crack tip stress and strain fields will be governed by either K or J. As time passes, creep deformation can cause considerable relaxation of the crack tip stresses, and time dependent integrals are required to characterise crack tip stress and strain fields. Eventually, when secondary creep deformation predominates, a steady state crack tip stress field is achieved which is characterised by C^*.

In many practical situations, the time required to establish this steady state may be significant compared to the life of a component or the duration of a laboratory test. It is, therefore, necessary to study stress distributions around stationary crack tips under non-steady state conditions.

4.5.1 Transition from Small Scale Creep to Extensive Secondary Creep

In creep problems, small scale creep means that elastic strains dominate everywhere except in a small 'creep zone', which grows around

the crack tip (figure 4.3). The creep zone boundary is defined as the locus of equality of creep strain and elastic strain. Assuming that the near tip stress fields, for both small scale creep and extensive creep, obey the generalised HRR singularity

$$\frac{\sigma_{ij}}{\sigma_o} = A(t) \cdot \left[\frac{1}{I_n}\right]^{1/n+1} \tilde{\sigma}_{ij}(\theta, n) \qquad (4.35)$$

where $\tilde{\sigma}_{ij}$ is a dimensionless angular function given graphically by Hutchinson (62,63), Riedel and Rice (68) have shown, that for small scale creep, the amplitude of the near tip stress field is given approximately by

$$A(t) = \left[\frac{G}{(n+1) I_n \dot{\varepsilon}_o \sigma_o t}\right]^{1/n+1} \qquad (4.36)$$

assuming approximate path independence of the J integral. When there is extensive secondary creep of the whole body, C^* determines the amplitude of the HRR stress singularity (equation 4.32) and

$$A(t) = \left[\frac{C^*}{I_n \sigma_o \dot{\varepsilon}_o}\right]^{1/n+1} \qquad (4.37)$$

is then the amplitude of the near tip stress field.

Riedel and Rice (68) have shown that after a characteristic time, t_I, there is a transition from small scale creep to extensive creep (and equations 4.36 and 4.37 become identical for $t = t_I$) Thus,

$$t_I = \frac{G}{(n+1) C^*} \qquad (4.38)$$

Wilkinson et al (69) have analysed the time dependent development of the stress fields at the tips of stationary cracks using finite

element methods. Energy rate integrals, $C(t)$, were evaluated for several contours, of radius p, around the tips of cracks loaded to $K = 40 MPa\sqrt{m}$ with $n = 5$ in a range of specimen geometries. Figure 4.9 shows the time dependent energy rate integral, $C(t)$, plotted against time for several contours around the tip of a stationary crack in a centre cracked plate, CCP, specimen. In general, for any time, t, the stress distribution near the crack tip is characterised by a parameter, $C_B(t)$, given by

$$C_B(t) = \lim_{p \to 0} C(t) \qquad (4.39)$$

where p is the radius of the contour, measured from the crack tip, along which $C(t)$ is evaluated.

Figure 4.10 shows a plot of $C_B(t)/C^*$ versus t/t_I for a range of specimen geometries, where t_I is the characteristic transition time estimated by Riedel and Rice (equation 4.38). The data for four different specimen configurations all lie on a single curve, which reaches a steady state after a time, t_{ss}, where $t_{ss} \simeq 10 t_I$. Thus, the characteristic time, t_I, estimated by Riedel and Rice (68) may significantly underestimate the time, t_{ss}, required to reach a steady state. An approximate analytical expression for the crack tip parameter, $C_B(t)$, was given by Wilkinson et al (69) as

$$\left.\begin{aligned} C_B(t) &= \kappa\left[\frac{t_I}{t}\right]^{\delta} C^* \qquad t < \kappa t_I \\ &= C^* \qquad\qquad\quad t > \kappa t_I \end{aligned}\right\} \qquad (4.40)$$

where $\kappa = t_{ss}/t_I$ and the authors suggest that δ may be a function of the creep exponent, n.

4.5.2 Influence of Primary Creep

Implicit in the preceding analysis, is the assumption that the influence of primary creep is negligible. This assumption may be erroneous in certain materials, which exhibit a pronounced primary stage of creep deformation. Riedel (70) has considered the development of primary creep zones in initially elastic, or elastic-plastic media, and also the development of a secondary creep zone in a body deforming in primary creep. The constitutive relation for primary creep may be expressed as

$$\dot{\varepsilon} = A_p \sigma^{n_p} \varepsilon^{-p} \tag{4.41}$$

for the uniaxial case. A path independent integral, C^*_h, was defined by Riedel (70), which can correlate the near crack tip stress field to the applied load in a body deforming according to equation 4.41. For conditions of constant load, the path independent J integral exhibits the same time dependence as the product $\sigma \cdot \varepsilon$, so that $J(t) \alpha t^{1/(1+p)}$. By analogy with C^*, Riedel (70) defined a path independent integral, C^*_h, which was time dependent under constant load conditions in a material deforming by primary creep.

$$C^*_h = J(t) \left[P(t)^{n_p} / \int_o^t P(t')^{n_p} \, dt' \right]^{1/(1+p)} \tag{4.42}$$

where $P(t)$ is the time dependent load and $J(t)$ is the time dependent J integral.

For a material deforming in primary creep, the HRR crack tip stress singularity may be expressed in terms of C^*_h, and the near tip stress distribution is given by

$$\sigma_{ij} = \left[\frac{C^*_h}{(A_p(1+p))^{1/1+p}\, I_m\, r}\right]^{1/m+1} \tilde{\sigma}_{ij}(\theta,m) \qquad (4.43)$$

where $m = n_p/(1+p)$.

4.6 Stress and Strain Fields near the Tip of a Growing Crack

Stress and strain fields near stationary crack tips have been characterised for a range of material behaviour by fracture mechanics parameters such as K, J, C^* and C^*_h. Hui and Riedel (71) have analysed the stress and strain fields at the tip of a growing crack in an elastic-creeping material, whose uniaxial behaviour is given by

$$\dot{\varepsilon} = \frac{\dot{\sigma}}{E} + B\sigma^n \tag{4.44}$$

Mode I and mode III loading were both considered. For $n < 3$, the asymptotic stress field is dominated by the elastic strain rates and

$$\sigma \propto r^{-\frac{1}{2}} \tag{4.45}$$

For $n > 3$, a new type of stress and strain field develops at the tip of a growing crack. For plane stress, mode I loading, the stresses and strains are given by

$$\sigma_{ij} = \alpha_n \left[\frac{\dot{a}(t)}{BEr}\right]^{1/n-1} \hat{\sigma}_{ij}(\theta,n) \tag{4.46}$$

$$\varepsilon_{ij} = \frac{\alpha_n}{E} \left[\frac{\dot{a}(t)}{BEr}\right]^{1/n-1} \hat{\varepsilon}_{ij}(\theta,n) \tag{4.47}$$

where α_n is a dimensionless factor slightly greater than one, and the dimensionless angular functions, $\hat{\sigma}_{ij}$ and $\hat{\varepsilon}_{ij}$, are given graphically by Hui and Riedel (71).

Similar expressions to those in equations 4.46 and 4.47 were derived for plane strain mode I loading and for mode III loading. The

results suggest that the asymptotic near tip fields are independent of applied load. Therefore, any crack growth criterion based on these near tip stress and strain fields will lead to a crack growth rate independent of the applied load, which is contrary to all experimental evidence. To explain this anomaly, the authors consider steady state crack growth for small scale creep conditions under mode III loading. Assuming that their results are equally applicable to mode I loading, then from considerations of dimensional consistency, the stress field is of the form

$$\sigma_{ij} = \left[\frac{\dot{a}}{K^2 E B}\right]^{1/n-3} \Sigma_{ij}(R,\theta,n) \tag{4.48}$$

with

$$R = \frac{r}{r_1} \; ; \; r_1 = \left[\frac{E B K^{n-1}}{\dot{a}}\right]^{2/n-3} \tag{4.49}$$

where Σ_{ij} is a dimensionless function of R, θ and n.

In addition to small scale creep, Riedel and Wagner (72) consider crack growth for extensive creep conditions under mode I loading. Again using dimensional arguments, they derive a stress field of the form

$$\sigma_{ij} = \left[\frac{EC^*}{\dot{a}}\right]^{\frac{1}{2}} \Sigma_{ij}(R,\theta,n) \tag{4.50}$$

with

$$R = \frac{r}{r_2} \; ; \; r_2 = \left\{\frac{\dot{a}}{EB}\right\}^{(n+1)/2} \left[\frac{B}{C^*}\right]^{(n-1)/2} \tag{4.51}$$

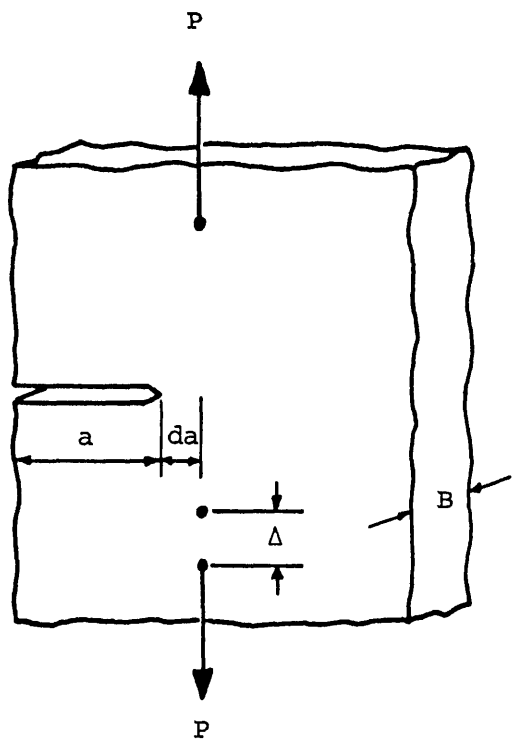


Fig. 4.1 Cracked body subjected to tensile loading

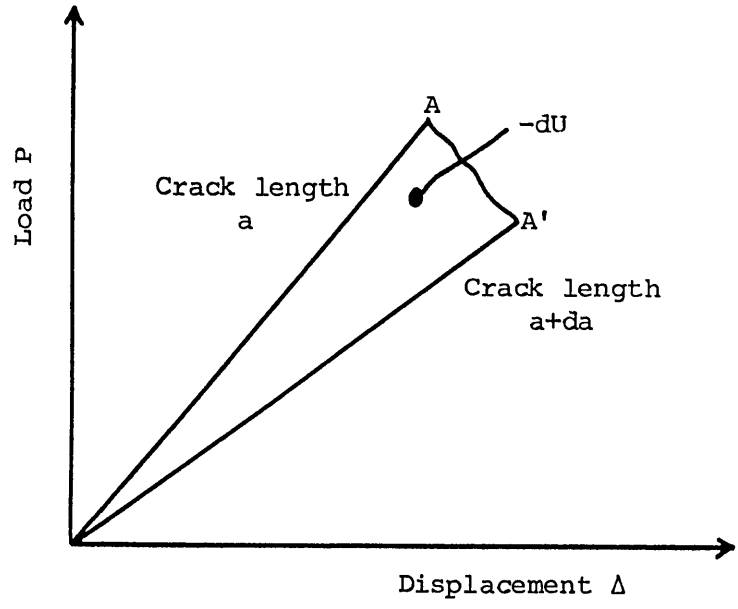


Fig. 4.2 Derivation of G from energy considerations

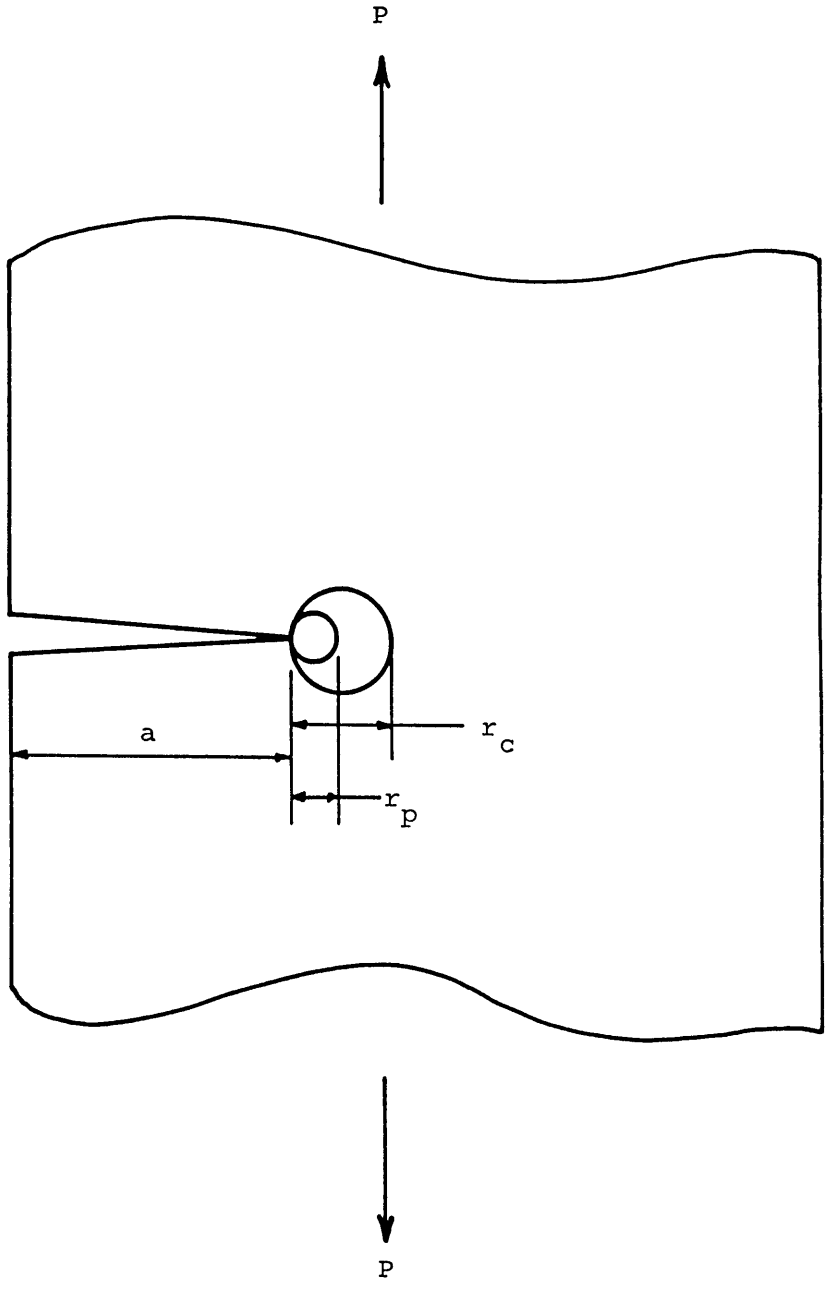


Fig. 4.3 Plastic and creep zones at a crack tip

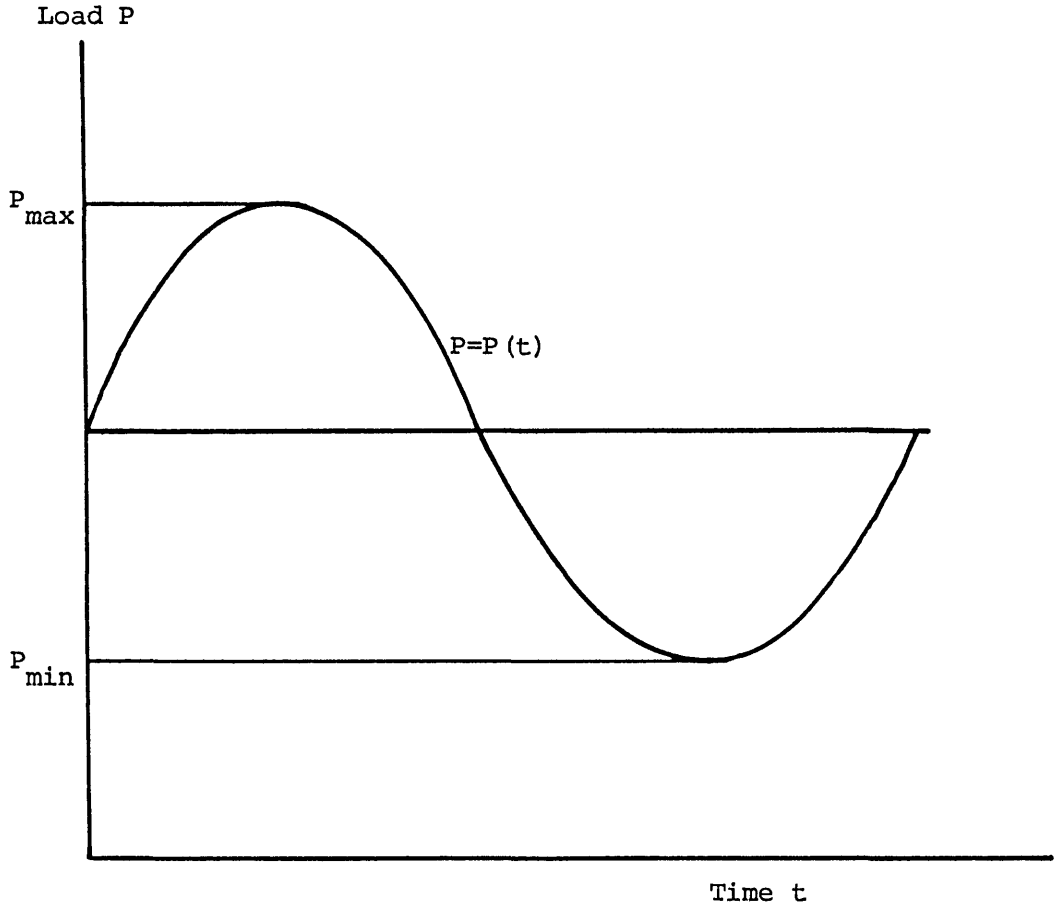


Fig. 4.4 Typical cyclic loading waveform

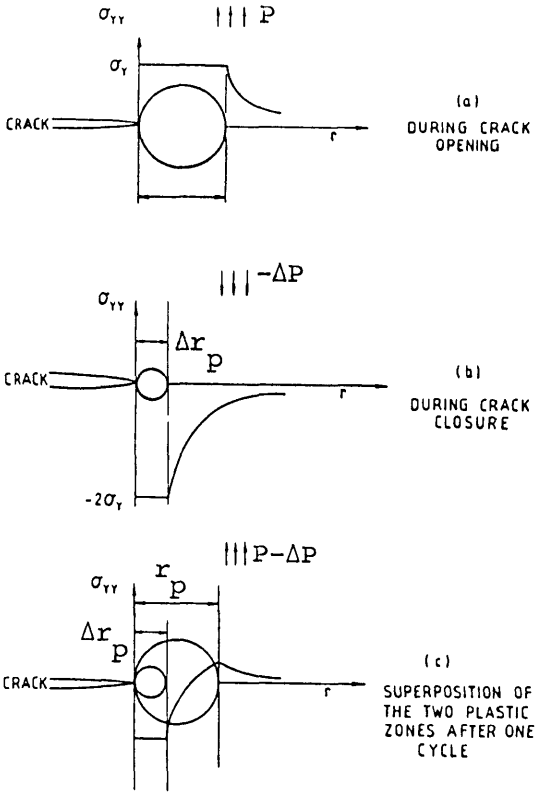


Fig. 4.5 Diagrammatic idealisation of the reversed plastic zone following Rice (59)

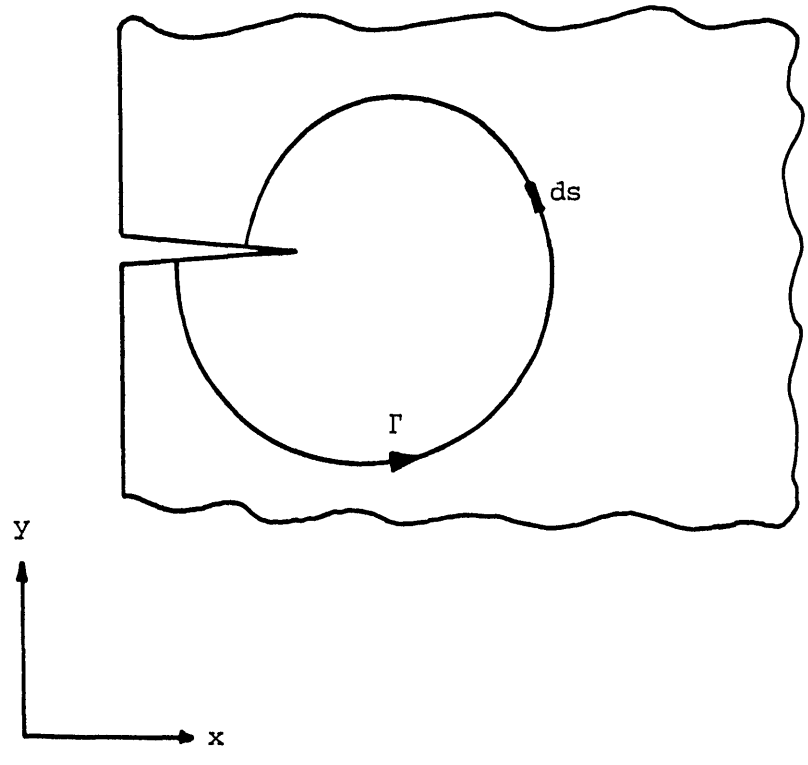


Fig. 4.6 Arbitrary contour surrounding a crack tip in a two dimensional body of uniform thickness subjected to a remote tensile load

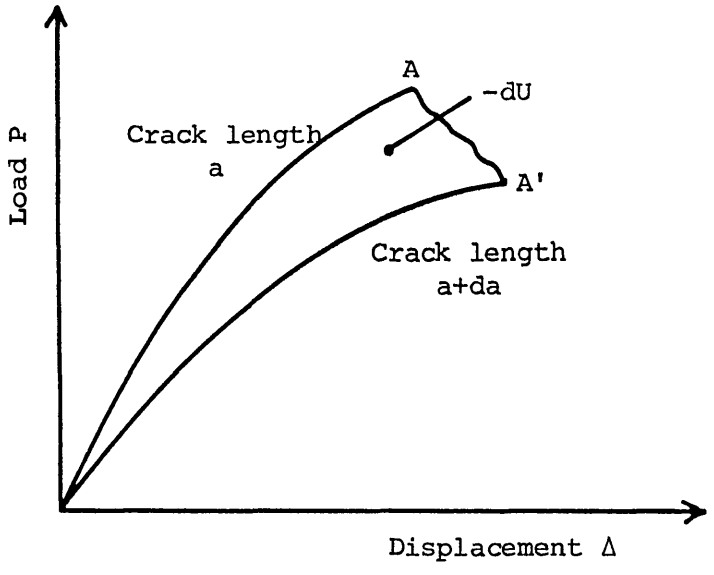


Fig. 4.7 Derivation of J from energy considerations

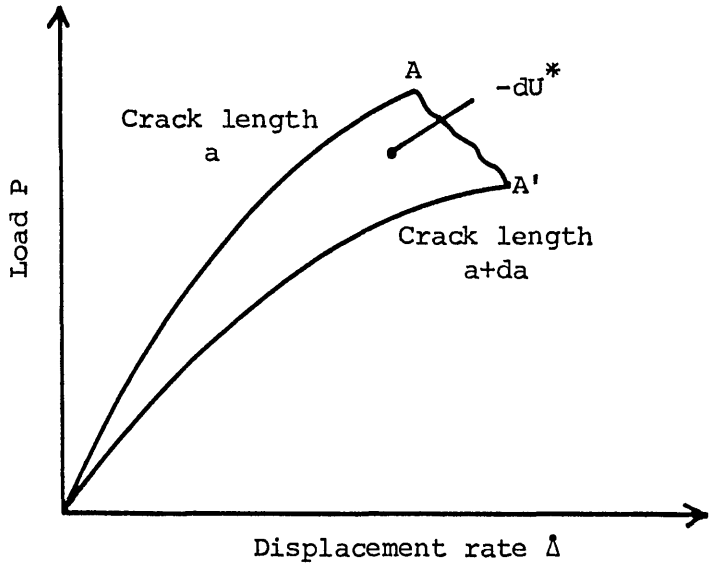


Fig. 4.8 Derivation of C^* from energy rate considerations

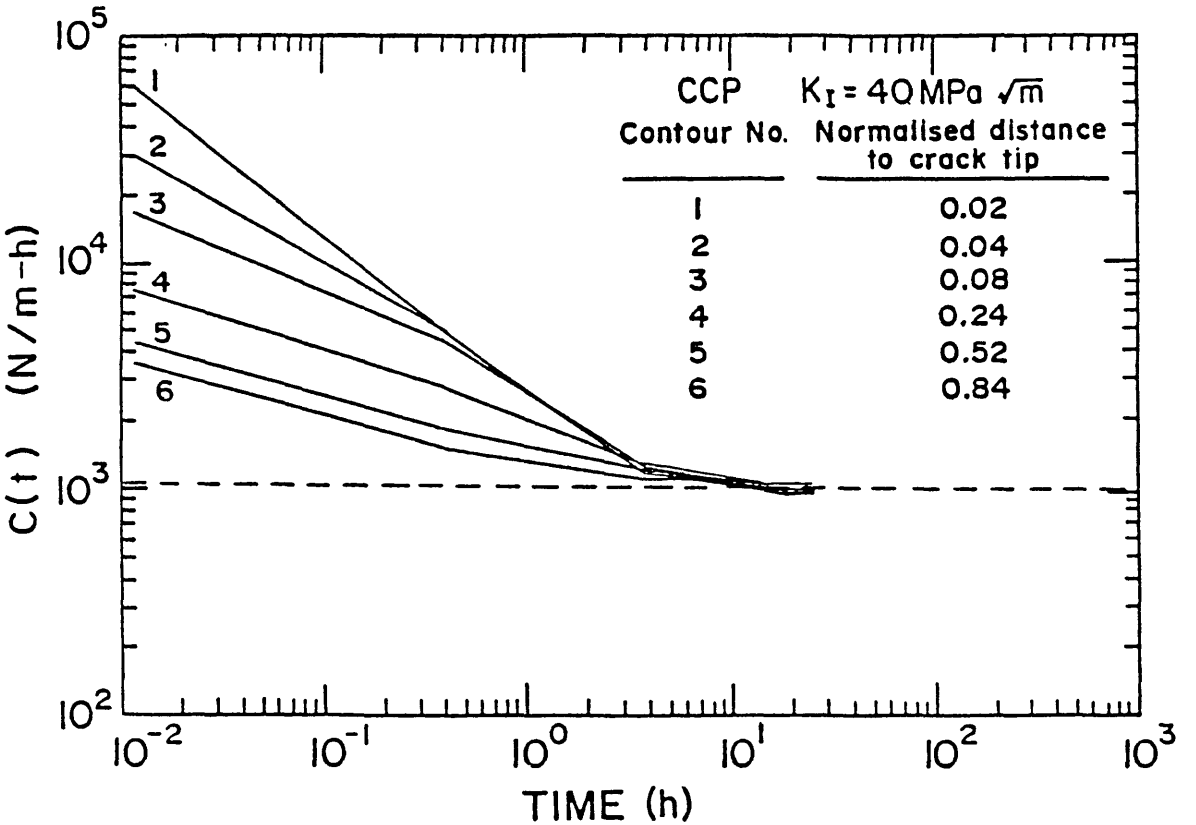


Fig. 4.9 C(t) plotted as a function of time for the CCP geometry using several crack tip contours(69)

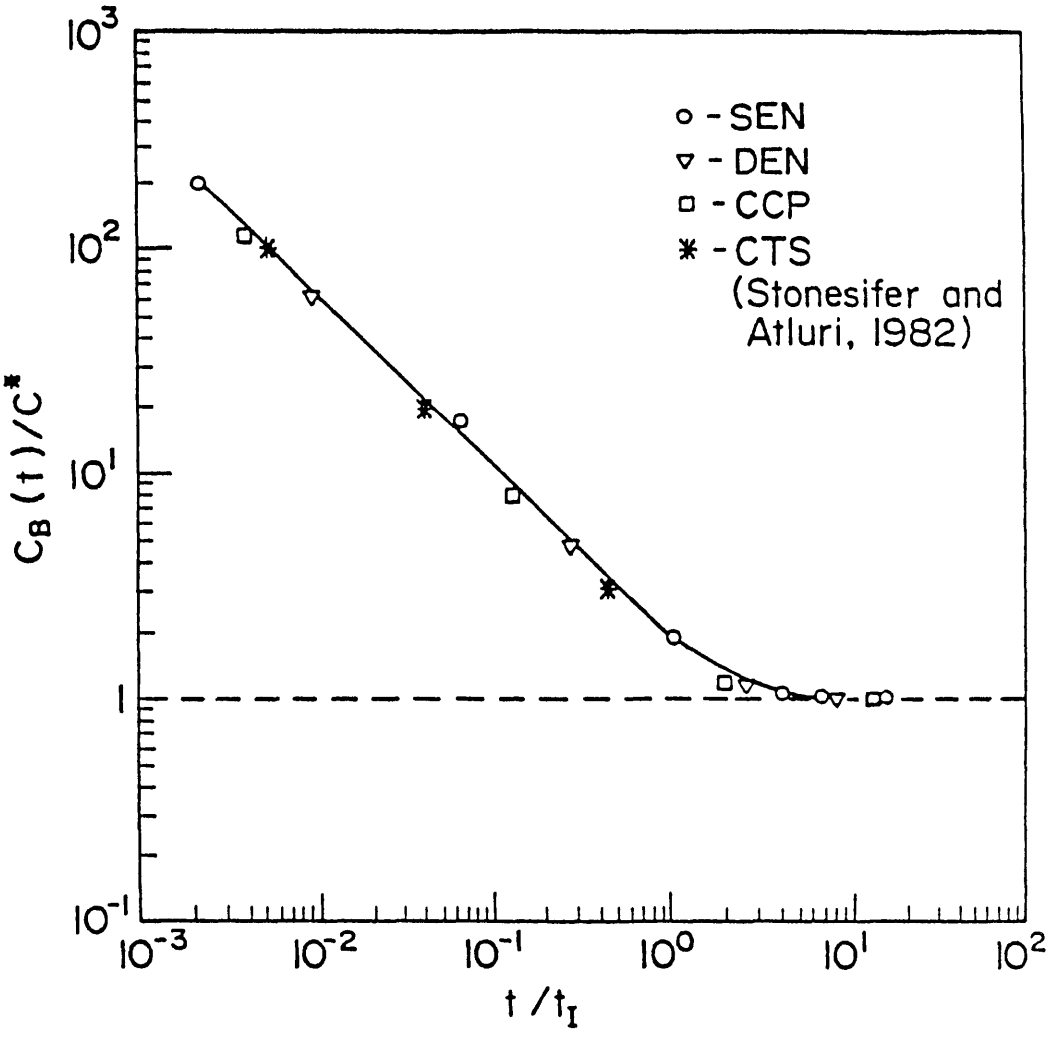


Fig. 4.10 Plot of $C_B(t)/C^*$ versus t/t_I for a range of specimen geometries(69)

CHAPTER 5

MODELLING HIGH TEMPERATURE CRACK GROWTH BEHAVIOUR

5.1 Introduction

Theoretical modelling of high temperature crack growth is useful for two reasons. Firstly, if the crack growth process can be successfully modelled, it may be possible to predict crack growth rates for service applications under conditions not directly covered by laboratory experiments. This type of extrapolation of data also requires a detailed knowledge of the underlying mechanisms responsible for crack growth in the two situations. Secondly, discrepancies between actual and predicted behaviour may help to identify discrepancies between actual and theoretical crack growth mechanisms.

Crack growth under static loading at high temperatures has been studied extensively by a number of authors. These models may also be of relevance to high temperature fatigue crack growth in situations, in which crack growth occurs by a predominantly intergranular mode (high R ratios, low frequencies, high temperatures and tensile hold times all favour intergranular fracture). At high frequencies and low R ratios, crack growth tends to occur by a transgranular mode, suggesting that standard ambient temperature fatigue crack growth models may adequately describe the crack growth process.

The following chapter reviews some of the models which have been proposed to predict crack growth under both static (creep) and cyclic (fatigue) loading. The range of applicability of these models is also investigated.

Finally, theories of creep facture, involving failure caused by accumulation of diffuse damage, are discussed in Appendix 5.

5.2 Creep crack growth Models

Models of high temperature creep crack growth fall into two main categories

1. Continuum models
2. Micromechanistic models

Examples of each type of model are reviewed in the following two sections

5.2.1 Continuum Models

In general, these models assume that the cracked body behaves as a continuum and rely on a knowledge of the crack tip stress distribution and a postulated failure criterion at some point ahead of the crack tip. Examples of failure criteria include critical strain, critical damage accumulation and critical CTOD.

Barnby (73) showed that, under steady state creep conditions, the relaxed stress distribution ahead of the crack tip could be expressed as

$$\sigma \propto \left[K' / r^{\frac{1}{2}} \right]^{1/n} \qquad (5.1)$$

where K' is a quantity, like K, which is derived by assuming that the relaxed stress distribution possesses the same load bearing capacity as original elastic distribution, governed by K. For materials, which show the following relation between minimum creep rate, $\dot{\varepsilon}_{min}$, and time to rupture, t_R,

$$\dot{\varepsilon}_{min} \cdot t_R = constant \qquad (5.2)$$

he proposes that the use of a critical strain criterion, for crack advance, is justified. Assuming that crack growth occurs when a critical strain develops at a certain microstructural distance ahead of the crack tip, he predicts

$$\dot{a} \alpha \sigma_{net}^{n} \quad \text{for large} \quad n \tag{5.3}$$

where σ_{net} is the net section stress, and

$$\dot{a} \alpha K^{n} \qquad \text{for small} \quad n \tag{5.4}$$

Floreen and Kane (74) also assumed a critical strain criterion for crack advance, which occurred in an intermittent manner over a distance equal to the material grain size, d. Further assuming that the crack growth rate was proportional to the crack tip strain rate and that material at the crack tip was deforming in tertiary creep according to

$$\dot{\varepsilon} = B_t \varepsilon^{p} \tag{5.5}$$

they predicted the following dependence of crack growth rate

$$\dot{a} \alpha (K^2/Ed\sigma_y)^{p} \tag{5.6}$$

More recently, models have assumed that, under steady state creep conditions, the crack tip stress field is of the HRR singular type

$$\frac{\sigma_{ij}}{\sigma_o} = \left[\frac{C^*}{I_n \sigma_o \varepsilon_o r}\right]^{1/n+1} \tilde{\sigma}_{ij}(\theta, n) \tag{5.7}$$

which was introduced in Section 4.4. Nikbin et al (75) considered a creep zone ahead of the crack tip (figure 5.1), which encompasses the region in which creep damage is accumulating ahead of the crack. They proposed that material first experiences creep damage on entering the

creep zone, at a distance r_c ahead of the crack tip, and has accumulated a critical amount of strain on reaching the crack tip. The critical strain used was the creep ductility of the material appropriate to the state of stress at the crack tip, ε_f^*. Assuming the crack tip stress field is of the HRR type (equation 5.7), they developed the following expression for crack growth rate

$$\dot{a} = (n+1)\frac{\dot{\varepsilon}_o}{\varepsilon_f^*}\left[\frac{C^*}{I_n \sigma_o \dot{\varepsilon}_o}\right]^{n/(n+1)} \cdot r_c^{1/(n+1)} \qquad (5.8)$$

The same authors have recently extended the above model to allow for primary, secondary and tertiary creep in an approximate manner (76). They defined an average creep rate, $\dot{\varepsilon}_A$, which can be obtained from creep rupture data as shown in figure 5.2. Thus,

$$\dot{\varepsilon}_A = \varepsilon_f / t_R \qquad (5.9)$$

and the stress dependence of average creep rate may be expressed as

$$\frac{\dot{\varepsilon}_A}{\dot{\varepsilon}_{oA}} = \left[\frac{\sigma}{\sigma_{oA}}\right]^{n_A} \qquad (5.10)$$

For a typical stress rupture plot, illustrated in figure 5.3,

$$t_R = \frac{D}{\sigma^\nu} \qquad (5.11)$$

where D and ν are material constants. Substituting equations 5.10 and 5.11 into equation 5.9, yields a general expression for the failure strain

$$\varepsilon_f = \frac{\dot{\varepsilon}_{oA} D \sigma^{(n_A - \nu)}}{(\sigma_{oA})^{n_A}} \qquad (5.12)$$

Assuming, once again, that the crack tip stress field is of the form of equation 5.7, except that n_A is substituted for n, and that material accumulates a critical amount of strain on reaching the crack tip, they developed the following expression for crack growth rate,

$$\dot{a} = \left[\frac{n_A + 1}{n_A + 1 - \nu}\right] \cdot \frac{\dot{\varepsilon}_{oA}}{\varepsilon_{fOA}} \cdot \left[\frac{C^*}{I_{nA}\, \sigma_{oA}\, \dot{\varepsilon}_{oA}}\right]^{\nu/(n_A+1)} \cdot r_c^{(n_A+1-\nu)/(n_A+1)} \tag{5.13}$$

where ε_{fOA} is the uniaxial creep ductility at a stress σ_{oA}. In the special case, where creep ductility is constant, $n_A = \nu$ and equation 5.13 reduces to a form similar to equation 5.8 (with n_A replacing n).

Kubo et al (77) assumed a crack tip stress singularity of the HRR type (equation 5.7), and proposed that damage, η, accumulated ahead of the crack according to

$$\dot{\eta} \;\alpha\; \sigma^{b_1} \tag{5.14}$$

where b_1 is a constant, and $\eta = 0$ for virgin material and $\eta = 1$ at fracture. Crack advance occurred when the value of the damage variable, η, reached unity at a characteristic microstructural distance ahead of the crack tip. For $b_1/(n+1) > 1$, damage accumulates primarily in a small zone near the crack tip, and crack growth rates can be expressed as a function of C^*. However, when $b_1/(n+1) \lesssim 1$, significant damage accumulation occurs ahead of the crack tip, and crack growth rates depend on crack length in addition to C^*. Therefore, when damage accumulates primarily in the region governed by the HRR singular field (and C^*), then crack growth rates should correlate with C^*. However, when significant damage accumulates due to the influence of the non-singular terms of the stress (ie σ_{net}), damaged material will enter the

region governed by the HRR field, causing crack growth rates higher than those predicted by C^* alone.

A computer simulation, of the time dependent development of a plastic zone ahead of a crack loaded in uniform tension, was performed by Vitek (78). Assuming a critical CTOD as the criterion for the onset of crack growth, he calculated the time required for the initiation of a creep crack.

5.2.2 Micromechanistic Models

High temperature creep crack growth commonly occurs by the initiation and growth of voids, or microcracks ahead of the main crack, which, in time, coalesce and join the main crack, causing the crack to extend. Micromechanistic models represent an attempt to model the mechanisms responsible for crack growth on a microscopic level.

Modelling crack growth mechanisms, which involve the accumulation of cavitation damage ahead of the crack tip, requires a knowledge of the mechanisms responsible for cavity growth. These mechanisms were discussed in Section 3.2. In summary, once nucleated cavities may grow by one of the following mechanisms

1. Diffusion ; modelled by Hull and Rimmer (18), Chuang and Rice (19) and Raj and Ashby (20).
2. Coupled diffusion and power law creep; modelled by Needleman and Rice (21).
3. Power Law creep; modelled by Pavinich and Raj (22).

Micromechanistic models of creep crack growth assume that crack extension is related to the growth of cavities in the stress field

ahead of the crack tip.

Diffusional growth of cavities has been considered by a number of authors. Miller and Pilkington (79) defined the crack tip stress field in terms of stress intensity factor, K, for brittle materials and assumed that crack growth was intermittent over a length corresponding to a grain boundary facet. Cavity growth was assumed to be the dominant process in determining the crack growth rate, and occurred by a surface diffusion mechanism (19). A K^3 dependence of crack growth rate was predicted.

Wilkinson (80) also studied intergranular creep crack growth by a diffusional mechanism, again assuming that the crack tip stress field may be characterised by K. Both equilibrium (18) and crack like (19) cavities were considered and depending on the number of cavities growing simultaneously, dependence of crack growth rates varied from K to K^6.

The use of stress intensity factor to characterise the crack tip stress field seems reasonable for cases where crack growth occurs by a diffusional mechanism and is accompanied by only a relatively small amount of creep deformation. In general, at low stress levels, cavities growing by a diffusional mechanism are constrained by creep deformation of the surrounding grains (21). Hutchinson (81) has proposed a constitutive relation for a material undergoing creep constrained grain boundary cavitation, and he found that for $n \gtrsim 3$ the crack tip stress and strain rate distributions remain unchanged by cavitation (except that for a given C^* value, the stress level decreases and the strain rate level increases). Bassani (82) considered cavity growth

by a coupled diffusion and power law creep mechanism, assuming that the time dependent crack tip stress field evolved from the linear elastic to the extensive creep case (see section 4.5.1). Crack extension was assumed to be intermittent over a length equivalent to a grain boundary facet. Numerical results, for a CCP specimen of type 304 stainless steel, were plotted in terms of crack length versus time, and showed qualitative agreement with corresponding experimental data.

In high strength nickel base superalloys, which contain a significant number of grain boundary precipitates, grain boundary diffusion is inhibited and crack growth may occur by deformation controlled mechanisms over much of the service temperature range. At high temperatures, crack growth by a deformation controlled mechanism, involves cavity growth by power law creep (22). Models of this type of crack growth mechanism, assuming that the crack tip stress field is governed by K predict a K^n dependence of crack growth rate (79,83).

Creep crack growth models have been reviewed by Sadananda and Shahinian (84) and Ellison and Harper (85), while Wilkinson and Vitek (86) have developed a generalised theory for the propagation of cracks by cavitation, making the following assumptions:

(*a*) The growth of cavities does not significantly affect the crack tip stress field.

(*b*) The number of cavities, growing at any one time, is constant.

(c) All of the cavities nucleate at a well-defined distance ahead of the crack and are equally spaced.

(*d*) Cavities grow from nucleation to linkage by the same mechanism.

Figure 5.4 shows, schematically, the growth of uniformly spaced cavities in the stress field of a creep crack. The authors assume a generalised crack tip stress distribution of the form

$$\sigma = (F/\chi)^{\alpha} \tag{5.15}$$

where F and α depend on material behaviour, and a cavity growth law of the form

$$\upsilon = \phi(\ell,\lambda)\sigma^{\beta} \tag{5.16}$$

where ℓ is the cavity half length, λ the cavity spacing, and β depends on the cavity growth mechanism.

The characteristic half length of nucleated cavities is assumed to be ℓ_{δ}, and nucleation may occur in one of two ways.

(a) Critical stress nucleation; a critical stress level must be reached at a point for cavity nucleation to occur.

(b) Nucleation governed by grain size; grain boundary sliding may produce sufficient stress concentration for N cavities to nucleate simultaneously on a grain boundary facet of length d $(N = d/\lambda)$. Once nucleated the cavities may grow by either diffusion or deformation controlled mechanisms. For diffusional cavity growth, equilibrium shaped cavities result from the Hull and Rimmer (18) growth mechanism $(\beta = 1)$, while crack like cavities result from the Chuang and Rice (19) mechanism $(\beta = 1.5)$. For deformation controlled growth, $\beta = n$.

The results arising from the model, proposed by Wilkinson and Vitek (86), are summarised in Tables 5.1 and 5.2 for cavitation in a linear elastic stress field and a secondary creep zone, respectively. The authors showed that the cavity nucleation mechanism must

be considered for $\alpha\beta < 1$, and found that this inequality was always satisfied, except for the case of cavity growth by power law creep in an elastic stress field with $n > 2$.

Wilkinson et al (69) have recently adapted the generalised theory of Wilkinson and Vitek (86) in order to study crack growth in non-steady crack tip stress fields, governed by the time dependent parameter $C_\beta(t)$ (see Section 4.5.1). As expected, preliminary results show that crack growth rates depend on functions of both K and C^*. For the case of cavity growth by power law creep in a secondary creep zone, with nucleation governed by grain size, the following expression was obtained for crack growth rate.

$$\dot{a} \propto (K^2/t)^{ns/(n+1)} (C^*)^{(1-s)n/(n+1)} \qquad (5.17)$$

where the meaning of s is explained following equation 4.40.

5.3 Fatigue Crack Growth Models

At elevated temperatures, creep and environmental effects play an important part in determining the micromechanisms responsible for crack growth under cyclic loading. For high frequencies and low R ratios, crack propagation may occur by a transgranular mode, involving mechanisms similar to those which operate at ambient temperatures. Lower frequencies, higher R ratios and tensile hold times favour a transition to intergranular crack propagation, which occurs by mechanisms similar to those responsible for crack growth under static loading.

The striation mechanism for stage II transgranular fatigue crack growth has been extensively modelled, while stage I growth has received relatively little attention. Lloyd (39) has reviewed models of stage II growth, which are generally based on the Paris - Erdogan (87) law,

$$\frac{da}{dN} = C(\Delta K)^m \qquad (5.18)$$

and fall into three categories, depending on the criterion for crack advance, which may be one of the following:

1. Critical damage or strain accumulation at the crack tip: almost all theories of this type predict

$$\frac{da}{dN} \alpha \Delta K^4 \qquad (5.19)$$

2. Critical cyclic crack tip opening displacement (CTOD): these theories are based on the assumption that da/dN α CTOD, and all predict

$$\frac{da}{dN} \alpha \Delta K^2 \qquad (5.20)$$

3. Energy balance applied within a crack tip process zone: these theories predict

$$\frac{da}{dN} \alpha \Delta K^2 \text{ or } \Delta K^4 \tag{5.21}$$

depending on the size of the process zone compared to the plastic zone.

However, these models may be of limited significance to crack growth in cast nickel base superalloys, which often exhibit extensive stage I cracking. Also, when considerable creep deformation accompanies crack extension, the stress intensity factor may cease to characterise the crack tip stress field and have limited use in crack growth modelling.

A crack-tip-zone interaction model has been recently proposed by Jaske (87) in an attempt to explain interactions between creep and fatigue processes during crack growth. He assumed that both a creep zone, r_c, and a fatigue zone, r_f, are formed at the tip of a crack in a body subjected to high temperature fatigue loading (figure 5.5), and that the zone sizes were estimated by

$$r_c = \frac{1}{\pi}\left[\frac{K_{max}}{\sigma_f}\right]^2 \tag{5.22}$$

$$r_f = \Delta r_p = \frac{1}{4\pi}\left[\frac{\Delta K}{\sigma_f}\right]^2 \tag{5.23}$$

where σ_f is the material flow stress. As shown in figure 5.5, two situations are possible, depending on the relative sizes of r_c and r_f. The author suggests that the dominant crack growth mechanism depends on the relative magnitudes of r_c and r_f. The model agrees qualitatively with experimental observations of crack growth behaviour under continuous cycling, predicting an increasing influence of creep effects with

increasing R ratio and decreasing frequency.

Crack tip stress and strain fields and crack growth under creep-fatigue conditions have been studied by Riedel (89). Considering load increases in proportion to a power β of time, he derived a generalisation of the characteristic time for transition from K controlled, to C* controlled, crack tip stresses, such that

$$t_I = \frac{1 + 2\beta n}{n + 1} \cdot \frac{G(t_I)}{C^*(t_I)} \qquad (5.24)$$

When $\beta = 0$, for a step load, the above expression reduces to the simplified form derived by Riedel and Rice (equation 4.38). A characteristic frequency, $W_I \approx \pi/t_I$, was proposed to discriminate between slow and rapid cycling. Four types of loading waveform were considered, as shown in figure 5.6.

(a) Slow cycling without rapid load variations

When $W < W_I$, and the cyclic rise time, t_h, is much greater than t_I, the crack tip stress and strain fields and the crack growth behaviour should all be governed by C*. For $R > 0$, the model predicts no crack growth by the striation mechanism, assuming that the growth rate per cycle is of the order of $CTOD_c$. However, crack growth can occur by grain boundary cavitation, assuming that $da/dt \propto (C^*)^{n/n+1}$, resulting in the following expression for crack growth rate.

$$\frac{da}{dN} \propto \frac{(C^*_{max})^{n/n+1}}{w} \int_0^{2\pi} \left[f(\tau) \right]^{n/n+1} d\tau \qquad (5.25)$$

where $C^* = C^*_{max}\, f(wt)$.

(b) Slow cycling with rapid load variations

When the cycle rise time is short, such that $t_r << t_I$, which may occur in square or trapezoidal loading waveforms, the crack tip stress field will exhibit a peak at the end of the rise time. The magnitude of this stress peak is determined by ΔK and the rate of loading. For loading in proportion to a power β of time, the crack tip stress field is given by

$$\frac{\sigma_{ij}}{\sigma_o} = \left[\frac{C(t)}{I_n \sigma_o \dot{\varepsilon}_o r}\right]^{1/n+1} \tilde{\sigma}_{ij}(\theta, n) \qquad (5.26)$$

where the amplitude, $C(t)$, of the HRR field is given approximately by

$$C(t) = \left[\frac{1 + 2\beta n}{n + 1}\right] \cdot \frac{\Delta K^2(t)}{Et} + C^*(t) \qquad (5.27)$$

for plane stress loading. The first term in the above equation determines the amplitude of the stress peak. When the hold time at maximum load is greater than t_I, the near tip stress field will eventually relax, so that C^* governs long term behaviour after the load increase.

At low applied stress levels, the time required to nucleate cavities may be the dominant factor in determining the crack growth rate by cavitation. Peaks in the crack tip stress field can significantly shorten the nucleation time, thereby accelerating the crack growth rate markedly compared with sustained loading. Rapid crack tip opening, caused by the stress peaks, may rupture the stable oxide layer which covers the crack tip, permitting increased environmental interaction, and causing an increase in crack growth rates.

(c) Rapid balanced cycling ($R = -1$)

For balanced cycling, no creep strain is accumulated over long periods of time in a proportional stress field, and the time dependent crack tip stress field is determined by the stress intensity factor if the frequency is high enough to satisfy

$$w \gtrsim w_I = \pi / t_I \tag{5.28}$$

(d) Rapid unbalanced cycling

In the case of rapid unbalanced cycling, a time independent stress is superimposed on the cyclic stresses. The time dependent component of the crack tip stress field is determined by the stress intensity factor if the size of the creep zone at the crack tip is small compared to crack length. This requirement may be expressed in terms of frequency

$$w >> \frac{\dot{\varepsilon}_o E}{a^{(n-1)/2(n+1)} \sigma_o^{\,n} \Delta K} \left[\frac{C^* \sigma_o^{\,n}}{\dot{\varepsilon}_o} \right]^{n/(n+1)} \tag{5.29}$$

The time independent component of the crack tip stress field is characterised by C^*, only if $R \simeq 1$.

For low R ratios, the near tip HRR field is given by

$$\frac{\sigma_{ij}}{\sigma_o} = Z(wt) \left[\frac{(\Delta K)^2 w}{I_n \dot{\varepsilon}_o \sigma_o r} \right]^{1/n+1} \tilde{\sigma}_{ij}(\theta, n) \tag{5.30}$$

where the dimensionless function $Z(wt)$ depends on n, ν and wave shape. Assuming that crack growth occurs by the striation mechanism, the author derived the following expression for crack growth rate

$$\frac{da}{dN} \alpha \frac{(\Delta K)^{2n/n+1}}{w^{1/n+1}} \int_0^{\pi} |Z(wt)|^n \, d(wt) \tag{5.31}$$

assuming that the cyclic crack growth rate is proportional to $CTOD_c$. The problem of crack growth due to rapid cycling at high R ratios is, as yet unresolved.

Saxena and his co-workers (90,91,92) have developed a series of semi-empirical models in order to predict the effects of frequency and hold times on high temperature fatigue crack growth.

Acceleration in cracking rates caused by decreases in frequency (90), or imposition of tensile hold times (91), were attributed primarily to creep effects. Noting that the parameter K^2/t characterised the time dependence of the crack tip stress and strain fields in the case of small scale creep, the authors suggested that the same parameter should also characterise crack growth rates according to

$$\frac{da}{dt} = b\left\{\frac{K^2}{t}\right\}^q \qquad (5.32)$$

where b and q are material constants. Figure 5.7 shows, schematically, the variation of crack growth rate with frequency for a typical alloy tested at elevated temperature and constant ΔK(90). Three distinct regions are apparent. Saxena showed that, in region II, the dependence of crack growth rate on frequency could be given by

$$\frac{da}{dN} = \left[\frac{da}{dN}\right]_o + \left[\int_o^{1/f} \frac{da}{dt} \cdot dt - \int_o^{1/f_o} \frac{da}{dt} \cdot dt\right] \qquad (5.33)$$

which may be expressed as

$$\frac{da}{dN} = C_o(\Delta K)^{q_o} + C(\Delta K)^{2q}\left[g(f) - g(f_o)\right] \qquad (5.34)$$

where the function $g(f)$ depends on loading waveform. No time dependent

effects are apparent at and above a frequency f_o. The constants C_o, C, q_o, q can be determined from da/dN versus ΔK data at two different frequencies, although rigorous definition of f_o requires crack growth data at three different frequencies. The model gave good predictions of the variation of experimental crack growth rates with frequency for tests on A470 steel and type 304 stainless steel at 538°C.

A similar model was developed to predict the influence of tensile hold times on high temperature fatigue crack growth behaviour (91). A typical fatigue cycle containing a hold period is shown in figure 5.8. Assuming that small scale creep prevails in the transient region of the hold time (before stresses relax due to creep), then the crack tip stress and strain fields may be characterised by K^2/t (compare with the expression obtained by Reidel, for the amplitude of the crack tip stress field under square or trapezoidal loading, given in equation 5.27). If the hold time, t_h, is short in comparison to the characteristic time, t_I (equation 4.38 for a step loading, or equation 5.24 for loading rates proportional to a power β of time), then K^2/t will characterise the crack tip stress field, and crack growth rates, over the entire hold time. Summation of the crack growth occurring during loading/unloading and during the hold time gives an expression for the crack growth rate per cycle

$$\left[\frac{da}{dN}\right]_h = \left[\frac{da}{dN}\right]_N + \int_o^{t_h} \frac{da}{dt} \cdot dt \qquad (5.35)$$

where $$\frac{da}{dt} = b\left[\frac{K^2}{t}\right]^q \text{ or } b^1\left[\frac{\Delta K^2}{t}\right]^q, \text{ so that}$$

$$\left[\frac{da}{dN}\right]_h = C_N(\Delta K)^{q_N} + A^1(\Delta K)^{2q} t_h^{(1-q)} \qquad (5.36)$$

where $(da/dN)_N = C_N(\Delta K)^{q_N}$ is the crack growth rate for the same loading cycle without any hold time. Determination of the constants C_N, A^1, q_N, q_o requires experimental data from one test without a hold time and at least one set of data with a hold time.

For long hold times, $t_h > t_I$ and significant creep deformation may result. The expression given in equation 5.36 is valid up until $t = t_I$, after which the crack tip stresses relax and subsequent crack growth rates are governed by C^*. Saxena et al (91) derived the following expression for crack growth rate, in cases where $t_h > t_I$,

$$\left[\frac{da}{dN}\right]_h = C_N(\Delta K)^{q_N} + A^1(\Delta K)^{2q}\, t_I^{(1-q)} + C^1(C^*)^{\phi}\,(t_h - t_I) \qquad (5.37)$$

Evaluation of C_N, A^1, C^1, q_N, q, ϕ then requires experimental data from one test without a hold, one test with a short hold $(t_h < t_I)$ and one test with a long hold $(t_h > t_I)$. The model gave good predictions of hold time effects on the crack growth rates in type A470 steel and the nickel base superalloy, Inconel 718, at a temperature of 538°C.

Saxena (92) has also considered the case where frequency and hold time effects can be attributed to an environmental effect. In the presence of an aggressive environment, such as air, he proposed that an environment affected zone, EAZ, forms around the crack tip in addition to a plastic zone and a creep zone (figure 5.9). Assuming that diffusion is the rate limiting process in the formation of this zone, he derives the following expression for ℓ, the EAZ size,

$$\ell = \sqrt{\mathcal{D}t} \qquad (5.38)$$

where $\mathcal{D}$ is the diffusion coefficient. Confining his model to

situations in which time dependent effects are dominated by the environment, he postulated that crack growth, caused by the influence of the environment, was proportional to $d\ell/dt$ and could be expressed as

$$\frac{da}{dt} = \frac{C_E}{\sqrt{t}} \cdot K^e \qquad (5.39)$$

where C_E and e are constants, The crack growth rate in region II (see figure 5.7) for a triangular waveform was given by

$$\left[\frac{da}{dN}\right]_t = C_{Eo}(\Delta K)^{e_o} + C_{E1}(\Delta K)^e f^{-0.5} \qquad (5.40)$$

where $C_{Eo}(\Delta K)^{e_o}$ is the crack growth rate in the cycle dependent region I. Crack growth rates were also determined for a trapezoidal waveform, having the same loading/unloading rates as the triangular waveform (equation 5.40) and with a tensile hold of duration t_h,

$$\left[\frac{da}{dN}\right]_{th} = \left[\frac{da}{dN}\right]_t + C_{E2}(\Delta K)^e \sqrt{t_h} \qquad (5.41)$$

Determination of the constants C_{Eo}, C_{E1}, C_{E2}, e_o and e from equations 5.40 and 5.41 requires experimental crack growth data from tests at two different frequencies without hold times, and from one test involving a hold period. The model successfully represented the effects of frequency and hold times on fatigue crack growth behaviour in Astroloy at 655°C and Inconel 718 at 650°C, under conditions where environmental effects dominate over creep.

Table 5.1 Crack Propagation by Cavitation in a Linear Elastic Stress Field

	Cavity growth by Diffusion		Cavity growth by Power Law Creep
	Equilibrium shaped cavities	Crack like cavities	
Critical Stress Nucleation	$\dot{a} \alpha K^2 \lambda^{-3}$	$\dot{a} \alpha K^2 \lambda^{-2.5}$	$\dot{a} \alpha \lambda (K/\lambda^{0.5})^n / \ell n(\lambda/2\ell s)$ for $n > 2$.
Nucleation governed by grain size	$\dot{a} \alpha K d^{0.5} \lambda^{-3}$	$\dot{a} \alpha K^{1.5} d^{0.25} \lambda^{-2.5}$	

Table 5.2 Crack Propagation by Cavitation in a Secondary Creep Zone

	Cavity growth by Diffusion		Cavity growth by Power Law Creep
	Equilibrium shaped cavities	Crack like cavities	
Critical Stress Nucleation	$\dot{a} \alpha C^*$	$\dot{a} \alpha C^*$	$\dot{a} \alpha C^*/\ell n(\lambda/2\ell_s)$
Nucleation governed by grain size	$\dot{a} \alpha (C^*)^{1/n+1}$	$\dot{a} \alpha (C^*)^{3/2(n+1)}$	$\dot{a} \alpha d(C^*/d)^{n/n+1}$

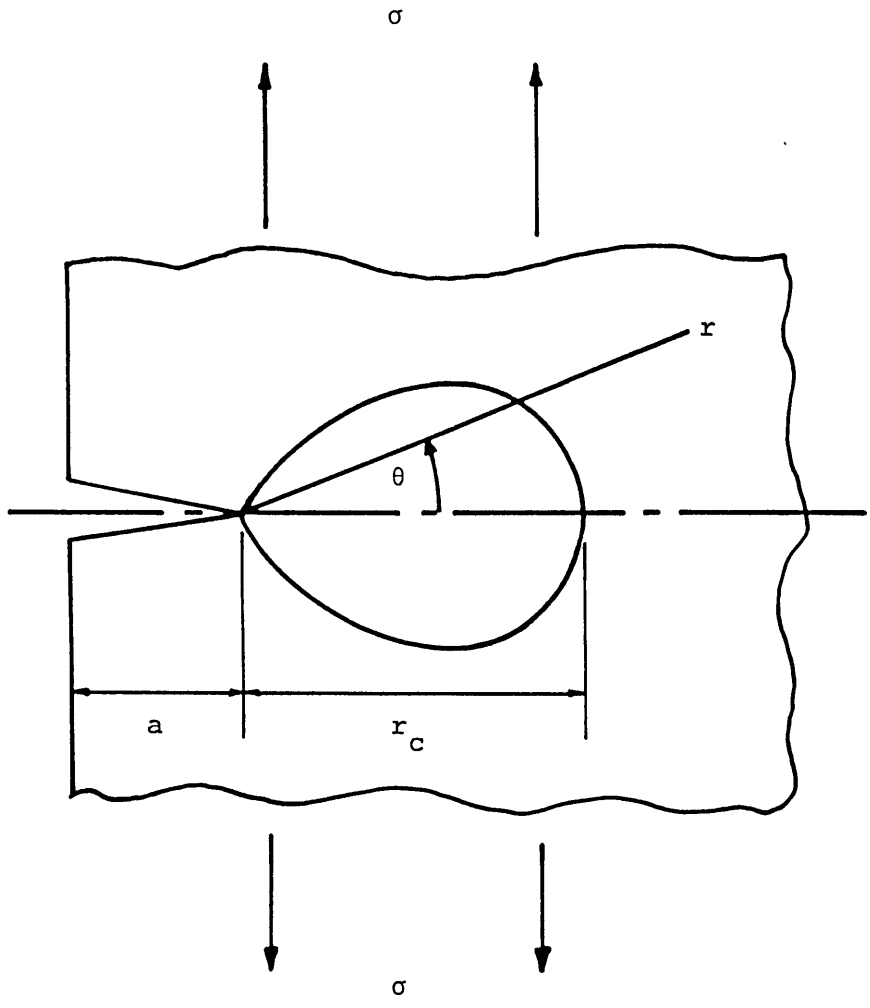


Fig. 5.1 Creep zone ahead of a crack tip(75)

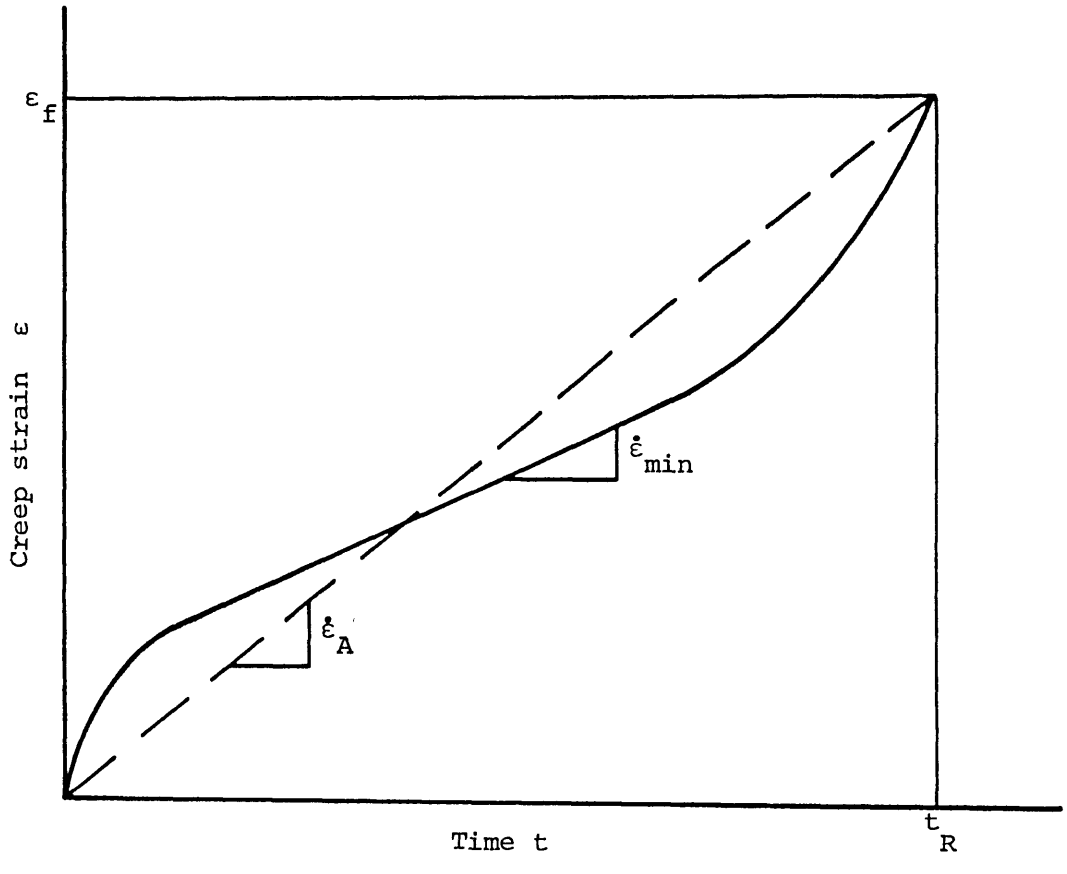


Fig. 5.2 Method of obtaining an average creep rate

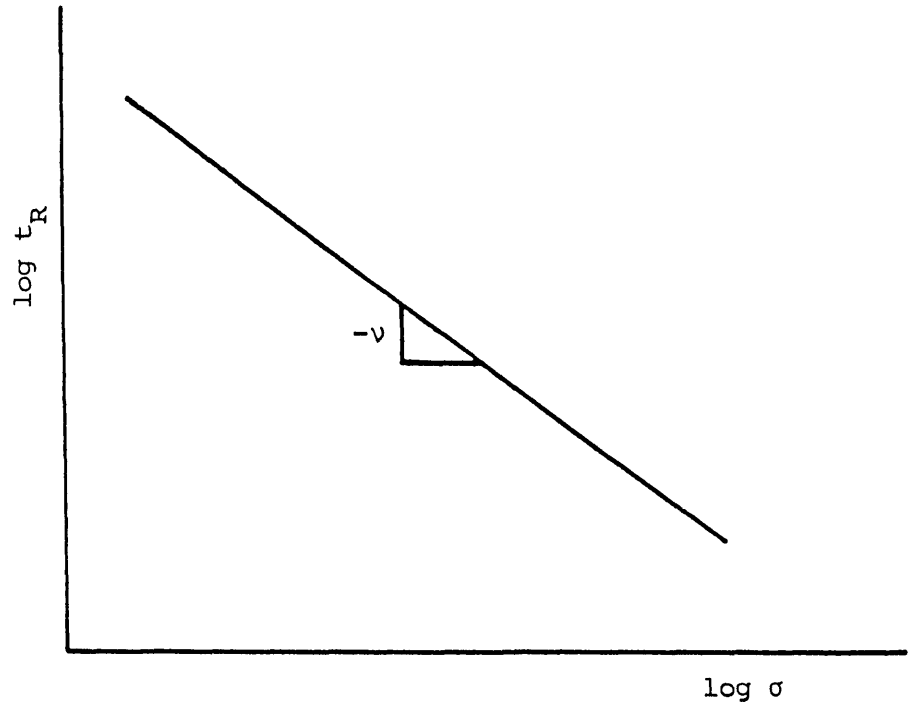


Fig. 5.3 Typical stress rupture plot

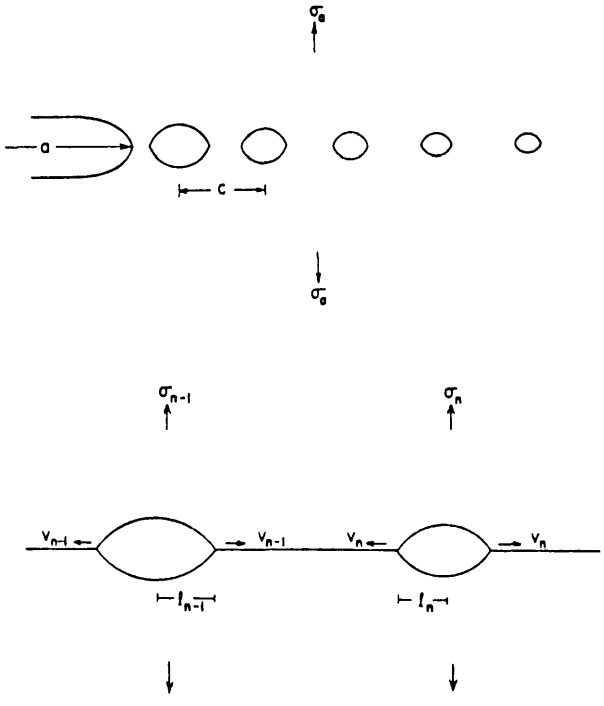
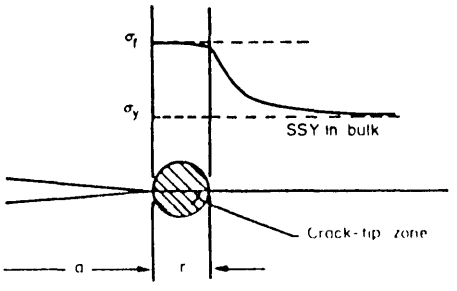
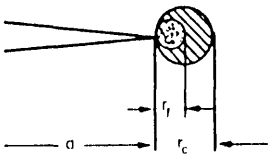


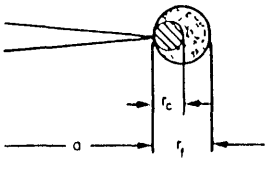
Fig. 5.4 Growth of uniformly spaced cavities in the stress field of a creep crack (86)



(a) Crack-tip-zone model

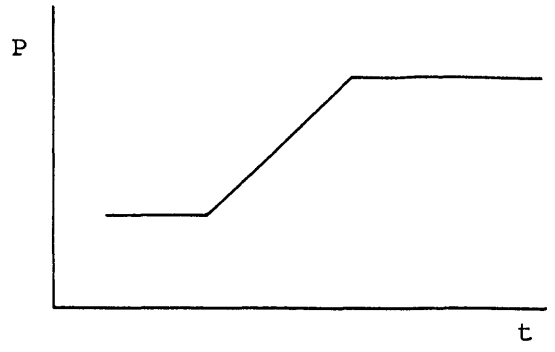


(b) Creep zone larger than fatigue zone

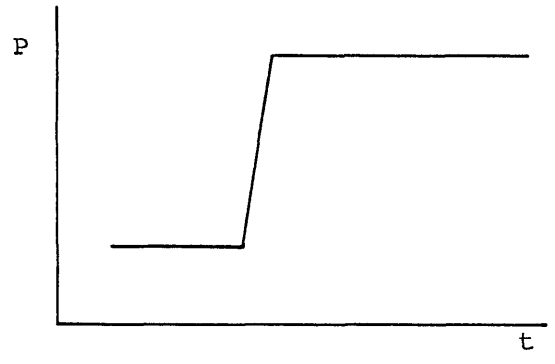


(c) Fatigue zone larger than creep zone

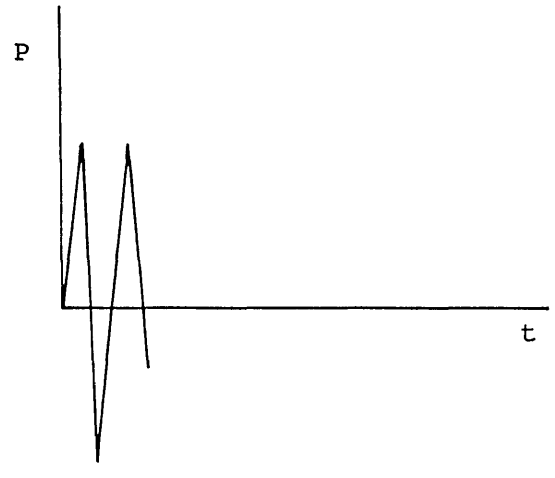
Fig. 5.5 Creep and fatigue zones formed at a crack tip subjected to high temperature fatigue loading (88)



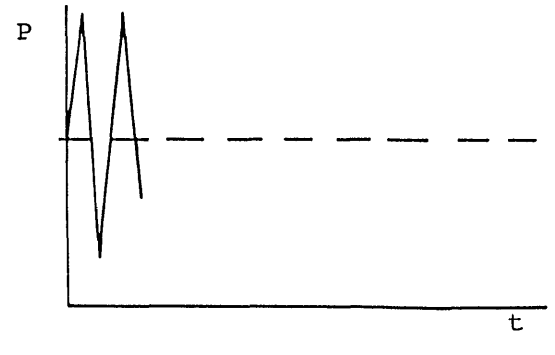
(a) Slow cycling without rapid load variations



(b) Slow cycling with rapid load variations



(c) Rapid balanced cycling(R=-1)



(d) Rapid unbalanced cycling

Fig. 5.6 Loading waveforms considered by Riedel(89)

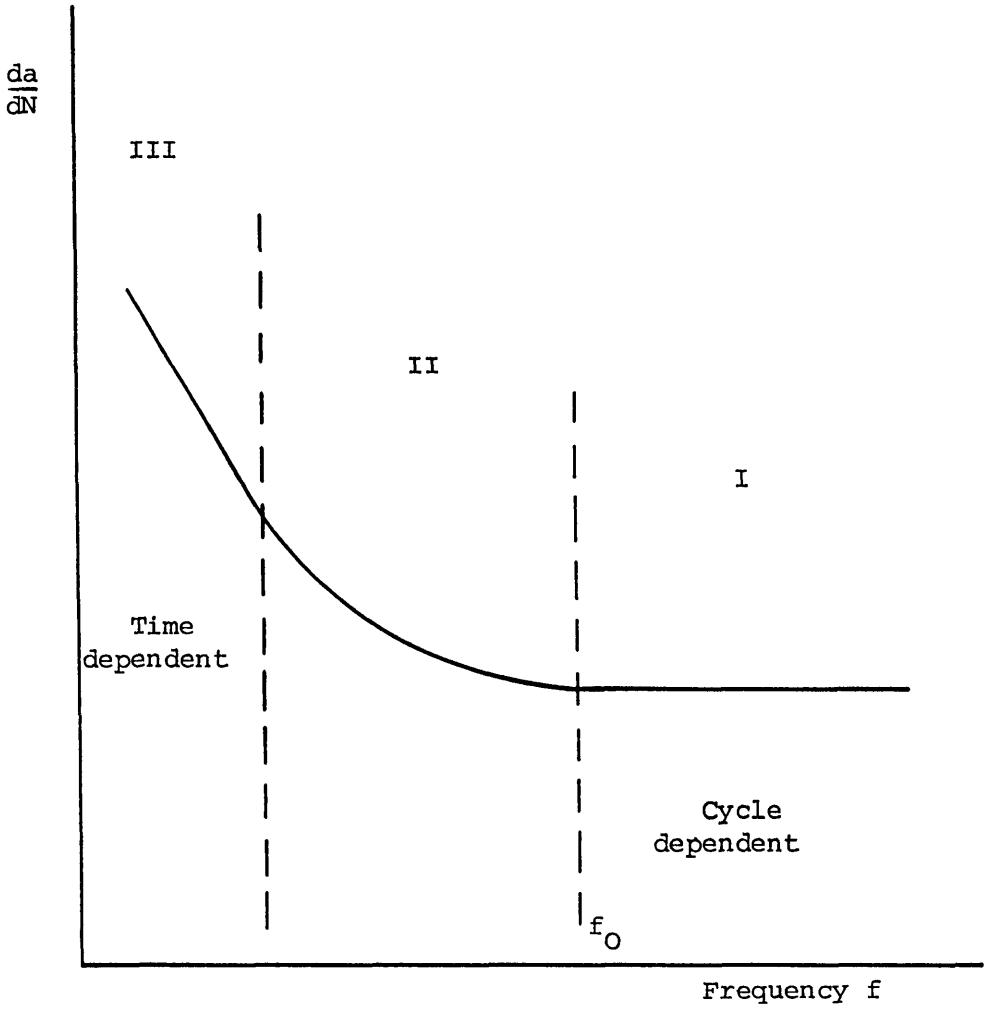


Fig. 5.7 Typical variation of crack growth per cycle with frequency for an alloy tested at elevated temperature and constant ΔK

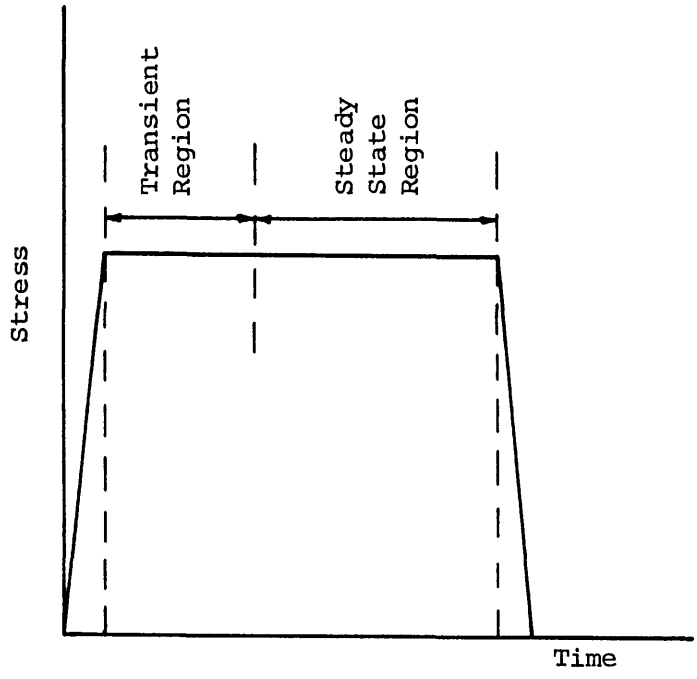


Fig. 5.8 Typical fatigue cycle containing a hold period(91)

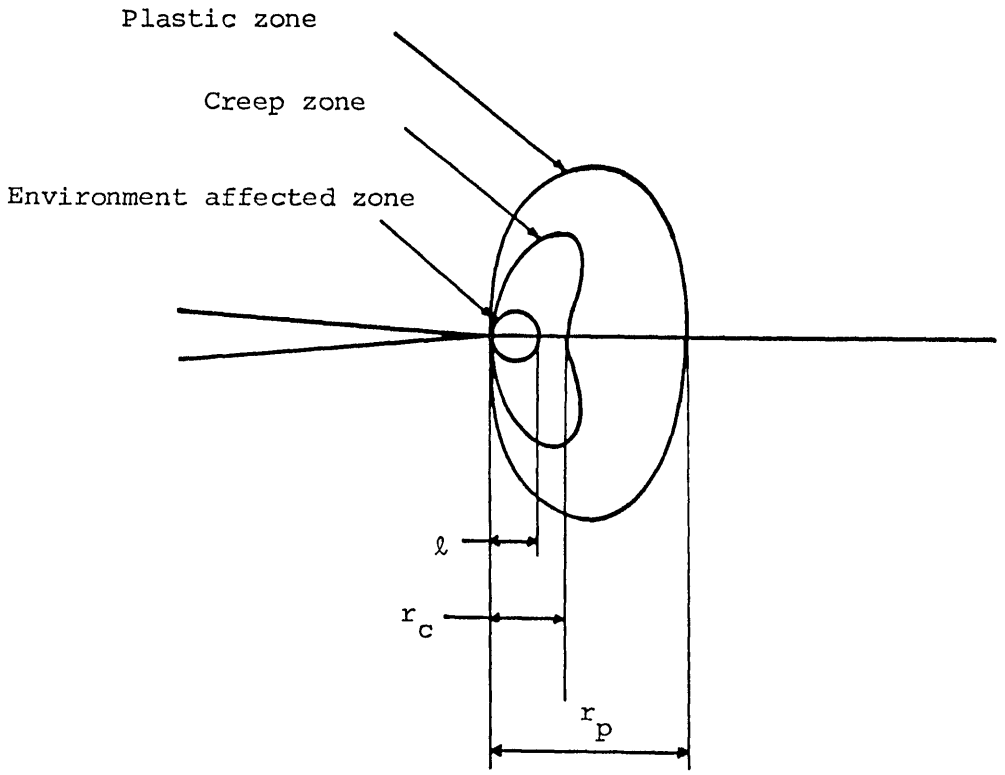


Fig. 5.9 Crack tip zones in the presence of an aggressive environment(92)

APPENDIX 5

MODELS OF CREEP FAILURE

Creep failure is a complex process, which is generally associated with a gradual deteriation of the material (eg. by the formation of voids and microcracks). This section reviews the brittle rupture theories of Kachanov and Rabotnov, which are referred to later in the present work.

Kachanov (93) identified the use of a term, known as the continuity, ψ, in order to describe the deteriation which occurs during tertiary creep. The value of ψ was assumed to be unity for virgin material, decreasing to a value of zero at failure. Increases in strain rate, observed during the tertiary part of the creep curve, were attributed to changes in material continuity, which increase the 'effective' applied stress, σ_{eff}. For a uniaxial specimen, subjected to a constant stress, σ, the effective applied stress is given by

$$\sigma_{eff} = \frac{\sigma}{\psi} \tag{A5.1}$$

A term more commonly used to describe material deteriation is the degree of damage, η, where

$$\eta = 1 - \psi \tag{A5.2}$$

Strain rate and damage rate may then be expressed as functions of stress and damage

$$\dot{\varepsilon} = f(\sigma, \eta) \tag{A5.3}$$

$$\dot{\eta} = g(\sigma, \eta) \tag{A5.4}$$

Rabotnov (94), neglecting initial elastic and plastic deformation, suggested power law expressions for the functions $f(\ )$ and $g(\ )$. Assuming the following forms for $f(\ )$ and $g(\ )$,

$$\dot{\varepsilon} = \dot{\varepsilon}_o \left[\frac{\sigma}{\sigma_o(1-\eta)}\right]^n \tag{A5.5}$$

$$\dot{\eta} = \dot{\eta}_o \left[\frac{\sigma}{\sigma_o}\right]^\nu \frac{1}{(1-\eta)^\gamma} \tag{A5.6}$$

expressions may be derived for the failure strain, ε_f, and the time to rupture, t_R, assuming that primary creep may be neglected and that $\eta = 1$ at failure.

$$\varepsilon_f = \frac{1}{(\gamma + 1 - n)} \frac{\dot{\varepsilon}_o}{\dot{\eta}_o} \left[\frac{\sigma}{\sigma_o}\right]^{n-\nu} \tag{A5.7}$$

$$t_R = \frac{1}{(\gamma + 1)\ \dot{\eta}_o} \left[\frac{\sigma}{\sigma_o}\right]^{-\nu} \tag{A5.8}$$

Current values of strain, ε, and damage, η, are given by

$$\frac{\varepsilon}{\varepsilon_f} = 1 - (1 - t/t_R)^{(1 - n/\gamma+1)} \tag{A5.9}$$

$$\eta = 1 - (1 - t/t_R)^{1/\gamma+1} \tag{A5.10}$$

The constants n, ν, γ, σ_o, $\dot{\varepsilon}_o$, and $\dot{\eta}_o$ may be determined from experimental creep data. Minimum creep rate, $\dot{\varepsilon}_{min}$, is commonly plotted against stress, σ in log-log form as shown in figure A5.1. The theoretical expression for minimum creep rate can be deduced from equation A5.5 by substituting $\eta = 0$.

$$\dot{\varepsilon}_{min} = \frac{\dot{\varepsilon}_o}{\sigma_o^{\,n}} \cdot \sigma^n \qquad \text{(A5.11)}$$

Thus, the slope of the line in figure A5.1 is given by n, while the intercept on the $\dot{\varepsilon}_{min}$ axis gives the value of $\dot{\varepsilon}_o/\sigma_o^{\,n}$.

Figure A5.2 shows a plot of log t_R versus log σ. The slope of the line is given by - ν, while the intercept on the t_R axis gives the value of $\sigma_o^{\,\nu}/(\gamma+1)\dot{\eta}_o$ (equation A5.8).

Figure A5.3 shows a typical plot of log ε_f versus log σ (assuming $n > \nu$). The slope of the line is given by n - ν, and the intercept on the ε_f axis gives $\dot{\varepsilon}_o/(\gamma+1-n)\dot{\eta}_o\ \sigma_o^{\,(n-\nu)}$.

The above procedure yields six equations for the six unknowns, n, ν, γ, σ_o, $\dot{\varepsilon}_o$ and $\dot{\eta}_o$. However, since one of these equations is redundant, solutions to the problem may only be obtained by specifying the value of either σ_o, $\dot{\varepsilon}_o$ or $\dot{\eta}_o$. Conventionally, the value of $\dot{\varepsilon}_o$ is specified as $1\ h^{-1}$, thereby allowing values of n, ν, γ, σ_o and $\dot{\eta}_o$ to be determined using the procedure outline above.

The form of the theoretical creep curve, predicted by equation A5.9, is solely determined by the ratio $n/(\gamma + 1)$. Figure A5.4 shows the form of the predicted creep curve for a range of values of $n/(\gamma + 1)$. Small values of $n/(\gamma + 1)$ mean that the material creep behaviour exhibits an extended steady state, or secondary, stage and only a small tertiary stage. When $n/(\gamma + 1)$ approaches unity, the tertiary stage becomes predominant. The validity of the Kachanov/Rabotnov theory, for a particular material and temperature, may be assessed by comparing the theoretical creep curve, predicted by equation A5.9, with typical experimentally determined creep curves.

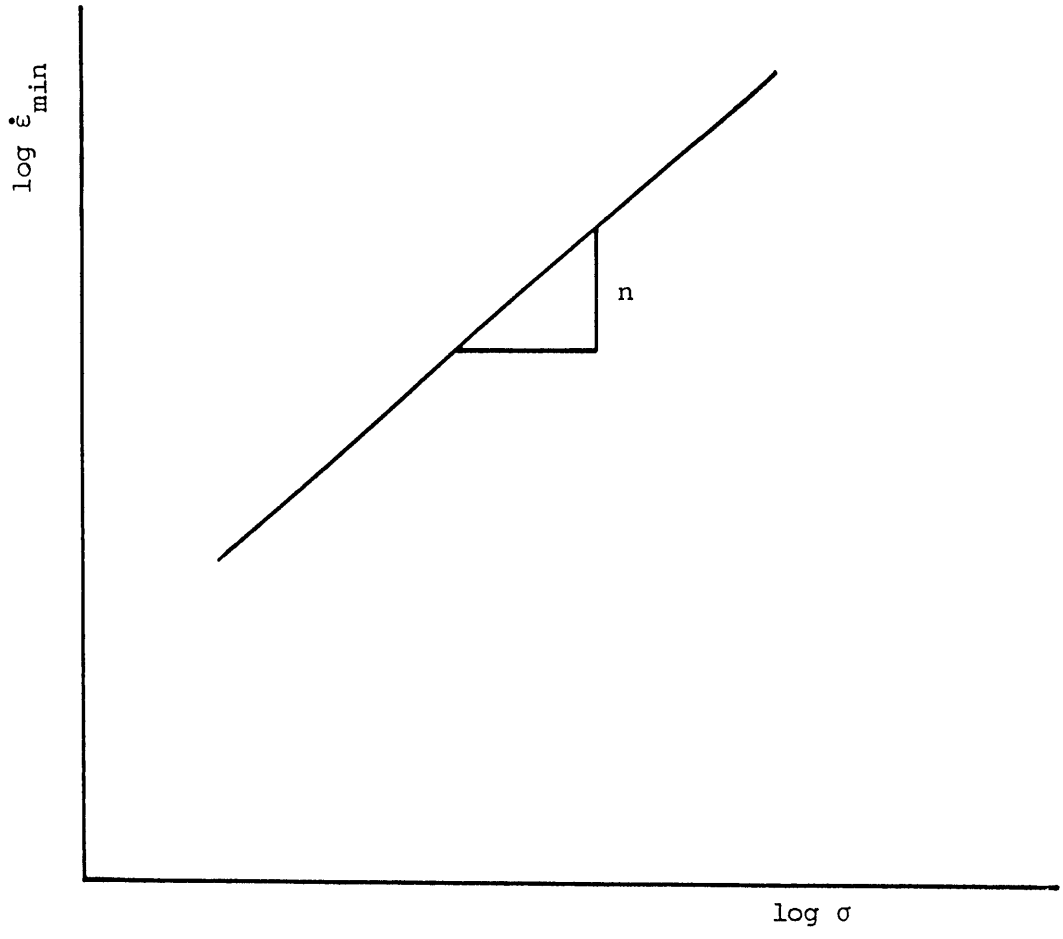


Fig. A5.1 Variation of minimum creep rate with applied stress

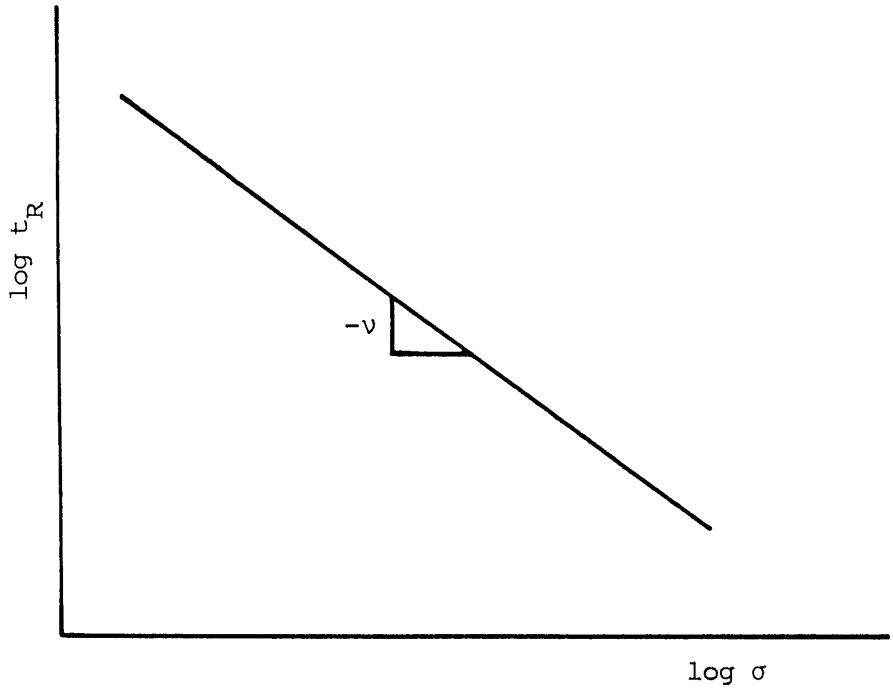


Fig. A5.2 Variation of rupture time, t_R, with applied stress

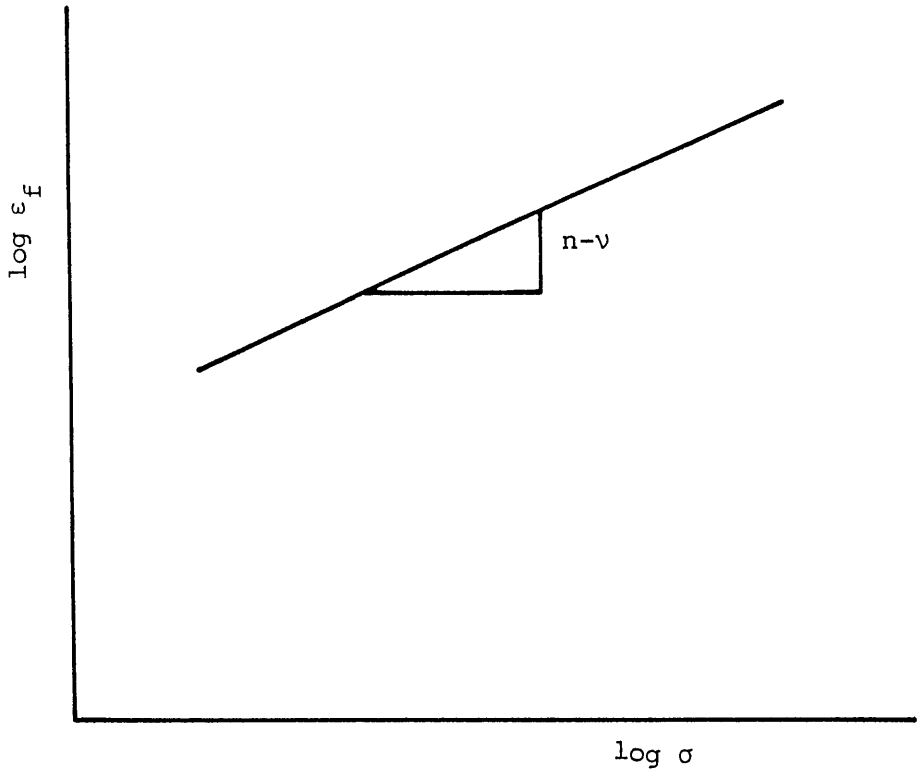


Fig. A5.3 Variation of failure strain, ε_f, with applied stress

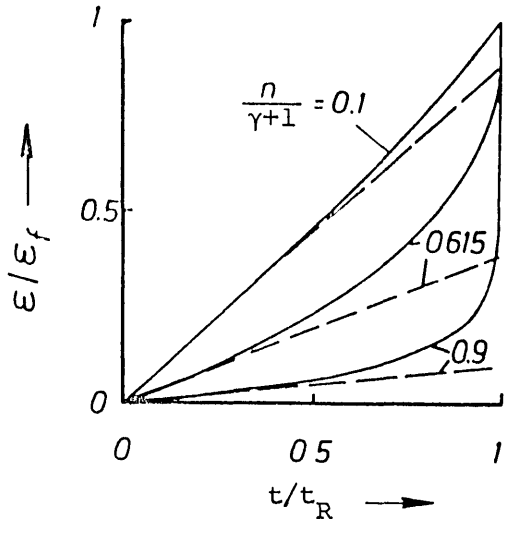


Fig. A5.4 Form of theoretical creep curves predicted by equation A5.9

CHAPTER 6

CORRELATION OF HIGH TEMPERATURE CRACK GROWTH DATA

6.1 Introduction

The fracture mechanics approach has been widely used in the correlation of crack growth data under a variety of loading conditions. Several parameters have been proposed to correlate data, and although each of these parameters may be relevant for certain conditions, none have yet found universal acceptance.

At elevated temperatures, crack growth under static loading occurs as a result of time dependent processes. These processes may occur as a result of creep effects, environmental effects or from combinations of the two (Section 3.2). Crack growth under cyclic loading involves cycle dependent plastic deformation at the crack tip in addition to time dependent creep and environmental effects (Section 3.3). In general, the fatigue crack growth process tends to be cycle dependent at low R ratios and high frequencies, when creep and environmental effects are minimised. Higher temperatures, higher R ratios, lower frequencies and the imposition of hold times favour time dependent fatigue crack growth, which often occurs as a result of mechanisms similar to those which cause crack growth under static loading. Further complications may result if there is any interaction between cycle and time dependent processes. The similarities in crack growth mechanisms observed in creep crack growth and time dependent fatigue crack growth suggest that fracture mechanics parameters which have been used to correlate creep crack growth data may also be useful in time dependent fatigue.

The following chapter introduces some of the fracture mechanics parameters which have been used to correlate crack growth data obtained under both creep and fatigue loadings. Methods available for evaluation of these parameters are also reviewed.

6.2 Correlation of High Temperature Creep Crack Growth Data

Several parameters such as stress intensity factor, K, crack tip opening displacement, CTOD, CTOD rate, J Integral, C^* Integral, net section stress, σ_{net}, or reference stress, σ_{ref}, have been used to correlate creep crack growth rate data for a number of alloys. Although the number of studies, using several specimen geometries to rigorously investigate the range of applicability of these parameters, is limited, the available data indicate that K, C^* and σ_{ref} are valid, each for a limited range of materials and test conditions. Several authors (15,31,85,95-102) have studied the application of these fracture mechanics parameters to the correlation of creep crack growth rates. Relationships proposed are generally of the form

$$\dot{a} = BK^m \tag{6.1}$$

$$\dot{a} = D\sigma_{ref}^{\ p} \tag{6.2}$$

$$\dot{a} = HC^{*\phi} \tag{6.3}$$

where B, D, H, m, p and ϕ are material constants. Typically $m \approx p \approx n$ and ϕ is slightly less than unity.

Experimental evidence indicates that for materials which are 'creep brittle', or highly sensitive to environment in the temperature range of interest, creep deformations are small and crack growth can occur under essentially elastic conditions. Stress intensity factor, K, then characterises the crack tip stresses, and can be used to correlate crack growth rates. If the material is very ductile and less sensitive to environment, rapid stress redistribution occurs at the

crack tip, implying that reference stress, σ_{ref}, can best be used to correlate crack growth rates. Reference stress (103) is the equivalent uniaxial stress, applied to a uniformly stressed specimen, which gives rise to the same displacement rate as that of the cracked body. Finally, in intermediate situations, where failure is due to the growth of a main crack, C^* integral appears to correlate crack growth rates better than any other parameter. C^* is also consistent with K in the 'creep brittle' case and with σ_{ref} in the case of high ductility

Sadananda and Shahinian (16) correlated creep crack growth rates with C^* for a variety of structural alloys. (figure 6.1). They concluded that C^* appeared to be the controlling parameter for crack growth, which occurs by a deformation controlled process with little environmental contribution. Based on observations that creep crack growth occurs by such a process in type 304 stainless steel, they argued that substantial deviations from the scatter band of type 304 stainless steel data indicate strong environmental effects. Sadananda and Shahinian also claim that a unique relationship, independent of material and temperature, may exist between crack growth rate and C^*. However, a simplified analysis by Nikbin et al (75) shows that a unique relationship between crack growth rate and C^* does not exist, but that creep ductility has an effect (equation 5.8).

Although the rates of creep crack growth in particular materials depend on the microstructural features and the micromechanisms responsible for crack growth, macroscopic loading parameters may be successfully employed to correlate crack growth data. Experimental evidence indicates that creep crack growth rates in most materials are best correlated by C^*.

6.3 Correlation of High Temperature Fatigue Crack Growth Data

Linear elastic fracture mechanics techniques have been used successfully to correlate fatigue crack growth rates in many materials, particularly at low or room temperature. This success is based on the fact that the stress intensity factor, K, can adequately describe the stress field at the crack tip provided the extent of plastic flow is small. Paris and Erdogan (87) have shown that a large body of fatigue crack growth data may be uniquely correlated by the stress intensity factor range ΔK

$$\frac{da}{dN} = B(\Delta K)^m \qquad (6.4)$$

where the constants B and m depend on the material. The extent to which linear elastic fracture mechanics is applicable is limited if plasticity effects at the crack tip are appreciable.

The limitations of linear elastic fracture mechanics become more evident with increasing temperature, due to decrease in yield stress and the increasing significance of creep and environmental effects. Non linear parameters such as J integral or C^* may be better suited to correlating crack growth rates under these conditions.

Crack growth rates, obtained from high temperature fatigue studies of nickel base superalloys have generally been correlated with ΔK (13,23,35,40,104,105). Justification for the use of LEFM at temperatures up to 850^{o}C has been attributed to the high strength and creep resistance exhibited by these alloys. Scarlin (104) suggested that if a material is prone to brittle crystallographic type fracture, crack growth rates may be more easily correlated with K_{max}. Shahinian

and Sadananda (45) found that time dependent fatigue crack growth rates could be best correlated with K_{max}.

Sadananda and Shahinian (34) developed a method of calculating ΔJ for load controlled fatigue which was consistent with previous ΔK calculations. They showed that ΔJ gave the same type of correlation of fatigue crack growth rate data as ΔK except that ΔJ gave less spread in the data (28,34). Reviewing elastic-plastic fracture mechanics (106), the same authors suggested that crack growth rates could be expressed in terms of ΔJ by analogy with the Paris law

$$\frac{da}{dN} = B(\sqrt{\Delta J.E})^m \qquad (6.5)$$

where constants B and m depend on the material. They also suggested, and demonstrated, that when fatigue crack growth occurs by a time dependent process, parameters K_{max} or J_{max} correlate crack growth rates better than ΔK or ΔJ.

Taira et al (107) and Ohtani (108) found that frequency dependent fatigue crack growth rates correlated with ΔJ, while time dependent fatigue crack growth rates correlated with C^*. Koterazawa and Mori (109) compared the parameters ΔK, ΔJ and C^* for correlating fatigue crack growth rates in type 304 stainless steel at 650°C. Centre cracked specimens of variable thickness, width and initial crack lengths were used and C^* values were determined experimentally from load-displacement rate curves. They found crack growth rates correlated with ΔK at low crack growth rates and with C^* at high rates.

Although rigorous analysis of the parametric representation of fatigue crack growth in an alloy requires tests to be carried out on

different specimen geometries, the following trends have emerged from previous studies. When fatigue crack growth occurs as a result of cycle dependent processes, cyclic loading parameters ΔK or ΔJ are most appropriate to correlate crack growth rates. If, however, crack growth is time dependent K_{max}, J_{max} or C^* appear to be more relevant loading parameters (as the majority of the crack growth is occurring at or near maximum load and not as a result of the load range).

6.4 Evaluation of Fracture Mechanics Parameters used to correlate high temperature crack growth data

This section introduces the methods available for evaluating the fracture mechanics parameters relevant for correlating crack growth rates in the present work. The previous sections have indicated that time dependent crack growth rates may be correlated by K_{max}, J_{max} or C^*, while cycle dependent cracking rates may be correlated by ΔK or ΔJ. Crack growth in Mar MOO2 occurs under conditions where the crack tip plastic zone is small in comparison to crack length and remaining ligament. Under these circumstances crack tip stress and strain fields and crack growth rates are governed by the stress intensity factor if creep effects are minimal. (eg. instantaneous loading, rapid cycling). When time is available for extensive creep deformation to occur (eg sustained loading, slow cycling), crack tip stress and strain fields and crack growth rates will be governed by C^*. Attention will therefore be restricted to methods of evaluating K and C^*.

6.4.1 Evaluation of K

For an infinite plate, containing a central crack,

$$K_o = \sigma\sqrt{\pi a} \tag{6.6}$$

and for any other geometry

$$K = Y(a/w) \cdot \sigma\sqrt{\pi a} = Y.K_o \tag{6.7}$$

where $Y(a/w)$ is a non-dimensional factor which depends on crack length and component dimensions. Values of Y for a selection of test piece and component geometries can be obtained from reference handbooks (110,111). Appendix 6 gives values of Y for some common

test piece geometries. K calibrations for other geometrical configurations may be calculated numerically using finite element or boundary integral methods.

Stress intensity factor range, ΔK, can be calculated for fatigue loading (figure 6.2) from the following expression

$$\Delta K = K_{max} - K_{min} = K_{max} (1 - R) \qquad (6.8)$$

where K_{max} and K_{min} are the stress intensity factors calculated at σ_{max} and σ_{min} respectively.

6.4.2 Evaluation of C^*

To date, three distinct types of method exist for determining the parameter C^*

1. Experimental Data Reduction method.
2. Approximate methods.
3. Numerical methods.

This section describes the methods of evaluating C^*.

6.4.2.1 Experimental Data Reduction Method

Determination of C^* by this method involves experimental measurement of crack length and load line, or crack opening, displacement as functions of time and then following a step by step data reduction scheme. Although initially introduced by Landes and Begley (66) for displacement controlled tests, the method has since been adapted for load controlled tests by Sadananda and Shahinian (15). The method is limited in application, as the data reduction scheme is complex and requires experimental data from tests on several specimens at different

loads or displacement rates. Practical difficulties in applying this method have necessitated the development of simpler methods, which may be used to determine C^* values from data collected from a single test.

6.4.2.2 Approximate Methods

Approximate methods assume that the whole body is deforming by secondary creep according to

$$\frac{\dot{\varepsilon}}{\dot{\varepsilon}_o} = \left[\frac{\sigma}{\sigma_o}\right]^n \tag{6.9}$$

When this secondary creep law applies throughout the body, the deformation and stress histories at all points in the body are proportional and it can be shown from Illyushin's theorem (112), that

$$\dot{\Delta} = C_n P^n \tag{6.10}$$

where $\dot{\Delta}$ is the displacement rate, P the load and C_n is a measure of the creep compliance of the body. It was shown in Section 4.4 that C^* could be evaluated from energy considerations according to

$$C^* = -\frac{1}{B}\frac{dU^*}{da} \tag{6.11}$$

where B is the thickness of the body and dU^* is the change in strain energy rate density for a crack extension da. For a material deforming by secondary creep,

$$dU^* = (n\dot{\Delta}dP - Pd\dot{\Delta})/(n+1) \tag{6.12}$$

or

$$dU^* = -\frac{P^{n+1}}{(n+1)}\,dC_n \tag{6.13}$$

Therefore C^* may be expressed as

$$C^* = \frac{P^{n+1}}{(n+1)B} \frac{dC_n}{da} \tag{6.14}$$

which may be rewritten as

$$C^* = \frac{P\dot{\Delta}}{BW} \left[\frac{W}{(n+1)} \frac{1}{C_n} \frac{dC_n}{da} \right] \tag{6.15}$$

where W is the width of the body and the term in square brackets is a non-dimensional factor. Thus,

$$C^* = \frac{P\dot{\Delta}}{BW} \cdot F \tag{6.16}$$

where F is a dimensionless function of n, a/w and specimen geometry. In the special case where crack extension occurs at constant load, combining equations 6.11 and 6.12 with $\Delta P = 0$ gives

$$C^* = \frac{P\dot{\Delta}}{BW} \left[\frac{W}{(n+1)} \frac{1}{\dot{\Delta}} \frac{d\dot{\Delta}}{da} \right] \tag{6.17}$$

And, for crack extension at constant displacement rate, $d\dot{\Delta} = 0$, and

$$C^* = \frac{P\dot{\Delta}}{BW} \left[-\frac{n}{(n+1)} \frac{W}{P} \frac{dP}{da} \right] \tag{6.18}$$

The dimensionless factor F may be evaluated from any one of the terms in square brackets in equations 6.15, 6.17 or 6.18

Harper and Ellison (113) proposed an approximate method for evaluating C^* based on limit analysis techniques. They obtained an expression for C^* of the following form

$$C^* = \frac{P\dot{\Delta}}{BW}\left[-\frac{n}{n+1}\ \frac{1}{q}\ \frac{dq}{d(a/w)}\right] \tag{6.19}$$

where the yield load ratio, q, is defined as

$$q = P_{LC}/P_L \tag{6.20}$$

the ratio of the tensile limit load of a cracked body, P_{LC}, to the limit load of an uncracked body, P_L. Equation 6.19 was shown to be valid for crack extension under both constant load and constant displacement rate conditions. Since P_L is independent of crack length, equation 6.19 can be rewritten as

$$C^* = \frac{P\dot{\Delta}}{BW}\left[-\frac{n}{(n+1)}\ \frac{W}{P_{LC}}\ \frac{dP_{LC}}{da}\right] \tag{6.21}$$

The above expression for C^* was also obtained by Smith and Webster (114). Assuming $n >> 1$, they applied limit analysis techniques to express the load, P, as a proportion of P_{LC}, the limit load of the cracked body. Provided that P/P_{LC} is only weakly dependent on crack length, they showed

$$\frac{1}{P}\ \frac{dP}{da} \approx \frac{1}{P_{LC}}\ \frac{dP_{LC}}{da} \tag{6.22}$$

Substituting the above expression in equation 6.18 yielded an expression for C^* identical to that obtained by Harper and Ellison in equation 6.21. Using equation 6.16

$$F = -\frac{n}{(n+1)}\ \frac{W}{P_{LC}}\ \frac{dP_{LC}}{da} \tag{6.23}$$

Approximate estimates of C^* can be obtained for a range of values of n and specimen geometries provided appropriate limit load solutions

are available (115,116). Values of F as a function of a/w and n are given in Appendix 6 for some common test piece geometries.

The geometry of most relevance to the current work is the centre cracked plate (CCP) (Figure 6.3). The collapse load for the cracked plate, P_{LC}, is given, for plane stress loading, by

$$P_{LC} = 2\sigma_o B(w - a) \tag{6.24}$$

where the factor of 2 arises because a symmetrical crack length of $2a$ is assumed. Substituting in equation 6.23 gives

$$F = \frac{n}{n + 1} \frac{1}{2(1 - a/w)} \tag{6.25}$$

A further approximate solution for F, and C^*, may be obtained by considering the approach of Rice, Paris and Merkle (RPM) (117). Applied to the CCP geometry, and expressing their equations in a form relevant to a material deforming by secondary creep, leads to

$$\dot{\Delta} \alpha (W - a) \left[\frac{P}{P_{LC}}\right]^n \tag{6.26}$$

Using the solution for P_{LC} from equation 6.24 and substituting in equation 6.15 gives

$$F_{RPM} = \frac{(n - 1)}{(n + 1)} \frac{1}{2(1 - a/w)} \tag{6.27}$$

which may be compared with equation 6.25. F and F_{RPM} only differ by the factor $(n - 1)/n$ for the CCP geometry. Values of F and F_{RPM} differ by the same factor for other specimen geometries (eg. SENT and DENT) which are subjected to predominantly tensile loading. Appendix 6 shows values of F and F_{RPM} for a range of common test piece geometries.

It may be noted that F and F_{RPM} are essentially the same for all geometries when $n >> 1$.

Harper and Ellison (113) tested the approximate limit analysis method described here against the data reduction method of Landes and Begley (66). Using test data supplied by Landes and Begley from constant displacement rate crack growth tests on both CCP and CT specimens, they found good agreement between C^* values obtained from the two methods.

Approximate methods allow C^* values to be calculated from a record of experimental load and displacement rate throughout a test. Strictly, crack opening displacement rates or displacement rates due to the crack alone should be used in conjunction with F or F_{RPM} to evaluate C^* values from equation 6.16. However, experimental displacement rates are more often measured at the specimen loading points, and include displacement rates due to creep deformation of the uncracked portion of the specimen. Assuming that creep dominates over elastic behaviour, then elastic displacements can be neglected and the total displacement rate of the specimen, $\dot{\Delta}_T$, may be expressed as

$$\dot{\Delta}_T = \dot{\Delta}_o + \dot{\Delta}_c \qquad (6.28)$$

where $\dot{\Delta}_o$ is the displacement rate which would be observed in an uncracked body of the same dimensions subjected to the same loading and $\dot{\Delta}_c$ is the displacement rate due to the crack alone.

Consider, for example, a CCP specimen of length 2ℓ as shown in figure 6.3. For plane stress loading where creep strains dominate, the displacement rate of an uncracked specimen

$$\dot{\Delta}_o = 2\ell \cdot \frac{\dot{\varepsilon}_o}{\sigma_o^n} \left[\frac{P}{2BW}\right]^n \qquad (6.29)$$

Therefore, if $\dot{\Delta}_o$ can be calculated for a particular geometry and $\dot{\Delta}_T$ is measured during a test then $\dot{\Delta}_c$ may be obtained from equation 6.28.

Smith and Webster (114) have recently shown that C^* can be expressed in terms of either $\dot{\Delta}_T$, $\dot{\Delta}_c$ or $\dot{\Delta}_o$, provided appropriate dimensionless factors are used, so that

$$C^* = \frac{P\dot{\Delta}_T}{BW} \cdot F_T = \frac{P\dot{\Delta}_c}{BW} \cdot F_c = \frac{P\dot{\Delta}_o}{BW} \cdot F_o \qquad (6.30)$$

where $\dot{\Delta}_T F_T = \dot{\Delta}_c F_c = \dot{\Delta}_o F_o$, which requires

$$\frac{1}{F_T} = \frac{1}{F_c} + \frac{1}{F_o} \qquad (6.31)$$

The non dimensional factors F and F_{RPM}, derived from limit analysis, should strictly be referred to as F_c and $F_{c(RPM)}$ and only used in conjunction with $\dot{\Delta}_c$ values. However, $\dot{\Delta}_o$ values are only significant when a crack is short and in most other cases $\dot{\Delta}_o << \dot{\Delta}_c$ so that F_c values may be used in conjunction with total displacement rates.

6.4.2.3 Numerical Methods

Several authors (65,118,119) have used numerical methods to determine J integral values for fully plastic cracked bodies. Kumar et al (119) have presented fully plastic crack solutions for a range of common test piece geometries. They showed that for a fully plastic material characterised by

$$\varepsilon/\varepsilon_o = (\sigma/\sigma_o)^N \qquad (6.32)$$

the fracture parameters such as the J-integral, the crack mouth opening displacement, δ, and the remote load point displacement due to the crack, Δ_c, were scalable, and the normalised quantities were functions of a/w and n. By analogy, in the steady state creep regime described by

$$\dot{\varepsilon}/\dot{\varepsilon}_o = \left[\sigma/\sigma_o\right]^n \tag{6.33}$$

the parameters C^*, $\dot{\delta}$ and $\dot{\Delta}_c$ are also scalable and may be determined from the fully plastic solutions. To illustrate this, we may consider the CCP geometry shown in figure 6.3. The creep equivalents of the fully plastic solutions (119) then become

$$C^* = \sigma_o \dot{\varepsilon}_o a (1 - a/w) h_1 (a/w, n)(P/P_{LC})^{n+1} \tag{6.34}$$

$$\dot{\delta} = \dot{\varepsilon}_o a h_2 (a/w, n)(P/P_{LC})^n \tag{6.35}$$

$$\dot{\Delta}_c = \dot{\varepsilon}_o a h_3 (a/w, n)(P/P_{LC})^n \tag{6.36}$$

where P is the load and P_{LC} is the limit load given by

$$P_{LC} = 4/\sqrt{3}\ \sigma_o B(W - a) \qquad \text{plane strain} \tag{6.37}$$

$$P_{LC} = 2\sigma_o B(W - a) \qquad \text{plane stress} \tag{6.38}$$

The expressions for h in equations 6.34 - 6.36 are functions of a/w and n only, and are given in both tabular and graphical form for a range of of values of a/w and n in reference 119. For plane stress conditions, substituting equation 6.38 in equations 6.34 and 6.36 gives

$$C^* = \frac{\dot{\varepsilon}_o}{\sigma_o^n} \; a(1 - a/w) \; h_1 \left[\frac{P}{2B(w - a)}\right]^{n+1} \tag{6.39}$$

$$\dot{\Delta}_c = \frac{\dot{\varepsilon}_o}{\sigma_o^n} \; a h_3 \left[\frac{P}{2B(w - a)}\right]^{n} \tag{6.40}$$

and using equation 6.30

$$F_c = \frac{h_1}{2h_3} \tag{6.41}$$

The displacement rate of the uncracked specimen, $\dot{\Delta}_o$, may be calculated and F_o deduced from $\dot{\Delta}_o F_o = \dot{\Delta}_c F_c$. F_T is then given by equation 6.31.

Numerical estimates of C^* may be used in two distinct ways.

1. Equation 6.39 may be used to calculate C^* values from a knowledge of experimental load and crack length assuming that the material obeys a known secondary creep law.

2. C^* values may be calculated from

$$C^* = \frac{P\dot{\Delta}_T}{BW} \; . \; F_T \tag{6.42}$$

where F_T is estimated numerically and $\dot{\Delta}_T$ is the load point displacement rate measured during the test.

Saxena (120), using the former procedure, calculated C^* values from creep crack growth tests in CCP and CT specimens of type 304 stainless steel. C^* values were also evaluated by the experimental data reduction method and compared with numerical calculations. Discrepancies of up to 40% were observed between C^* values obtained from the two methods. Smith and Webster (114) compared C^* values

obtained from limit analysis with those obtained numerically. Discrepancies arose due to differences in the numerical factor F_T. They assumed that the dimensionless factor obtained from limit analysis was equal to F_T. This assumption is only justified for long cracks, where $\dot{\Delta}_o << \dot{\Delta}_c$ and $F_c \approx F_T$, and explains why discrepancies between the two values of F_T were greatest at shorter crack lengths. As limit analysis techniques are only strictly applicable when $n >> 1$, discrepancies between the two values were accentuated at low values of n.

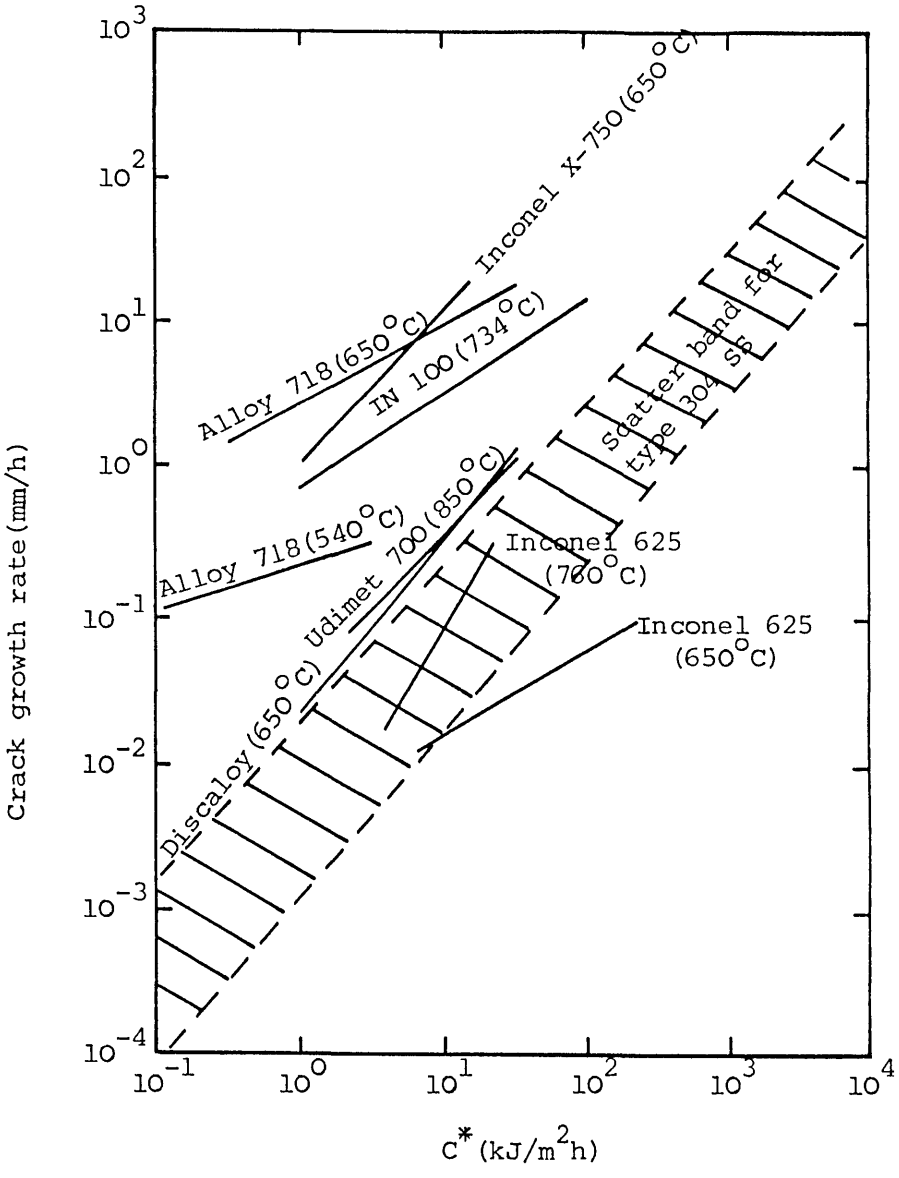


Fig. 6.1 Correlation of creep crack growth rates with C^* for a variety of structural alloys (16)

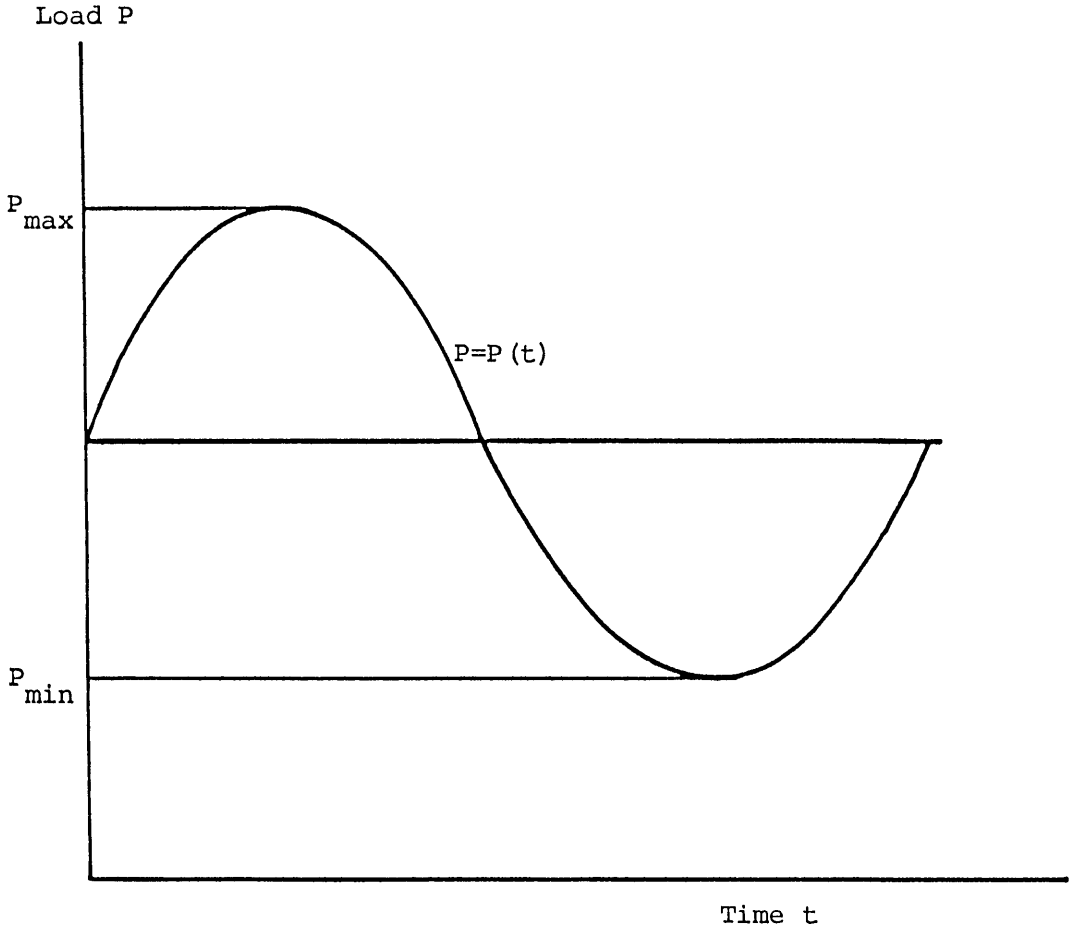


Fig. 6.2 Typical cyclic loading waveform

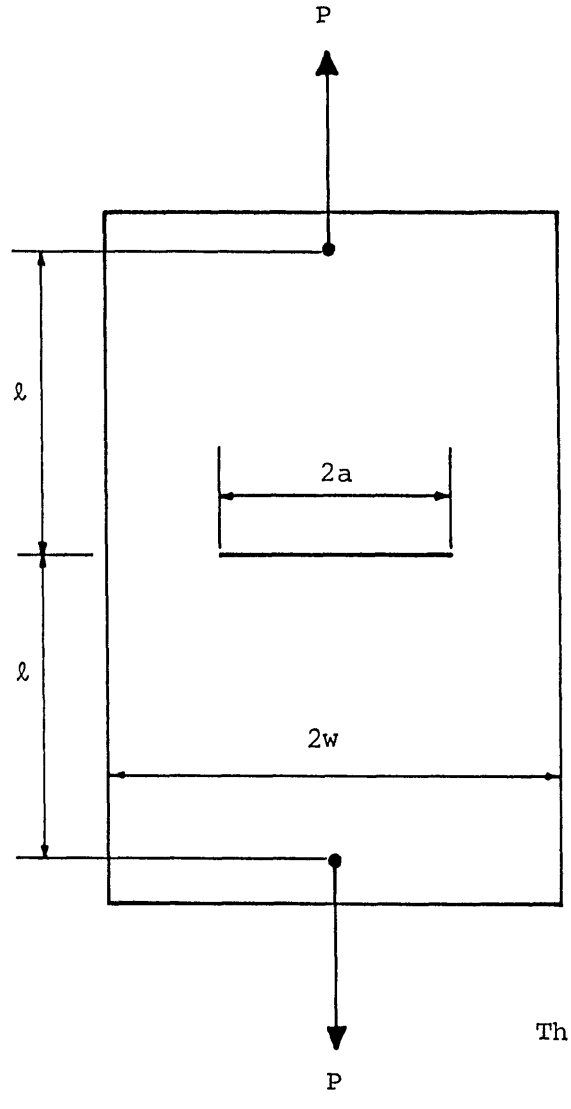


Fig. 6.3 CCP specimen geometry

APPENDIX 6

Common Test Piece Geometries

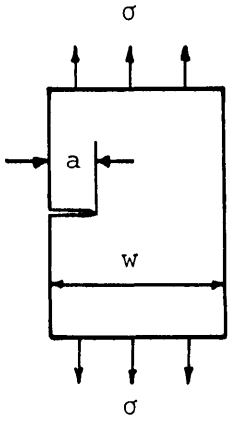
The relations for K and C^* are given in the form

$$K = Y\sigma\sqrt{a}$$

$$C^* = \frac{P\dot{\Delta}}{Bw} \cdot F$$

where F has been obtained using limit analysis methods or the Rice,Paris and Merkle(117) approach. When the latter approach has been used F_{RPM} replaces F.

(i) Single Edge Notch Tension (SENT)

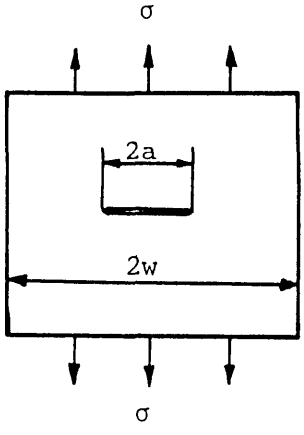


$$Y = 1.99-0.41(a/w)+18.7(a/w)^2 -38.5(a/w)^3+53.9(a/w)^4$$

$$F = \frac{n}{n+1} \cdot \frac{1}{(1-a/w)}$$

$$F_{RPM} = \frac{n-1}{n+1} \cdot \frac{1}{(1-a/w)}$$

(ii) Centre Cracked Plate (CCP)

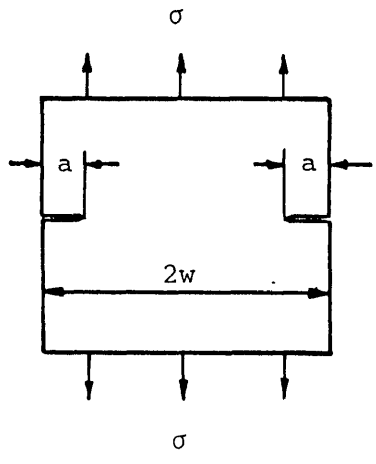


$$Y = \frac{1.77-0.89(a/w)+0.58(a/w)^2}{(1-a/w)^{0.5}}$$

$$F = \frac{n}{n+1} \cdot \frac{1}{2(1-a/w)}$$

$$F_{RPM} = \frac{n-1}{n+1} \cdot \frac{1}{2(1-a/w)}$$

(iii) Double Edge Notch Tension (DENT)

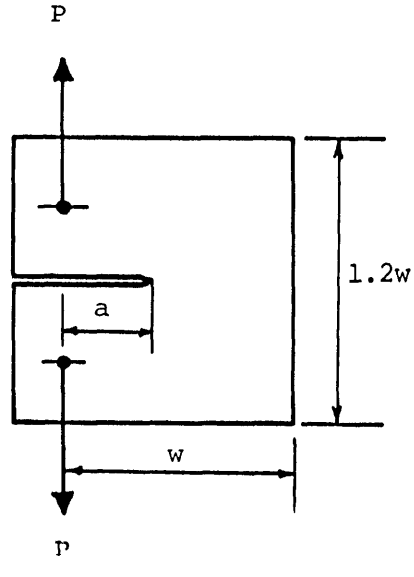


$$Y = 1.99+0.35(a/w)-2.13(a/w)^2 +3.42(a/w)^3$$

$$F = \frac{n}{n+1}\ \frac{1}{2(1-a/w)}$$

$$F_{RPM} = \frac{n-1}{n+1}\ \frac{1}{2(1-a/w)}$$

(iv) Compact Tension (CT)



$$K = \frac{P}{Bw^{0.5}}\left[29.6(a/w)^{0.5}-185.5(a/w)^{1.5} +655.7(a/w)^{2.5}-1017(a/w)^{3.5} +638.9(a/w)^{4.5}\right]$$

$$F = \frac{n}{n+1}\cdot X$$

a/w	0.25	0.375	0.50	0.625	0.75
X	1.96	3.13	4.70	6.04	7.90

CHAPTER 7

EXPERIMENTAL PROGRAMME

7.1 Introduction

This chapter describes the experimental programme carried out to study high temperature crack growth in the cast nickel base superalloy Mar M002. The majority of the work involved crack growth under cyclic loading, although several tests were also conducted under static loading. The material, specimen geometry and experimental equipment, used in the present study, are described. The methods, by which the relevant test variables are measured, are presented together with experimental procedures adopted during testing. Finally, a synopsis of the experimental testing programme is given.

7.2 Material : Composition and Heat Treatment

The material used in the experimental investigations was the conventionally cast nickel base superalloy Mar M002. This alloy has been used in the aircraft industry for engine gas turbine blading operating at temperatures up to 950°C. Table 7.1 gives the nominal chemical composition of the alloy in weight per cent.

Mar M002 cast turbine blades are subjected to brazing and aluminising cycles after casting, which can alter the microstructure and material properties. The cast specimens, used in the current investigation, were given heat treatments designed to simulate both the brazing and aluminising cycles seen by the cast blades. Details of the heat treatments are given in Table 7.2. The material used in the experimental investigations should therefore be representative of material used in service conditions and possess similar material properties and microstructural features. Typical microstructural features for the alloy are shown in figure 7.1.

The microstructure of Mar M002 is complex and contains a high volume fraction ($\sim$ 60%) of the γ' precipitate. The γ' phase exists in a large range of sizes and is precipitated throughout the γ matrix. A $\gamma - \gamma'$ eutectic is also formed in the last areas to solidify (generally at grain boundaries). The primary MC carbides, formed by tantalum, titanium and hafnium, tend to occur in grain boundary areas and are generally blocky in appearance, although script type carbides may also be formed. Grain boundaries are decorated by very small $M_{23}C_6$ carbides, formed by chromium and tungsten, which are essential for the development of good high temperature properties. Formation of $M_{23}C_6$ carbides is encouraged by ageing the alloy for 16 hours at 870°C prior to use in

service (Table 7.3). The casting procedures resulted in very large grain sizes in the range 0.2 - 3mm.

Crack growth tests were carried out at two temperatures, 750°C and 950°C. Relevant material properties are given in Table 7.3 for these two temperatures.

7.3 TCP Specimen Geometry

The specimen geometry used in the experimental investigations is shown in figure 7.2. Design of the specimen geometry was based on two requirements.

1. The thickness of the gauge section (1.5mm) is representative of the thickness of metal found in the trailing edge portion of a typical cast Mar MOO2 turbine blade containing cooling holes.

2. The microstructure and material properties of the specimen gauge section are representative of those in a typical Mar MOO2 blade.

Specimens were cast almost to size and, after heat treatment, the gauge section and 'T slot' ends were machined to size. 'T slot' ends prevented rotation of the ends of the specimen during crack growth, leading to a lower value of K, at a given crack length, than for a specimen with pinned ends, allowing stable crack growth over a greater range of crack lengths.

A small notch, with a depth of between 0.2 and 0.23 mm, was introduced into one side of the specimen, in the centre of the gauge section, by means of a fine slitting wheel. This notch was provided to act as a crack starter. A notch depth between 0.2 and 0.23mm was found to be adequate for initiating a fatigue crack at both 750°C and 950°C. However, under static loading a larger starter notch was required. A spark machined notch of depth 1.5mm was used as a crack starter for specimens tested under static loading at both 750°C and 950°C.

7.4. Experimental Equipment

7.4.1 Cyclic Loading Equipment

Cyclic loads were applied to the specimen using a servo-hydraulic testing machine. The servo-hydraulic machine used was a Mayes, model ESHF 100kN, with a facility for cyclic testing over a range of frequencies using various waveforms. A general layout of the rig with ancilliary equipment is shown in figure 7.3.

Load was applied to the specimen via Nimonic 80A pull-rods and Nimonic 115 shackles. The shackles, which were specially designed to accept the specimen 'T slot' ends, are shown diagrammatically in Figure 7.4. The specimen was heated by either a rectangular or cylindrical furnace, incorporating automatic temperature control via a platinum resistance thermometer.

The servo-hydraulic equipment was fitted with a load cell and displacement transducer so that loads and displacements, applied to the complete loading train, could be measured. Specimen extension was measured by an extensometer system, shown in figure 7.5. The specimen extension was measured by a single direct current LVDT (linear variable differential transformer) type transducer, clamped centrally between perspex plates attached to the lower end of Incoloy extensometer legs, external to the furnace. The top ends of the extensometer legs were rigidly attached to the upper and lower shackles so that extension of the whole specimen was measured. To prevent 'bouncing' during high frequency cycling, both the transducer stem and body were rigidly attached to the perspex plates. This system allowed load line extension of the whole specimen to be measured over a range of frequencies at

elevated temperatures. Chrome-alumel thermocouples were attached to the specimen to measure the temperature during testing.

For automatic crack length measurement (see Section 7.5.2) a direct current potential drop (DCPD) was used. A steady current of 35A was supplied to the specimen by a Mayes current supply unit. To ensure proper electrical insulation of the specimens, the pull-rod assembly was fitted with insulating bushes in the upper and lower halves of the loading train. The extensometer legs were electrically insulated from each other by using perspex plates to clamp the transducer. Copper leads were used for current supply external to the furnace, while the high testing temperatures necessitated the use of Nimonic strips for current supply to the specimen within the furnace. The Nimonic strips were attached via studs welded to the specimen in the locations shown in figure 7.6. Output voltages, designated V_c and V_{ref} in figure 7.6, were measured by spot-welding 0.3mm Brightray 'C' wires to the specimen in the required locations. These voltage sensing leads were electrically insulated using Refrasil (trade name) high temperature sleeving. Output voltages were of the order of millivolts.

7.4.2 Static Loading Equipment

The loading frame equipment used for applying steady loads to the specimen consisted of a dead load creep machine incorporating a 10:1 lever ratio loading arm. This equipment allowed static loads of up to 20kN to be applied to the specimen via pull-rods and shackles described in the previous section. The extensometer equipment used was similar to that described for cyclic loading. Chrome-alumel thermocouples were used to monitor specimen temperatures during testing. Crack lengths were measured using a DCPD system, similar to that described for cyclic

loading, except that the current supply unit manufactured by Coutant, Model ASA 1000, delivered a steady current of 10A. Output voltages were again of the order of millivolts.

7.5 Measurement Methods

7.5.1 Temperature, Displacement and Load Calibration

Before using each furnace for crack growth testing, a dummy specimen, fitted with four thermocouples along the length of the specimen, was used to ensure that the temperature was constant over the length of the specimen to ± 2°C. Temperature controller settings, required to achieve an adequate temperature distribution at the test temperature, were noted and used as a guide for setting up subsequent crack growth tests. The chrome-alumel thermocouples were provided with a calibration chart which could be used to convert thermocouple output voltages, measured on a potentiometer , to the associated temperature. An adequate temperature distribution was achieved for each specimen prior to testing.

The LVDT transducers used to measure displacement were calibrated prior to testing of all specimens. Each transducer was calibrated in a rig consisting of a drum-type micrometer held in a frame, into which the LVDT transducer was fixed. The output voltage from the transducer could be altered by means of a variable resistor, thereby allowing the sensitivity of the transducer calibration to be changed if necessary. Calibration curves of transducer output voltage and micrometer setting were linear over the ranges of displacement considered (up to about 1mm) and a sensitivity of 1mV to 0.001in was chosen for all tests.

The servo-hydraulic equipment was provided with a direct reading meter which gave the applied load in kN via a digital voltmeter connected to the load cell. The meter also gave direct readings of the maximum and minimum loads (in kN) applied to the specimen during cyclic loading.

This equipment was regularly serviced and calibrated by a technician from the manufacturers, W H Mayes Ltd.

7.5.2 Crack Length Measurement

The most reliable methods of measuring crack length at elevated temperatures fall into three categories (121)

1. Optical methods
2. Compliance methods
3. Electrical methods

Optical methods rely on direct visual observation of the crack tip during testing and may be used to detect crack extensions of the order of 0.1mm., although the reliability of precisely locating the crack tip may be no better than ± 0.5mm. An advantage of the optical technique is that crack extensions are obtained directly so that no calibration is required. Disadvantages arise due to the manual nature of the technique, which relies on both operator skill and the presence of the operator during testing.

Compliance methods rely on the fact that the compliance of a specimen is a function of crack length. Changes in compliance are used to obtain crack lengths by means of a suitable calibration curve. Unloading of the specimen is necessary in order to separate elastic and plastic components of displacement. Advantages of the technique are that automatic recording is possible and that average crack lengths are measured. Disadvantages are that periodic unloading of the specimen is required and that the technique is insensitive to the growth of small cracks.

Electrical methods involve passing a constant current through a specimen. The change in electrical potential, between two points either side of the crack plane, is monitored as the crack extends. Positions of the current supply and potential monitoring leads are chosen to provide reliable and sensitive indications of crack length. The current supply may be either direct or alternating. The former gives an indication of the average crack length while the latter measures the surface crack length. Both DC and AC methods require a reliable calibration curve which may be determined experimentally or theoretically. Hicks and Pickard (122) showed good agreement between experimental and theoretical calibrations for a range of specimen geometries. Smith (123) compared the DC and AC methods, by testing the respective systems under high temperature conditions. He found that with the AC system, even the slightest movement of the monitoring leads produced large changes in the output voltage. This effect did not occur in the DC system. The DC system was also found to be more reliable over longer periods. Electrical methods have several advantages over optical and compliance methods, and these are summarised below.

1. Automatic recording is possible, allowing 24hr usage of testing machines.

2. No unloading of the specimen is required. Interrupting the test for periodic unloading may alter the crack tip stress distribution and subsequent crack growth rates.

3. Electrical methods are capable of detecting small increments of crack growth, which may not be resolved optically. This is particularly useful for crack growth in the threshold region.

Saxena (124) has demonstrated that the DC potential drop technique can accurately monitor crack extension, due to both cylic and static loading at elevated temperature, in the presence of significant creep deformation. The DC potential drop technique was adopted for crack length measurement in the present work because of its suitability to the problem of monitoring small increases in crack length for short cracks at elevated temperature.

A constant direct current was passed through the specimen via welded studs shown in figure 7.6. Two output voltages, designated V_c and V_{ref}, were monitored throughout each test via leads spot-welded to the specimen. Several precautions were taken in order to obtain accurate measurements. The pd calibration (see Section 8.2) was found to be very sensitive to the location of the crack pd monitoring leads relative to the crack plane (ℓ_1 and ℓ_2) (figure 7.6), so the positions of these leads were measured for each specimen prior to testing. Reference leads, attached at some position where the potential is insensitive to changes in crack length, were used to check for long term drift and changes in impedance caused by metallurgical instability. A pd calibration in the form of a (V_c/V_{ref}) vs (a/w) relation (see Section 8.2.3) is then independent of temperature and material for a given specimen geometry. Calibration of the pd system is discussed in detail in Section 8.2. Differences between the material of the specimen and the pd monitoring wires can cause thermal $emfs$ to be set up at welded junctions between the wire and the specimen. Thermocouple effects were estimated by measuring the crack and reference voltages with the current supply switched off. Thermal $emfs$ were found to be negligible throughout the test programme and in all cases the thermal $emfs$ were less than 1% of V_c or V_{ref}.

7.5.3 Data Acquisition

Test data were collected by means of a standard 4 channel y-t chart recorder. This enabled the crack pd, V_c, the reference pd, V_{ref}, the output voltage from the transducer, V_{tr}, and the output voltage from a thermocouple to be monitored throughout each test. Use of appropriate calibration curves allowed the raw data to be converted into a record of crack length, displacement and temperature for each test.

7.6 Experimental Procedure

Prior to being placed in the appropriate test rig, each specimen was prepared for crack growth testing in the following manner. Crack and reference *pd* monitoring leads were spot-welded to the specimen in the locations described in Section 7.5.2. The positions of the crack *pd* leads relative to the crack plane (ℓ_1, ℓ_2 see figure 7.6) were measured by means of a travelling microscope (ℓ_1 and ℓ_2 were generally in the range 0.5 - 1.0mm). *Pd* monitoring leads were then electrically insulated by means of 'Refrasil' high temperature sleeving. Nimonic current supply leads were attached to the specimen via welded studs (figure 7.6). Chrome-alumel thermocouples were placed at the ends of the specimen gauge section and held in place using high temperature string.

7.6.1 Cyclic loading tests

The prepared specimen was fitted into the servo-hydraulic test rig by operating the machine in displacement control. Each specimen was placed in the loading shackles (figure 7.4) into which locating pins were fitted. The rig was then placed in standby load. The LVDT displacement transducer was calibrated in the manner described in Section 7.5.1 prior to setting up the displacement extensometry. Current supply leads were attached and *pd*, displacement and temperature monitoring leads connected to the channels of the *y-t* chart recorder. Prior to closing and heating of the furnace, the *pd* system was tested to ensure that the correct response was obtained. The thermocouple cold junction was placed in an equilibrium mixture of ice and water and thermocouples checked to ensure correct reading. The furnace was then closed and the required temperature was selected on the furnace

controller. Heating of each specimen commenced 20 hours prior to starting the test. This allowed time for a stable temperature distribution to develop and also allowed time for minor alterations to the settings on the furnace controller if required.

Prior to loading, the current supply was switched off and thermocouple effects checked for both the crack and reference pd monitoring leads. The machine was then transferred from standby load into load control (all tests were conducted under load control) and the load command set to the required mean level. The desired frequency was set on the signal generator and the load amplitude set to zero. The signal generator was then switched to the operating mode and the load amplitude gradually increased until the required loading conditions were established. Maximum and minimum loads were checked on the digital voltmeter (see Section 7.5.1). Crack and reference voltages, specimen extension and temperature were monitored throughout each test on a y-t chart recorder. Temperature readings were also periodically checked using a potentiometer.

In order to initiate a crack from the starter notch, relatively high cyclic loads were required, although in all cases these loads were lower than those needed to cause general yielding of the specimen. After a crack had been initiated, loads were gradually stepped-down until the required crack length/load combination had been established for the particular specimen. Once this situation had been reached, the loading conditions were kept constant for the remainder of the test, which proceeded under increasing ΔK conditions. All crack growth data obtained from the current test program were acquired from load controlled testing, under increasing ΔK conditions, after the crack had grown out

of the plastic zone formed ahead of the crack tip by the preceding loading.

7.6.2 Static loading tests

The prepared specimen was fitted manually into the dead load creep machine. Each specimen was placed in the loading shackles (figure 7.4), into which locating pins were fitted. A small pre-load of the order of $0.5kN$ was applied to the specimen by placing a small weight on the loading pan. The pre-load maintained alignment of the load train during setting up and subsequent heating of the specimen. The remainder of the procedure, prior to loading, was the same as described in Section 7.6.1 for cyclic loading. Once an adequate temperature distribution had been established, and all appropriate checks completed, the required load was gradually applied to the loading pan using a motorised jack. Crack and reference voltages, specimen extension and temperature were monitored throughout each test on a y-t chart recorder. Temperature readings were also periodically checked using a potentiometer.

A starter notch of approximately 0.2mm was used for the initial crack growth test under static loading. However, the stress concentration produced by this small starter notch was not sufficient and failure occurred across the change in section at the end of the gauge section. Presumably creep deformation caused rapid relaxation of the stresses at the notch root, thereby reducing the effective stress concentration. Subsequent specimens tested under static loading were provided with a 1.5mm spark machined notch, which was found to be satisfactory. All crack growth data acquired from tests conducted

under static loading in the current program were obtained from testing under constant load conditions.

7.7 Test programme

The following section briefly summarises the experimental test programme, conducted in order to investigate high temperature crack propagation in the cast nickel base superalloy Mar M002. Two temperatures, 750°C and 950°C, were chosen to be representative of typical service conditions experienced by cast turbine blades. Crack length and specimen elongation were monitored during each test. The programmes of tests carried out under cyclic and static loading are summarised in Sections 7.7.1 and 7.7.2.

Prior to design and manufacture of the extensometer equipment, for measuring specimen elongation, a series of preliminary tests were conducted under cyclic trapezoidal loading at a frequency of 0.25Hz. Details of these tests are given in Appendix 7.

7.7.1 Crack growth under cyclic loading

7.7.1.1 Crack growth at 750^{0}C

(a) Crack growth in the threshold region

Sinusoidal waveform; f = 20Hz

Specimen	R ratio
TCP 29	0.7
TCP 31	0.9

(b) Effect of R ratio

Sinusoidal waveform; f = 20Hz

Specimen	R ratio
TCP 30	0.5
TCP 27	0.7
TCP 28	0.9

(c) Changing R ratio during a test

Sinusoidal waveform; f = 20Hz

Specimen	Details
TCP 30	Change of R 0.5 → 0.7 → 0.9 → 1
TCP 36	Change of R 0.9 → 1

(d) Effect of frequency

Sinusoidal waveform; R = 0.5

Specimen	frequency/Hz
TCP 30	20
TCP 49	0.2

Sinusoidal waveform; R = 0.9

Specimen	frequency/Hz
TCP 41	20
TCP 37	0.2
TCP 38	0.02

7.7.1.2 Crack growth at 950^{0}C

(a) Crack growth in the threshold region

Sinusoidal waveform; f = 20Hz

Specimen	R ratio
TCP 22	0.1
TCP 21	0.7
TCP 33	0.9

(b) Effect of R ratio

Sinusoidal waveform; f = 20Hz

Specimen	R ratio
TCP 11	0.1
TCP 48	0.5
TCP 47	0.7
TCP 46	0.9

(c) Changing R ratio during a test

Sinusoidal waveform; f = 20Hz

Specimen	Details
TCP 48	Change of R 0.5 → 0.7 → 0.9 → 1

(d) Effect of frequency

Sinusoidal waveform; R = 0.5

Specimen	frequency/Hz
TCP 48	20
TCP 55	0.2
TCP 54	0.02

(e) Effect of waveform

R = 0.1

Specimen	Waveform	Frequency/Hz
TCP 51	SINE	0.2
TCP 53	TRAPEZOIDAL	0.2
TCP 52	TRIANGULAR	0.2
TCP 56	TRIANGULAR	6.87

The four waveforms are shown schematically in Figure 7.7. The triangular waveform of frequency 6.87Hz was chosen to have the same loading and unloading rates as the 0.2Hz trapezoidal waveform.

(f) Effect of prior creep damage

Creep damage was introduced into specimens TCP42 and TCP 45 prior to crack growth testing. The specimens were pre-strained to levels of between 1.5 and 2% at 950^{0}C prior to machining of the specimen gauge section and starter notch. Crack growth rates in the threshold region were measured for both virgin and creep damaged specimens subjected to sinusoidal loading at an R ratio of 0.9 and a frequency of 20Hz.

Specimen	Pre-strain/%
TCP 33	0
TCP 42	1.564
TCP 45	1.905

7.7.2 Crack growth under static loading

7.7.2.1 Crack growth at 750^{0}C

Constant load

Specimen	Load/kN
TCP 24	16.02

7.7.2.2 Crack growth at 950^{0}C

Constant load

Specimen	Load/kN
TCP 35	5.783

Table 7.1 Chemical Composition of Mar M002

Composition (wt.%)																
C	Si	Mn	S	Al	B	Co	Cr	Cu	Fe	Hf	Mg	Mo	Ta	Ti	V	W	Zr
.150	.100	.100	.005	5.50	.015	10.00	9.00	.050	.250	1.50	.002	.250	2.50	1.50	.050	10.00	.055

Remainder Ni.

Table 7.2 Heat Treatments of Mar M002

	Heat Treatment
Simulated Brazing Cycle	(i) 4 hours at 1190°C in vacuum. Vacuum furnace cool to 1000°C at 5°C/minute Gas fan quench (ii) 1 hour at 1150°C in vacuum. Vacuum furnace cool to 1000°C at 5°C/minute Gas fan quench
Simulated Aluminising	7 hours at 880°C
Aluminise Diffusion	1 hour at 1100°C
Ageing	16 hours at 870°C

Table 7.3 Material Properties of Mar MOO2

Temperature (^{o}C)	σ_y (MPa)	E (GPa)
750	806	167
950	429	151

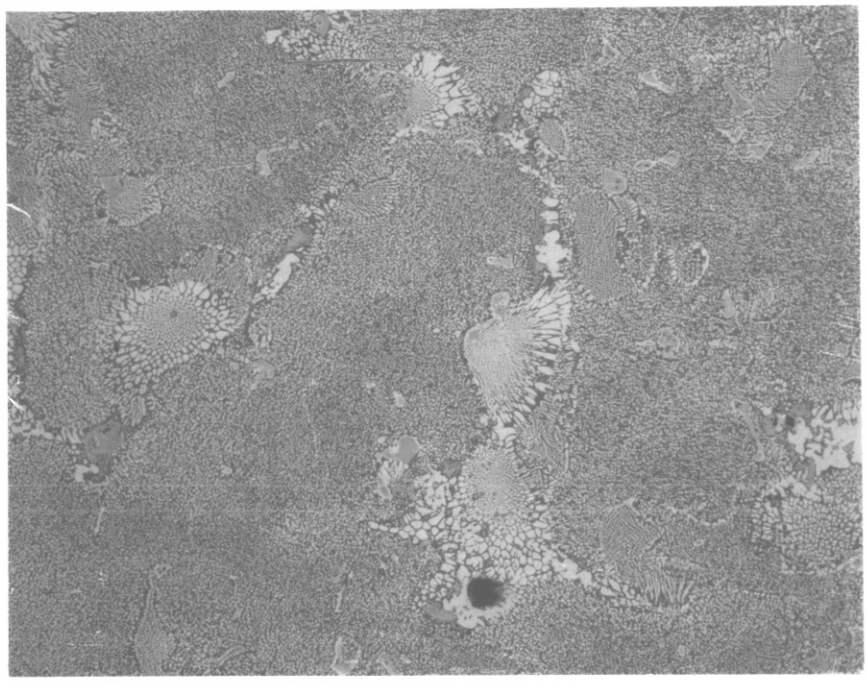
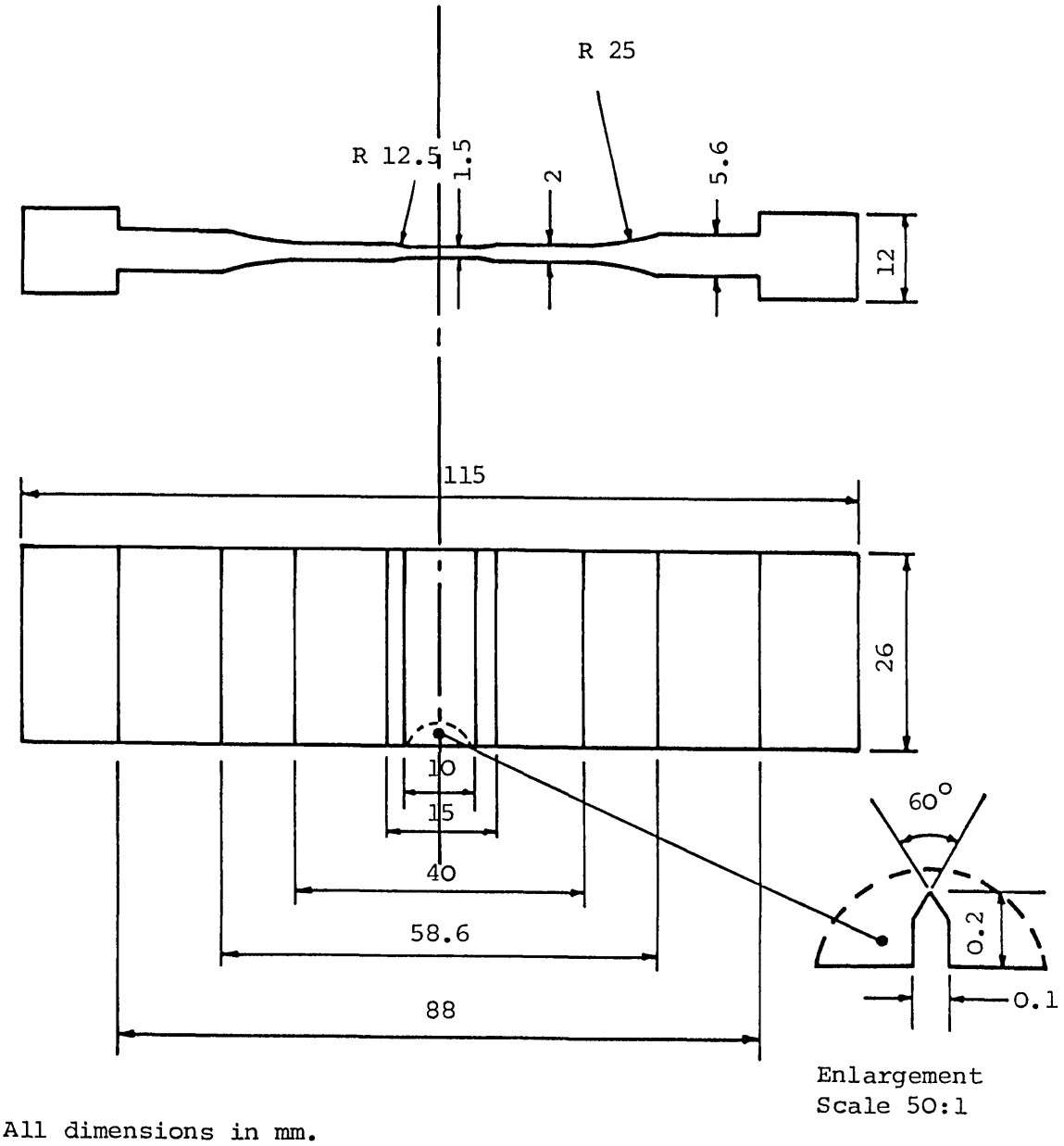


Fig. 7.1 Microstructure of cast Mar M002,x200



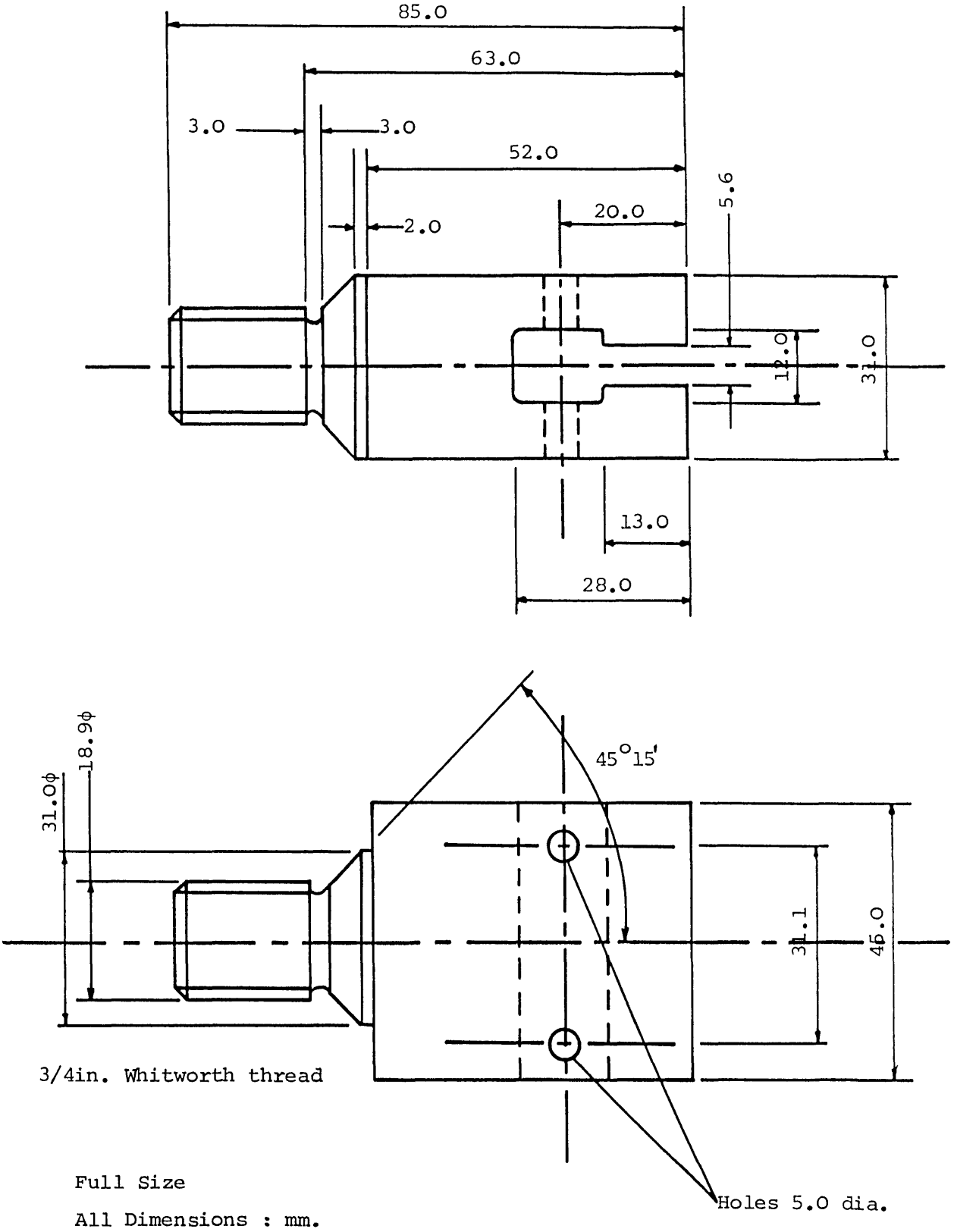
All dimensions in mm.

Scale : Full size

Fig. 7.2 TCP specimen geometry



Fig. 7.3 General layout of cyclic loading rig



Full Size

All Dimensions : mm.

Fig. 7.4 Loading shackles

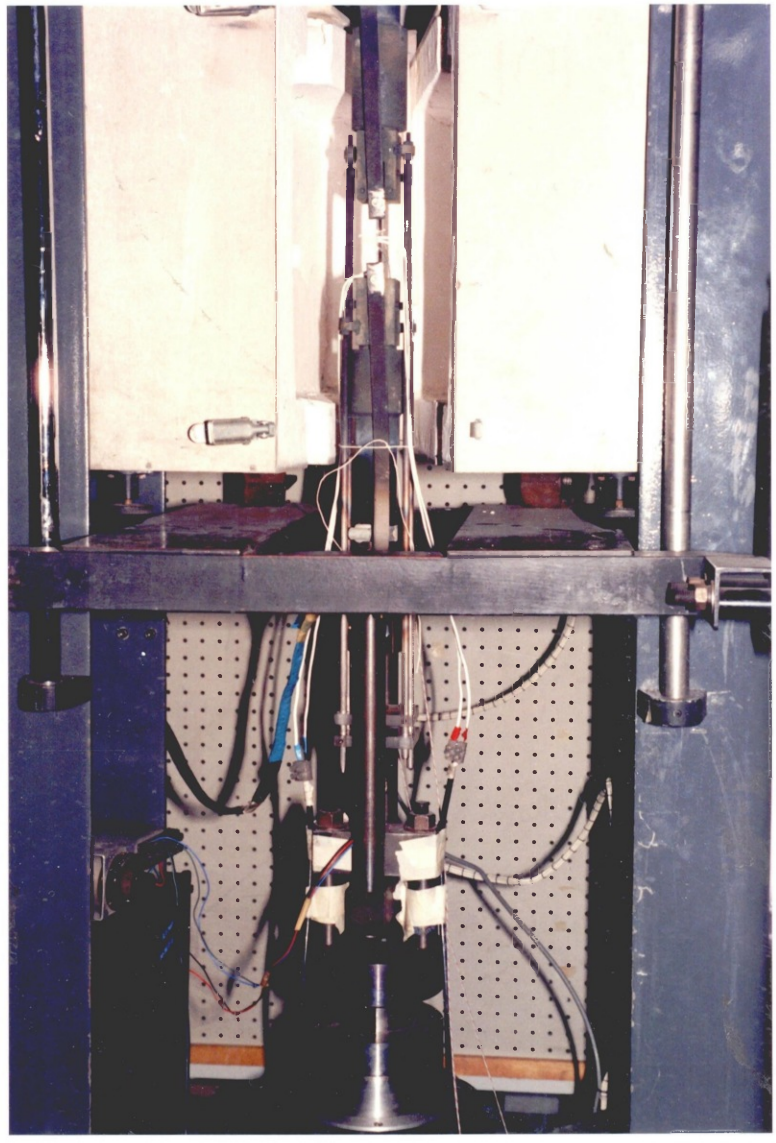


Fig. 7.5 Detail of extensometer system used for cyclic loading

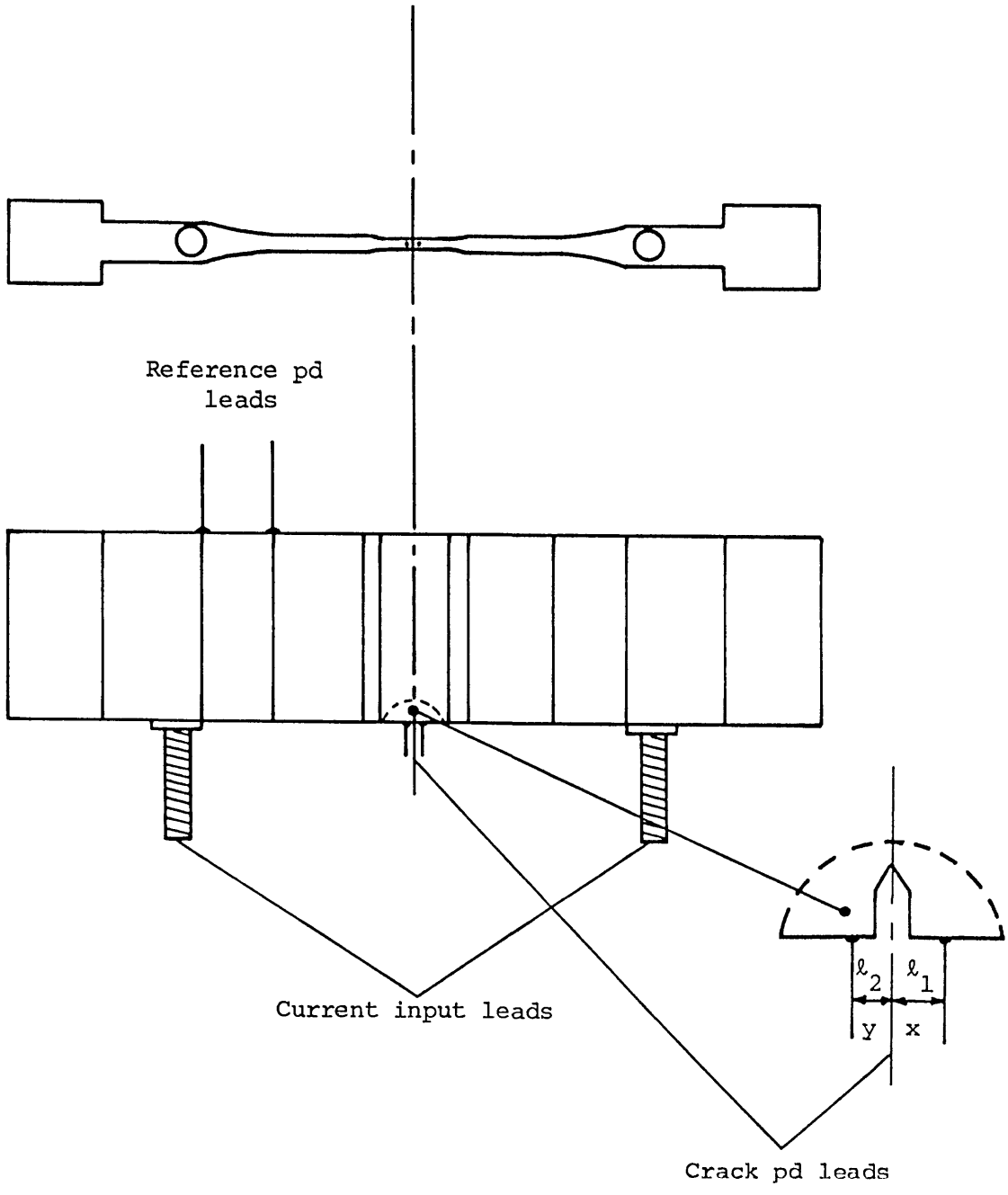


Fig. 7.6 Location of current input and pd monitoring leads on TCP specimens

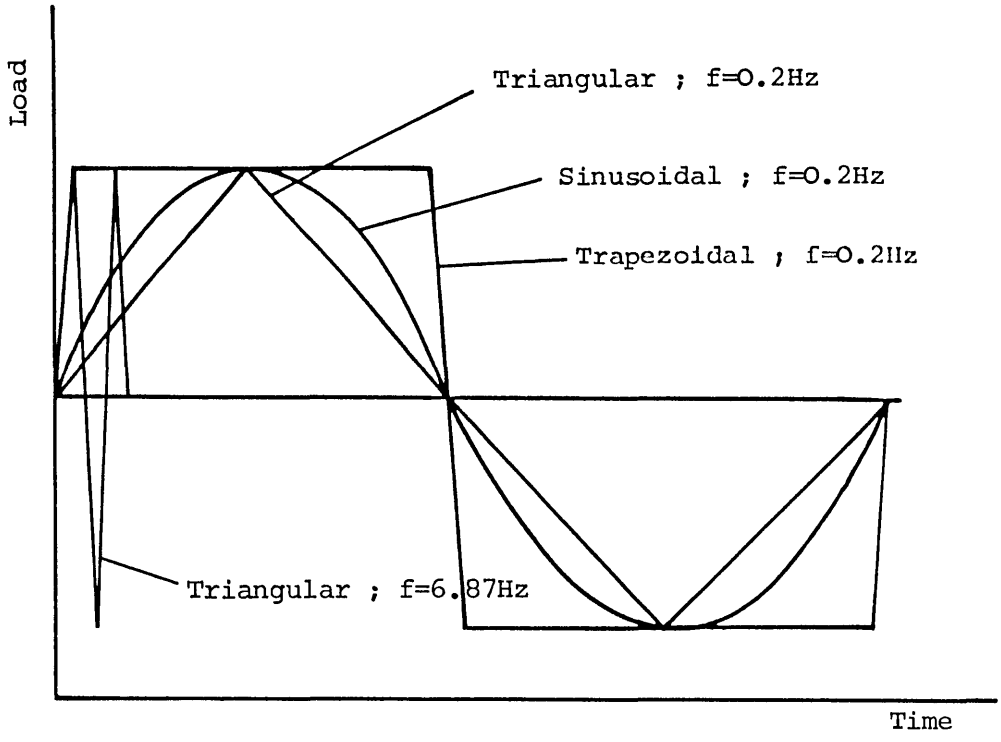


Fig. 7.7 Cyclic loading waveforms

APPENDIX 7

Preliminary Crack Propagation Tests

Trapezoidal waveform; $R = 0.1$; $f = 0.25$Hz.

(a) Room temperature

Specimen	Details
TCP 3	Crack lengths monitored by both optical and *pd* methods.
TCP 9	Crack growth test. Crack lengths monitored by both optical and *pd* methods.

(b) 750°C

Crack growth tests

Specimen
TCP 4
TCP 10

(c) 950°C

Crack growth rates were compared for tests in which the crack was grown from an initiated fatigue crack or directly from the starter notch.

Specimen	Crack Growth from
TCP 5 TCP 8	Initiated fatigue crack
TCP 7	Machined notch

CHAPTER 8

THEORETICAL Pd, K AND C^* CALIBRATIONS FOR THE CRACK PROPAGATION SPECIMEN

8.1 Introduction

Theoretical calibrations are required for the crack propagation specimen (figure 8.1) in order to convert experimental data into a useable form in terms of crack lengths and fracture mechanics parameters. The dc potential drop technique allows crack lengths to be calculated from experimentally measured voltages, V_c and V_{ref}, provided an appropriate calibration is available. Calibration curves are also required to determine values of the fracture mechanics parameters K and C^* from a knowledge of crack length and loading conditions. Theoretical pd, K and C^* calibrations have been determined for the crack propagation specimen, used in the present work, and these calibrations are discussed in detail in the following chapter.

8.2 *Pd* calibration

The theoretical *pd* calibration technique consisted of solving the analogous time-independent heat flow problem using the MARC - HEAT finite element programme.

Electrical	Thermal Analogy
Potential	Temperature
Current	Heat flow rate
Electrical conductivity	Thermal Conductivity
Capacitance	Specific Heat

A time-independent analysis was ensured by setting the capacitance (specific heat) to zero.

The finite element mesh of 120 elements and 405 nodes (figure 8.2) was generated to model one half of the specimen. Eight node quadrilateral elements were used. Zero potential was prescribed along the uncracked portion of the specimen centre line (by symmetry). Different crack lengths were modelled by altering the proportion of the specimen centre line along which the potential was zero. Current input was modelled by applying a uniform current to the external face of element C (a current of equal magnitude was assumed to flow out of the symmetrical element C'). The current supply positions were chosen as a compromise between providing a uniform current across the width of the specimen and experimental convenience. Finite element solutions were obtained for a/w values of 0, 0.1, 0.2, 0.3, 0.4, 0.5, 0.6, 0.7.

In order to determine the optimum locations for the crack and reference *pd* monitoring leads for the crack propagation specimen (figure 8.1), the theoretical variation of voltage along each side of

the specimen was plotted for a/w values of 0 and 0.7 (figure 8.3). Voltages were arbitrarily normalised with respect to the value of the voltage at node X for $a/w = 0.7$, $V_{X,0.7}$.

8.2.1 Location of Reference *Pd* Leads

Ideally, the reference leads should be located on the specimen in such a way that the reference *pd*, V_{ref}, is independent of crack length. However, figure 8.3 clearly shows that for the crack propagation specimen there are no locations (apart from point P where the potential is always zero) at which the potential remains unchanged during crack growth. An alternative method for locating the reference leads is to find two points on the specimen, between which the potential difference remains constant, or relatively constant, over a wide range of crack lengths. Using this criterion, points Y and Z were found to be the most suitable positions for attaching reference leads. The potential difference between these two points, V_{ref}, varied by only 15% over the entire range $0 \leq a/w \leq 0.7$ while the magnitude of V_{ref} was large enough to be conveniently monitored on the y - t chart recorder without the need for amplification.

8.2.2 Location of Crack *Pd* Leads

The criterion used for locating the crack *pd* leads was that they should experience maximum changes in potential caused by changes in crack length. Positions A and B (figure 8.3) and their symmetrical counterparts A' and B' were suitable locations in theory. (ie crack *pd* leads could theoretically be attached to A and A' or B and B').

8.2.3 Theoretical *Pd* calibration

Figure 8.4 shows the variation of crack *pd*, V_c, with crack length for monitoring leads attached either 0mm or 1.25mm from the crack

plane. The reference pd, V_{ref}, is also shown and all pd's are normalised with respect to their values at $a/w = 0.7$. A theoretical pd calibration which is independent of current supplied, temperature and material may be obtained by plotting (V_c/V_{ref}) versus (a/w) (figure 8.5). Clearly, for $0 \leq a/w \leq 0.1$, the calibration is highly sensitive to the location of the crack pd monitoring leads. An enlarged schematic view of the specimen starter notch is shown in figure 8.6. Clearly, crack pd leads cannot be attached at positions A and A', and experience showed that the crack pd leads could not be spot-welded with sufficient accuracy to guarantee location at positions B and B'. However, the crack pd leads could be attached somewhere between O and 1.25mm either side of the crack plane (as shown in figure 8.6). After spot-welding, the lead positions (ℓ_1, ℓ_2) were accurately measured by means of a travelling microscope and an interpolation procedure developed in order to establish an accurate theoretical pd calibration for each specimen.

In practice, crack length measurement was only necessary in the range $0 \leq a/w \leq 0.5$. Least squares techniques were used to fit polynomials to the (V_c/V_{ref}) versus (a/w) relations, for lead position Omm and 1.25mm from the crack plane (figure 8.7). For leads Omm from the crack plane

$$(V_c/V_{ref})_0 = F_A(a/w) \tag{8.1}$$

and for leads 1.25mm from the crack plane

$$(V_c/V_{ref})_{1.25} = F_B(a/w) \tag{8.2}$$

In general for leads situated ℓ mm from the crack plane

$$V_c/V_{ref} = F(a/w) \tag{8.3}$$

Figure 8.8 shows F/F_B plotted against ℓ for a range of values of a/w. Figure 8.9 shows schematically (F/F_B) plotted against ℓ for $a/w = 0, 0.008$ and an arbitrary value of a/w. The variation of (F/F_B) with crack *pd* lead location for the specimen starter notch is given by the contour $a/w = 0.008$, which may be expressed in the form

$$\left[F/F_B\right]_{0.008} = g(\ell) \tag{8.4}$$

Using figure 8.8 in conjunction with figure 8.9, it was discovered that in general, for $a/w > 0.008$

$$\Delta/\Delta_{0.008} \simeq (1 - (F_A/F_B))/0.803 \tag{8.5}$$

This may be more conveniently written as

$$\Delta \simeq \frac{\left[1-(F_A/F_B)\right]\Delta_{0.008}}{0.803} \tag{8.6}$$

where $\Delta_{0.008}$ may be calculated from figure 8.9 in conjunction with equation 8.4.

$$\Delta_{0.008} = (0.642\ell + 0.197) - g(\ell) \tag{8.7}$$

A general expression may be obtained for (F/F_B) which is valid for $a/w > 0.008$ and $0 \leq \ell \leq 1.25$

$$(F/F_B) = (F_A/F_B) + \left[1-(F_A/F_B)\right]\ell/1.25 - \Delta \tag{8.8}$$

where Δ is given approximately in equation 8.6. Referring, once again,

to figure 8.6 and assuming that the crack *pd* monitoring leads are attached at distances ℓ_1 and ℓ_2 from the crack plane where $\ell_1 \neq \ell_2$, the following procedure was observed in order to establish an accurate *pd* calibration for the specimen

1. For ℓ_1 calculate (F_1/F_B) as a function of a/w from equation 8.8.

2. For ℓ_2 calculate (F_2/F_B) as a function of a/w from equation 8.8.

3. The *pd* calibration for the specimen may then be expressed as

$$V_c/V_{ref} = \left[\frac{(F_1/F_B) + (F_2/F_B)}{2}\right] . F_B\ (a/w) \qquad (8.9)$$

The above procedure was followed for each specimen after the crack *pd* lead positions, ℓ_1 and ℓ_2, had been accurately measured prior to testing. Experimental values of $(V_c/V_{ref})_{exp}$ were adapted for use in the theoretical calibration (equation 8.9) by carrying out the following normalisation procedure

$$(V_c/V_{ref})_n = (V_c/V_{ref})_{exp} \left[\frac{(V_c/V_{ref})_{th}}{(V_c/V_{ref})_{exp}}\right]_{initial} \qquad (8.10)$$

where $(V_c/V_{ref})_n$ is the normalised value and the initial theoretical value, $(V_c/V_{ref})_{th,\ initial}$ may be calculated from equation 8.9, provided the initial notch depth is known. Normalisation with respect to initial values was chosen, as the initial values of a/w, V_c and V_{ref} were always determinate, even in cases where the tests were continued until failure occurred. In practice, the foregoing analysis is carried out numerically as part of a data analysis programme.

The interpolation procedure developed in this section is necessary, in order to achieve acceptable accuracy in crack length determination, for the following reasons:

1. Interpolation is required in the range, $0 \leq a/w \leq 0.1$, in which the *pd* calibration is highly sensitive to the positioning of the crack *pd* monitoring leads.

2. The normalisation procedure, described in equation 8.10, requires that $(V_c/V_{ref})_{th,\ initial}$ may be accurately determined. As the initial notch length, a_i, is always in the range $0 \leq \frac{ai}{w} \leq 0.1$, accurate determinination of $(V_c/V_{ref})_{th,\ initial}$ is only possible by means of the interpolation procedure.

Comparison of crack lengths, determined by the *pd* method, with optical readings, obtained from room temperature fatigue tests, showed good agreement (figure 8.10) although appreciable scatter was evident in the optical readings.

8.3 K Calibration

A stress analysis of the crack propagation specimen (figure 8.1) was carried out using the MARC finite element programme and assuming linear elastic behaviour. Finite element meshes were generated to model one half of the specimen, using plane stress, 8 node quadrilateral elements. Zero axial deflection was prescribed along the uncracked portion of the specimen centre line. The crack tip singularity was modelled using quarter-point degenerated triangular isoparametric elements. Different crack lengths were modelled by altering the position of the crack tip elements relative to the rest of the mesh.

Three distinct types of mesh were used:

Mesh 1

122 elements, 407 nodes (figure 8.11) used for
$a/w = 0.1, 0.2, 0.3, 0.4, 0.5$

Mesh 2

126 elements, 421 nodes (figure 8.12) used for
$a/w = 0.1$

Mesh 3

158 elements, 521 nodes (figure 8.13) Used for
$a/w = 0.05, 0.15$

Material properties for Mar M002 at 800°C were assumed ($E = 163.4\ GN/m^2$). The specimen was loaded by applying a uniform axial displacement to section AA (see figures 8.1, 8.11, 8.12, 8.13).

The differential stiffness method was used to evaluate energy release rates due to crack extension. For each crack length, the

energy release rate in half of the specimen, $\Delta U/2$, was determined for two different values of crack tip displacement, Δa ($\Delta a/w = 0.001$ and 0.002) and, for $\Delta a/w = 0.001$, for two different contours. The strain energy release rate was given by

$$G = \Delta U/B\Delta a \tag{8.11}$$

where B is the specimen thickness in the gauge section. Plane stress conditions are assumed as the specimen is thin, and

$$K^2 = EG \tag{8.12}$$

Values of K were determined for a range of values of crack length. In order to determine a stress intensity factor calibration, which was independent of temperature and material, stress intensity factors calculated from equation 8.12 were normalised with respect to K_o, the stress intensity factor for a central crack in an infinite plate, given by

$$K_o = \sigma\sqrt{\pi a} \tag{8.13}$$

Figure 8.14 shows the stress intensity factor calibration for the crack propagation specimen compared with the calibration curves for both CCP and SENT geometries (from Tada et al (111)). Clearly, the calibration curves for the crack propagation specimen and the CCP are of the same form and may be related by the following expression

$$K = 1.073\, K_{ccp} \tag{8.14}$$

for $0 \leq a/w \leq 0.5$.

8.4 C^* Calibration

Numerical methods for calculating theoretical C^* values, introduced in section 6.4.2.3, are based on an analogy between fully plastic power law hardening and secondary creep behaviour. Fully plastic solutions, obtained by Kumar et al (119) for a range of common specimen geometries, may therefore, by analogy, be applied to situations in which material behaviour is governed by secondary creep.

The TCP specimen used in the present work differs from a standard SENT specimen in that rotation of the ends of the specimen is prevented. It is not surprising that stress intensity factor calibrations for the two geometries differ significantly. (figure 8.14). However, the stress intensity factor calibrations for the TCP and CCP specimens show similar features, differing only by a constant numerical factor (1.073) over the range $0 \leq a/w \leq 0.5$. Huang and Pelloux (125) used a single edge notch specimen in which end rotations were prevented and suggested that the J-integral calibration, and by analogy the C^* calibration, for their specimen could be related to the calibration for a CCP specimen in the following manner

$$C^* = M \cdot C^*_{CCP} \qquad (8.15)$$

where M is a numerical factor, which they assumed to be independent of crack length and n. Assuming further that the stress intensity factor calibration for their specimen could be related to the calibration for a CCP specimen by

$$K = 1.12\, K_{CCP} \qquad (8.16)$$

they deduced a value of $(1.12)^2$ for M. The assumption that M is independent of crack length seems reasonable and in the case of the TCP specimen a value of $M = (1.073)^2$ is justified for $0 \leq a/w \leq 0.5$ when $n = 1$. However, upper bound estimates for M, in cases where $a/w \to 0$ (126), have shown that M varies with n, and for the case where $K = 1.12\ K_{CCP}$. M may be expressed as

$$M \simeq (1.12)^2 - 0.254\ exp(-5.85/n) \tag{8.17}$$

or if $K = 1.073\ K_{CCP}$ as in the case of the TCP specimen,

$$M \simeq (1.073)^2 - 0.151\ exp(-5.85/n) \tag{8.18}$$

assuming the same rate of decay as in equation 8.17. A graph of M plotted against $1/n$ is shown in figure 8.15. M reduces to $(1.073)^2$ when $n = 1$ and tends to unity as $n \to \infty$. Thus a theoretical C^* calibration for the TCP specimen may be estimated from numerical results for the CCP specimen using equations 8.15 and 8.18 and assuming that M is independent of crack length for all n.

A theoretical expression for C^* for the CCP specimen was shown to be of the form (equation 6.39),

$$C^*_{CCP} = \frac{\dot{\varepsilon}_o}{\sigma_o^n}\ a(1 - a/w)\, h_1 \left[\frac{P}{2B(w - a)}\right]^{n+1} \tag{8.19}$$

where h_1 is a function of a/w and n and is given, in both tabular and graphical form, for a range of values of a/w and n, in reference 119. Denoting the remote applied stress by σ_∞, where

$$\sigma_\infty = \frac{P}{2BW} \tag{8.20}$$

equation 8.19 may be rewritten in the alternative non dimensional form

$$\frac{C^*_{CCP}\ \sigma_o^{\,n}}{\dot{\varepsilon}_o\ W\sigma_\infty^{\,n+1}} = a/w\ (1 - a/w)\, h_1 \left[\frac{1}{(1 - a/w)}\right]^{n+1} \qquad (8.21)$$

Figure 8.16 shows a plot of log $(C^*_{CCP}\ \sigma_o^{\,n}/\dot{\varepsilon}_o\ W\sigma_\infty^{\,n+1})$ versus a/w for a range of values of n. Values of h_1 were given by Kumar et al (119) for $a/w = 0.125,\ 0.25,\ 0.375,\ 0.5,\ 0.625,\ 0.75,\ 0.875$. The present work on crack growth in the TCP specimen requires a theoretical C^* calibration for crack lengths within the range $0 \leq a/w \leq 0.5$. When $a/w = 0$, C^*_{CCP} and $(C^*_{CCP}\ \sigma_o^{\,n}/\dot{\varepsilon}_o\ W\sigma_\infty^{\,n+1})$ are also zero. Interpolation for C^*_{CCP} values in the range $0 < a/w < 0.125$ is not possible when values are plotted in the form shown in figure 8.16, because $\log(C^*_{CCP}\ \sigma_o^{\,n}/\dot{\varepsilon}_o\ W\sigma_\infty^{\,n+1})$ becomes indeterminate when $a/w = 0$.

Shih and Hutchinson (118) have derived an approximate formula for J-integral values for a finite central crack in an infinite plate. Their expression may also be applied to the finite CCP geometry in the limit when $a/w \to 0$, and by analogy, in the steady state creep regime may be written as

$$C^*_{CCP} = \frac{\dot{\varepsilon}_o}{\sigma_o^{\,n}}\ a\ \sigma_\infty^{\,n+1}\left[3.85\sqrt{n}\ (1 - 1/n) + \pi/n\right] \text{ for } a/w \to 0 \qquad (8.22)$$

The above expression may conveniently be expressed in non-dimensional form as

$$\frac{C^*_{CCP}\ \sigma_o^{\,n}}{\dot{\varepsilon}_o\ a\ \sigma_\infty^{\,n+1}} = \left[3.85\sqrt{n}\ (1 - 1/n) + \pi/n\right] \qquad (8.23)$$

It is convenient at this point to define a paramater, K^*, which is equivalent to the stress intensity factor K when $n = 1$, and is given, in general, by

$$K^* = \left[C^* \sigma_o^{\,n} / \dot{\varepsilon}_o \right]^{1/(n+1)} \tag{8.24}$$

Equation 8.21 may now be rewritten as

$$\frac{K^*_{CCP}}{a^{1/n+1}\,\sigma_\infty} = \left[\frac{h_1}{(1 - a/w)^n} \right]^{1/(n+1)} \tag{8.25}$$

The above equation may be used for a/w values 0.125, 0.25, 0.375, 0.5 for which values of h_1 have been tabulated by Kumar et al (119). For $a/w = 0$, equation 8.23 may be rewritten as

$$\frac{K^*_{CCP}}{a^{1/n+1}\,\sigma_\infty} = \left[3.85\sqrt{n}\,(1 - 1/n) + \pi/n \right]^{1/n+1} \tag{8.26}$$

In particular, when $n = 1$, equation 8.26 reduces to the infinite plate solution

$$K_{CCP} = \sigma_\infty \sqrt{\pi a} \tag{8.27}$$

Values of $(K^*/a^{1/n+1}\,\sigma_\infty)$ have therefore been determined for the CCP geometry subjected to plane stress loading for $a/w = 0$, 0.125, 0.25, 0.375, 0.5 for a range of values of n. For each value of n, least squares techniques may be used to fit a polynomial to the data values (as shown in figure 8.17) such that

$$\frac{K^*_{CCP}}{a^{1/n+1}\,\sigma_\infty} = g_n(a/w) \quad 0 \leq a/w \leq 0.5 \tag{8.28}$$

The above equation may be used to establish a C^* calibration for the

CCP specimen in the range $0 \leq a/w \leq 0.5$, which may be expressed as

$$C^*_{CCP} = \frac{\dot{\varepsilon}_o}{\sigma_o^n} a \left[\sigma_\infty g_n (a/w)\right]^{n+1} \qquad (8.29)$$

which in turn allows a C^* calibration to be determined for the TCP specimen of the form

$$C^* = M \cdot \frac{\dot{\varepsilon}_o}{\sigma_o^n} a \left[\sigma_\infty g_n (a/w)\right]^{n+1} \qquad (8.30)$$

where M can be calculated from equation 8.18. and the function $g_n(a/w)$ is plotted in figure 8.17 for a range of values of n.

8.4.1 Theoretical C^* Calibration for 750°C

Determination of the theoretical C^* calibration requires a knowledge of the relationship between minimum creep rate and applied stress at 750°C. Figure 8.18 shows a plot of the available minimum creep rate data for Mar M002 specimens subjected to the heat treatment listed in Table 7.2. Creep data was only available at stresses of 400 and 500MPa. The applied stresses used for crack growth testing at this temperature are in the range $250MPa \leq \sigma \leq 500MPa$. Expressing the minimum creep rate in the form

$$\dot{\varepsilon}_{min} = \frac{\dot{\varepsilon}_o}{\sigma_o^n} \cdot \sigma^n \qquad (8.31)$$

and rupture data in the form

$$t_R \propto \sigma^{-\nu} \qquad (8.32)$$

and adopting the brittle rupture theories of Kachanov and Rabotnov (Appendix 5), then for constant creep ductility, ε_f, $n = \nu$. The creep

ductility, ε_f, for Mar M002 at 750°C is approximately constant over the stress range $250MPa \leq \sigma \leq 500\ MPa$, so that the slope of the log t_R vs log σ plot, shown in figure 8.19, corresponds to $-n$. Unfortunately, no rupture data was available at this temperature for $\sigma < 380MPa$. The slope of the log t_R vs log σ plot in the range $380MPa \leq \sigma \leq 500MPa$ is best represented by $\nu = 7$, and is shown by a solid line in figure 8.19. Assuming that $n = \nu = 7$, a line of slope 7 was fitted to the minimum creep rate data, thereby allowing the constant $\dot{\varepsilon}_o/\sigma_o^n$ to be determined. Good agreement was found between the theoretical line and the experimental minimum creep rate data, and

$$\dot{\varepsilon}_o/\sigma_o^n = 2.80 \times 10^{-25}\ h^{-1}(MPa)^{-7} \tag{8.33}$$

Theoretical C^* values may then be calculated from equation 8.30, and, for $n = 7$

$$M = 1.086 \tag{8.34}$$

and

$$g_7(a/w) = G0 + G1(a/w) + G2(a/w)^2 + G3(a/w)^3 + G4(a/w)^4 \tag{8.35}$$

where

$$\begin{aligned} G0 &= 1.31933176 \\ G1 &= -0.148432664 \\ G2 &= 4.98615485 \\ G3 &= -9.95087732 \\ G4 &= 11.2273929 \end{aligned} \tag{8.36}$$

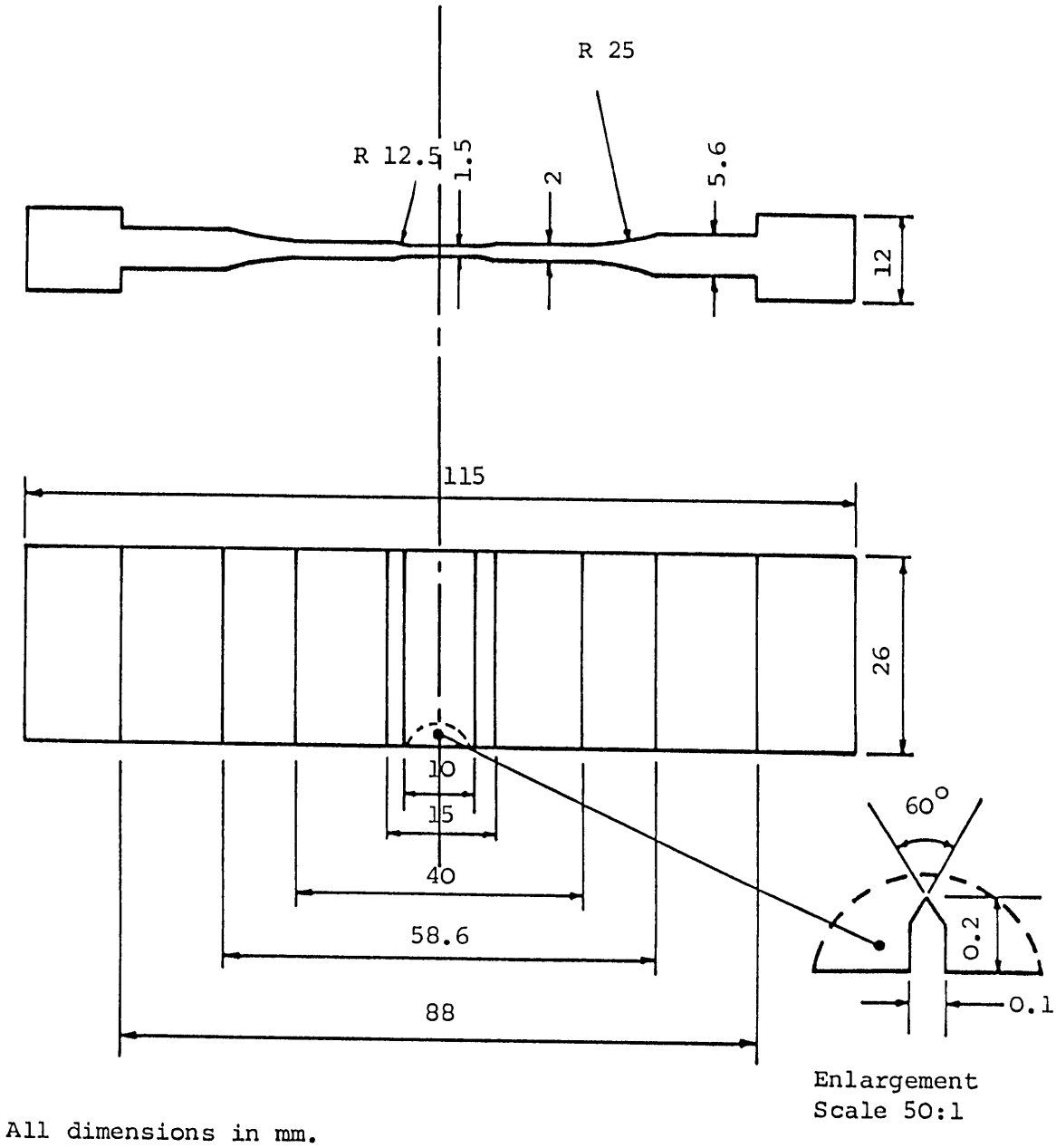
8.4.2 Theoretical C^* Calibration for 950°C.

Minimum creep rate data at 950°C was only available for hollow specimens, subjected to a conventional heat treatment (without the

simulated brazing and aluminising cycles). Figure 8.20 shows a plot of the available minimum creep rate data. Rupture data, for specimens subjected to the brazing and aluminising cycles (Table 7.2), are compared with rupture data for conventionally heat treated specimens in figure 8.21. Good agreement was found between conventional hollow specimens and solid specimens, subjected to the brazing and aluminising cycles, over the range $145MPa \leq \sigma \leq 375MPa$ (the range of applied stresses used for crack growth testing at 950°C). Assuming that minimum creep rates, for the two conditions, are also comparable, approximate values of n and $\dot{\varepsilon}_o/\sigma_o^n$ may be determined from figure 8.20. Thus, $n = 7$, and

$$\dot{\varepsilon}_o/\sigma_o^n = 1.05 \times 10^{-20}\ h^{-1}(MPa)^{-7} \qquad (8.37)$$

Theoretical C^* values for 950°C may then be calculated from equation 8.30 in conjunction with equations 8.34 - 8.36.



All dimensions in mm.

Scale : Full size

Fig. 8.1 TCP specimen

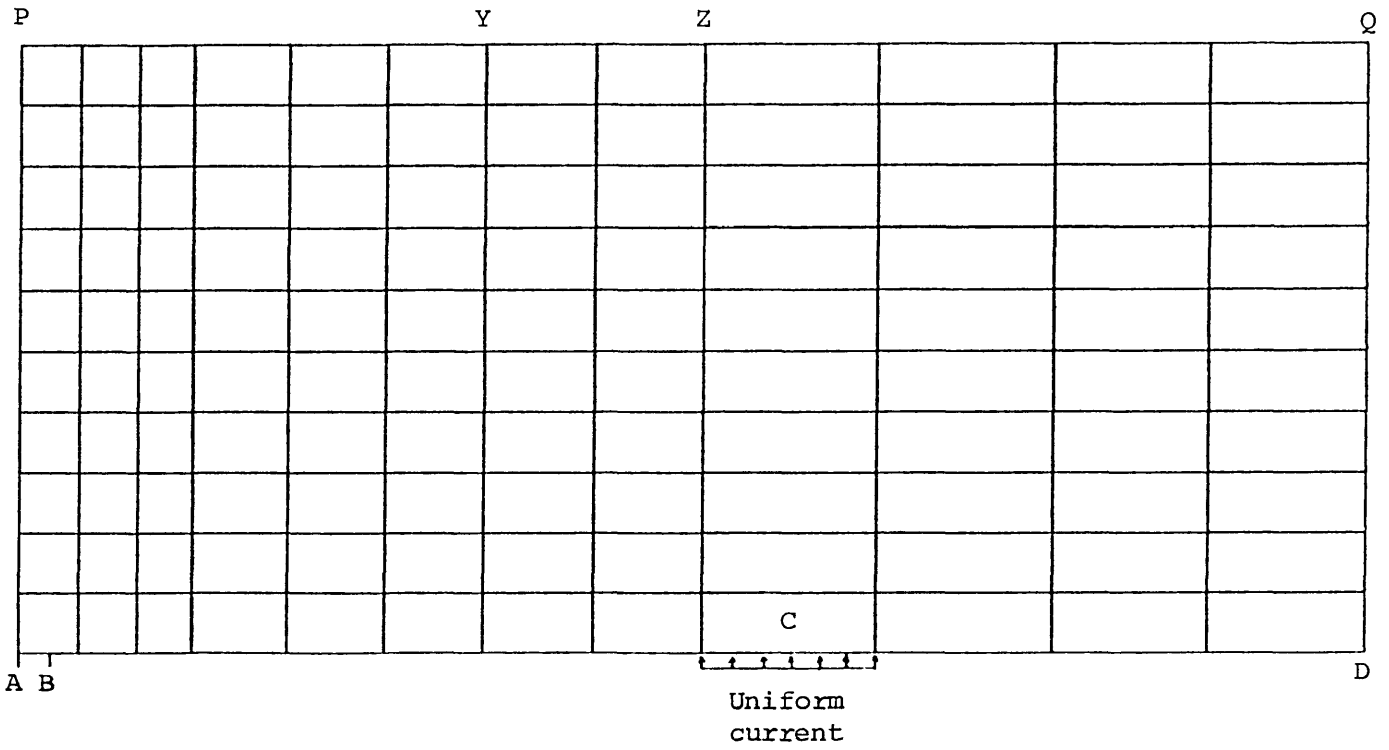


Fig. 8.2 Finite element mesh used to obtain the pd calibration

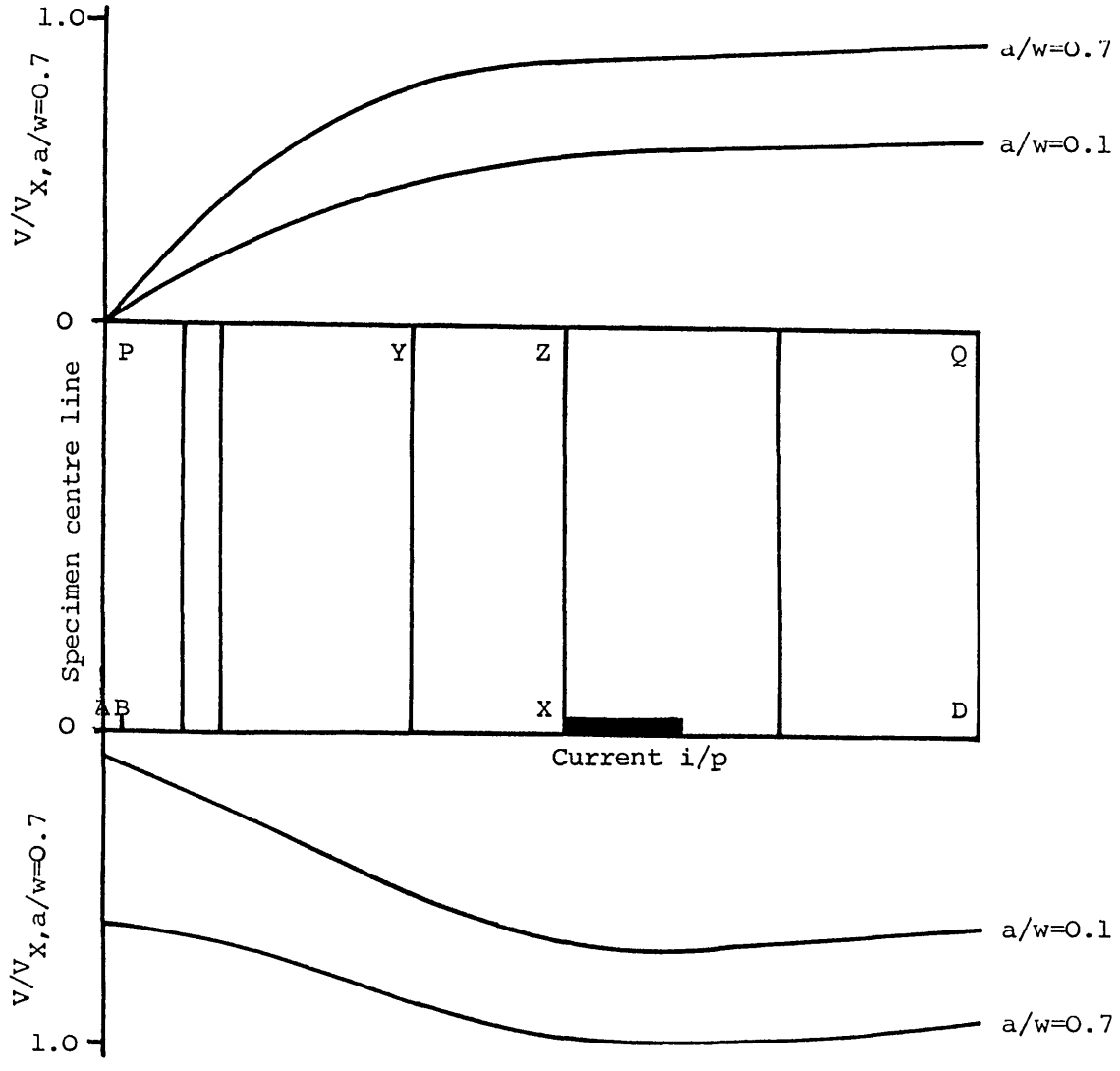


Fig. 8.3 Variation of voltage along each side of one half of the TCP specimen for a/w=0.1 and 0.7

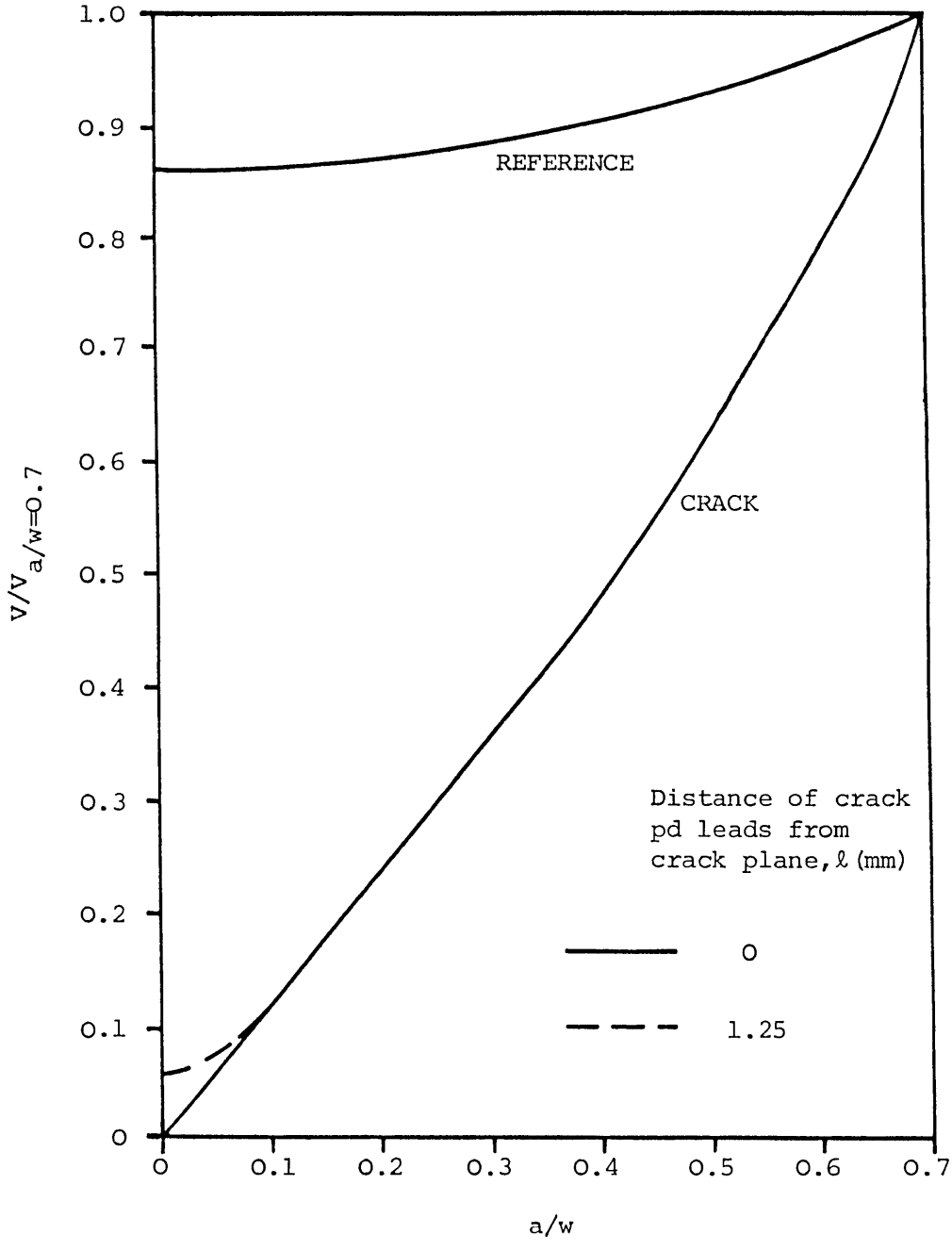


Fig. 8.4 Variation of crack pd, V_c, and reference pd, V_{ref}, with a/w for the TCP specimen

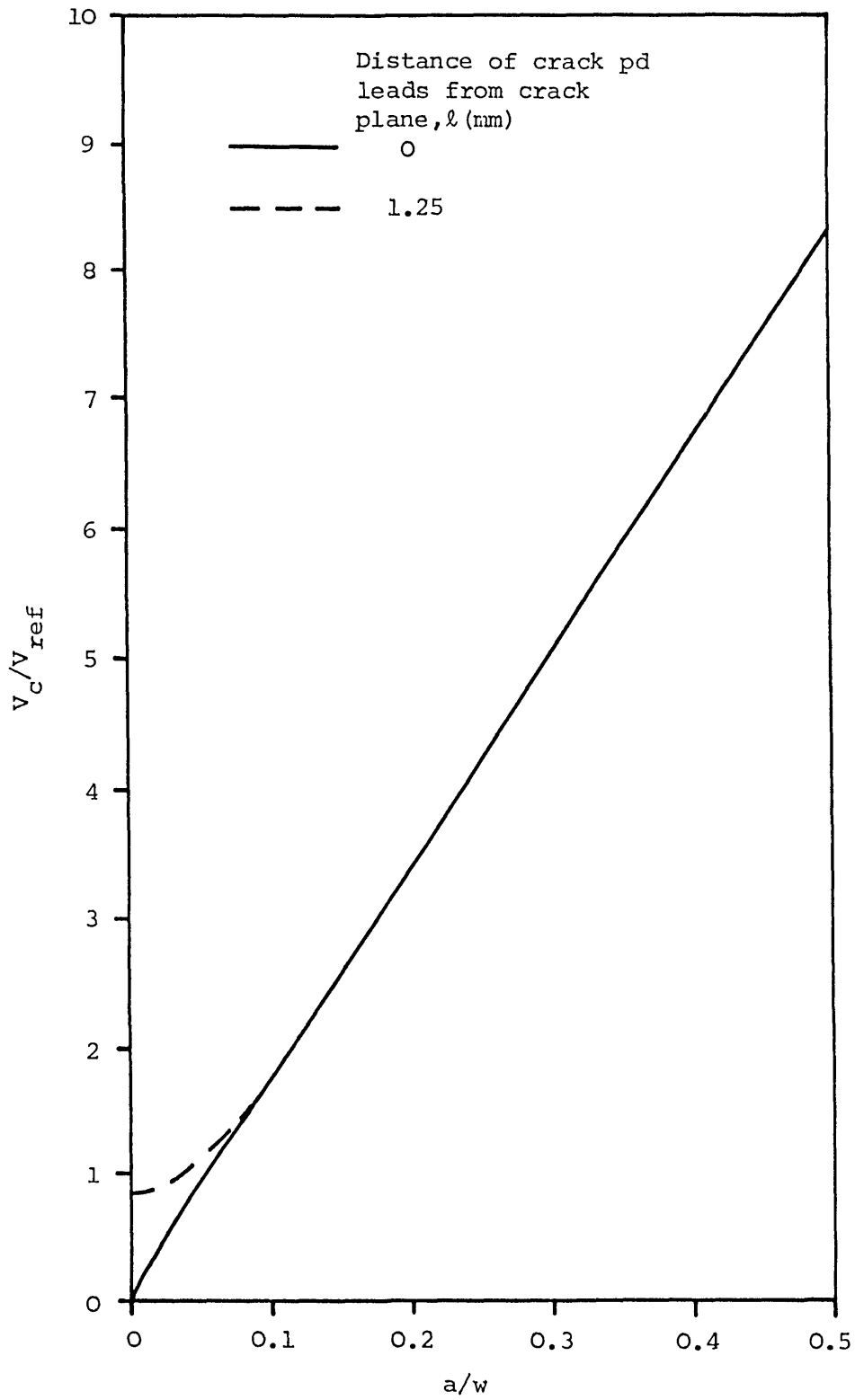


Fig. 8.5 Theoretical pd calibration for TCP specimen

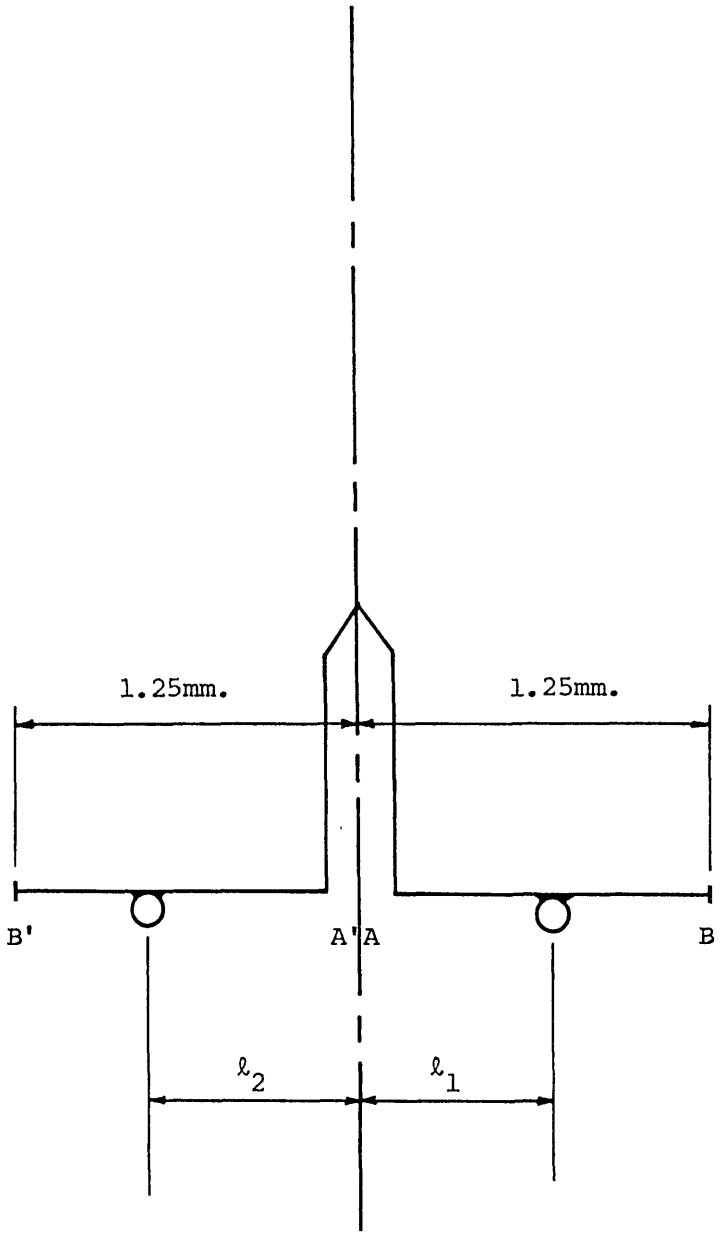


Fig. 8.6 Schematic view of starter notch showing the location of the crack pd monitoring leads

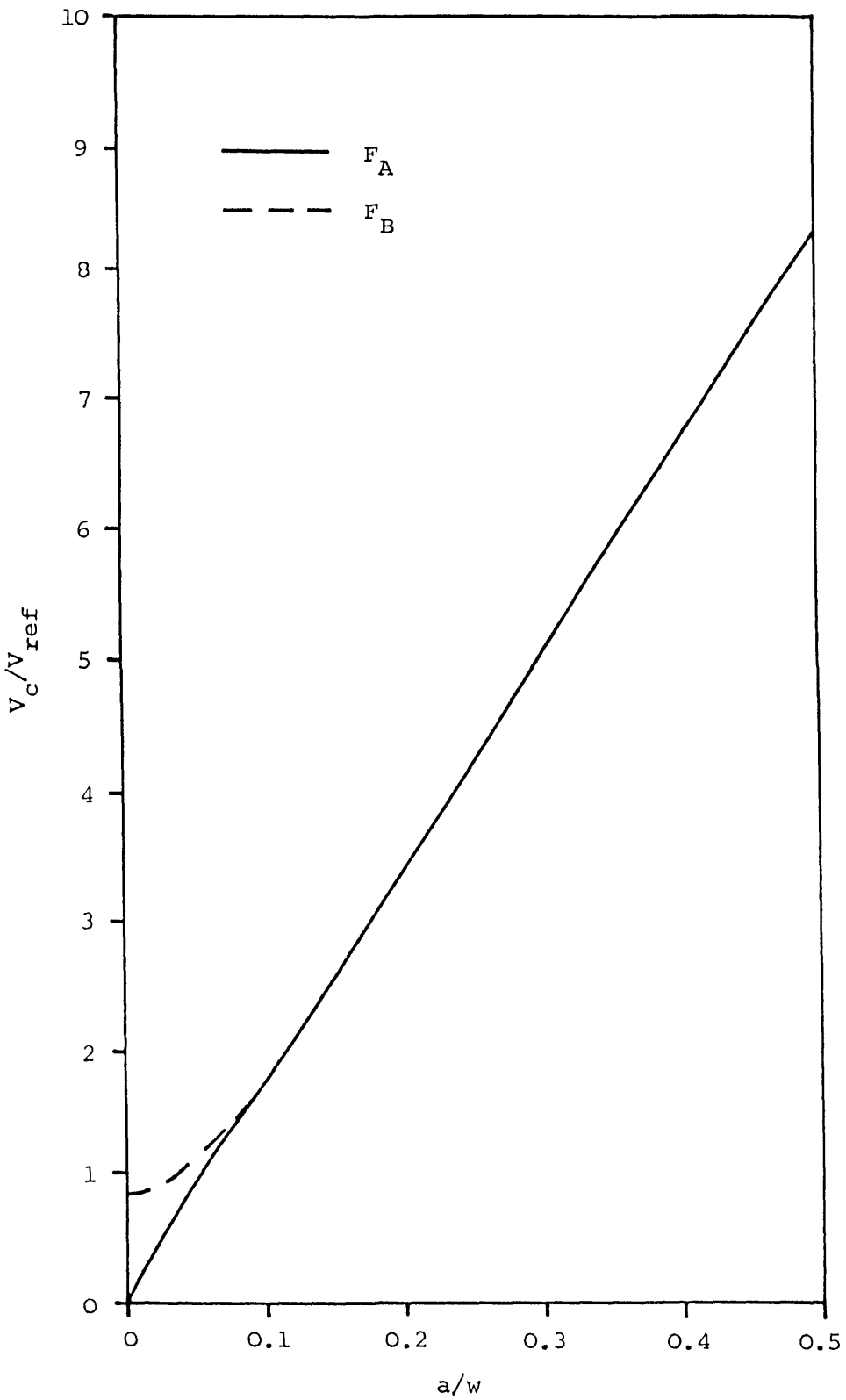


Fig. 8.7 Theoretical pd calibration showing F_A and F_B

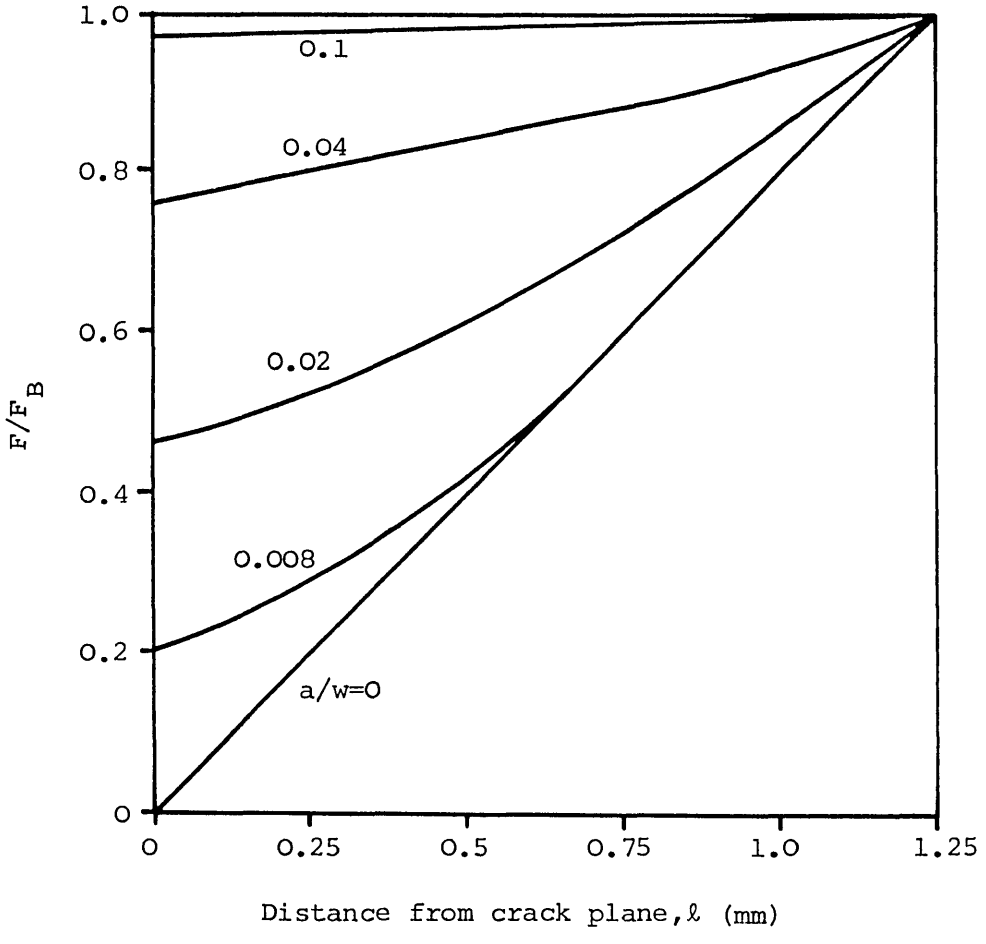


Fig. 8.8 Variation of F/F_B with distance of pd leads from crack plane, ℓ, for a range of values of a/w

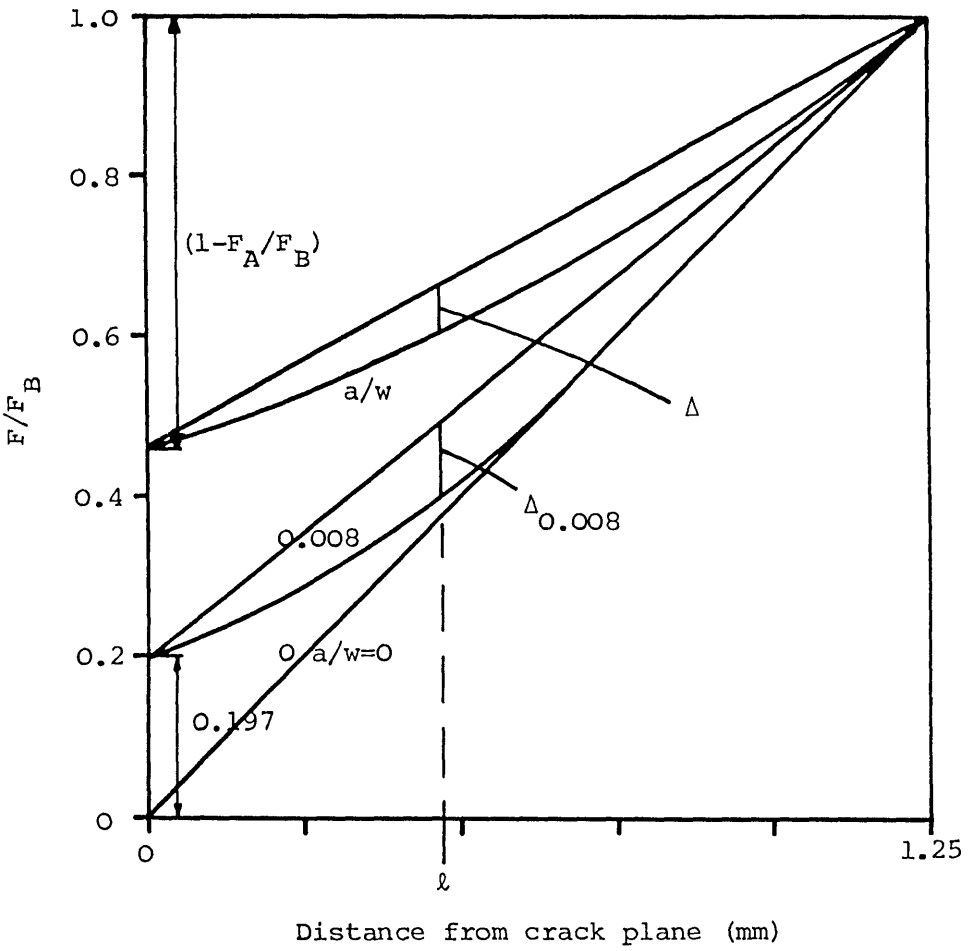


Fig. 8.9 Schematic variation of F/F_B with ℓ for an arbitrary value of a/w

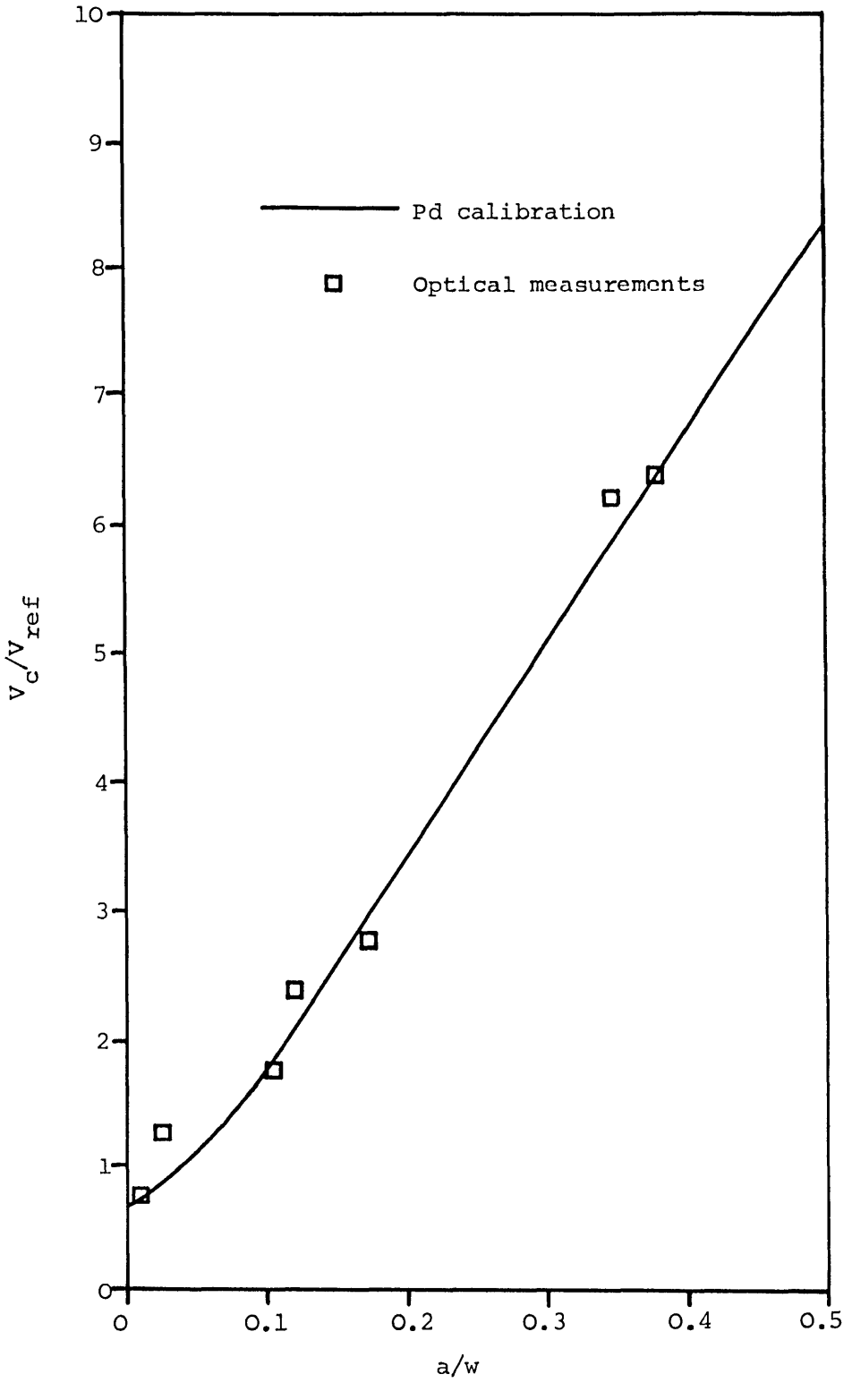


Fig. 8.10 Comparison of crack lengths obtained using the pd method with optical measurements for a fatigue test at room temperature

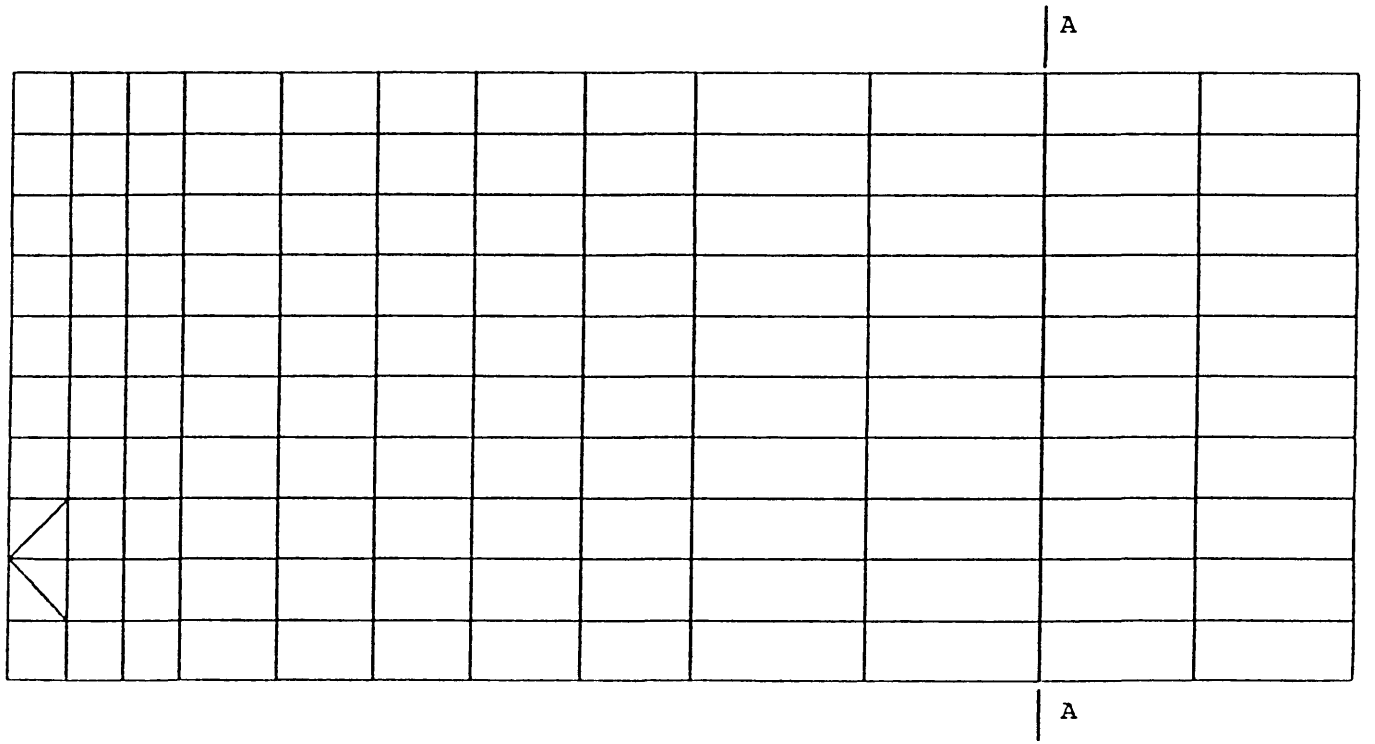


Fig. 8.11 K calibration : mesh 1

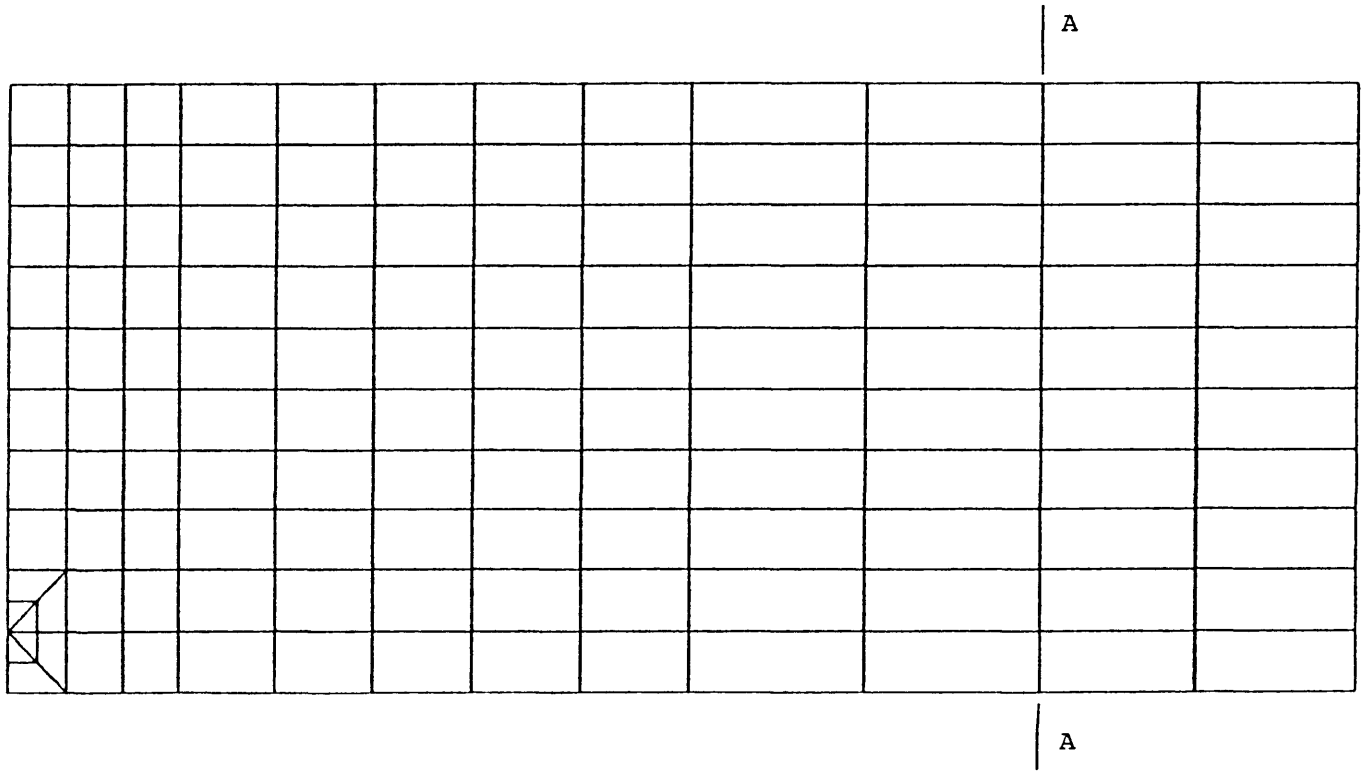


Fig. 8.12 K calibration : mesh 2

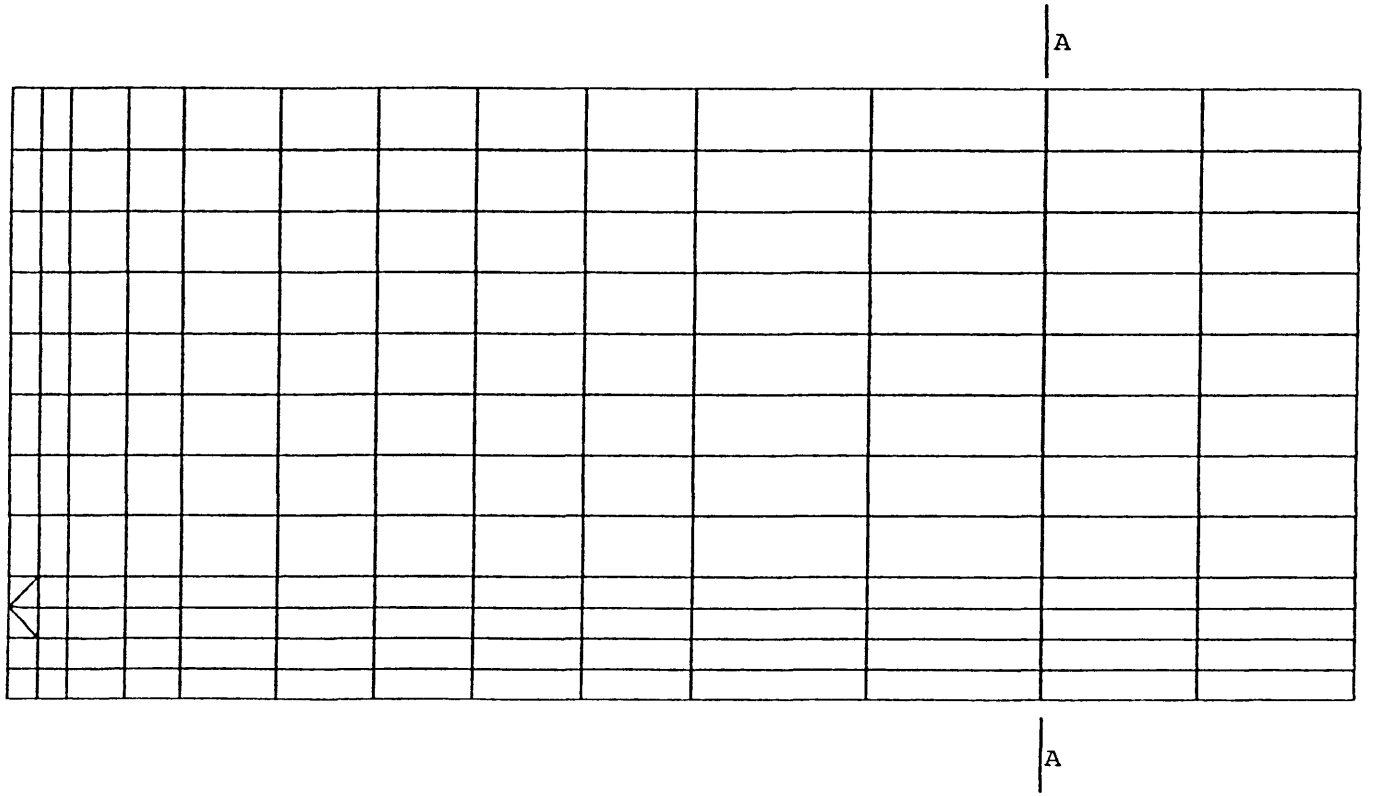


Fig. 8.13 K calibration : mesh 3

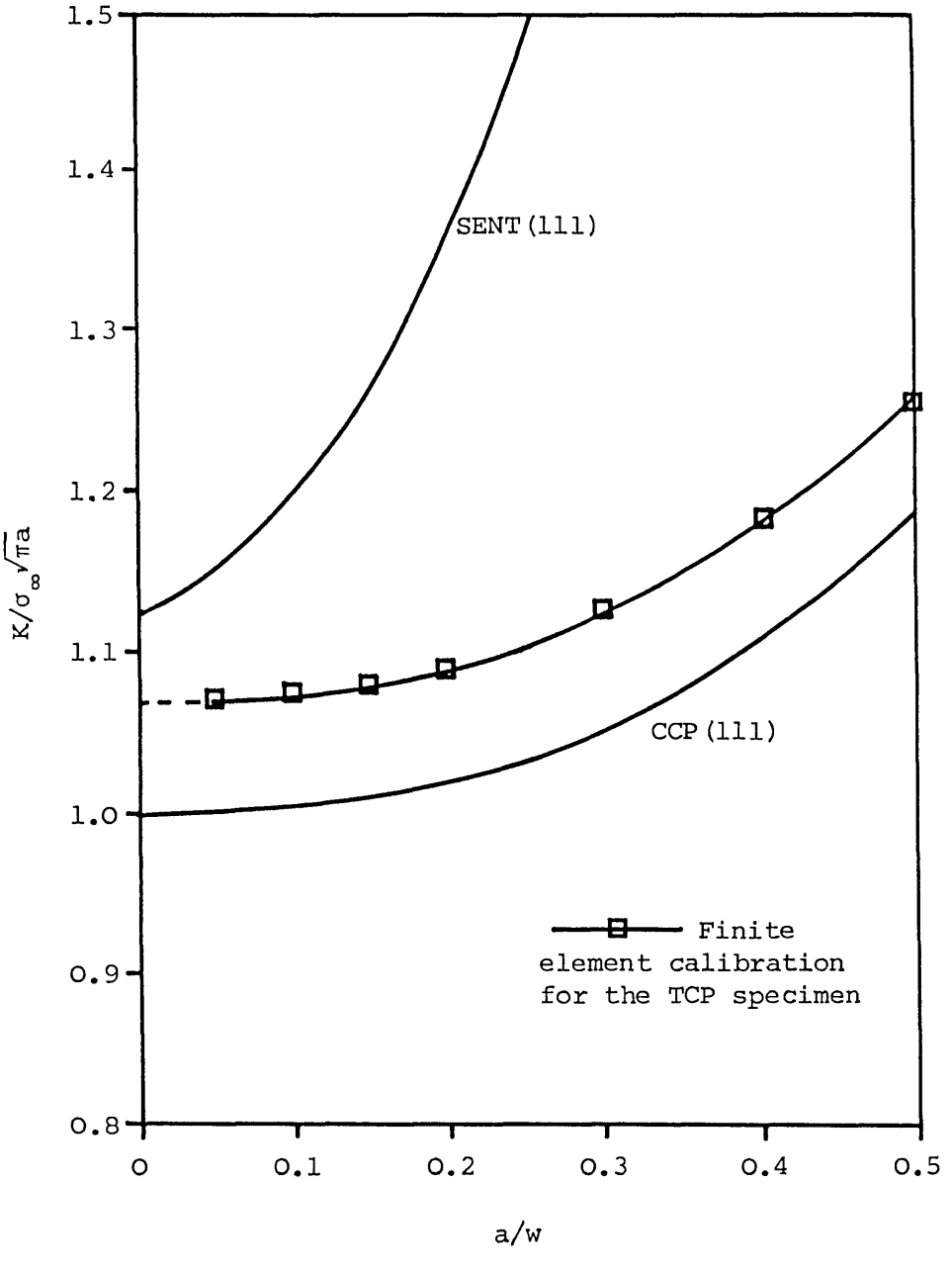


Fig. 8.14 Comparison of the K calibration for the TCP specimen with calibrations for both SENT and CCP geometries

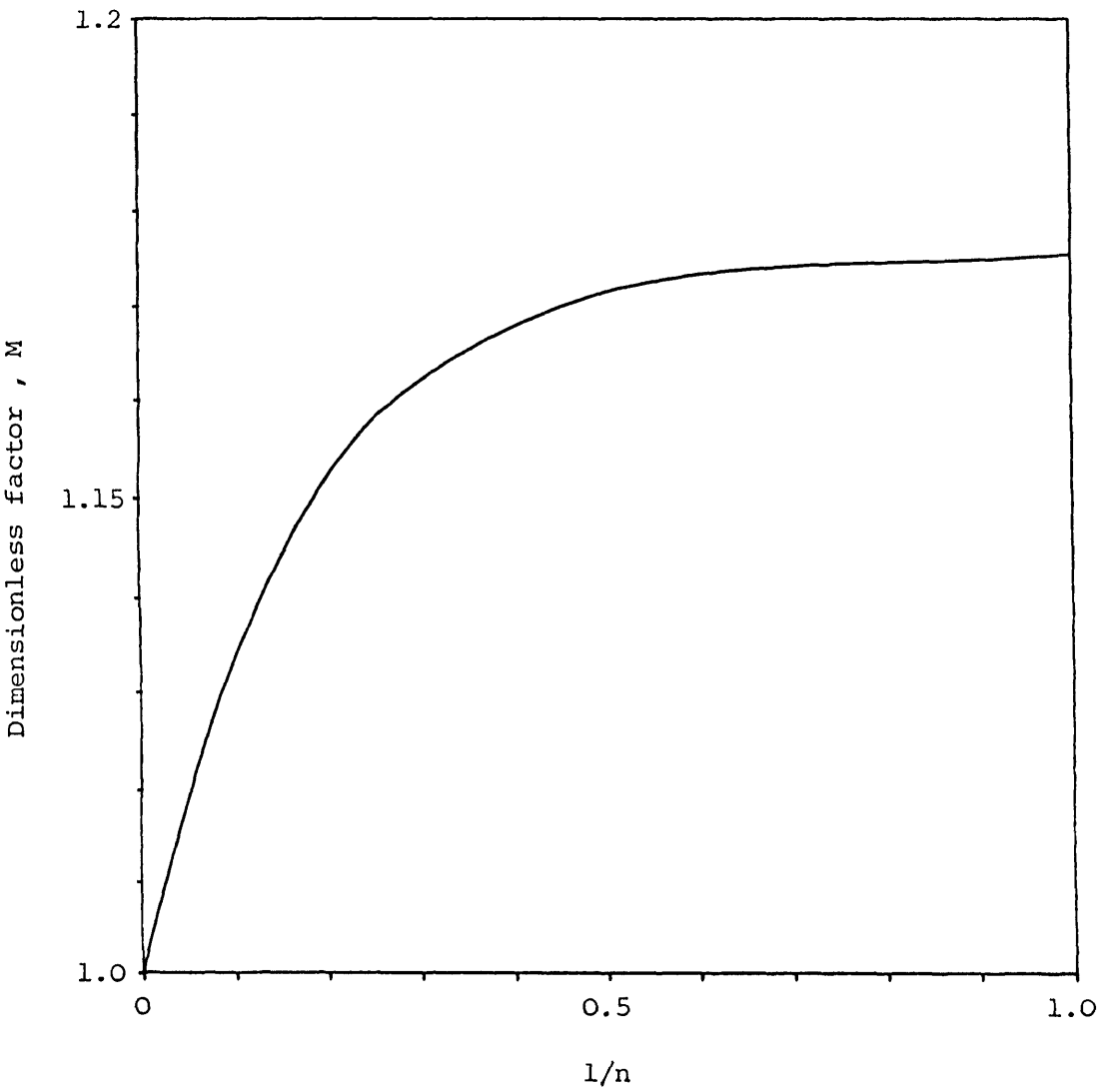


Fig. 8.15 Variation of dimensionless factor M with 1/n

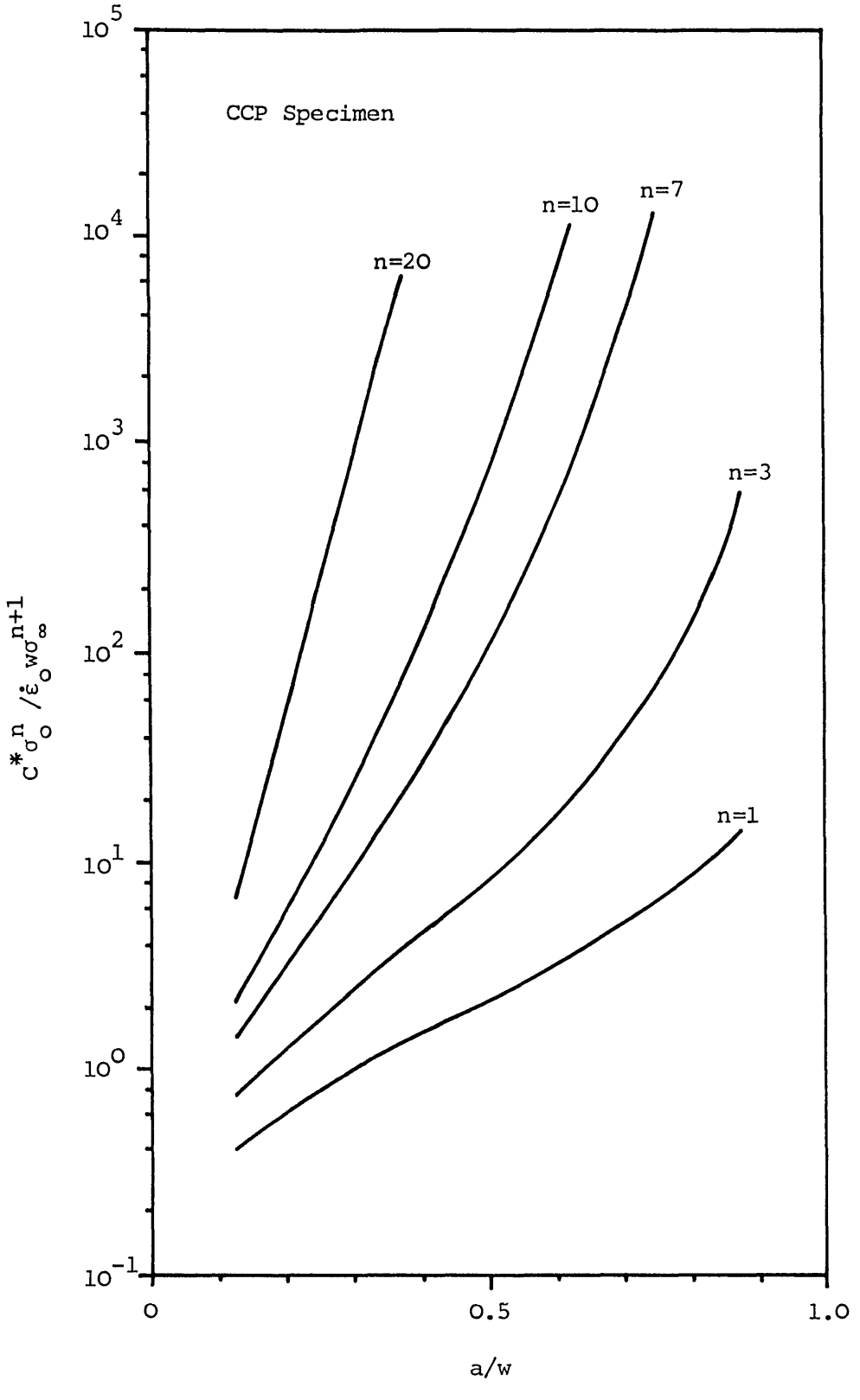


Fig. 8.16 Variation of $\log(C^*_{CCP}\sigma_o^n/\dot{\varepsilon}_o w\sigma_\infty^{n+1})$ with a/w for a range of values of n

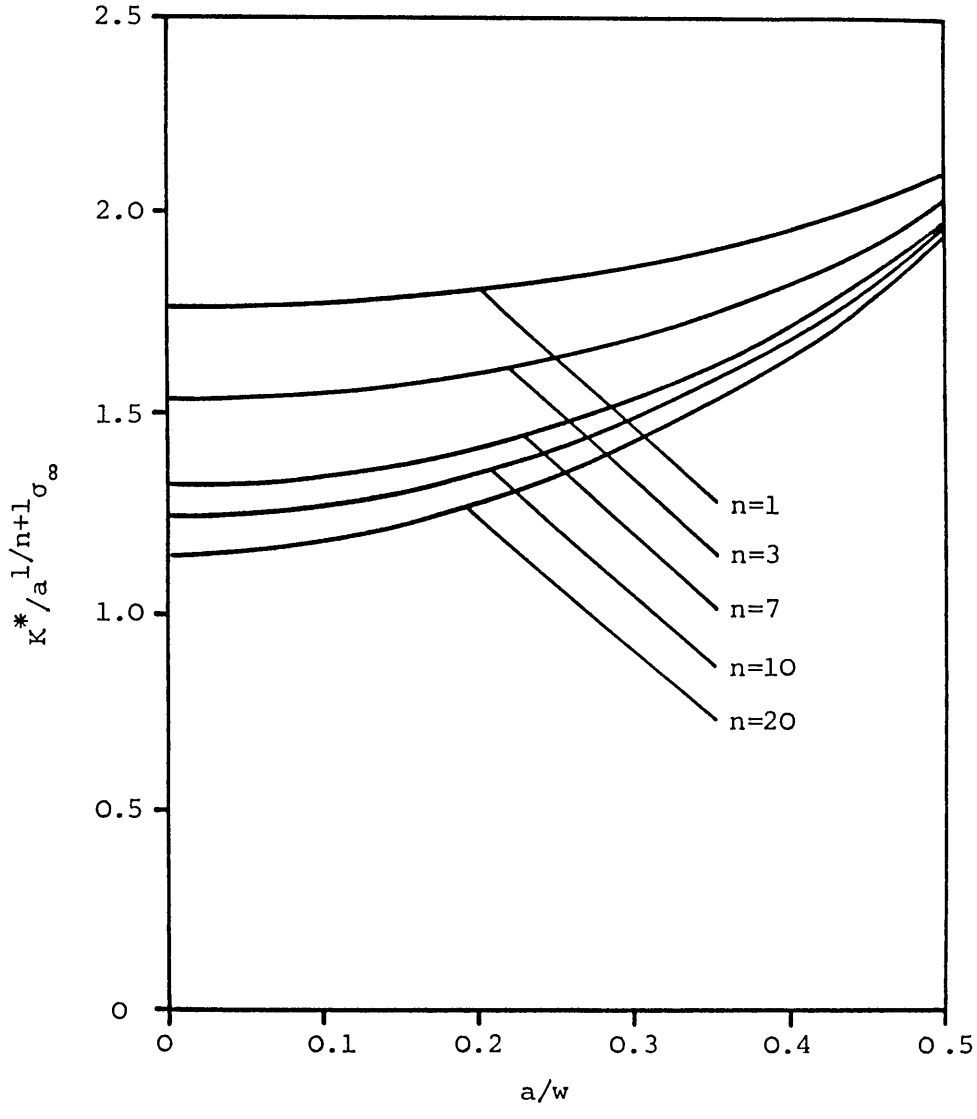


Fig. 8.17 Variation of $(K^*_{CCP}/a^{1/n+1}\sigma_\infty)$ with a/w for a range of values of n

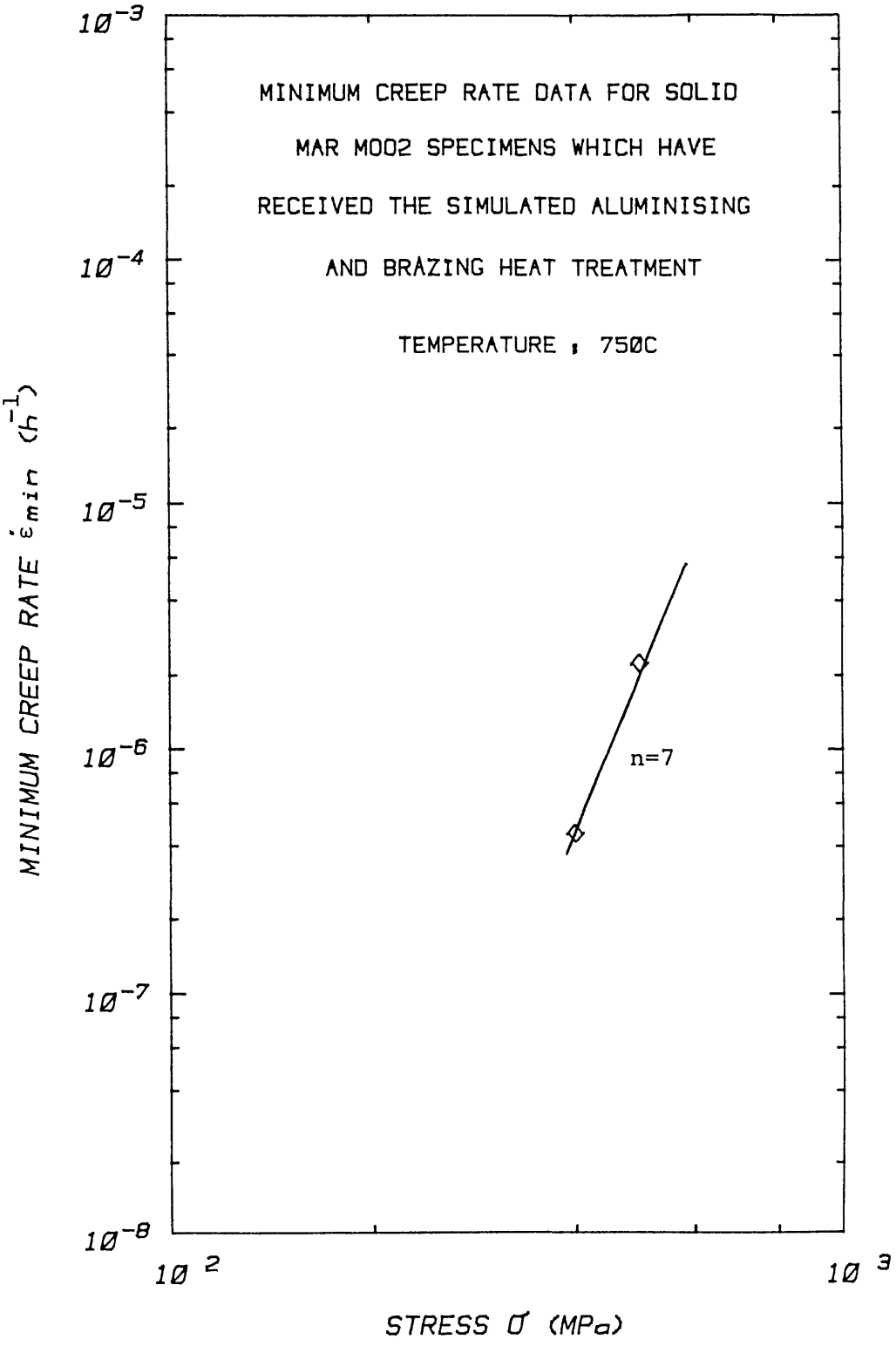


Fig. 8.18 Minimum creep rate data for Mar M002 at 750°C

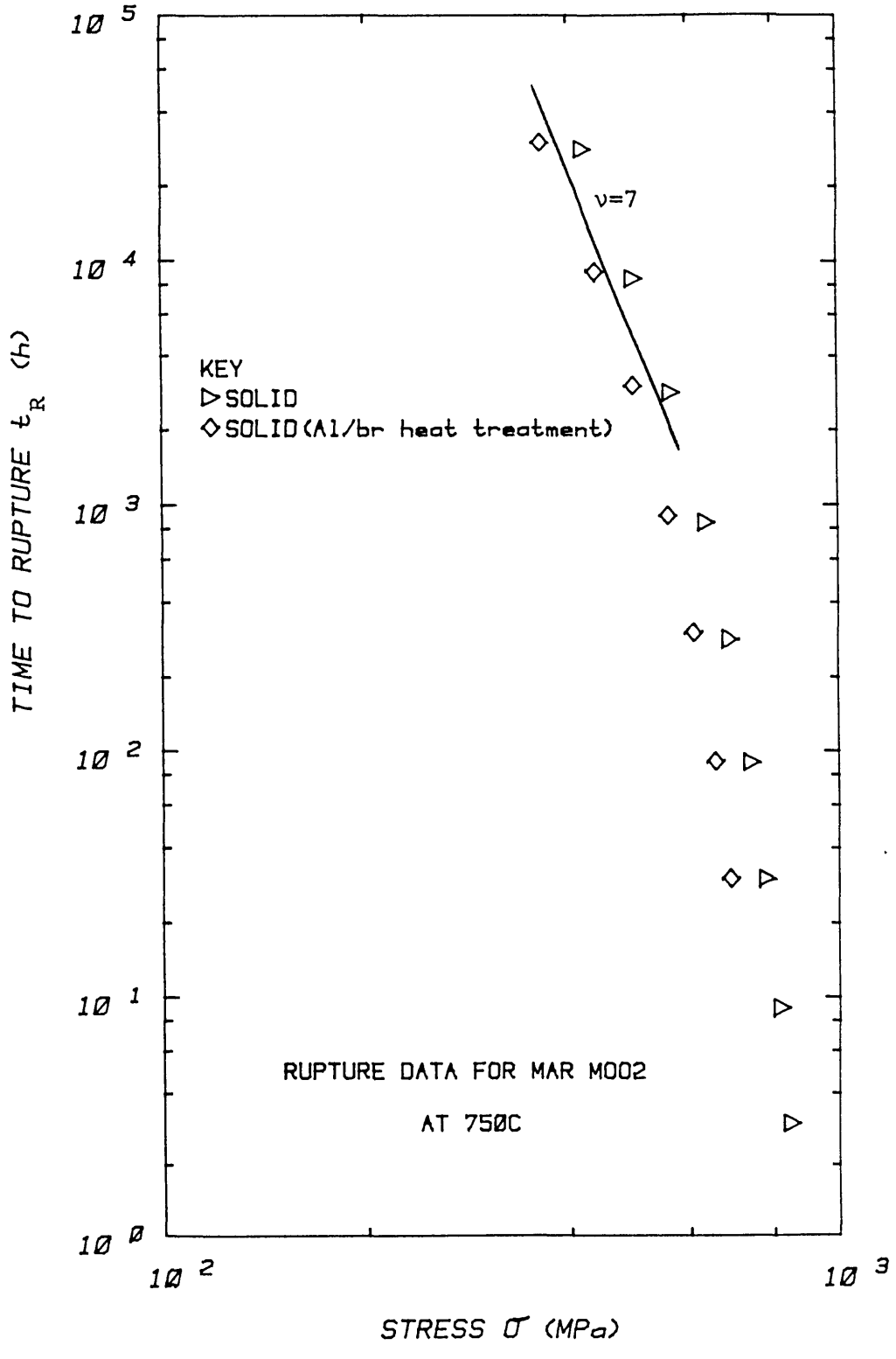


Fig. 8.19 Creep rupture data for Mar M002 at 750°C

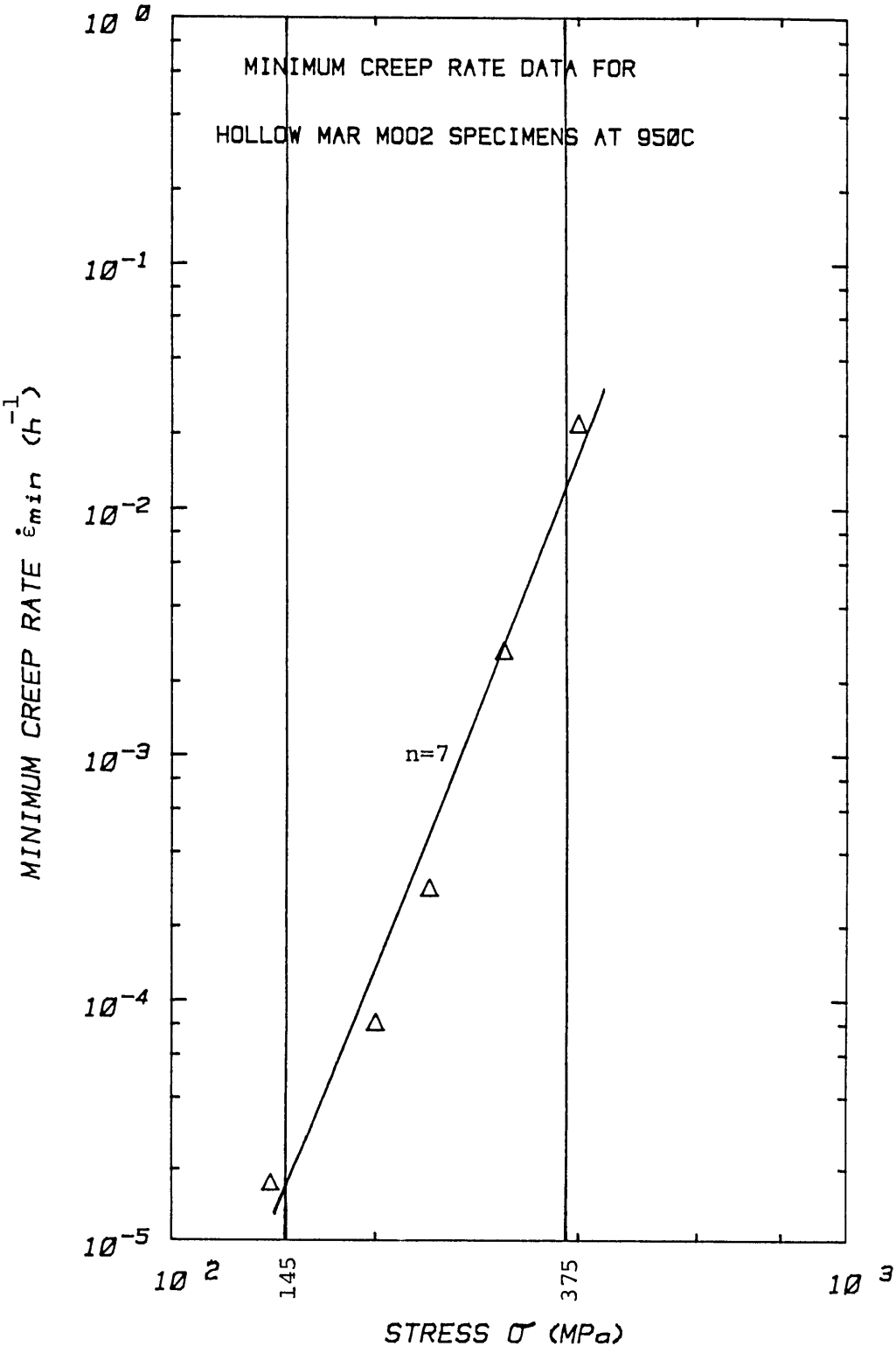


Fig. 8.20 Minimum creep rate data for Mar M002 at 950°C

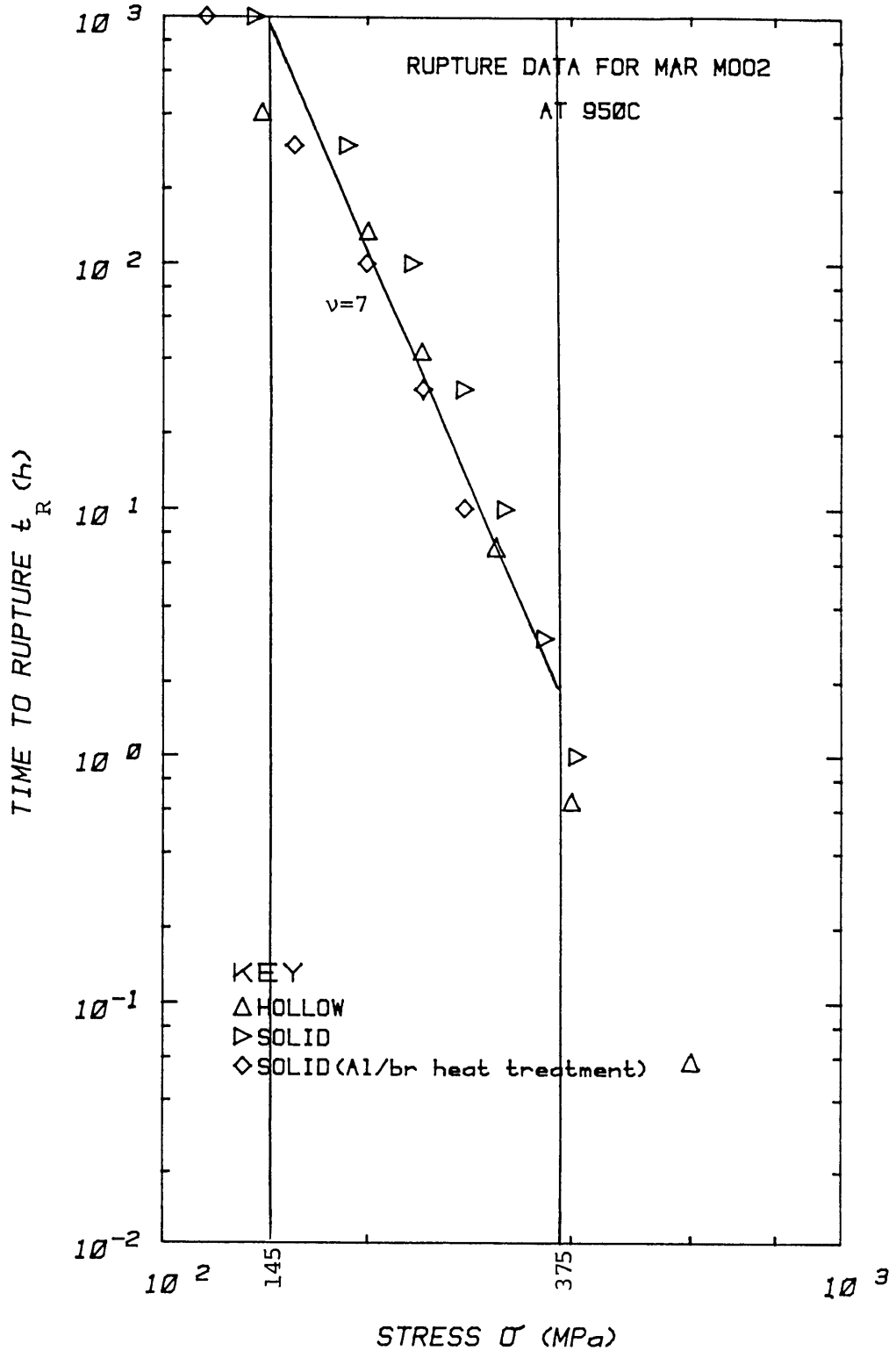


Fig. 8.21 Creep rupture data for Mar M002 at 950°C

CHAPTER 9

EXPERIMENTAL RESULTS

9.1 Introduction

Methods of calculating crack growth rates and relevant fracture mechanics parameters are presented together with results obtained from the experimental programme. Crack growth data are correlated in terms of the fracture mechanics parameters K and C^*, which have been shown to be the most relevant parameters for correlating high temperature crack growth rates in Mar MOO2.

9.2 Calculation of crack growth rates and displacement rates

All experimental crack growth data were acquired under constant temperature conditions. Crack growth under cyclic loading was, in general, measured by conducting tests at a constant maximum load, P_{max}, constant loading ratio, R, and constant loading frequency, f. Crack growth under static loading was measured by conducting tests at constant load, P. A standard y-t chart recorder was used in order to monitor the crack p.d., V_c, the reference p.d., V_{ref}, and the output voltage from the transducer, V_{tr}, throughout each test. Figure 9.1 shows a typical record of V_c, V_{ref} and V_{tr} plotted against time for a crack growth test carried out at a temperature of 950°C. (specimen TCP21).

Values of crack length, a, may be determined from values of the ratio V_c/V_{ref} by following the procedure outlined in Section 8.2.3. Values of displacement, Δ, were determined from values of V_{tr} in conjunction with a calibration curve for the transducer (see Section 7.5.1). Figure 9.2 shows a typical record of crack length and displacement plotted against time for a crack growth test carried out at a temperature of 950°C (specimen TCP21).

Crack growth rates and displacement rates were calculated, for each data point, by the procedure shown in figure 9.3. For any data point, j, quadratic curves were fitted to the crack length versus time and displacement versus time data so that the curves passed through the data points $j - 1$, j and $j + 1$. Thus, for each data point, j, quadratic expressions were obtained to relate crack length, a, and displacement rate, Δ, to the time, t,

$$a_j = f_j(t) \tag{9.1}$$

$$\Delta_j = g_j(t) \tag{9.2}$$

Crack growth rate, da/dt, and displacement rate, $\dot{\Delta}$, may then be determined from the following expressions

$$\left[\frac{da}{dt}\right]_j = \frac{df_j(t_j)}{dt} \tag{9.3}$$

$$(\dot{\Delta})_j = \frac{dg_j(t_j)}{dt} \tag{9.4}$$

Reliable values of da/dt and $\dot{\Delta}$ can be obtained by the above procedure by 'smoothing' the experimental data to eliminate any effects due to noise. Voltages monitored during the current experimental programme (V_c, V_{ref} and V_{tr}) did not generally require 'smoothing' as the effects of noise were usually minimal.

Values of da/dN may be calculated from da/dt values using the following expression

$$\frac{da}{dN} = \frac{1}{f} \frac{da}{dt} \tag{9.5}$$

9.3 Calculation of fracture mechanics parameters K and C*

9.3.1 Calculation of K

The theoretical K calibration for the TCP specimen, used in the present work, was obtained in Section 8.3 and is given graphically in figure 8.14. Values of the stress intensity factor, K, may thus be obtained from a knowledge of the remote applied stress, σ, and the current crack length, a. Figure 9.4 shows, schematically, a typical cyclic loading waveform. Referring to equation 6.8, the stress intensity factor range may be written as

$$\Delta K = K_{max} - K_{min} = K_{max} (1 - R) \qquad (9.6)$$

where K_{max} and K_{min} are the stress intensity factors calculated at P_{max} and P_{min} respectively. For static loading, $R = 1$, and $\Delta K = 0$.

9.3.2 Calculation of C*

Evaluation of the C^* parameter was discussed in detail in Section 6.4.2. C^* values may be obtained from experimental displacement rates, using the following expression

$$C^* = \frac{P\dot{\Delta}}{BW} \cdot F \qquad (9.7)$$

where the value of F may be estimated using limit analysis techniques. Alternatively, numerical methods may be used to calculate theoretical C^* values, as outlined in Section 8.4.

9.3.2.1 Experimental C* values

Figure 9.5 shows, schematically, a cracked TCP specimen subjected to a load P. Assuming that creep dominates over elastic behaviour,

then elastic displacements may be neglected and the total displacement rate of the specimen, $\dot{\Delta}_T$ (measured at the loading points), may be expressed as

$$\dot{\Delta}_T = \dot{\Delta}_o + \dot{\Delta}_c \tag{9.8}$$

where $\dot{\Delta}_o$ is the displacement rate which would be observed in an uncracked TCP specimen subjected to the same loading and $\dot{\Delta}_c$ is the displacement rate due to the crack alone.

Smith and Webster (114) showed that C^* could be expressed in terms of either $\dot{\Delta}_T$, $\dot{\Delta}_c$ or $\dot{\Delta}_o$ provided appropriate dimensionless factors are used, so that

$$C^* = \frac{P\dot{\Delta}_T}{BW} \cdot F_T = \frac{P\dot{\Delta}_c}{BW} \cdot F_c = \frac{P\dot{\Delta}_o}{BW} \cdot F_o \tag{9.9}$$

Values of F obtained from limit analysis (Appendix 6) should strictly be referred to as F_c and only used in conjunction with $\dot{\Delta}_c$ values. However, $\dot{\Delta}_o$ values are only significant in situations in which the crack length is small, and in most other cases $\dot{\Delta}_o << \dot{\Delta}_c$, so that F_c values may be used in conjunction with total displacement rates. The following convention has been adopted throughout the present work,

$$C^*_{exp} = \frac{P\dot{\Delta}_T}{BW} \cdot F_c \tag{9.10}$$

$$C^*_{mod} = \frac{P\dot{\Delta}_c}{BW} \cdot F_c = \frac{P(\dot{\Delta}_T - \dot{\Delta}_o)}{BW} \cdot F_c \tag{9.11}$$

For an uncracked TCP specimen subjected to a constant load, P,

$$\dot{\Delta}_o = \ell_e \frac{\dot{\varepsilon}_o}{\sigma_o^n} \left[\frac{P}{BW}\right]^n \tag{9.12}$$

where ℓ_e is the length of an equivalent specimen of width w and uniform thickness, B = 1.5mm, which would give the same displacement rate when subjected to the same loading. Figure 9.6 shows a plot of ℓ_e versus n. For $n \to \infty$, the value of ℓ_e reduces to the gauge length, 10mm, and for $n = 7$, ℓ_e = 16.9mm.

The above procedure outlines the method used to evaluate C^* values for static loading. Under cyclic loading conditions (figure 9.4), where

$$P = P(t) \tag{9.13}$$

an equivalent steady load, P_{eq}, may be defined such that

$$P_{eq} = \left[f \int_0^{1/f} P^n(t)\, dt \right]^{1/n} \tag{9.14}$$

P_{eq} is, therefore, the steady load which would give rise to the same displacement rate as the cyclic load $P(t)$ if applied for one cycle. Figure 9.7 shows values of P_{eq}/P_{max} plotted against n for a sinusoidal waveform for $R = 0.1$, 0.5, 0.7 and 0.9. Values of P_{eq}/P_{max} depend on n, R and loading waveform but are independent of loading frequency, f. Figure 9.8 shows values of P_{eq}/P_{max} plotted against n for sinusoidal, trapezoidal and triangular waveforms (figure 7.7) for $R = 0.1$.

Experimental C^* values may be calculated, for cyclic loading conditions, from the following expressions

$$C^*_{exp} = \frac{P_{eq}.\dot{\Delta}_T}{BW} \cdot F_c \tag{9.15}$$

$$C^*_{mod} = \frac{P_{eq}(\dot{\Delta}_T - \dot{\Delta}_o) \cdot F_c}{BW} \tag{9.16}$$

where $\dot{\Delta}_o$, for cyclic loading, may be calculated from

$$\dot{\Delta}_o = \ell_e \frac{\dot{\varepsilon}_o}{\sigma_o^n} \left[\frac{P_{eq}}{BW}\right]^n \qquad (9.17)$$

Equations 9.15 - 9.17 may be used for static loading by substituting $P = P_{eq}$.

Values of n and $\dot{\varepsilon}_o/\sigma_o^n$, appropriate to the testing temperatures 750°C and 950°C, are given in Sections 8.4.1 and 8.4.2. Over the range of remote applied stresses used in the present work, $n = 7$ was chosen as the most appropriate value of the creep exponent for both 750°C and 950°C.

9.3.2.2 Theoretical C^* Values.

Theoretical C^* values, known as C^*_{th}, were calculated using the procedure outlined in Section 8.4. Under cyclic loading conditions the remote stress, σ_∞, may be calculated from

$$\sigma_\infty = \frac{P_{eq}}{BW} \qquad (9.18)$$

Theoretical C^* values are highly sensitive to the value of the creep exponent, n.

9.3.2.3 Comparison of C^*_{exp}, C^*_{mod} and C^*_{th}

Figures 9.9 and 9.10 show crack growth rates, da/dt, plotted against C^*_{exp}, C^*_{mod} and C^*_{th} for creep crack growth tests conducted at temperatures of 750°C and 950°C respectively. Correlation of time dependent (creep) crack growth data with C^* generally yields a relation of the form

$$\frac{da}{dt} = HC^{*\phi} \qquad (9.19)$$

where H and ϕ are material constants and ϕ is generally slightly less than unity. Clearly, C^*_{exp} and C^*_{mod} conform to this pattern, while correlation with respect to C^*_{th} yields values of ϕ significantly greater than one. Discrepancies between theoretical and experimental values of C^* are discussed in detail in chapter 10. For the purpose of presenting the results of the experimental programme, crack growth data are generally plotted against the parameter C^*_{mod}, which strictly represents the true experimental value of C^* (see section 6.4.2.2).

9.4 Results of the Experimental Test Programme

An outline of the experimental test programme was given in Section 7.7. All crack growth data were obtained from tests carried out under constant loading and temperature conditions. Experimental crack growth data are presented in one or more of the following forms.

1. Crack length versus time
2. $Log(da/dN)$ versus $\ell og\ \Delta K$
3. $Log(da/dt)$ versus $\ell og\ K_{max}$
4. $Log(da/dt)$ versus $\ell og\ C^*$

The application of fracture mechanics parameters to the correlation of high temperature crack growth data has been studied by a number of authors (see Sections 6.2 and 6.3). In summary, for crack growth occurring in the creep range ($T > 0.5T_M$), the parameters K and C^* appear to offer the most promise for correlating crack growth data. Relationships proposed are generally of the form

$$da/dN = B(\Delta K)^m \tag{9.20}$$

$$da/dt = D\ K_{max}^p \tag{9.21}$$

$$da/dt = HC^{*\phi} \tag{9.22}$$

where B, D, H, m, p and ϕ are constants which may depend on material, testing temperature and loading conditions. The above relationships have been adopted to correlate experimental crack growth data in this thesis, and values of m, p and ϕ are quoted, where appropriate.

Results of the preliminary test programme, outlined in Appendix 7, are presented in section 9.4.1. Sections 9.4.2 and 9.4.3 present results

obtained from the experimental programme at temperatures of 750°C and 950°C.

9.4.1 Preliminary Crack Growth Tests

Prior to manufacture of the extensometry equipment, a series of preliminary crack growth tests were carried out under trapezoidal loading (figure 7.7) at a frequency of *0.25Hz* and R ratio of *0.1*. No displacement measurements were possible and all crack growth rates are presented as a function of ΔK.

Crack growth from initiated fatigue cracks was compared with crack growth directly from the machined starter notch at a temperature of 950°C. Figure 9.11 shows that crack growth rates, obtained from the two situations, showed good agreement when plotted as a function of ΔK, demonstrating that the machined notch may be considered to be equivalent to a crack of the same length (0.23mm). Crack growth rates were correlated by equation 9.20 with $m = 4$. The effect of temperature on crack growth rate is shown in figure 9.12. For a given value of ΔK, the crack growth rate increases with increasing temperature although $m = 4$ for all three temperatures.

9.4.2 Crack growth at 750°C.

9.4.2.1 Crack Growth in the Threshold Region

Crack growth in the threshold region was measured at R ratios of *0.7* and *0.9* for sinusoidal loading at a frequency of *20Hz*. Data were obtained under increasing K conditions. Crack growth rates are shown as a function of ΔK in figure 9.13. Data for both R ratios may be correlated by equation 9.20 with $m = 7$ (where *7* is the value of the creep exponent at this temperature), although the value of ΔK required

to give a particular crack growth rate at $R = 0.9$ is approximately one third of the value required at $R = 0.7$. This suggests that crack growth rates for the two R ratios may correlate better in terms of K_{max}. Figure 9.14 shows crack growth rates for $R = 0.7$ and 0.9 compared with growth rates obtained under static loading on a K_{max} basis. Although there is considerable scatter in the data, crack growth rates for $R = 0.7$ and 0.9 may each be correlated by equation 9.21 with $p = 7$. For a given value of K_{max}, crack growth rates for $R = 0.7$ are approximately four times greater than those for $R = 0.9$. Clearly, the stress intensities required to propagate a crack under static loading ($R = 1$) are considerably higher than those required under cylic loading with $R = 0.7$ or 0.9 and the exponent p for static loading is of the order of 45 (compared with a value of 7 for $R = 0.7$ and 0.9). While significant displacements were measured for $R = 1$, crack growth at $R = 0.7$ and 0.9 was accompanied by relatively little deformation. Displacement rates for $R = 0.7$ and 0.9 were too low to allow reliable values of C^* to be evaluated. Crack growth rates for static loading are shown as a function of C^*_{mod} in figure 9.15 and may be correlated by equation 9.22 with $\phi = 1.0$.

Fracture surfaces of specimens, tested at $R = 0.9$ and $R = 1$, were examined in a scanning electron microscope (SEM). Although the fracture surfaces of both specimens were heavily oxidised, figures 9.16 and 9.17 show that, despite significant differences in observed crack growth behaviour, close similarities were evident in the cracking modes observed for the two R ratios. In both cases, crack growth occurred in a predominantly intergranular manner.

9.4.2.2 Effect of R Ratio

Increases in crack growth rate, da/dN, (for a given value of ΔK)

have been observed with increases in R ratio (11,45). Crack growth rates were measured for sinusoidal loading at a frequency of $20Hz$ for $R = 0.5$, 0.7 and 0.9 and are shown as a function of ΔK in figure 9.18. Crack growth rates for both $R = 0.5$ and $R = 0.7$ may be correlated by equation 9.20 with $m = 4$, while for $R = 0.9$ the value $m = 7$ best describes the crack growth data (above $da/dN = 5 \times 10^{-6}$ mm/cycle) for both $P_{max} = 17kN$ and $P_{max} = 25kN$. Correlation of crack growth rate data for $R = 0.5$ and 0.7 suggests that crack growth at these R ratios is occurring primarily as a result of cycle dependent processes. Time dependent creep and/or environmental effects may become significant at $R = 0.9$. Results presented here agree qualitatively with a previous study on Inconel 718 at 650°C(45) in which increases in crack growth rate with increasing R ratio were found to be more marked at higher values of R. For completeness, crack growth rates are shown as a function of K_{max} in figure 9.19, although this only served to separate data obtained for $R = 0.5$ and $R = 0.7$. Values of the exponent p in equation 9.21 were found to be 4 for $R = 0.5$ and $R = 0.7$ and 7 for $R = 0.9$.

Crack growth data, obtained for $R = 0.5$, 0.7 and 0.9, are shown as a function of C^*_{mod} in figure 9.20. Crack growth data, obtained under static loading, are shown as a solid line for comparison. Although scatter in the data is significant, the trend which is apparent is that the correlation between static and cyclic crack growth data, plotted on a C^* basis, improves with both increasing R ratio and increasing crack growth rate (da/dt).

9.4.2.3 Changing the R ratio during a test

Two tests were carried out in order to illustrate the effect of

R ratio on the cracking rate at 750°C. Both tests were carried out under conditions of constant maximum load, P_{max}, constant cyclic frequency (20Hz) and wave shape (sinusoidal).

The first test, using specimen TCP 30, involved changing the R ratio in the sequence 0.5, 0.7, 0.9, 1. A record of crack length plotted against time for this test is shown in figure. 9.21. Clearly, significant changes in the slope of the curve (da/dt) accompany the transitions from $R = 0.7$ to $R = 0.9$ and $R = 0.9$ to $R = 1$. Figure 9.22 shows that substantial reductions in cracking rate are evident as R changes from 0.7 to 0.9 and again from 0.9 to 1. The solid lines in figure 9.22 represent da/dt versus K_{max} characteristics obtained from previous tests at $R = 0.7$, 0.9 and 1. Agreement between previous data and those obtained from TCP 30 indicates that the effect of prior loading history had no significant effect on the crack growth rates for $R = 0.7$, 0.9 and 1. Crack growth rates are shown as a function of C^*_{mod} in figure 9.23. As in figure 9.20, correlation between static and cyclic crack growth rates, plotted on a C^* basis, improves with both increasing R ratio and increasing crack growth rate.

The fracture surface of specimen TCP 30 was examined in an SEM. Once again the surface was heavily oxidised. The cracking mode changed from transgranular fatigue at $R = 0.5$ (figure 9.24) to predominantly intergranular creep at $R = 1$ (see figure 9.17 for creep cracking). The transition from fatigue cracking at $R = 0.7$ through $R = 0.9$ to creep cracking at $R = 1$ is shown in figure 9.25.

The second test, using specimen TCP 36, involved attempting to change the R ratio in the sequence 0.9, 1, 0.9. However, the specimen subsequently failed during static loading. A record of crack length plotted

against time for this test is shown in figure 9.26. The change of slope (da/dt), accompanying the transition from $R = 0.9$ to $R = 1$ is not nearly so marked as the transition for specimen TCP 30. The reduction in cracking rate during the transition from $R = 0.9$ to $R = 1$ (figure 9.27) was of the order of a factor of 1.5 (compared with approximately 75 for TCP 30). Discrepancies of this type occur as a result of the very high gradient (of the order of 45) of the da/dt versus K relation for static loading. The solid lines in figure 9.27 represent da/dt versus K_{max} characteristics obtained from previous tests at $R = 0.9$ and 1 and show good agreement with data obtained from specimen TCP 36. Thus, once again, the prior loading history had no significant effect on crack growth rates for $R = 1$. Crack growth data for $R = 0.9$ and 1 show good agreement with previous creep crack growth data, plotted on a C^* basis, despite significant scatter (figure 9.28).

9.4.2.4 Effect of Frequency

Many authors (11,23,26,29,40-42) have observed an increase in cracking rate with a reduction in cyclic loading frequency for nickel base superalloys tested at elevated temperatures. The effect of cyclic loading frequency on the crack growth rate was studied for sinusoidal loading at R ratios of 0.5 and 0.9.

Crack growth rates are shown as a function of ΔK in figure 9.29 for cyclic loading frequencies of 0.2Hz and 20Hz at an R ratio of 0.5. The data for 0.2Hz may be correlated by equation 9.20 with $m = 13$, while the 20Hz data correlates better with $m = 4$. For a given value of ΔK, crack growths per cycle (da/dN) are lower at 0.2Hz than at 20Hz for ΔK values less than $25 MPa\sqrt{m}$, while for ΔK values in excess of $25 MPa\sqrt{m}$ crack growth

rates for the lower frequency appear to be of the same order as or greater than those expected for the higher frequency (assuming $da/dN \alpha \Delta K^4$ describes the crack growth behaviour at 20Hz) at a given value of ΔK. Displacement rates only permitted C^* values to be determined during the latter part of each test. Crack growth rates are shown as a function of C^*_{mod} in figure 9.30. Crack growth data, obtained under static loading, are shown for comparison. Although data from neither frequency agree with the static data on a C^* basis, it appears that correlation between static and cyclic crack growth data improves with both decreasing frequency and increasing crack growth rate (da/dt).

The effect of frequency on the crack growth rate was also studied for $R = 0.9$. Records of crack length versus time are shown in figure 9.31 for frequencies of 0.02 Hz, 0.2Hz and 20Hz. Failure times for the three frequencies are largely determined by the initial cracking rate. Crack growth rates are shown as a function of ΔK in figure 9.32. Values of the exponent m from equation 9.20 vary from 7 and 8 for 0.2Hz and 0.02Hz, respectively, to a value of 20 for 20Hz. The high value of m for the 20Hz data is possibly due to the fact that crack growth rates at this frequency were obtained in the threshold region. The general trend is for higher values of da/dN at lower frequencies for a given value of ΔK. However, crack growth data for all three frequencies were unified when plotted in terms of da/dt, suggesting that crack growth was time dependent at $R = 0.9$ over the range of frequencies considered. Crack growth rates (da/dt) are shown as a function of K_{max} in figure 9.33 and as a function of C^*_{mod} in figure 9.34. Crack growth data, for all three frequencies, were correlated by equation 9.21 with $p = 13$. (figure 9.33). Crack growth data, plotted as a function of C^*_{mod} in figure 9.34, showed

reasonably good agreement with data obtained under static loading for all three frequencies. At a given crack growth rate, C^* values for $R = 0.9$ were consistently slightly lower than for $R = 1$.

9.4.3 Crack Growth at 950°C

9.4.3.1 Crack Growth in the Threshold Region

Crack growth in the threshold region was measured at R ratios of 0.1, 0.7 and 0.9 for sinusoidal loading at a frequency of $20Hz$. Data were obtained under increasing K conditions. Crack growth rates are shown as a function of ΔK in figure 9.35. Data for all three R ratios may be correlated by equation 9.20 with $m = 7$ (where 7 is the value of the creep exponent at this temperature), although the value of ΔK required to give a particular crack growth rate increases with decreasing R ratio. This suggests that crack growth rates for the three R ratios correlate better in terms of K_{max}. Figure 9.36 shows crack growth rates for $R = 0.1$, 0.7 and 0.9 compared with growth rates obtained under static loading on a K_{max} basis. Data for all four R ratios may be correlated by equation 9.21 with $p = 7$. Closer examination of the results reveals that, for a given value of K_{max}, crack growth rates under cyclic loading are always greater than those measured for static loading. Crack growth rates are shown as a function of C^*_{exp} in figure 9.37. Good agreement is found for crack growth rates measured at $R = 0.7$, 0.9 and 1, while data obtained for $R = 0.1$ appear not to give meaningful correlation in terms of C^*. A and B denote the 'tails' frequently observed, when crack growth rates are shown as a function of C^*. The particular C^* value at which the 'tail' emerges increases with increasing applied load. Replotting the data for $R = 0.7$, 0.9 and 1 as a function of C^*_{mod} (figure 9.38) virtually eliminates the effect. Crack growth data for $R = 0.7$, 0.9 and 1

may then be correlated by equation 9.22 with $\phi = 1.0$.

Fracture surfaces of specimens, tested at $R = 0.1, 0.9$ were examined in an SEM. Fracture surfaces, once again, were heavily oxidised. The fracture surface for $R = 0.1$ (figure 9.39) revealed a possible initiation site (I) away from the starter notch on the side of the specimen, suggesting that crack growth data obtained at this R ratio may be suspect. Crack growth for $R = 0.1$ occurred in a predominantly transgranular manner. Examination of the fracture surfaces for $R = 0.9$ (figure 9.40) and $R = 1$ (figure 9.41) revealed close similarities in the cracking modes. In both cases crack growth occurred in a predominantly intergranular manner. Optical micrographs for $R = 0.9$ (figure 9.42) and $R = 1$ (figure 9.43) show that crack branching and microcracking are prevalent under these conditions. In both cases, microcracks were observed throughout the uncracked portions of the failed specimens, indicating that considerable damage accumulation accompanies crack growth (and that damage accumulation is not only confined to a small zone near the crack tip).

9.4.3.2 Effect of R Ratio

Crack growth rates were measured for sinusoidal loading at a frequency of 20Hz for $R = 0.1, 0.5, 0.7$ and 0.9 and are shown as a function of ΔK in figure 9.44. Crack growth rates for all four R ratios may be correlated by equation 9.20 with $m = 7$, although the value of ΔK, required to give a particular crack growth rate, increases with decreasing R ratio. Results agree qualitatively with those obtained for a temperature of 750°C, in that the effect of changing the R ratio is more marked at higher values of R. Crack growth rates are shown as a function of K_{max} in figure 9.45. Values of the exponent p in equation 9.21 were

found to be 7 for all four R ratios. At a given value of K_{max}, crack growth rates for $R = 0.7$ and $R = 0.9$ were identical, but decreasing the R ratio below 0.7 yielded substantial increases in da/dt. Crack growth data for $R = 0.5$, 0.7 and 0.9 are shown as a function of C^*_{mod} in figure 9.46 (no displacement measurements were available for $R = 0.1$) Crack growth data, obtained under static loading are shown as a solid line for comparison. Although scatter in the data is significant, the trend which is apparent is that correlation between static and cyclic crack growth data, plotted on a C^* basis, improves with increasing R ratio.

9.4.3.3 Changing the R ratio during a test

A test was carried out in order to illustrate the effect of R ratio on the cracking rate at 950°C. The test was carried out under conditions of constant maximum load, P_{max}, constant cyclic frequency (20Hz) and wave shape (sinusoidal). It involved changing the R ratio in the sequence 0.5, 0.7, 0.9, 1. A record of crack length plotted against time for this test is shown in figure 9.47. A significant change in the slope of the curve (da/dt) is evident at the transition from $R = 0.7$ to $R = 0.9$. Crack growth rates are shown as a function of K_{max} in figure 9.48. The solid line in figure 9.48, representing da/dt versus K_{max} data obtained from previous tests at $R = 0.7$ and 0.9, shows reasonably good agreement with $R = 0.9$ and $R = 1$ data obtained from the present test, indicating that the effect of loading history had no significant effect on the crack growth rates for $R = 0.9$ and $R = 1$. Insufficient data were available for $R = 0.7$ to allow any firm conclusions to be drawn for this R ratio. Crack growth rates are shown as a function of C^*_{mod} in figure 9.49. As in figure 9.46, correlation between

static and cyclic growth rates, plotted on a C^* basis, improves with increasing R ratio. Data for $R = 0.9$ and $R = 1$ show good agreement with previous data obtained under static loading.

The fracture surface of specimen TCP 48 was examined in an SEM. Surfaces were heavily oxidised in all cases. Figure 9.50 - 9.52 show the specimen fracture surfaces corresponding to A , B and C respectively, in figure 9.47. Fracture surfaces for $R = 0.5$ are essentially transgranular (figure 9.50), although at a crack length of about 3.5mm pockets of intergranular fracture begin to appear (figure 9.51). The transition from fatigue cracking at $R = 0.5$ through $R = 0.7$ and $R = 0.9$ to creep cracking at $R = 1$ is shown in figure 9.52.

9.4.3.4 Effect of Frequency

The effect of cyclic loading frequency on the crack growth rate was studied for sinusoidal loading at an R ratio of 0.5. A record of crack length versus time is shown in figure 9.53 for frequencies of $0.02Hz$, $0.2Hz$ and $20Hz$. Crack growths per cycle are shown as a function of ΔK in figure 9.54. Crack growth rates for all three frequencies may be correlated by equation 9.30 with $m = 7$, although, for a given value of ΔK, higher values of da/dN are observed at lower frequencies. However, if the crack growth data are plotted in the form $\ell og(da/dt)$ versus $\ell og\ K_{max}$ (figure 9.55), higher values of da/dt are observed at higher frequencies for a given value of K_{max}. Data for all three frequencies could be correlated by expressions of the form given in equation 9.21 with $p = 7$. Crack growth rates (da/dt) are shown as a function of C^*_{mod} in figure 9.56. Data obtained at the lowest frequency $(0.02Hz)$ showed good agreement with crack growth data obtained under static loading.

The trend which emerges is that correlation between static and cyclic crack growth data plotted on a C^* basis, improves with decreasing cyclic frequency.

9.4.3.5 Effect of Waveform

The effect of the cyclic loading waveform on the crack growth rate was studied for the waveforms shown in figure 9.57 at $R = 0.1$. Records of crack length versus time are shown in figure 9.58 for the four waveforms. Crack growth rates are shown as a function of ΔK in figure 9.59. Scatter in the results make interpretation difficult. However, some clarification is possible by using equation 9.20 to correlate the data for each waveform. Appropriate values of m, shown in figure 9.59, were chosen to fit the data for $da/dN > 10^{-5}$ $mm/cycle$. Below 10^{-5} $mm/cycle$, the proximity to the threshold region may cause values of m to be artificially high. For a given value of ΔK, cyclic crack growth rates (da/dN) were highest for the sinusoidal waveform of frequency $0.2Hz$ and lowest for the triangular waveform of frequency $6.87Hz$ Crack growth rates (da/dt) are shown as a function of C^*_{mod} in figure 9.60 for the $0.2Hz$ loading waveforms. Displacements measured for triangular loading at $6.87Hz$ were not large enough to allow reliable estimates of C^*_{mod} to be obtained. Crack growth data for the three waveforms are compared with data obtained under static loading conditions. Clearly, cyclic processes influence the crack growth rates measured for all three waveforms. Figure 9.59 also shows that crack growth rates are also influenced by time dependent processes (note the frequency effect for the triangular waveform). Thus, waveform effects occur due to a complex combination of cycle dependent and time dependent processes.

9.4.3.6 Effect of Prior Creep Damage

The effect of prior creep damage on the crack growth rate was investigated for the case of sinusoidal loading at a frequency of $20Hz$ and R ratio of 0.9. Creep damage, in the form of creep strain, was introduced into specimens TCP 42 and TCP 45 prior to crack growth testing. Specimens TCP 42 and TCP 45 were pre-strained to levels of 1.564% and 1.905% respectively as shown in figure 9.61. Crack growth rates are shown as a function of ΔK in figure 9.62 for a virgin specimen and pre-damaged specimens subjected to sinusoidal loading at a frequency of $20Hz$ and R ratio of 0.9. Lower stress intensity ranges (ΔK) are required to propagate cracks in damaged material. Correlation of the data using equation 9.20 yielded $m = 7$ for virgin material and $m = 13$ for the creep damaged material. In addition, prior creep strains of 1.564% and 1.905% both give rise to identical cracking rates for a given value of ΔK. Crack growth rates are shown as a function of C^*_{mod} in figure 9.63. For a given value of, da/dt, values of C^*_{mod} are approximately twice as large for the damaged material as for the virgin material.

The fracture surface of the specimen, pre-strained to a level of 1.905%, was examined in an SEM. The fracture surface was heavily oxidised, but figure 9.64 shows that the cracking mode was predominantly intergranular. Comparison with the fracture surface of the virgin specimen (figure 9.40) reveals that the crack propagates by a more brittle mode in the damaged material. Optical micographs of the damaged specimen (figure 9.65) reveal crack branching and substantial microcracking throughout the uncracked portion of the failed specimen. Microcracking was more widespread than in the virgin specimen (which was tested at a higher load).

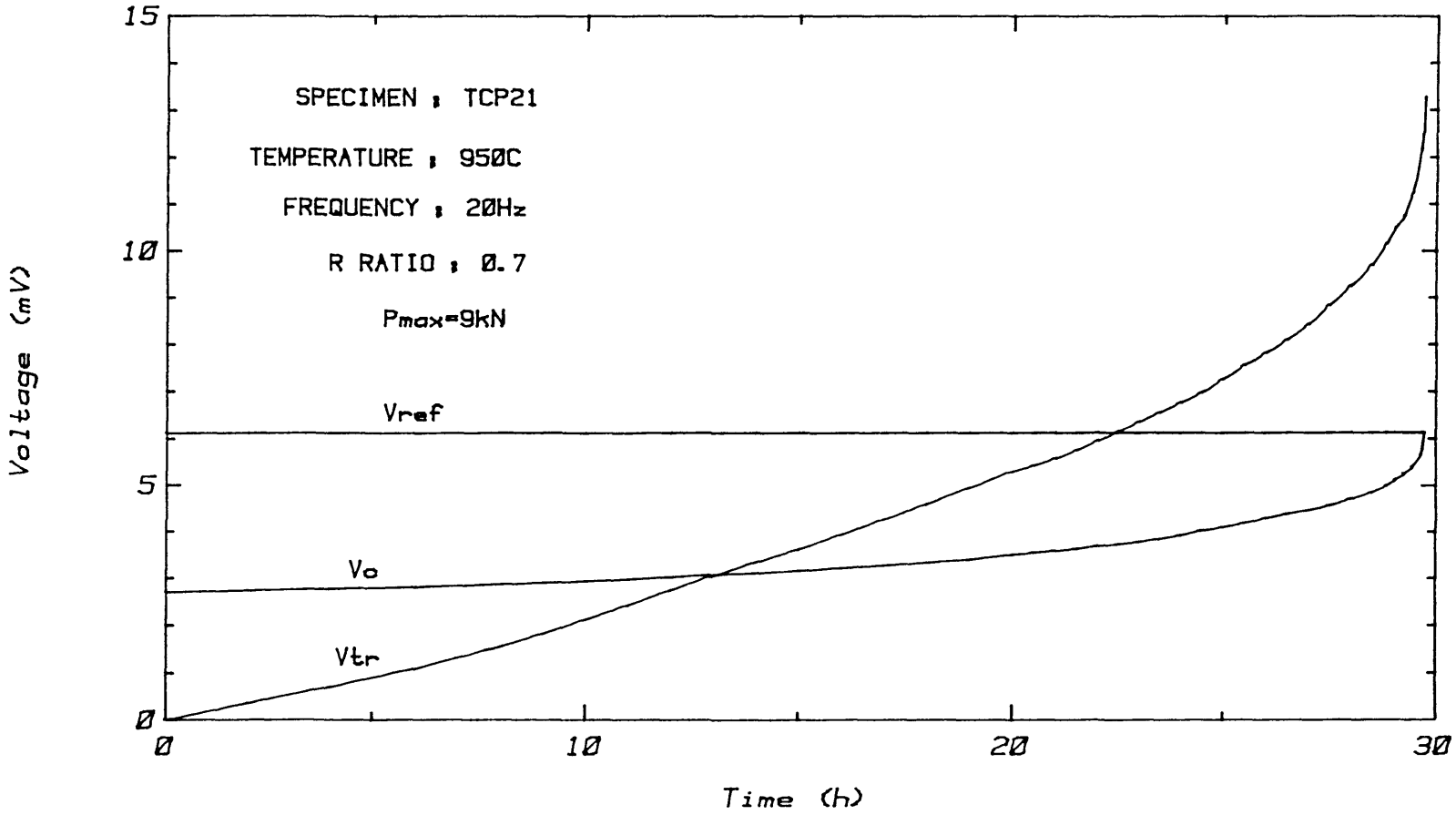


Fig. 9.1 Typical experimental voltage record

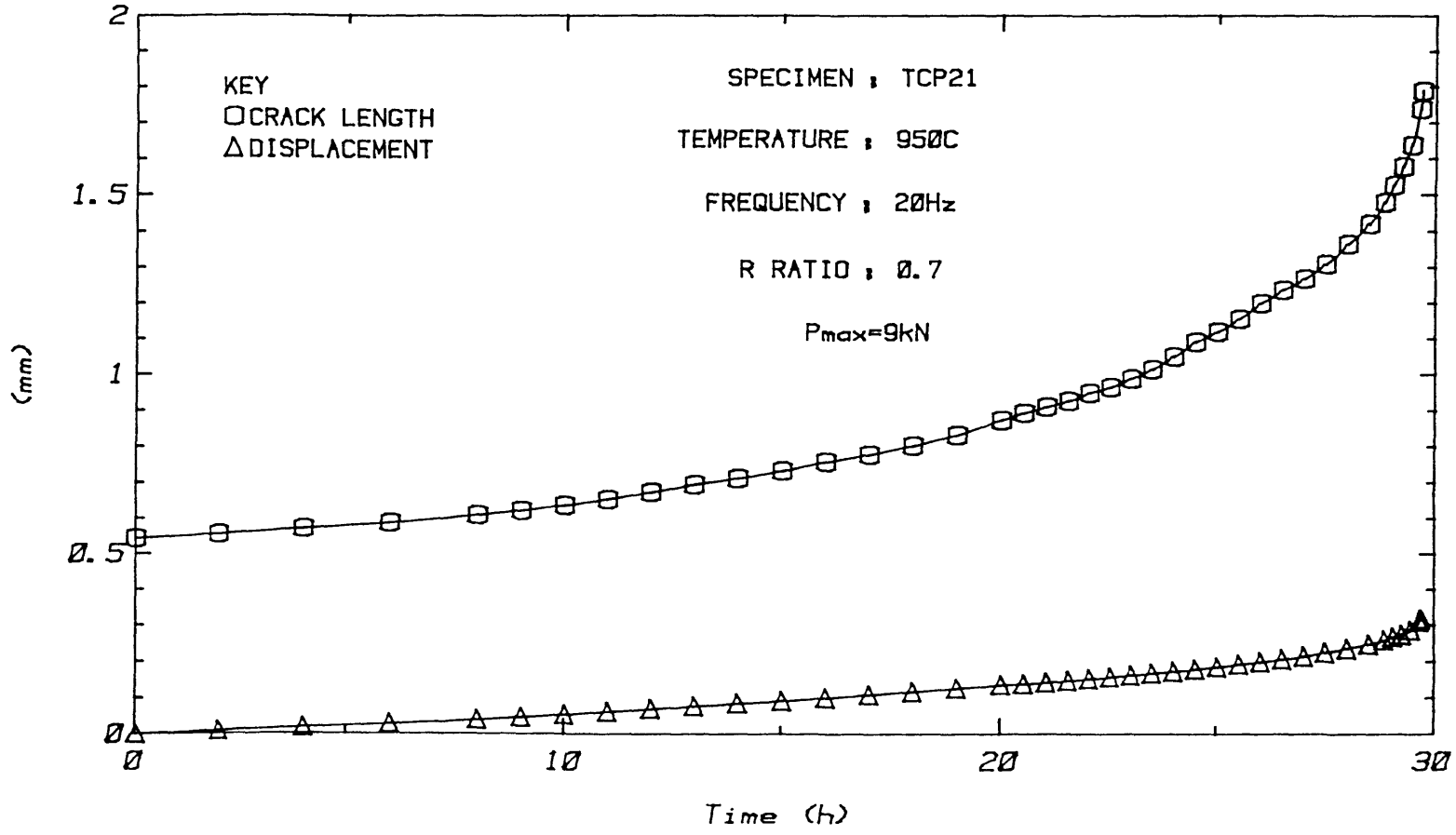


Fig. 3.2 Typical experimental record of crack length and load point displacement

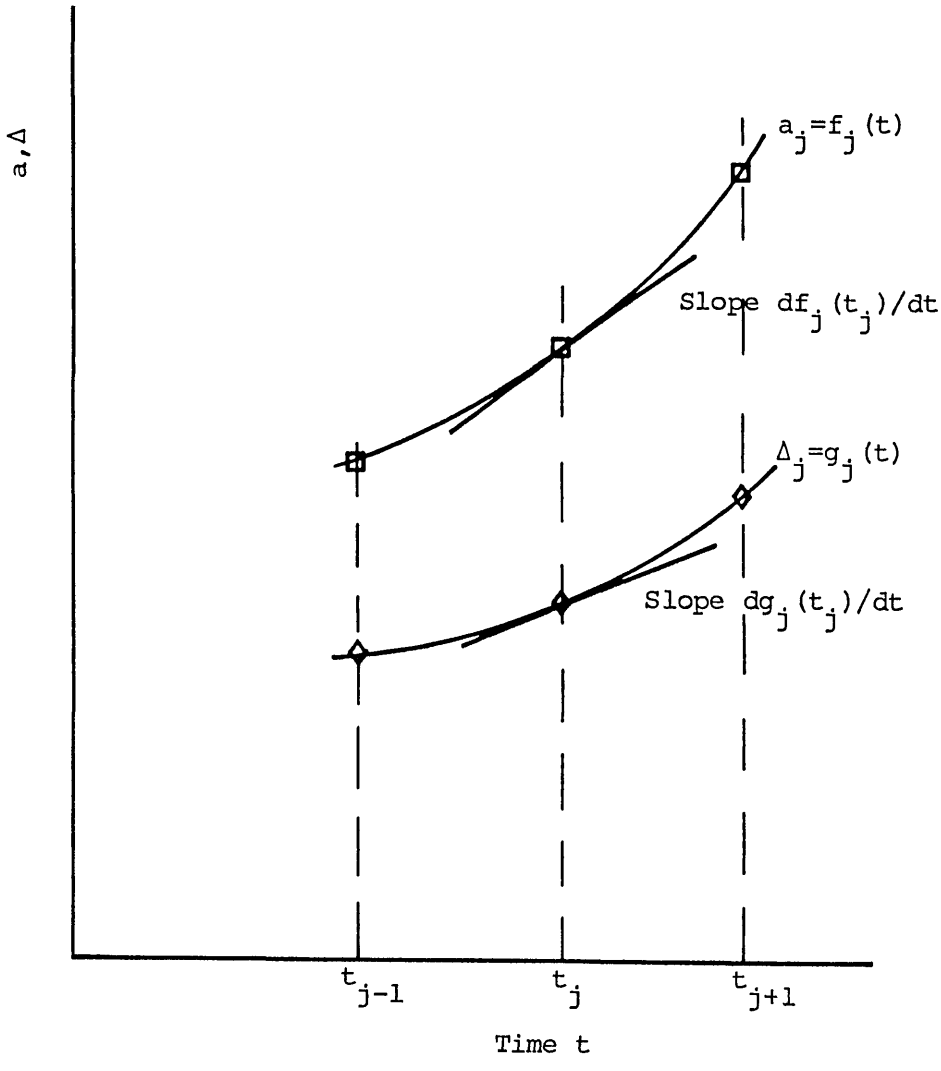


Fig. 9.3 Method of determination of da/dt and $\dot{\Delta}$

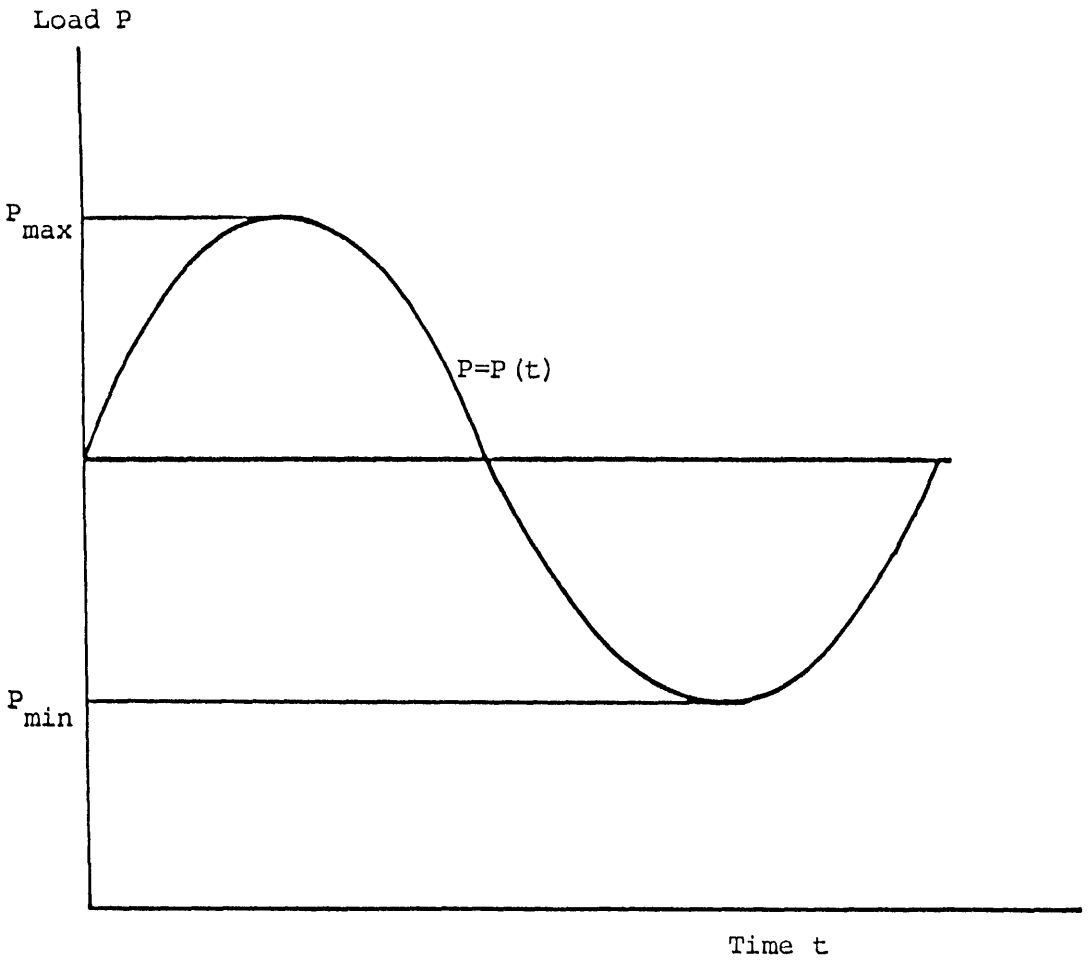


Fig. 9.4 Typical cyclic loading waveform

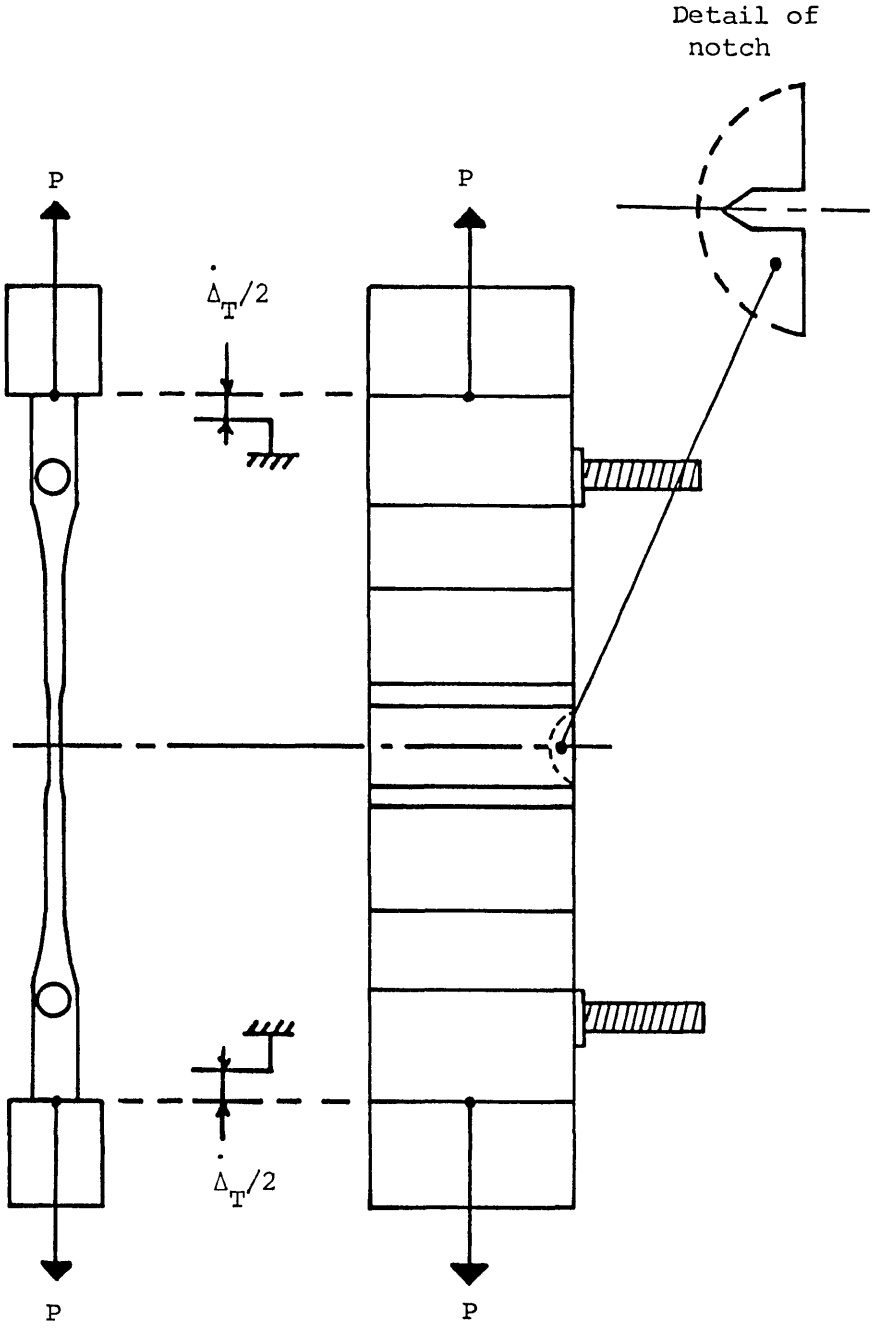


Fig. 9.5 Schematic diagram of a cracked TCP specimen subjected to a load P

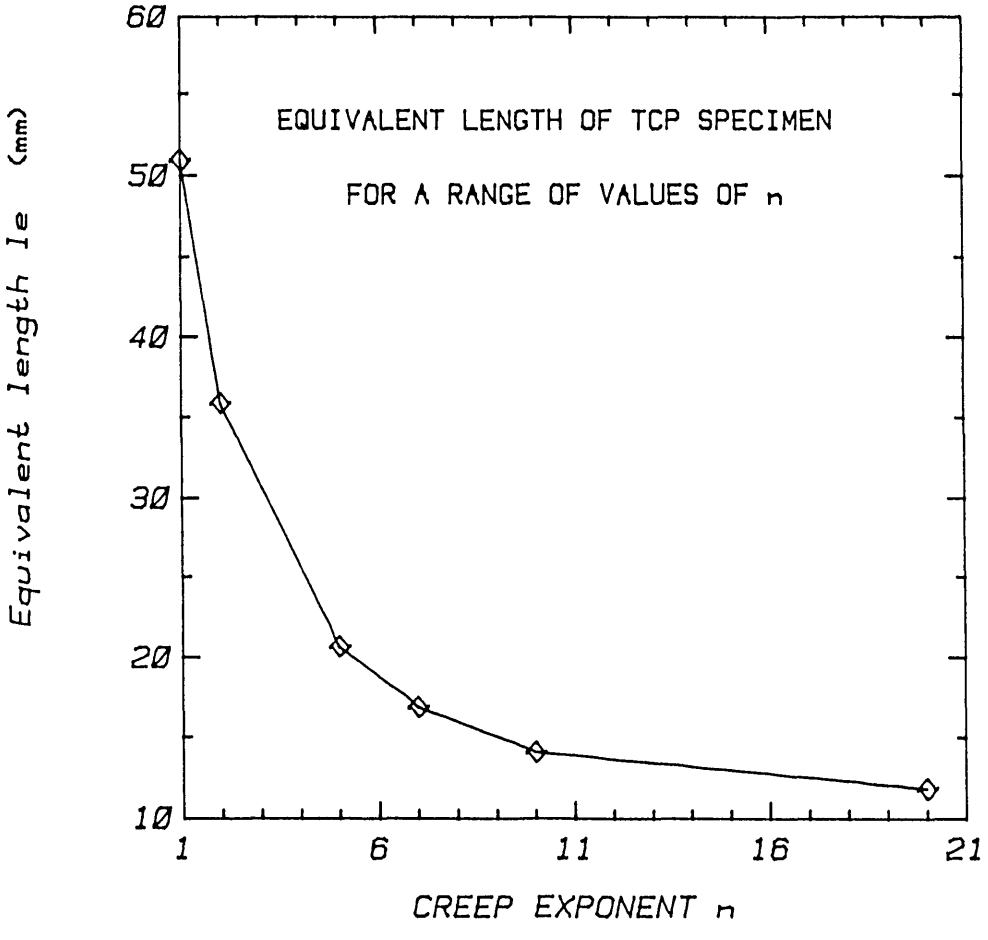


Fig. 9.6 Equivalent length, l_e, for the TCP specimen plotted against n

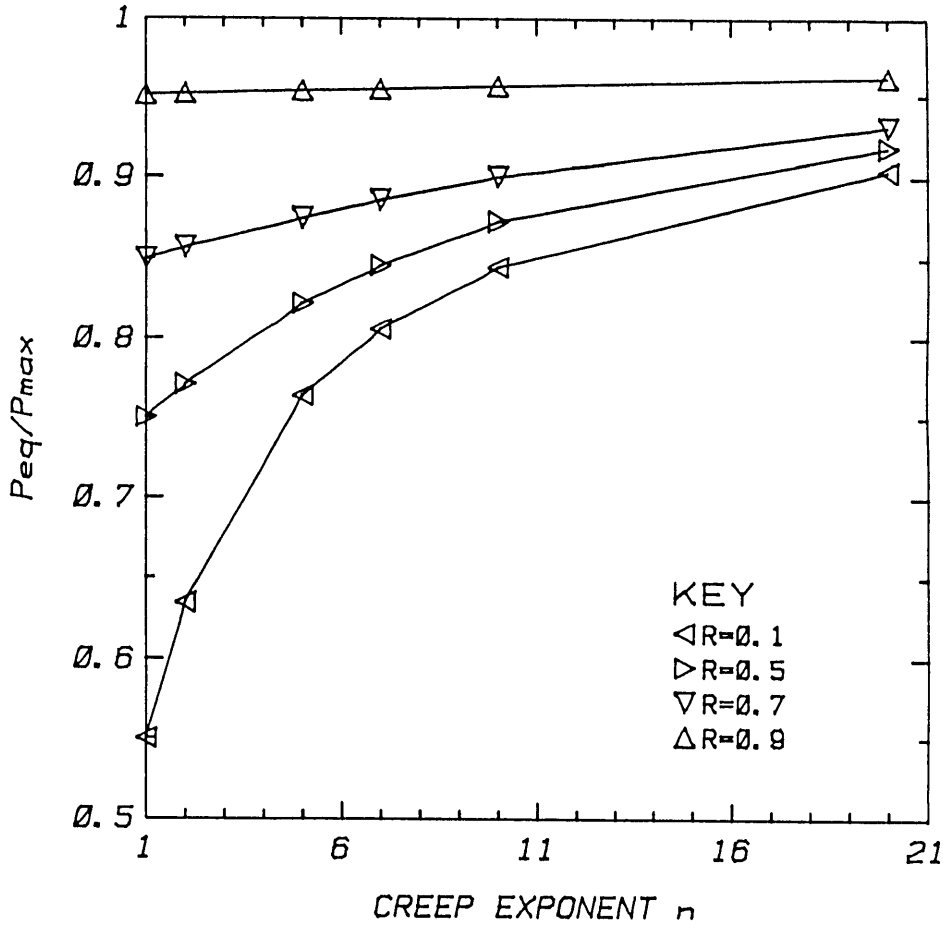


Fig. 9.7 Equivalent steady loads, P_{eq}, for a sinusoidal waveform at a range of R ratios

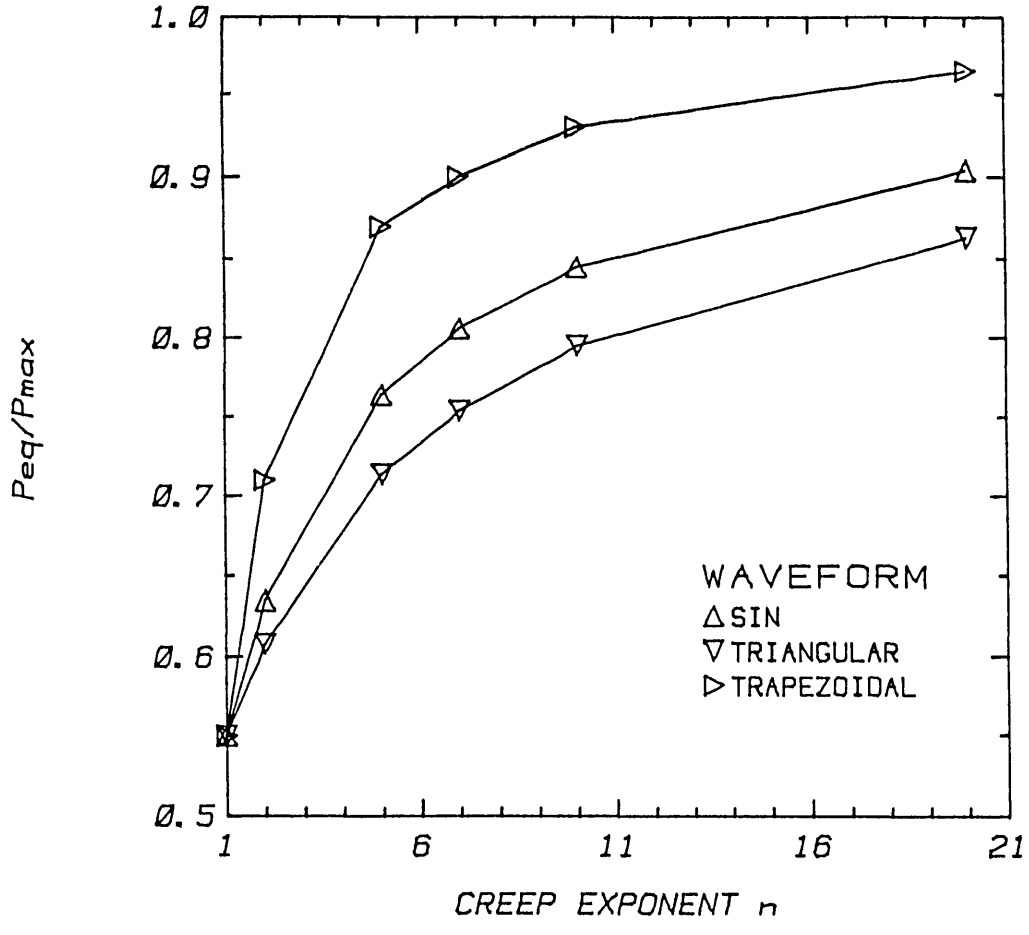


Fig. 9.8 Equivalent steady loads, P_{eq}, for a range of loading waveforms with R=0.1

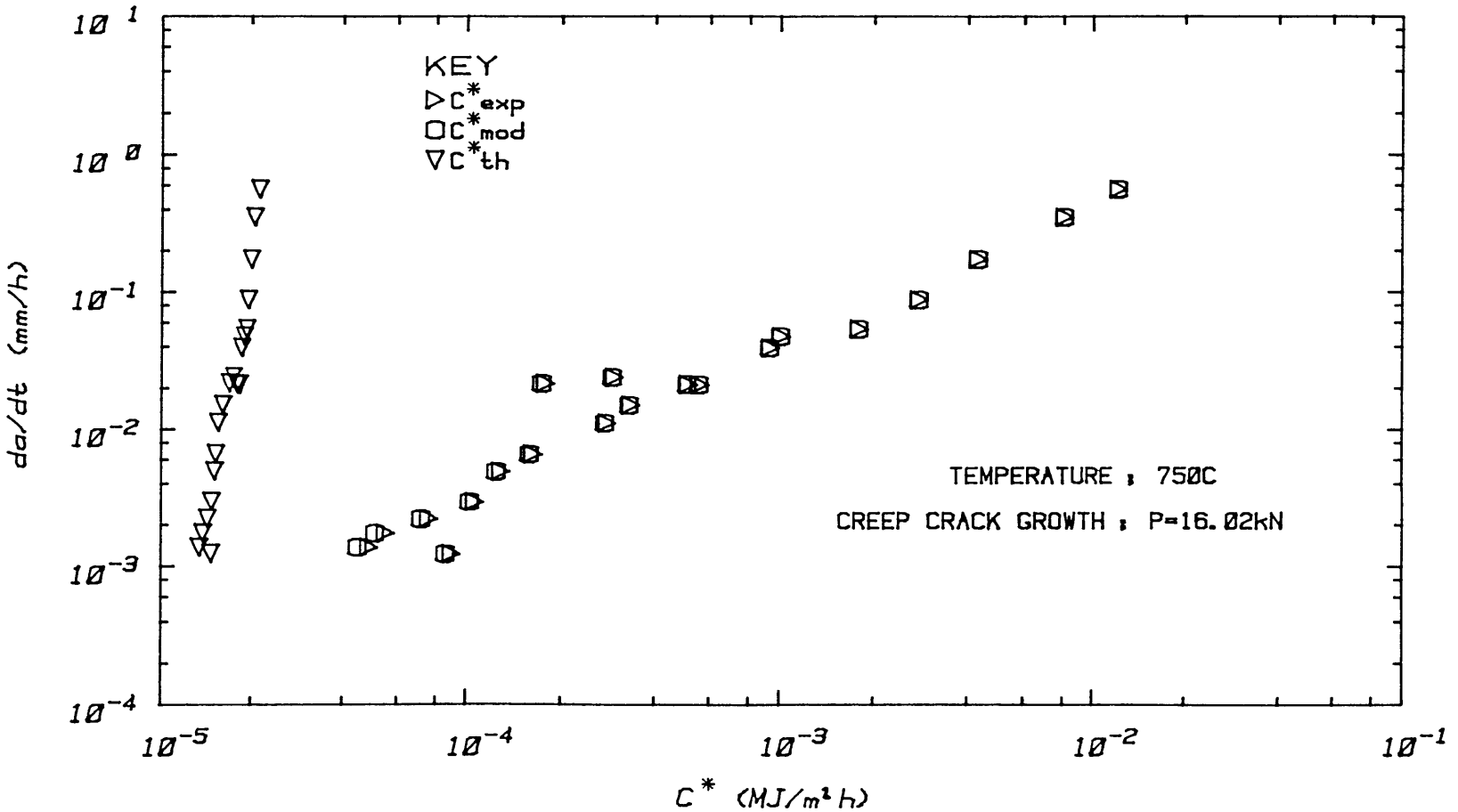


Fig. 9.9 Comparison of C^*_{exp}, C^*_{mod} and C^*_{th} for creep crack growth at 750°C

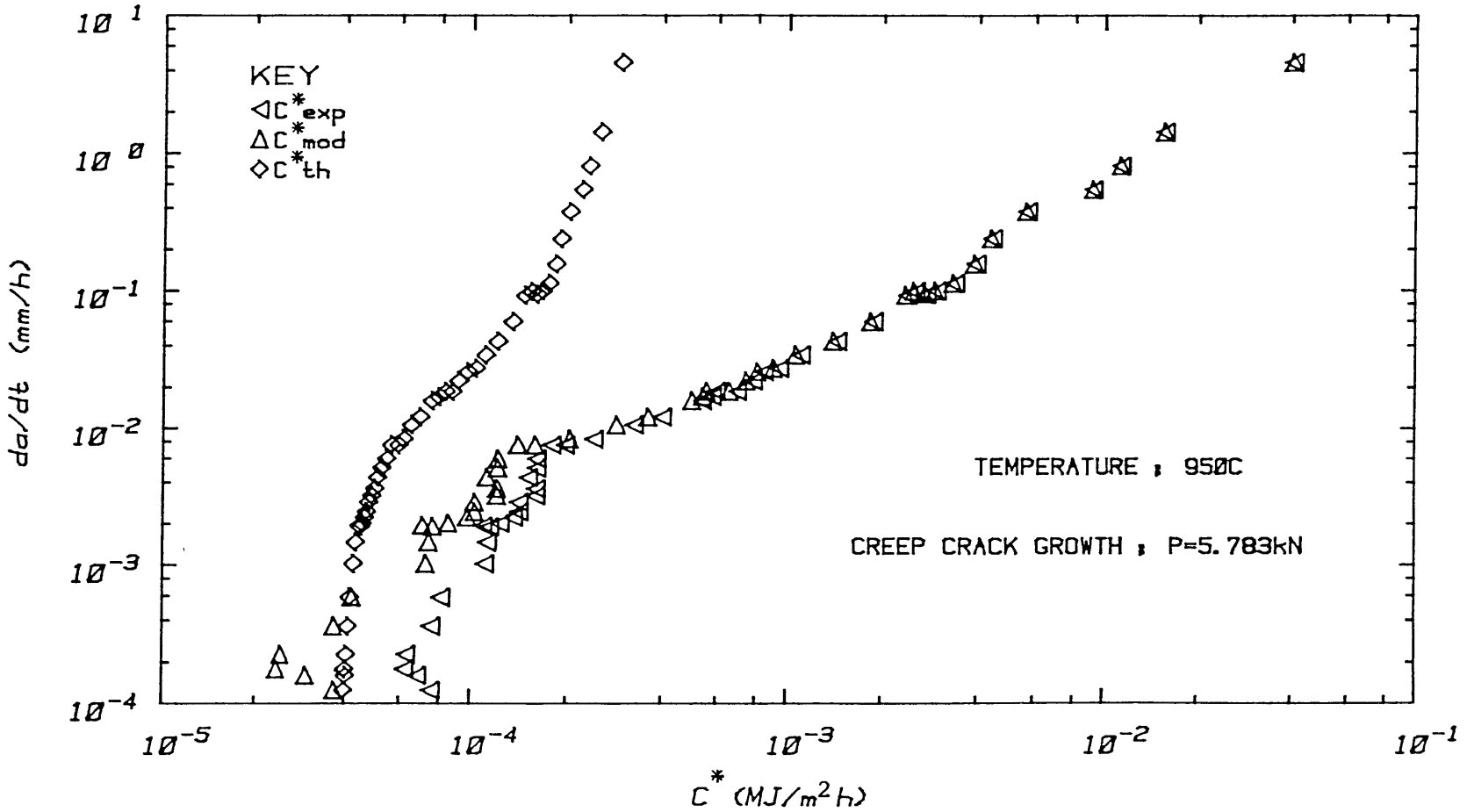


Fig. 9.10 Comparison of C^*_{exp}, C^*_{mod} and C^*_{th} for creep crack growth at 950°C

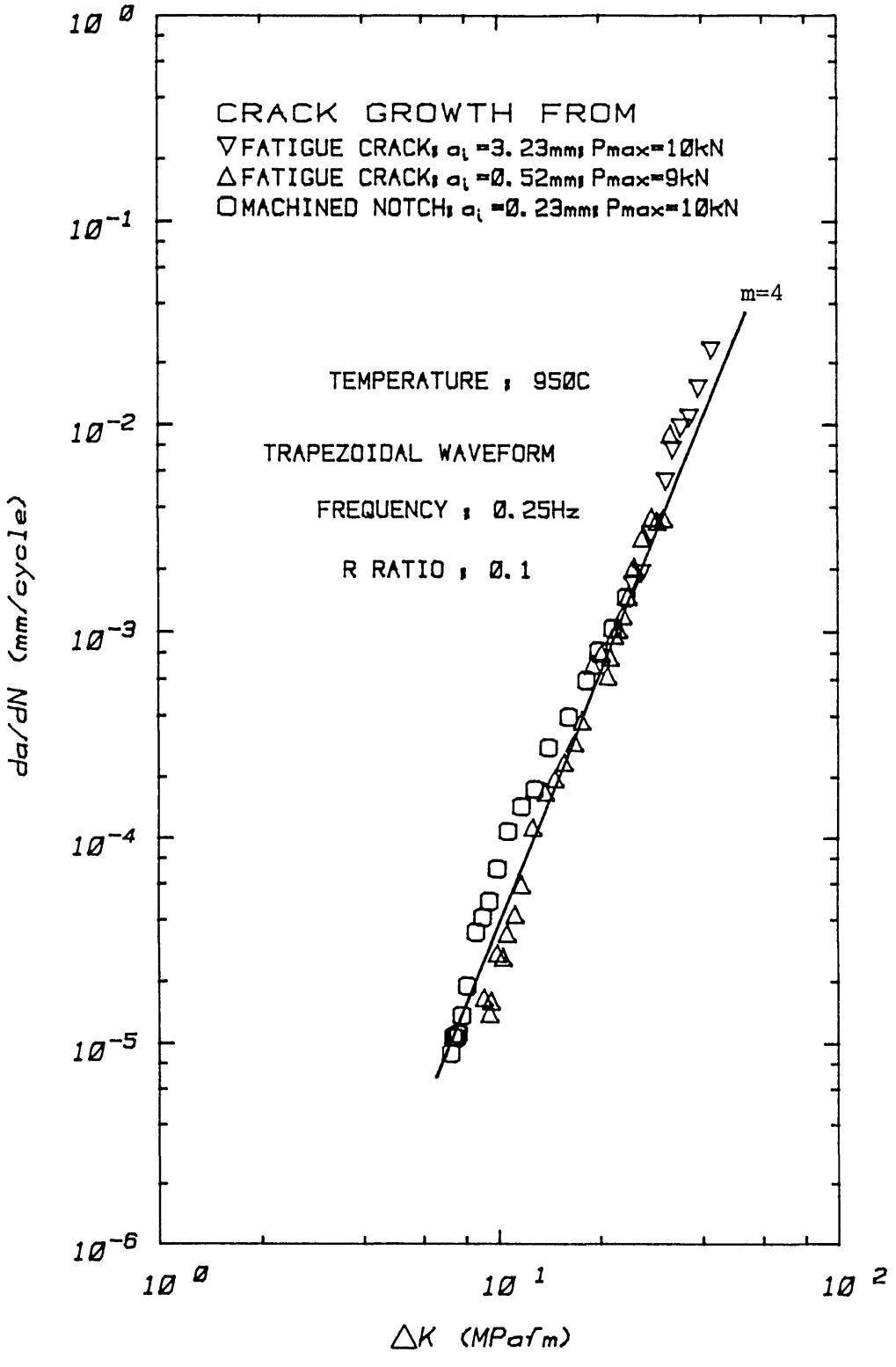


Fig. 9.11 Comparison of crack growth from a machined notch with growth from a fatigue crack

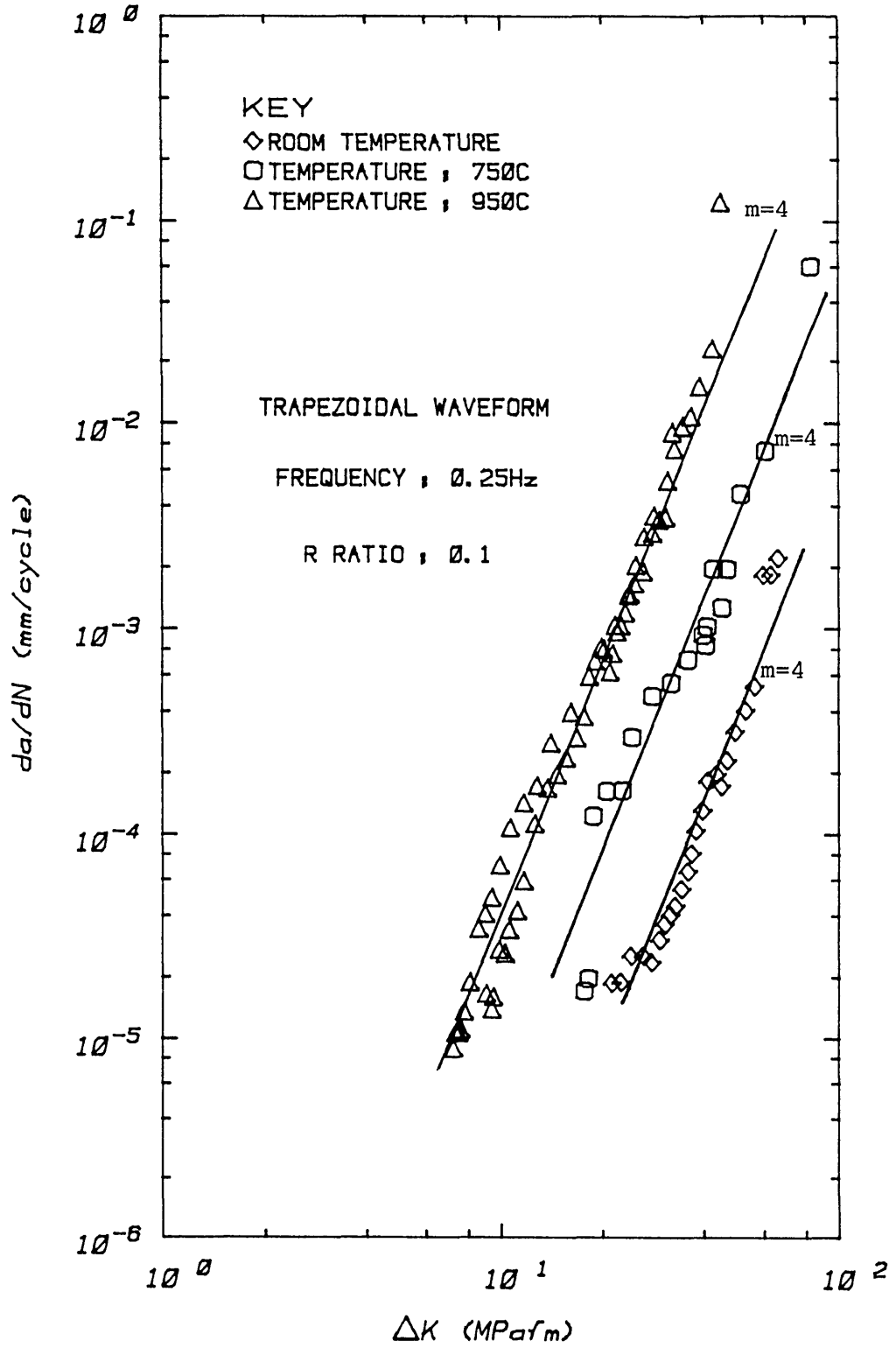


Fig. 9.12 Effect of temperature on crack growth per cycle

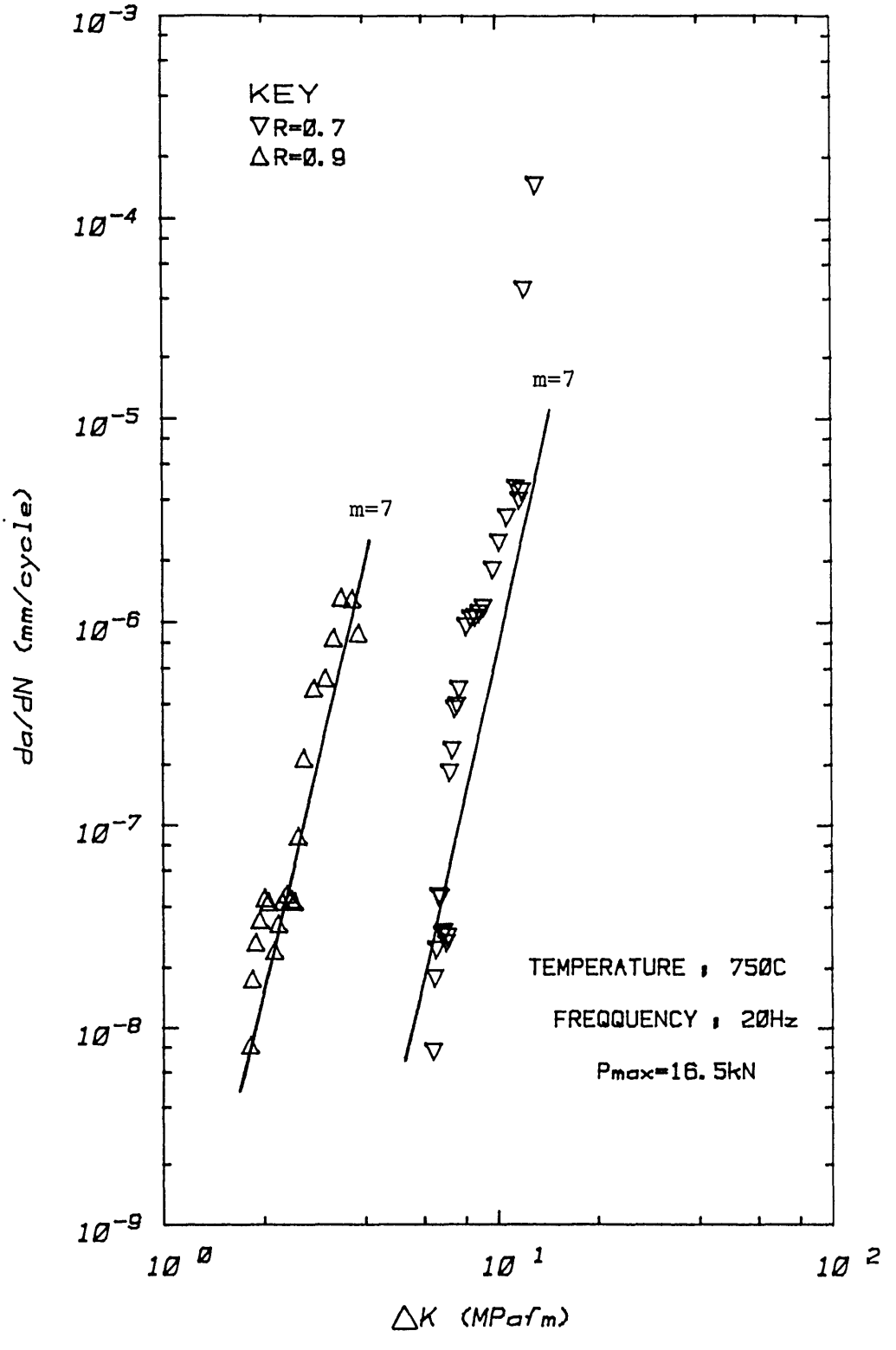


Fig. 9.13 Crack growth in the threshold region at 750°C for R=0.7 and 0.9

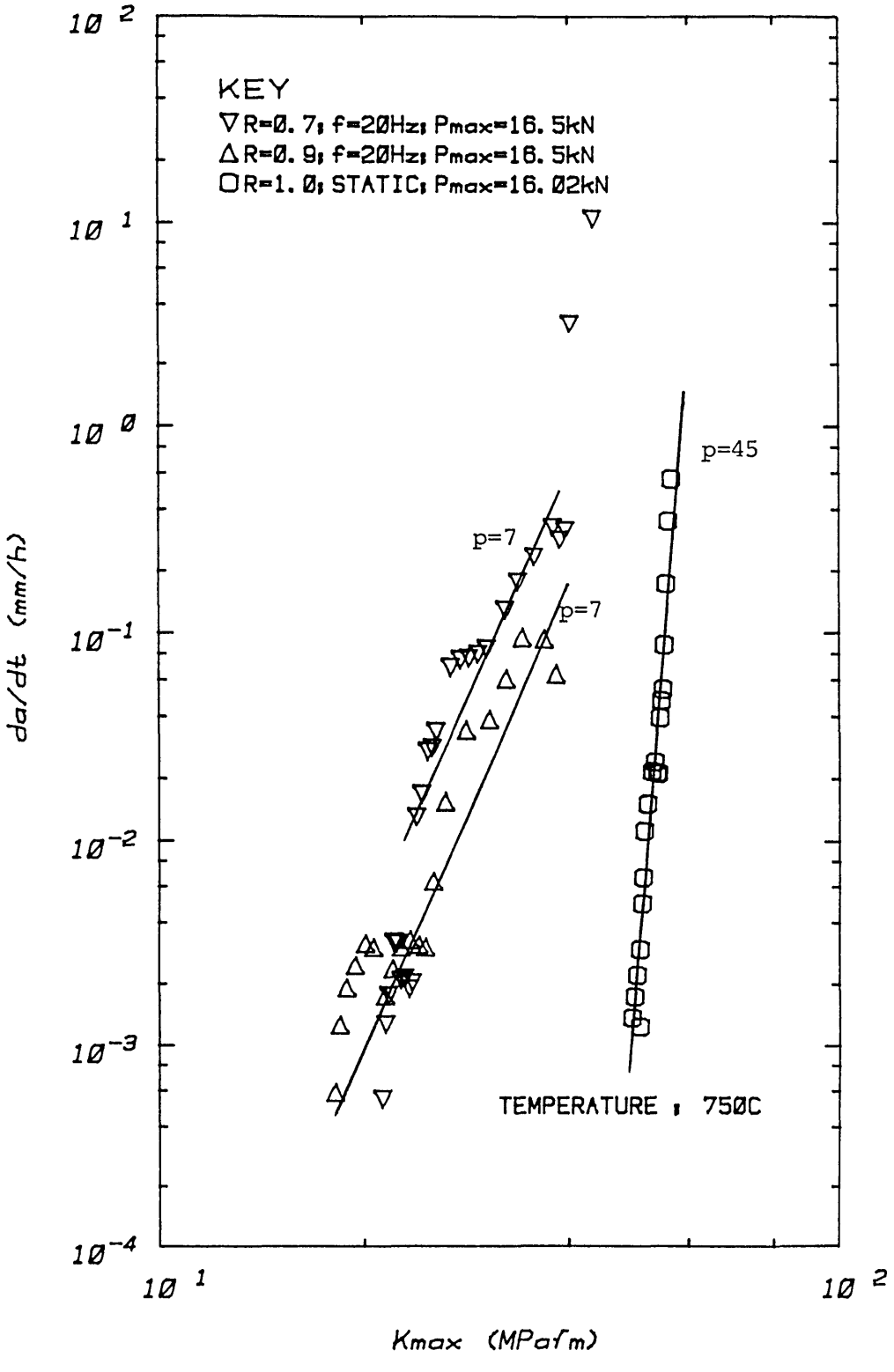


Fig. 9.14 Crack growth in the threshold region at 750°C for R=0.7,0.9 and 1

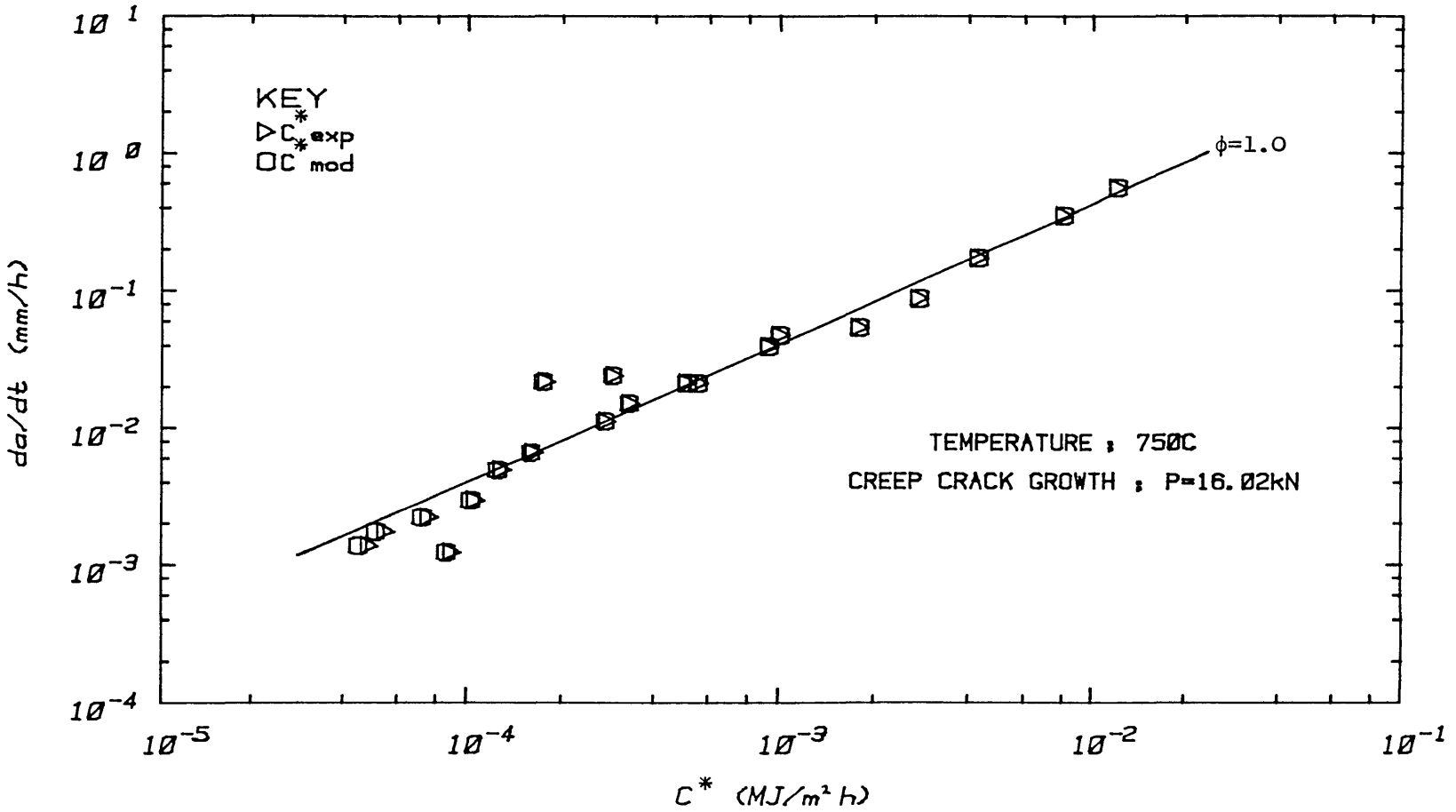
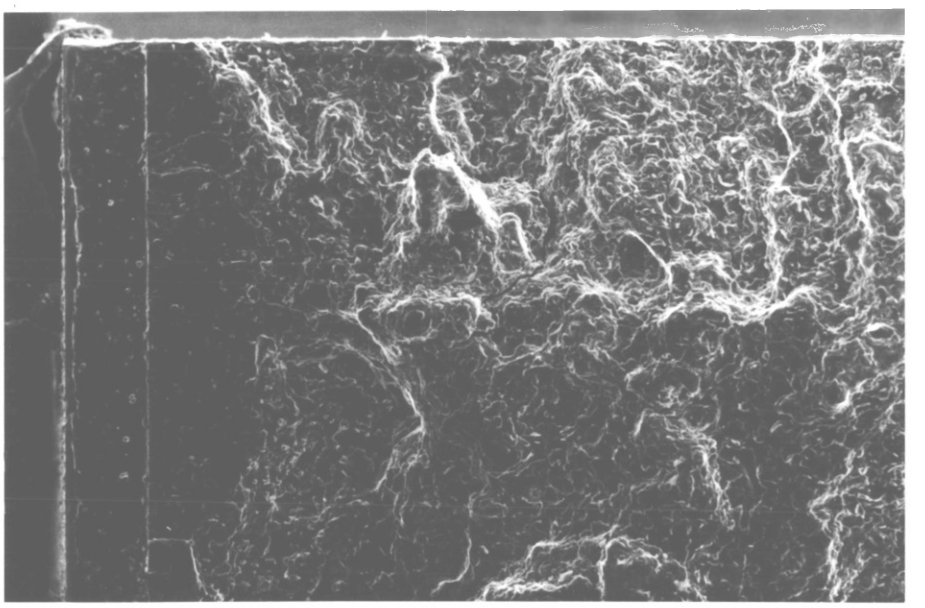
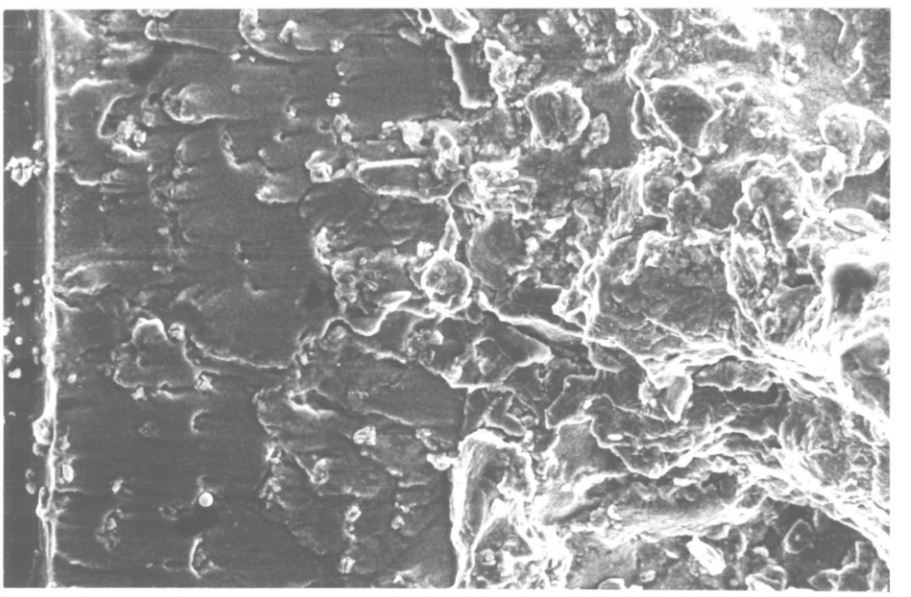


Fig. 9.15 Crack growth under static loading at 750°C

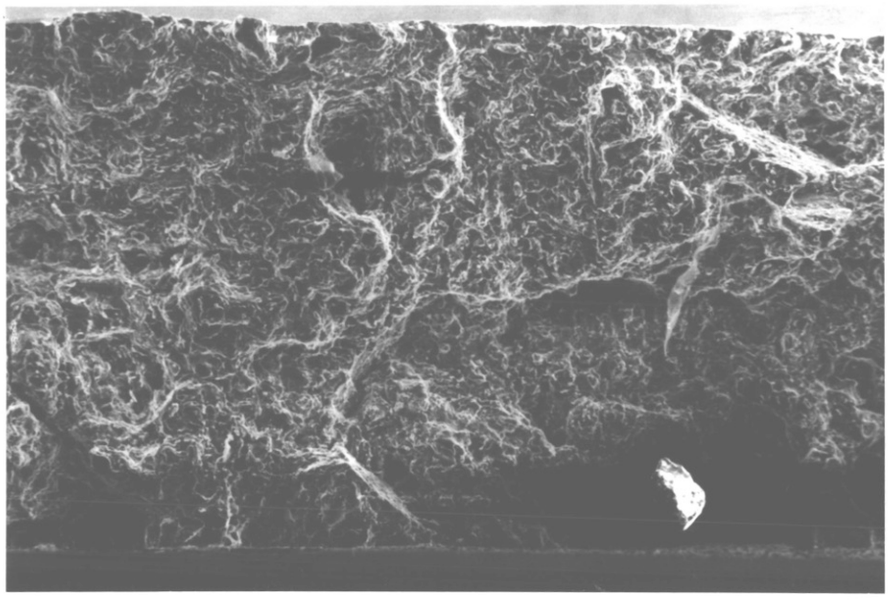


(a) x54

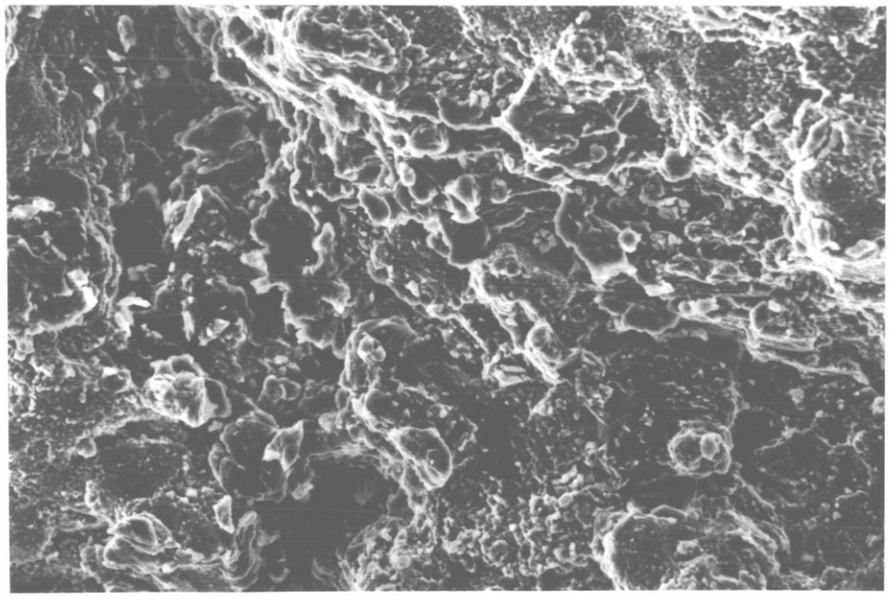


(b) x200

Fig. 9.16 Fracture surface of a specimen tested at R=0.9 and 750^{o}C showing starter notch,pre-crack at R=0.1 and crack growth in the threshold region at R=0.9



(a) x54



(b) x300

Fig. 9.17 Fracture surface of a specimen tested at R=1 and 750°C

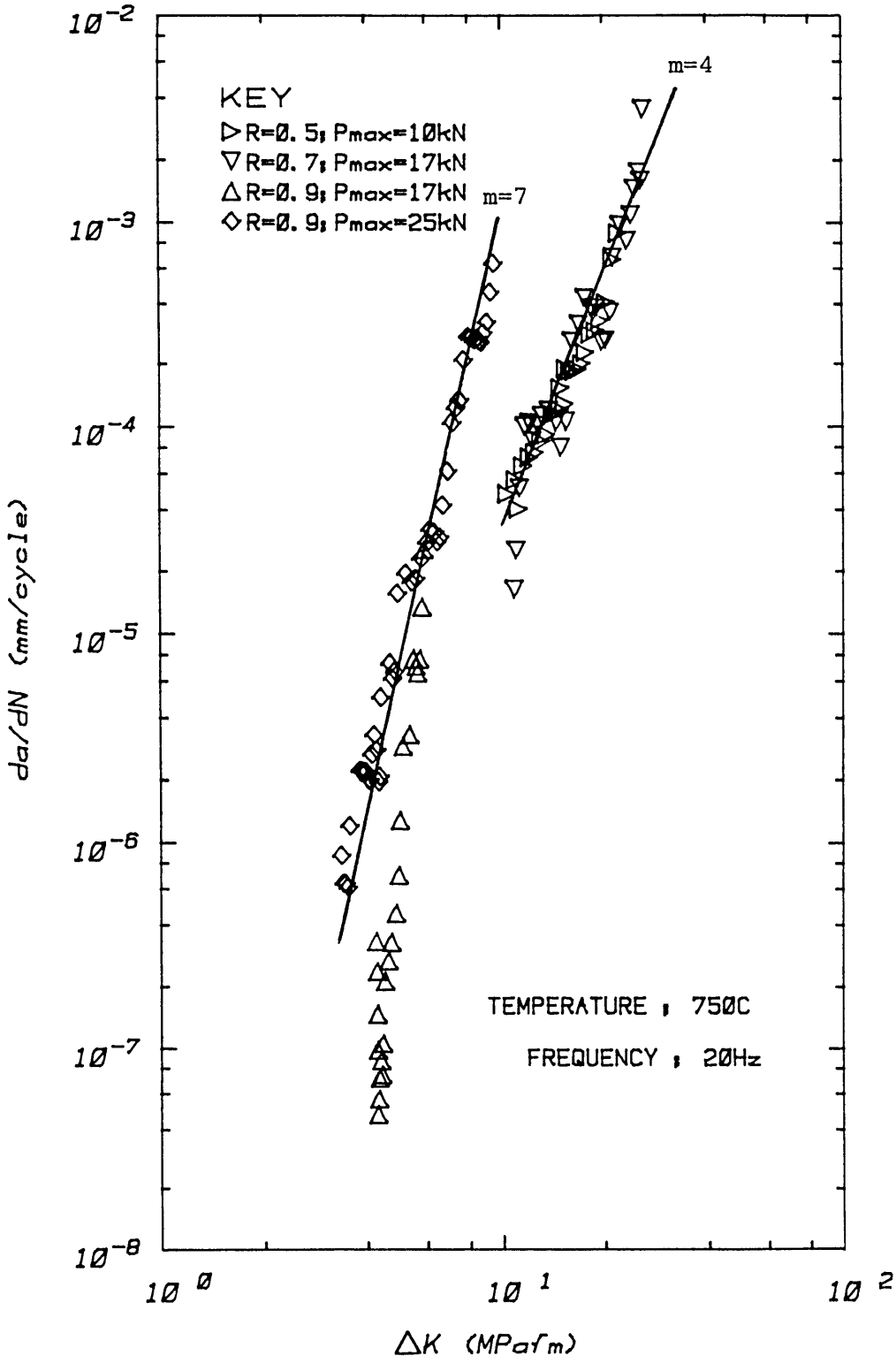


Fig. 9.18 Effect of R ratio on crack growth per cycle at 750°C

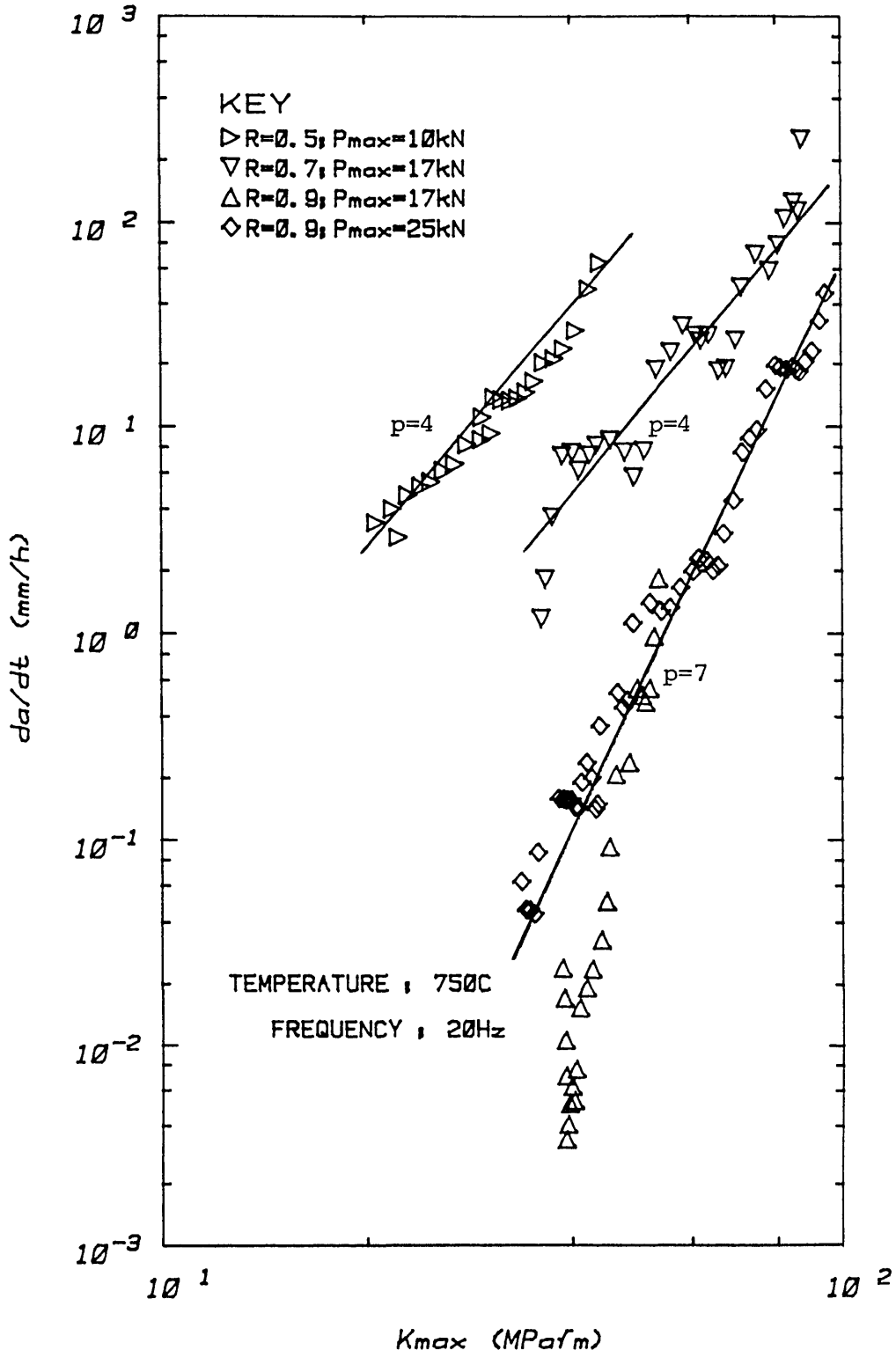


Fig. 9.19 Effect of R ratio on crack growth rate at 750°C

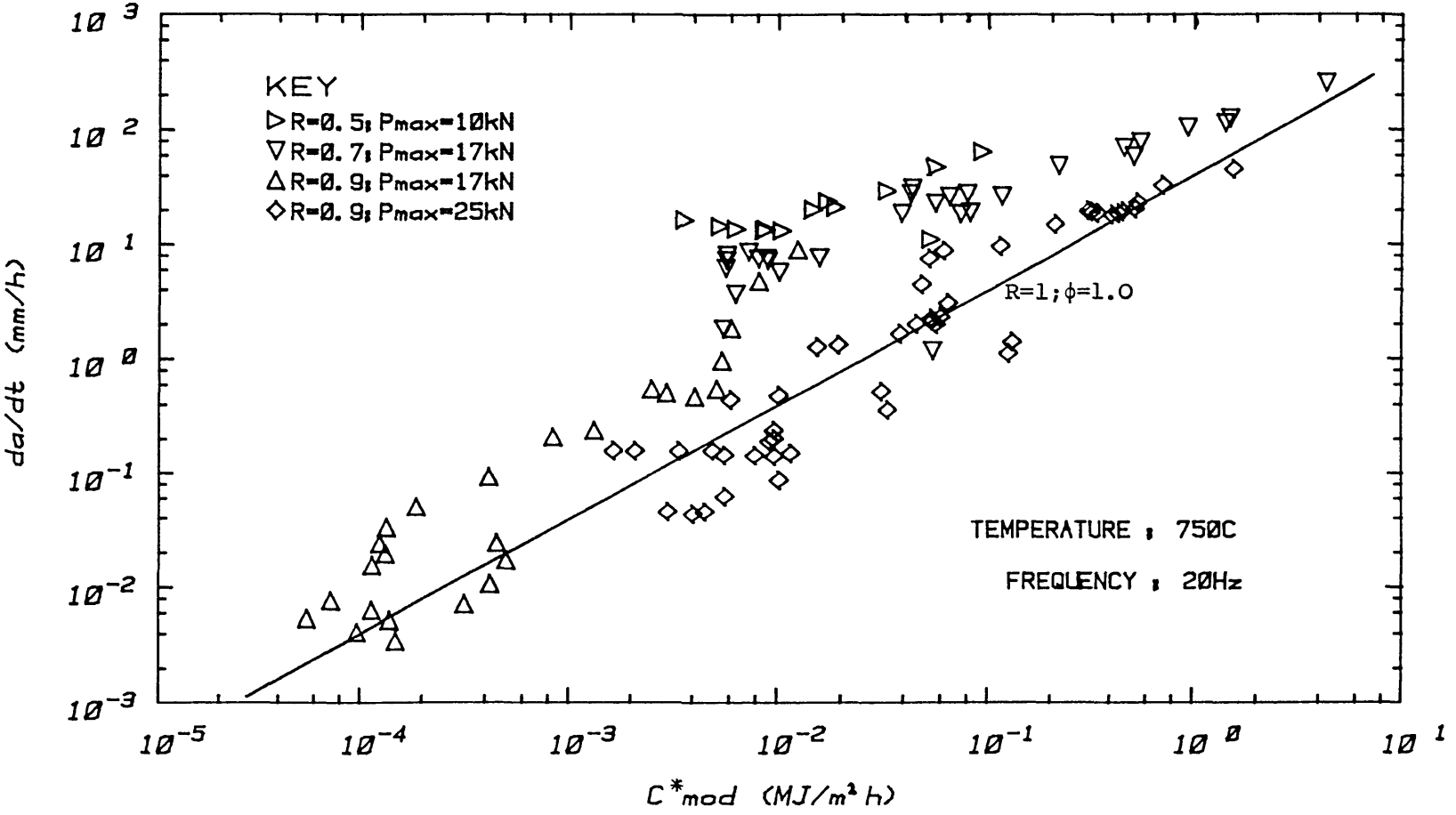


Fig. 9.20 Effect of R ratio on crack growth rate at 750°C

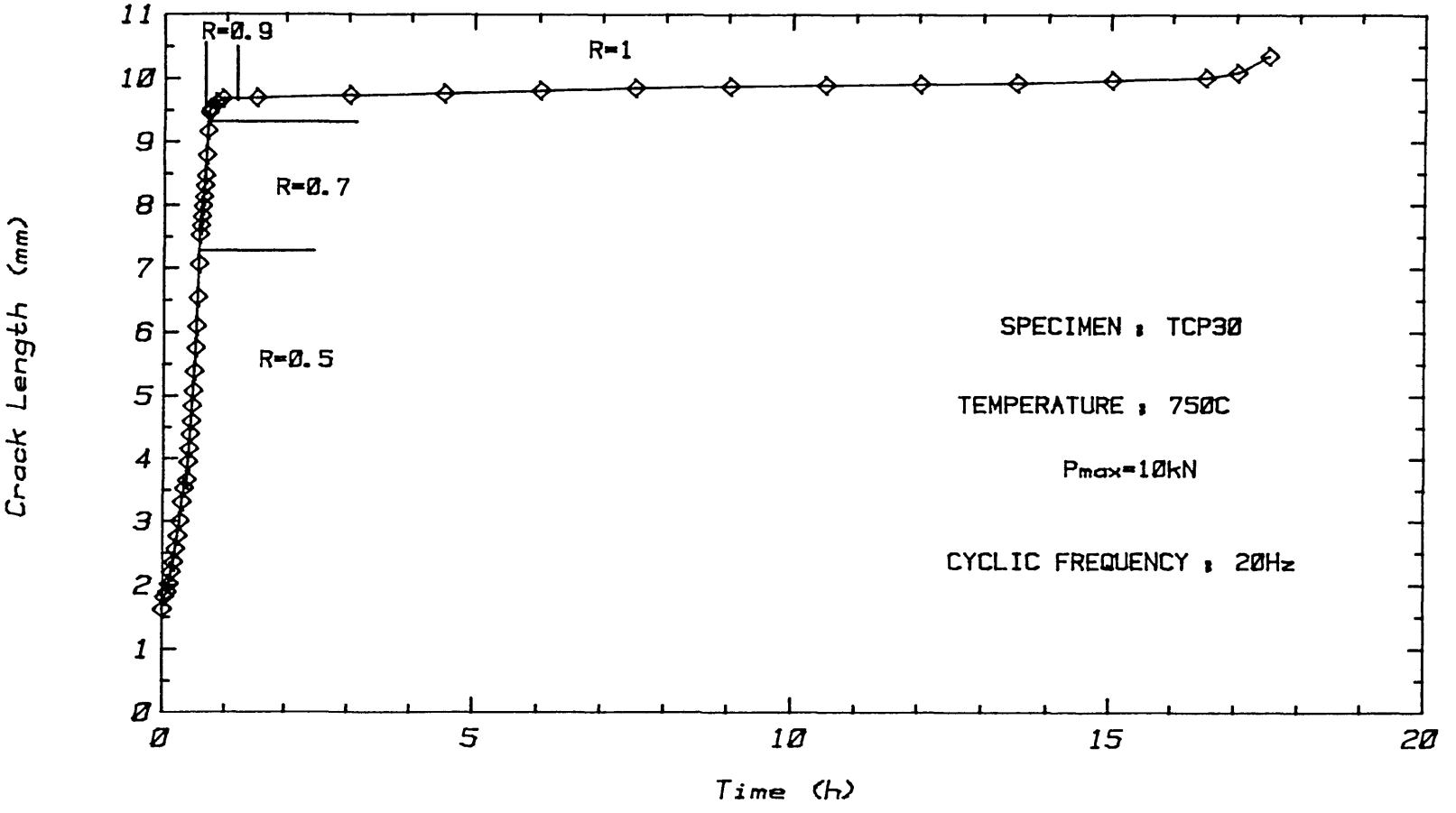


Fig. 9.21 Effect of changing the R ratio during a crack growth test at 750°C

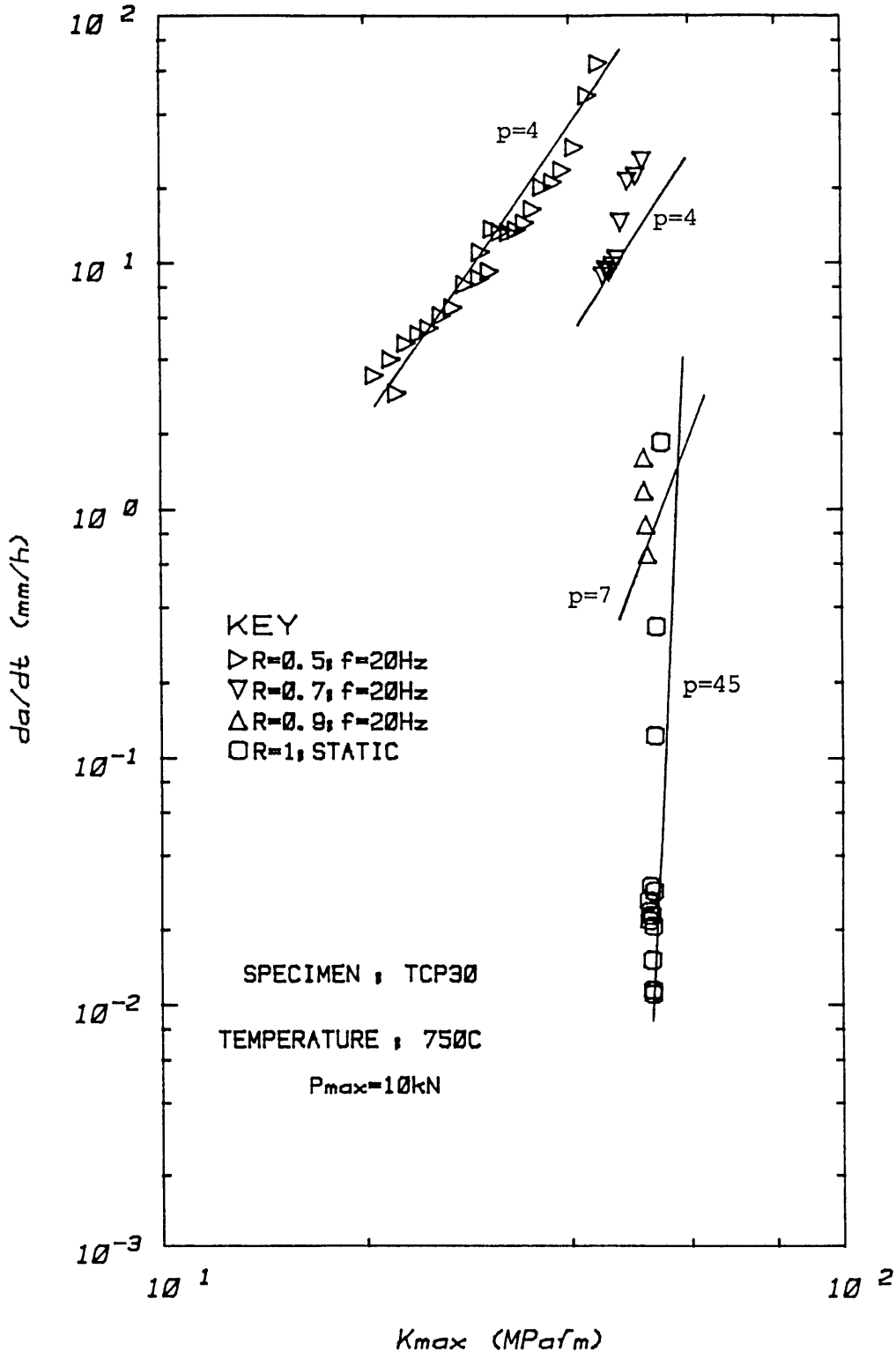


Fig. 9.22 Effect on crack growth rate of changing the R ratio during a test at 750°C

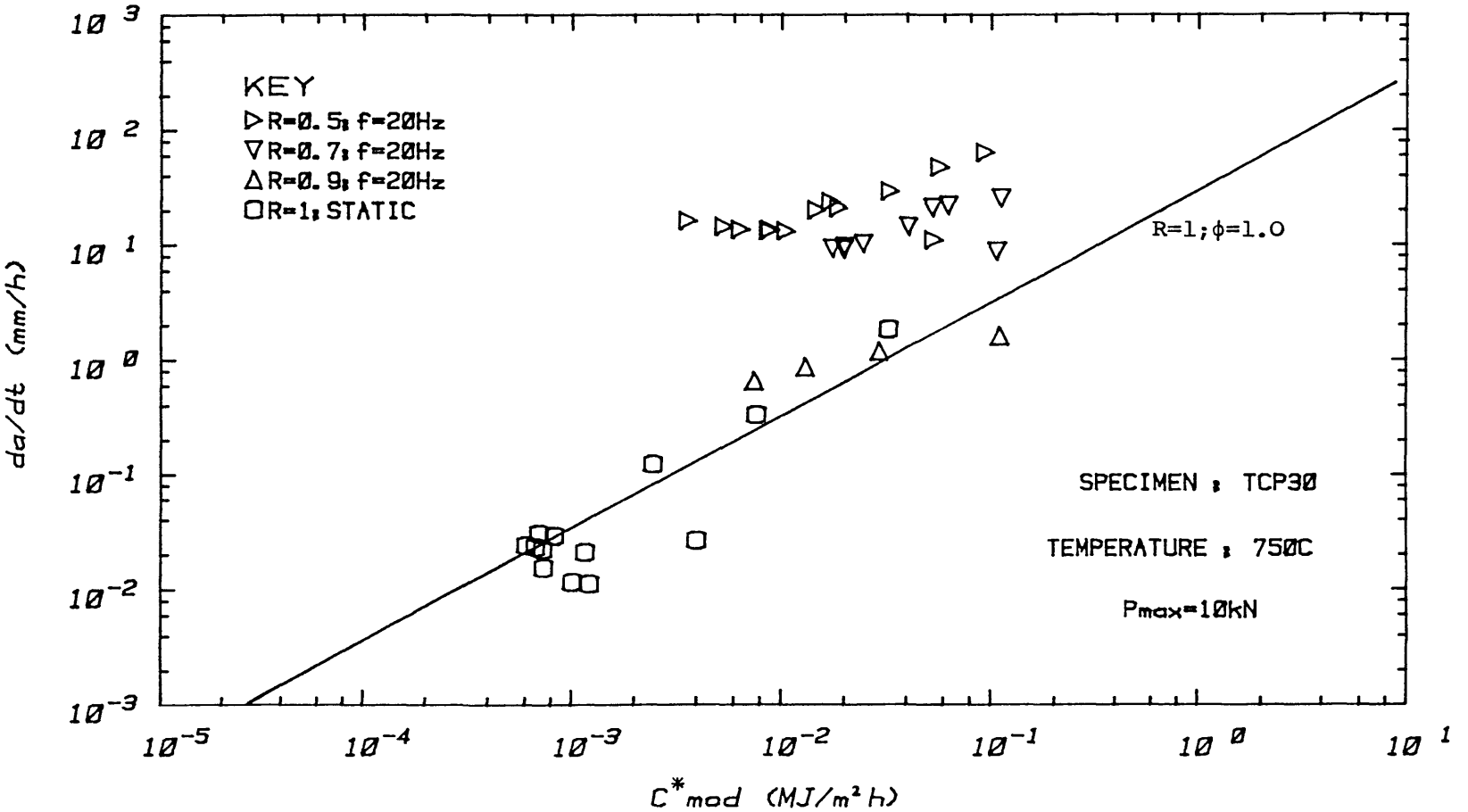
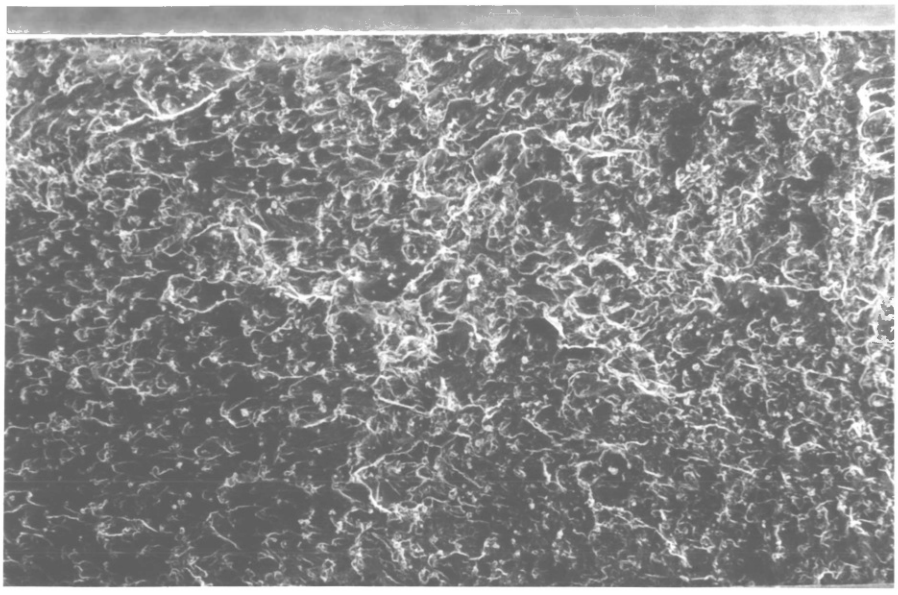
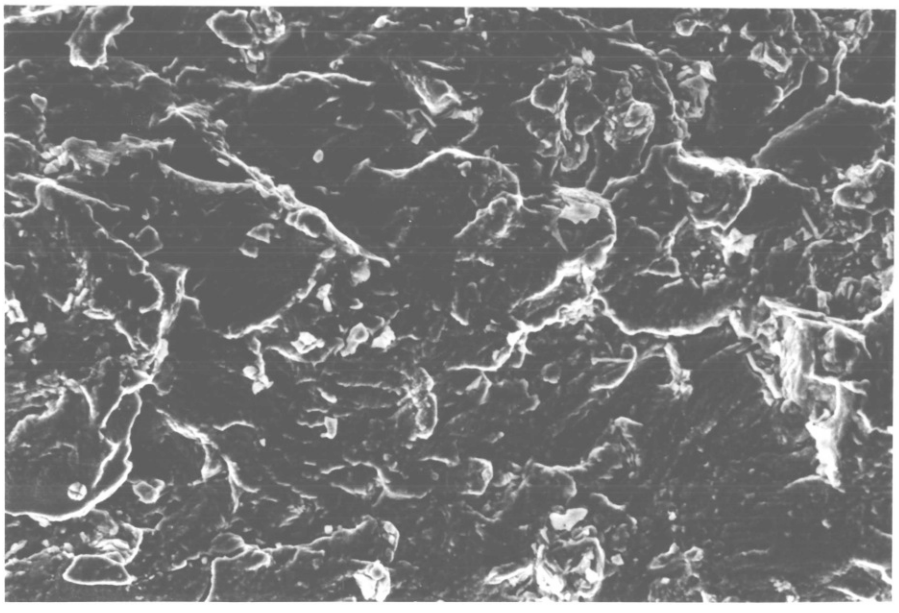


Fig. 9.23 Effect on crack growth rate of changing the R ratio during a test at 750°C



(a) x54



(b) x300

Fig. 9.24 Fracture surface of a specimen tested at R=0.5 and 750°C

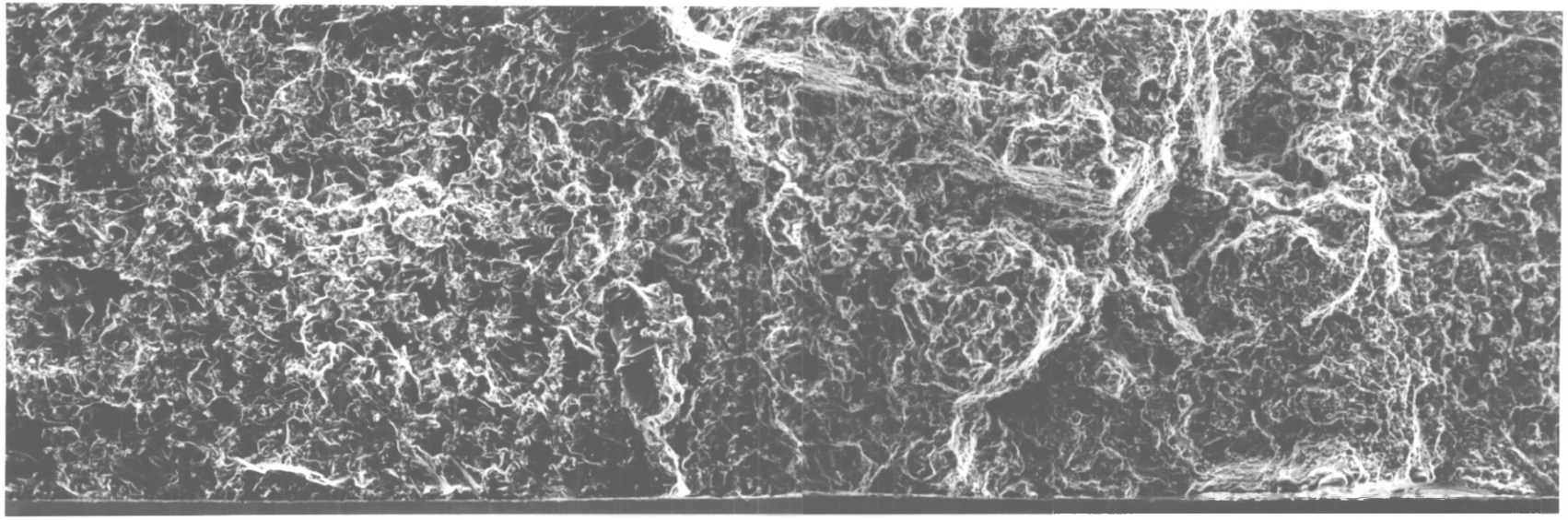


Fig. 9.25 Transition in fracture surface observed when changing the R ratio from 0.7 to 0.9 to 1 at 750°C,×54

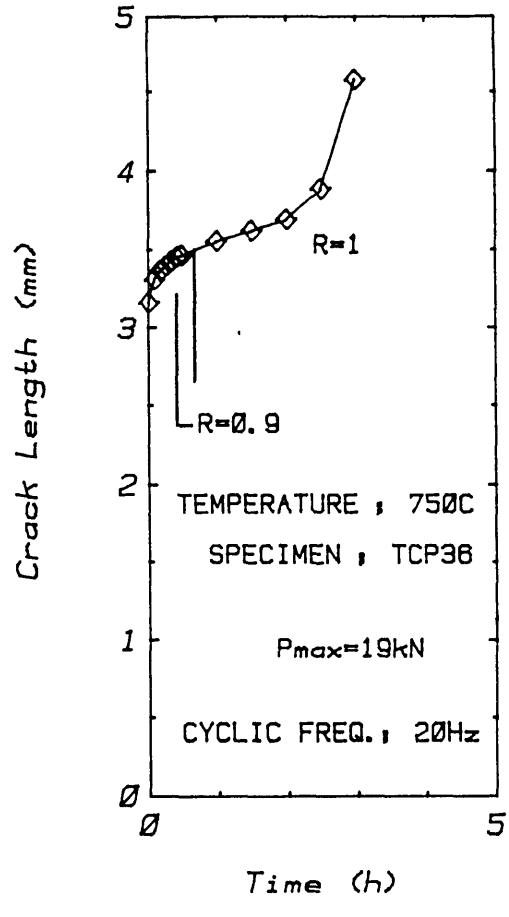


Fig. 9.26 Attempt to change the R ratio during a test at 950°C in the sequence 0.9,1,0.9

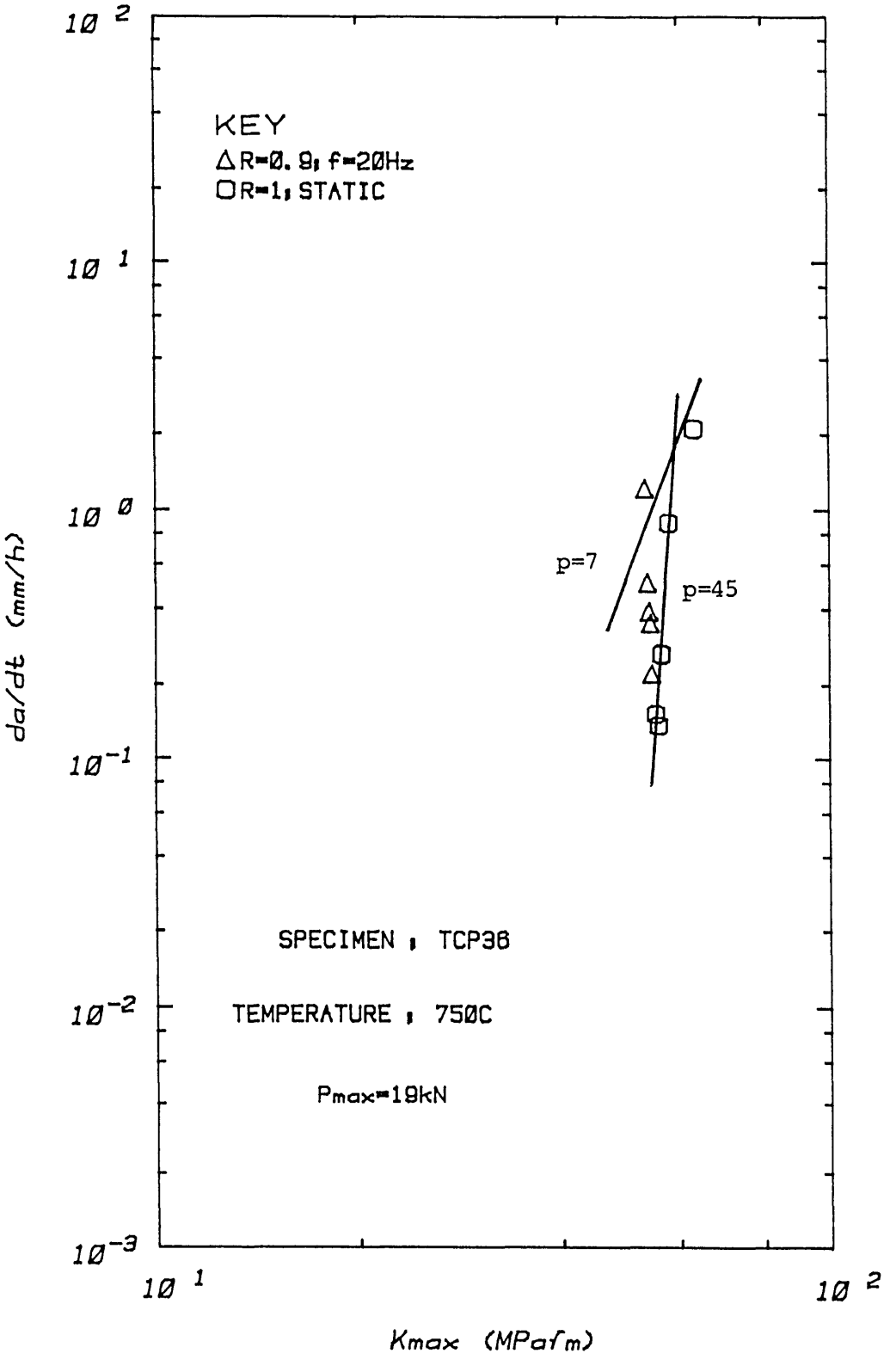


Fig. 9.27 Crack growth data obtained while attempting to change the R ratio during a test in the sequence 0.9,1,0.9

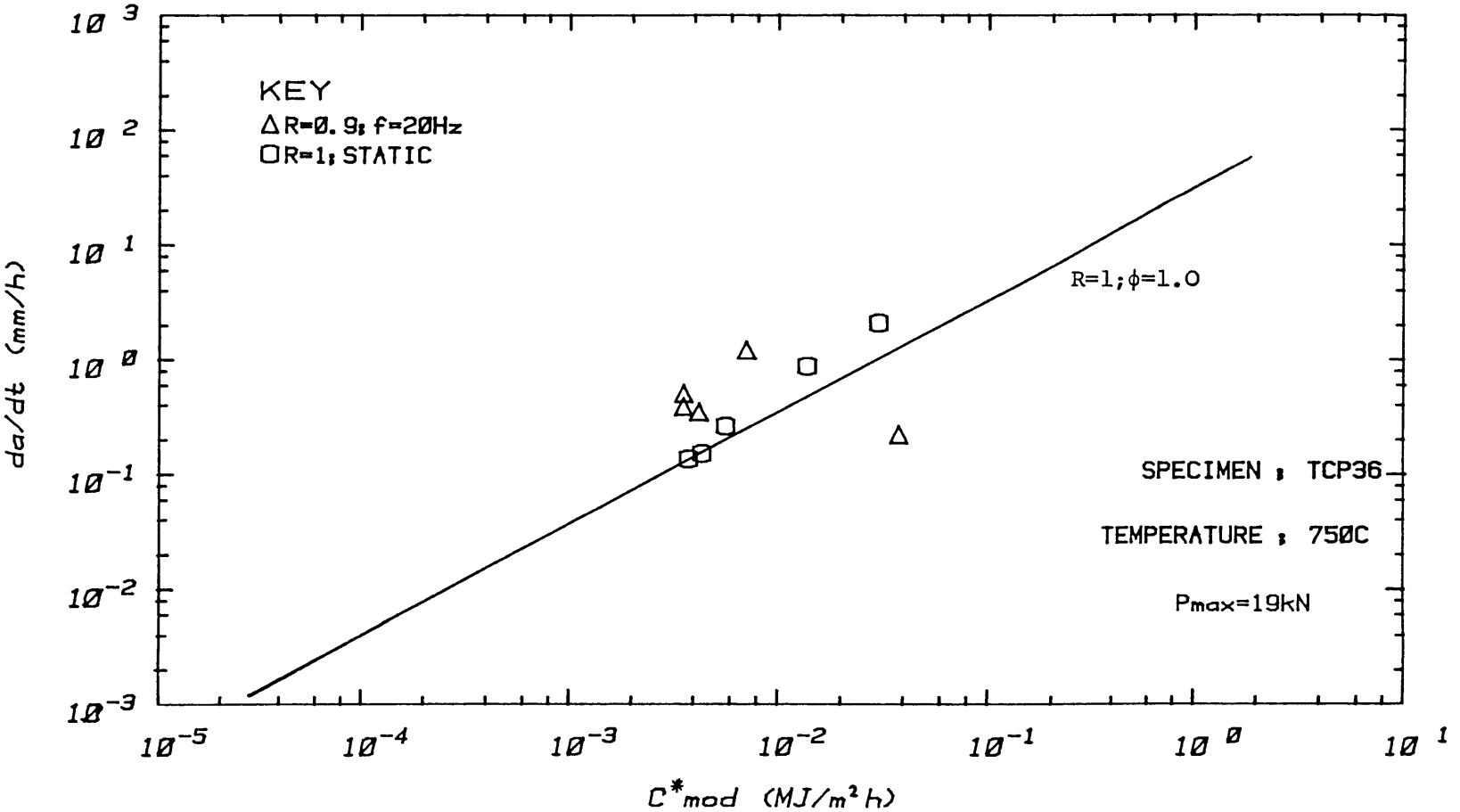


Fig. 9.28 Crack growth rates plotted against C^*_{mod} for a test in which an attempt was made to change the R ratio in the sequence 0.9,1,0.9

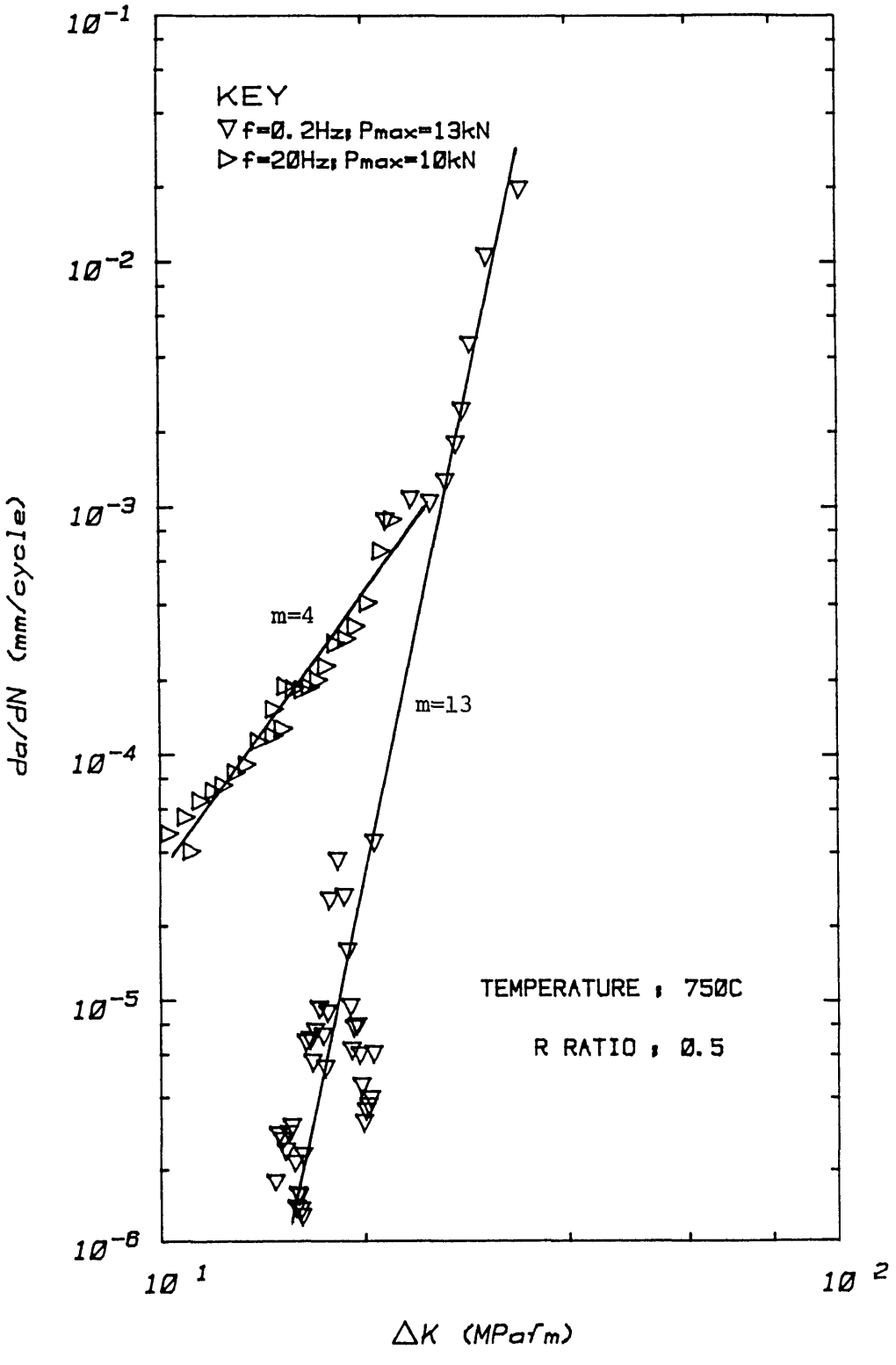


Fig. 9.29 Effect of frequency on crack growth per cycle at 750°C for R=0.5

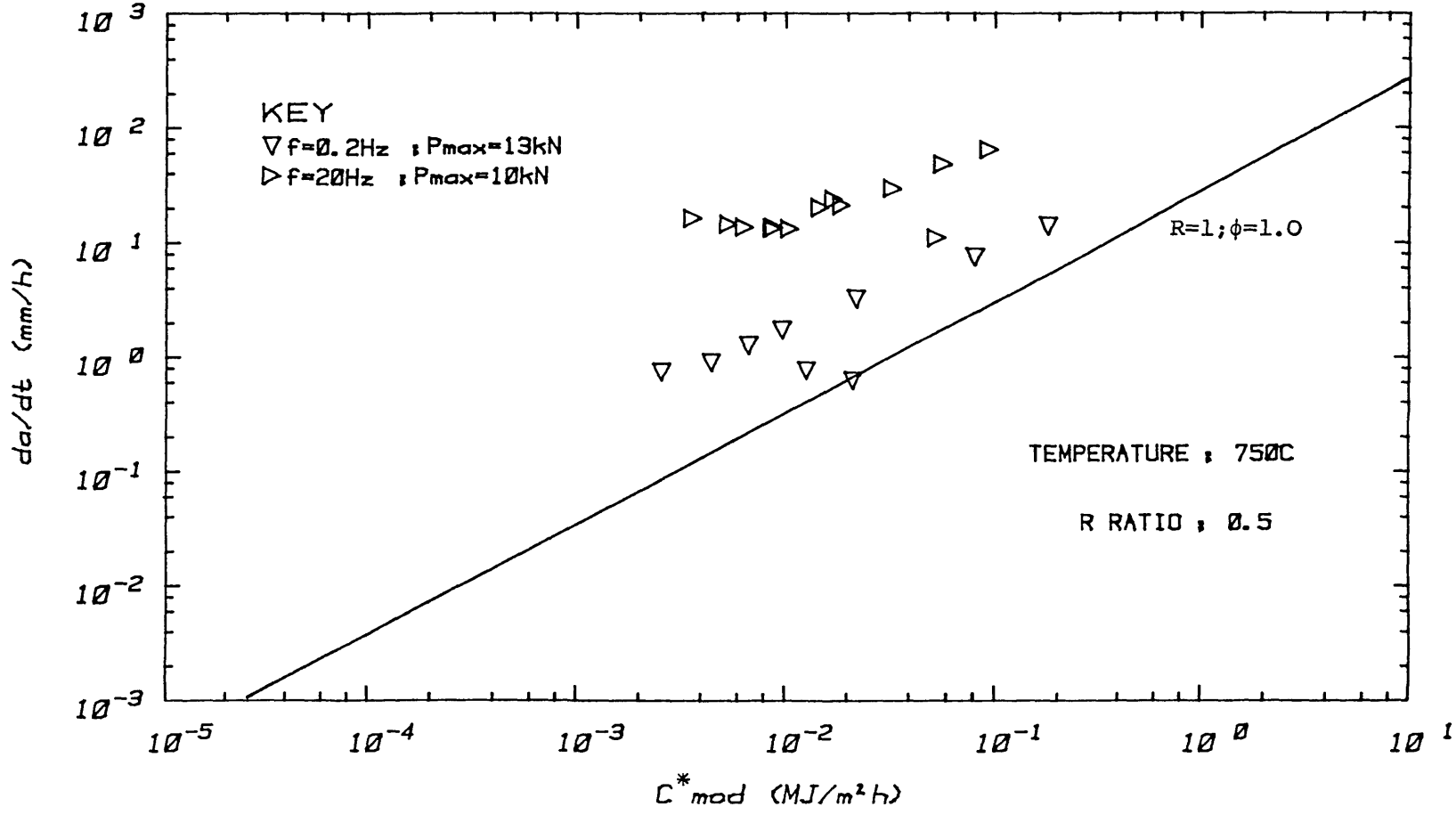


Fig. 9.30 Effect of frequency on crack growth rate at 750°C for R=0.5

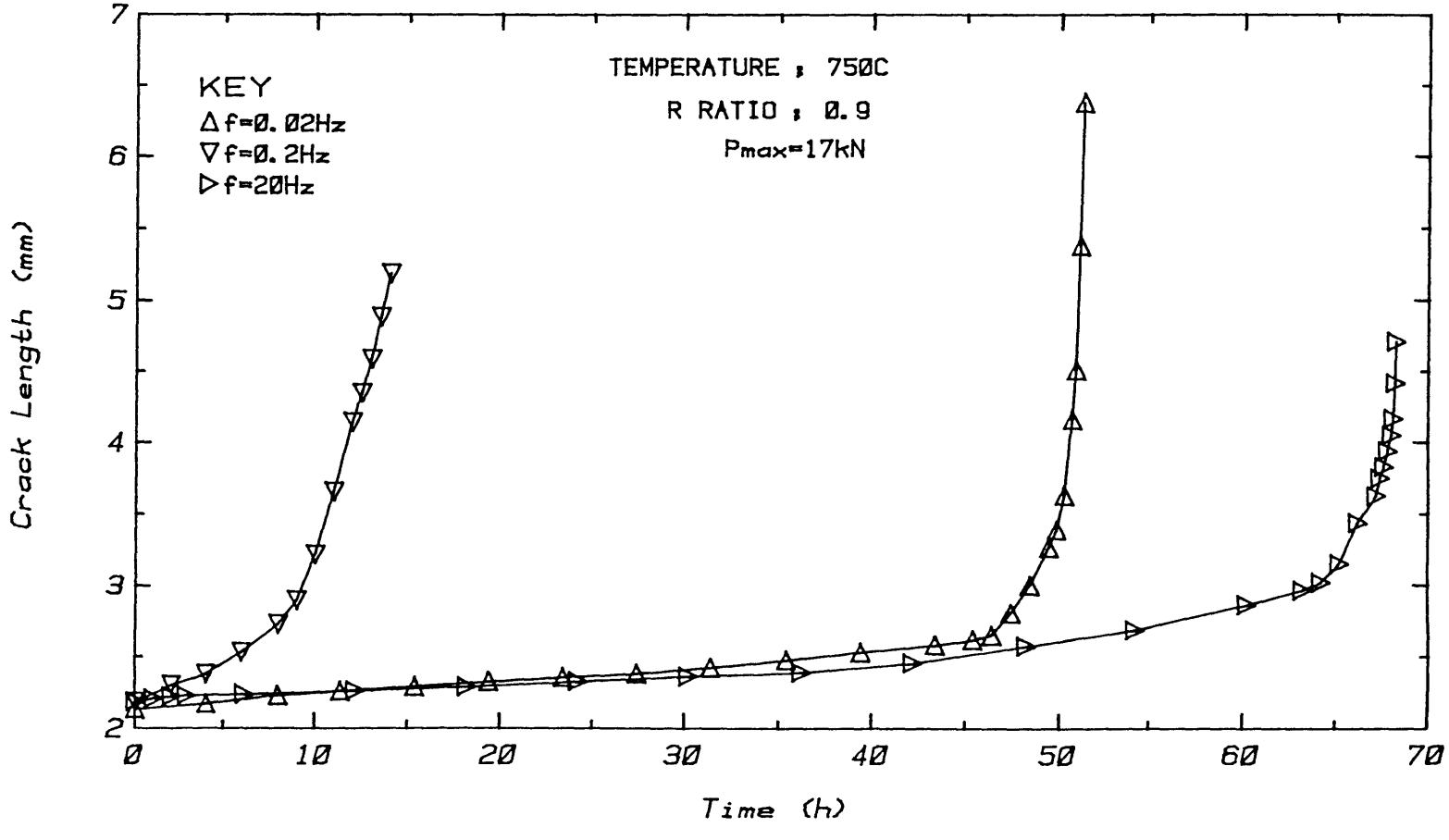


Fig. 9.31 Effect of frequency on crack growth at 750°C for R=0.9

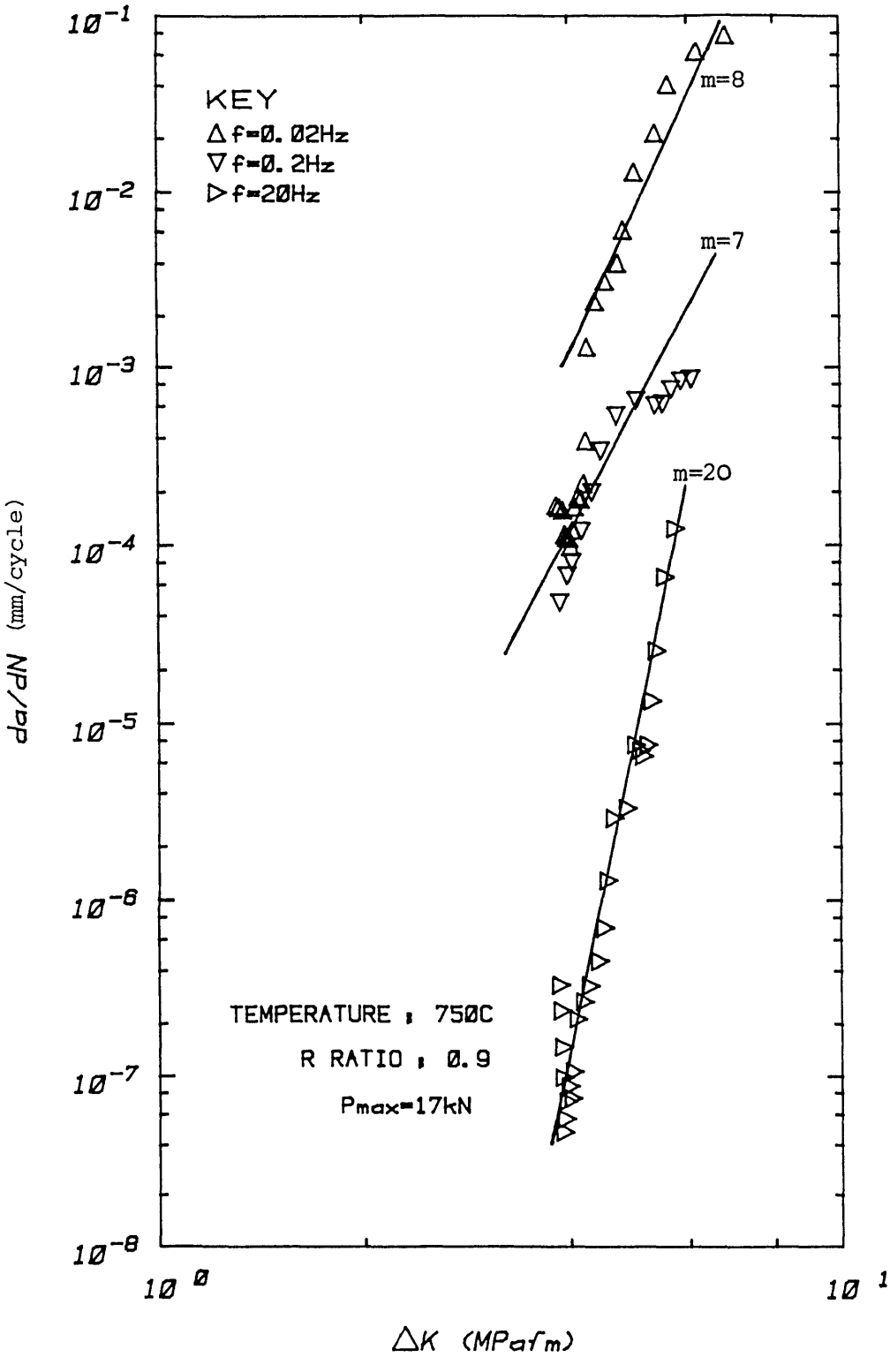


Fig. 9.32 Effect of frequency on crack growth per cycle at 750°C for R=0.9

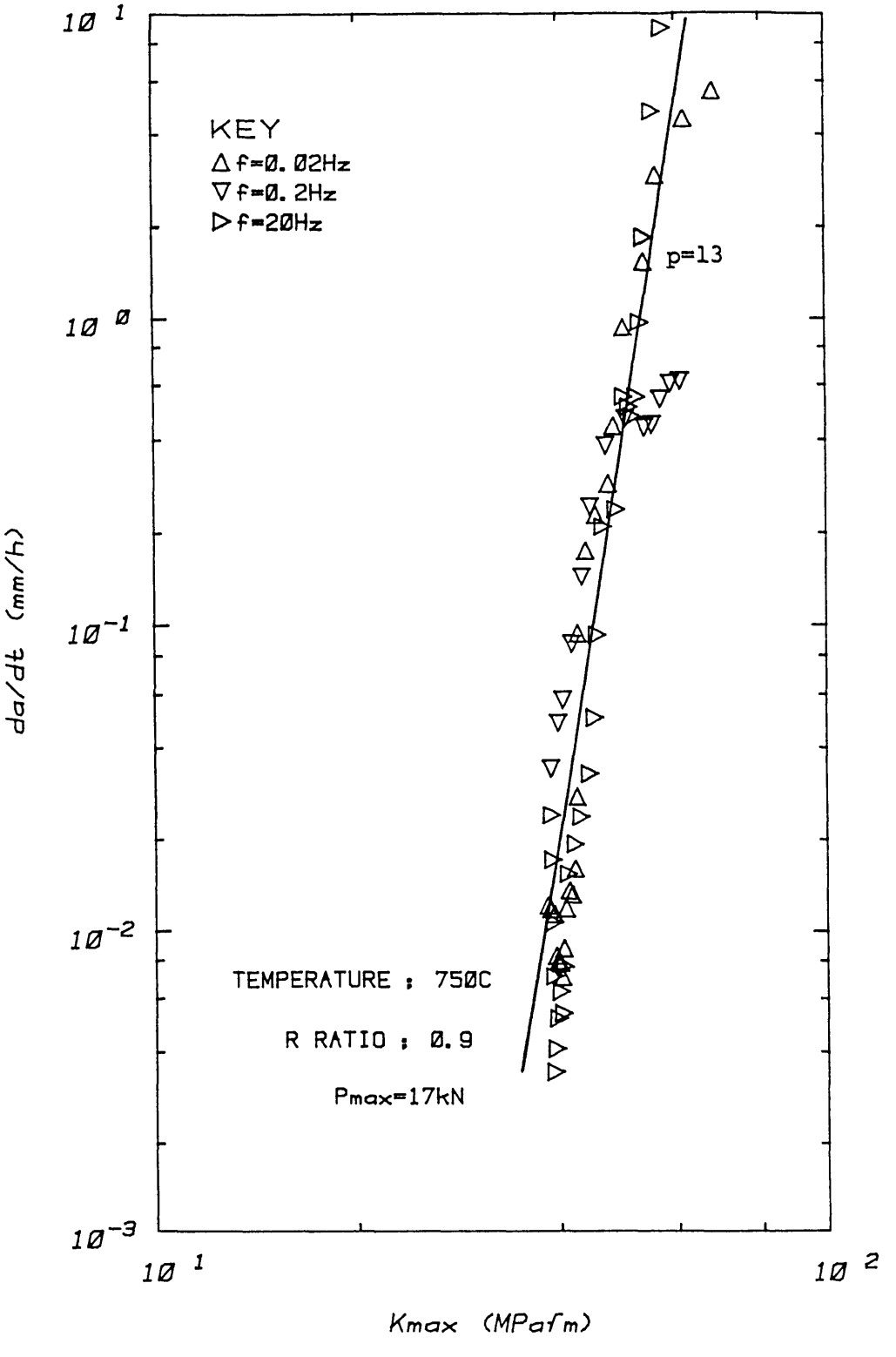


Fig. 9.33 Effect of frequency on crack growth rate at 750°C for R=0.9

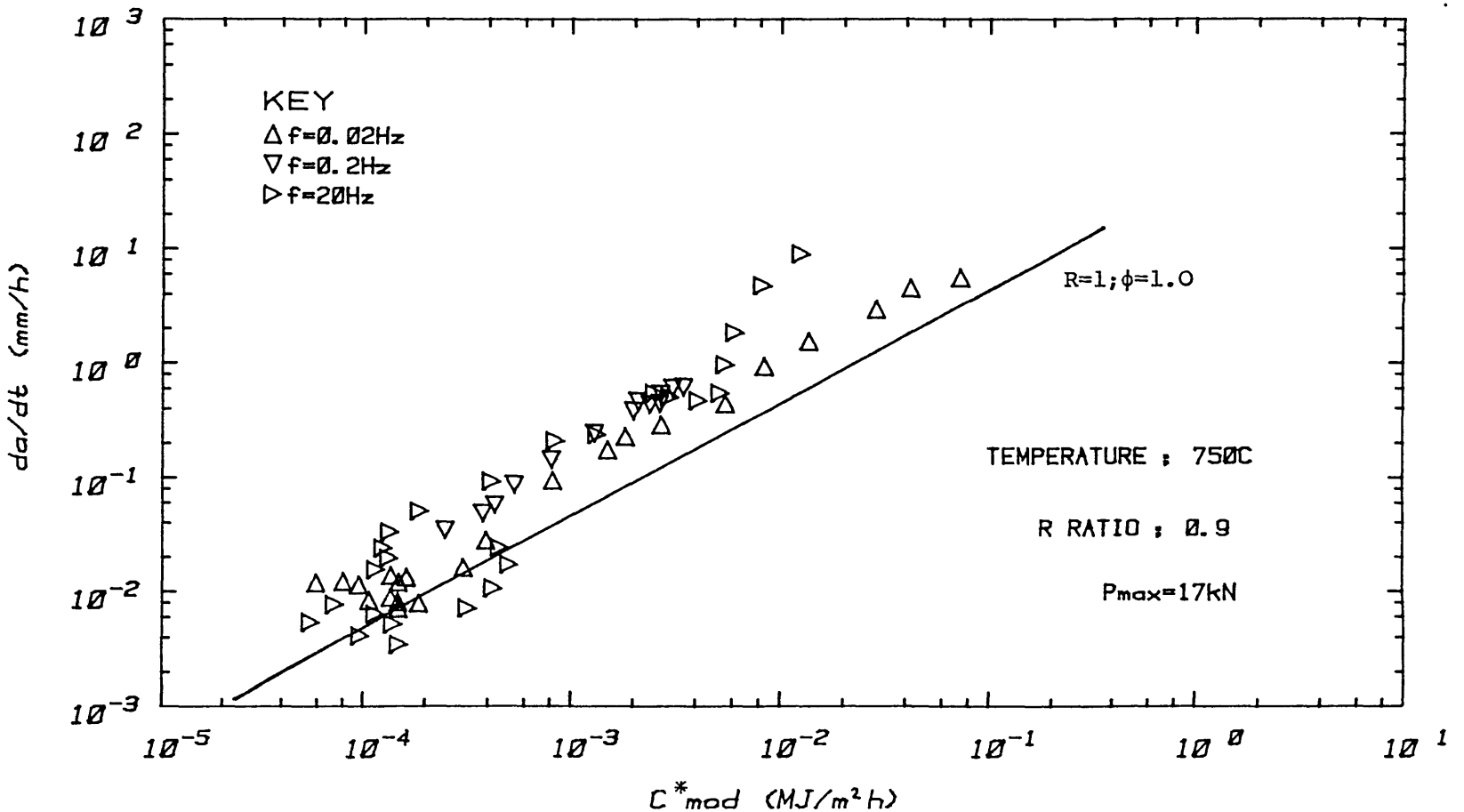


Fig. 9.34 Effect of frequency on crack growth rate at 750°C for R=0.9

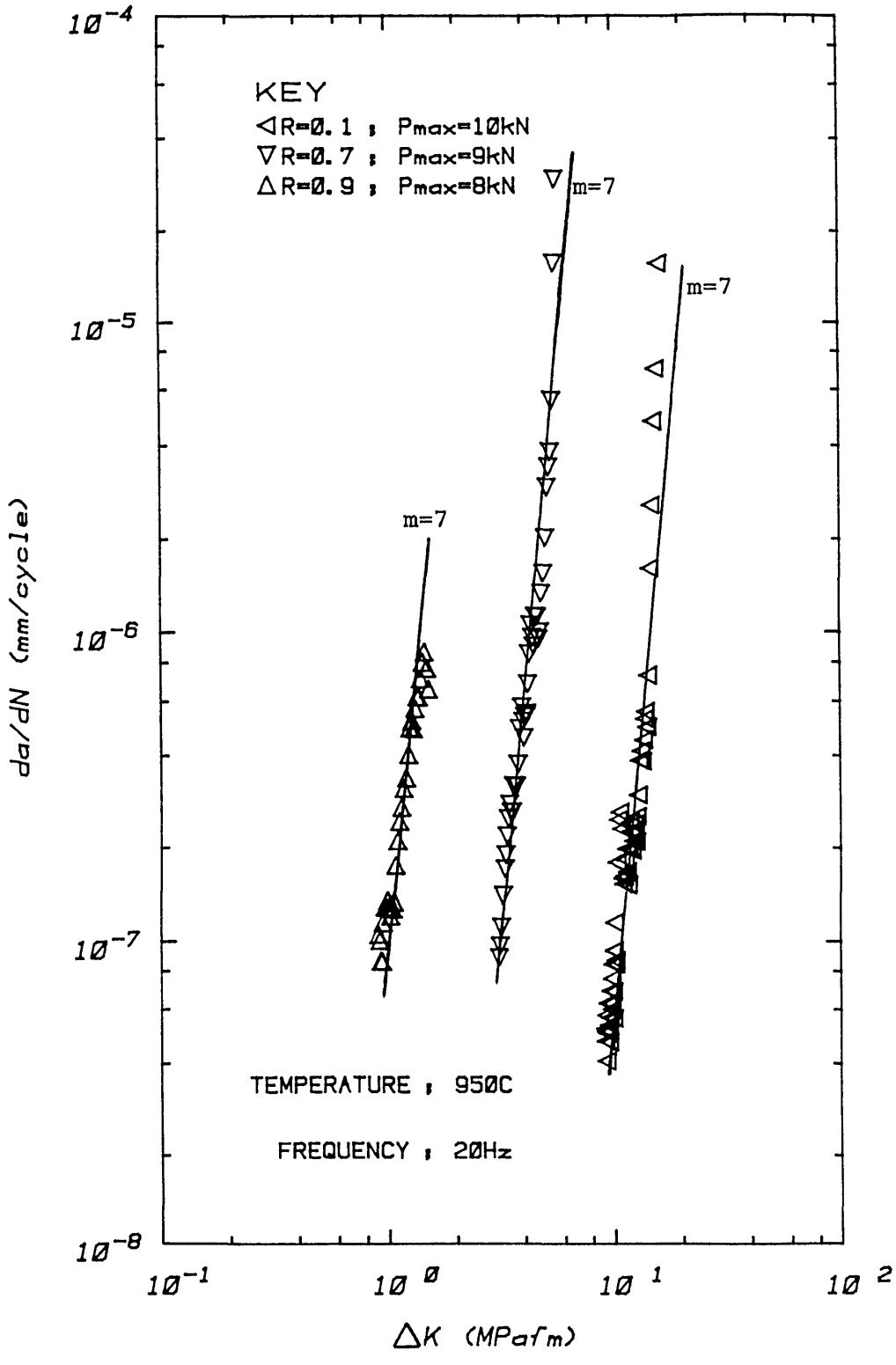


Fig. 9.35 Effect of R ratio on crack growth per cycle in the threshold region at 950°C

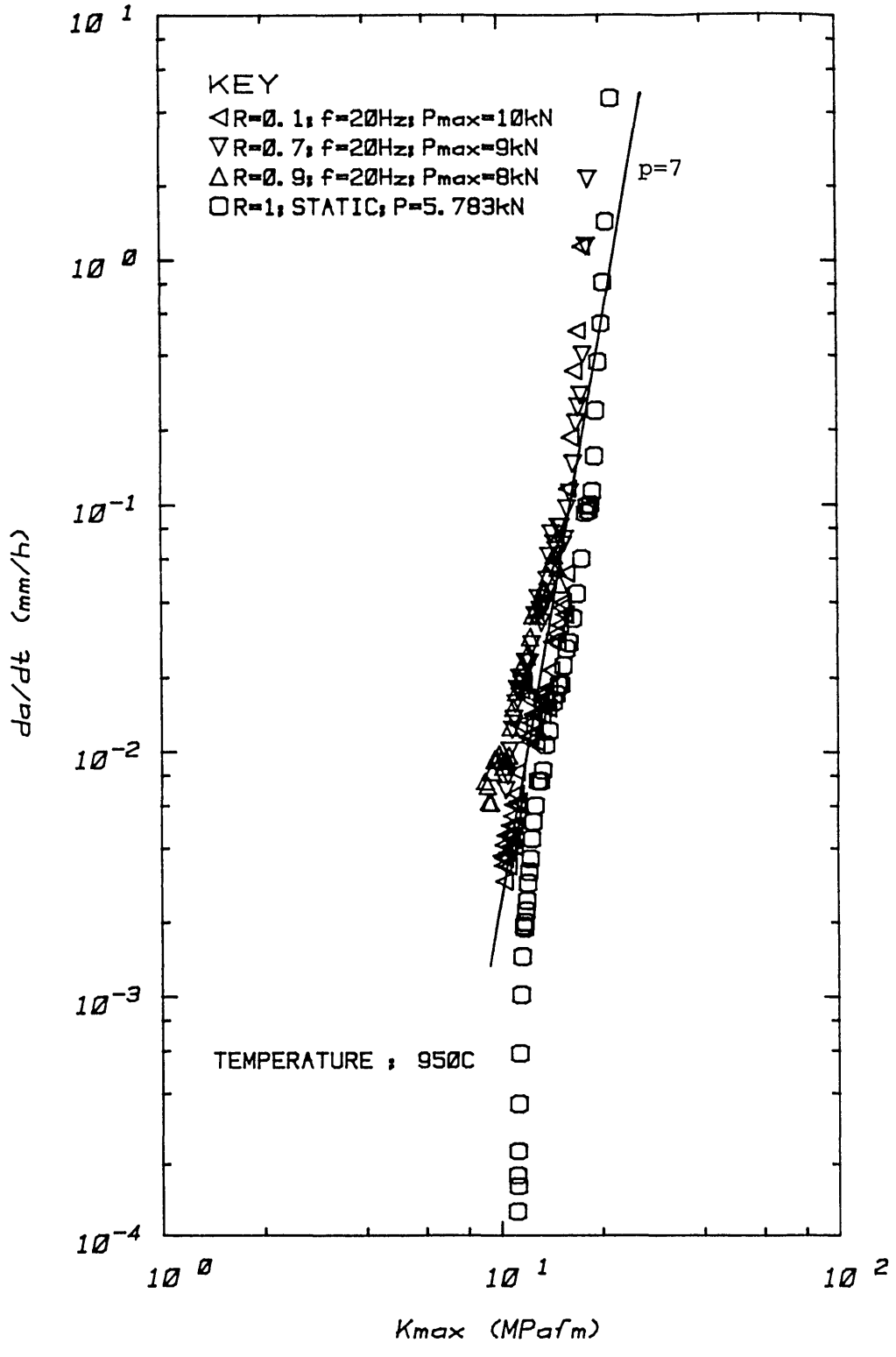


Fig. 9.36 Effect of R ratio on crack growth rate in the threshold region at 950°C

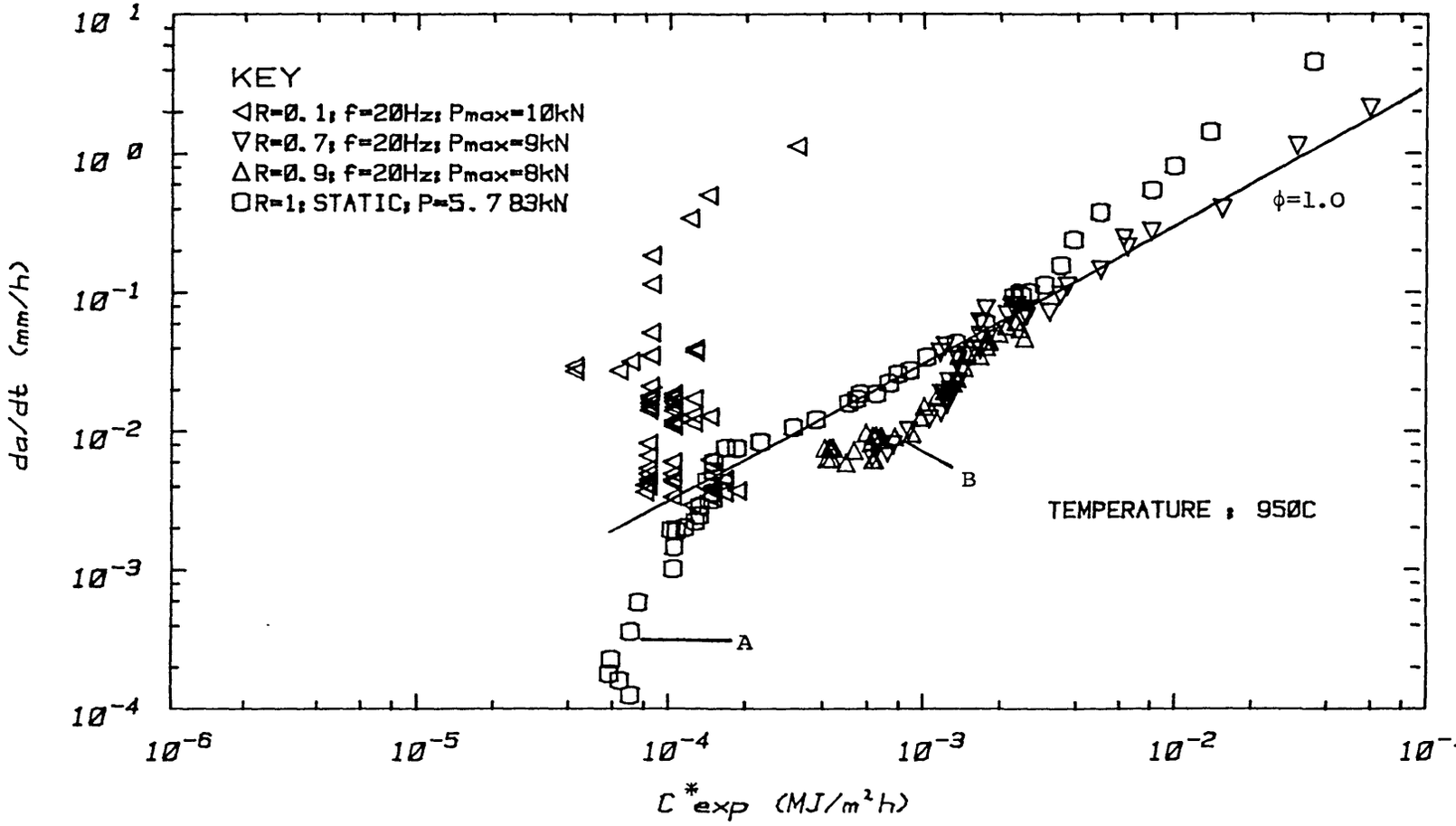


Fig. 9.37 Crack growth rates plotted against C^*_{exp} for the threshold region at 950°C

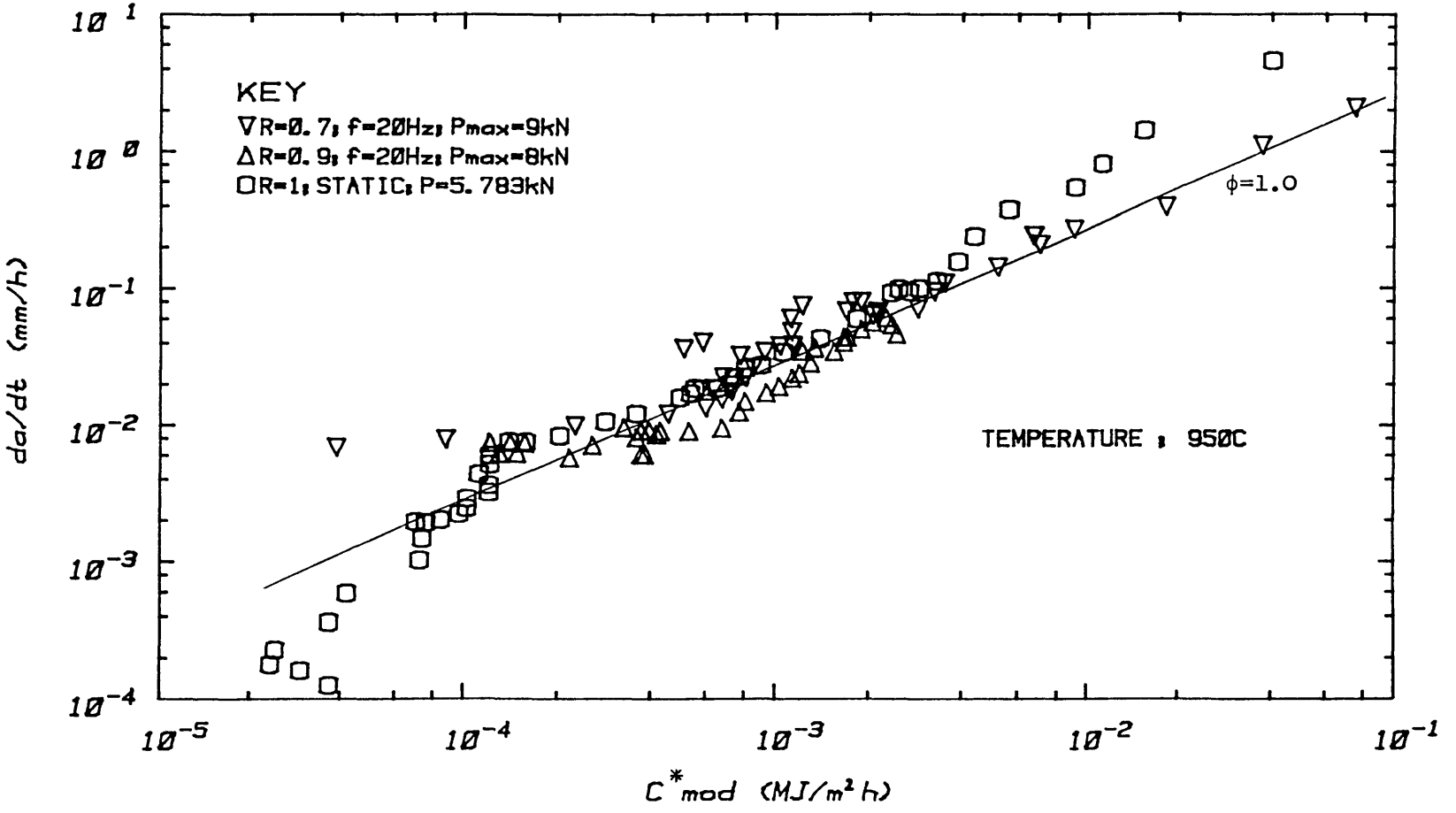


Fig. 9.38 Crack growth rates plotted against C^*_{mod} for the threshold region at 950°C

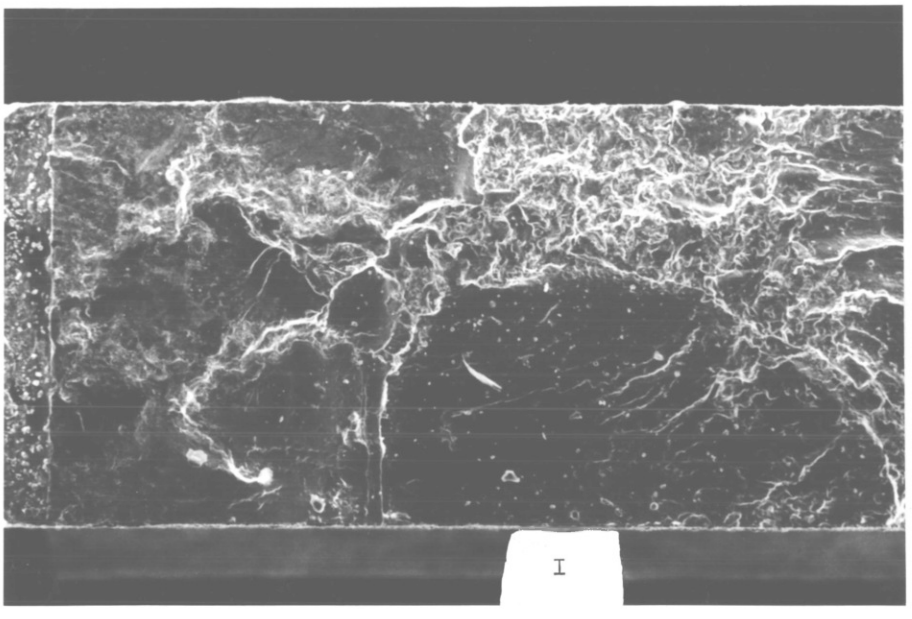
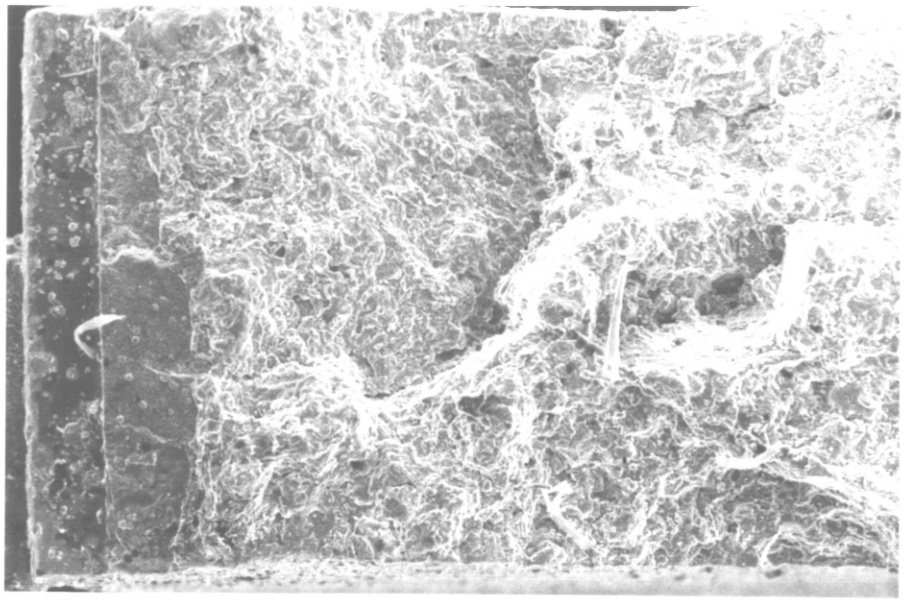
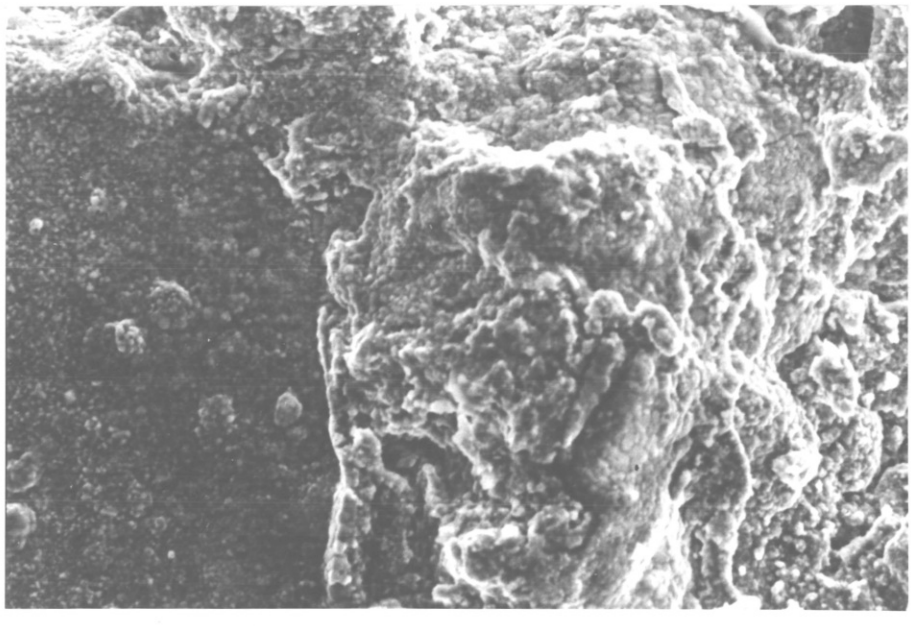


Fig. 9.39 Fracture surface of a specimen tested at R=0.1 in the threshold region at 950^{o}C,x40. Note the possible initiation site,I,on the side of the specimen.

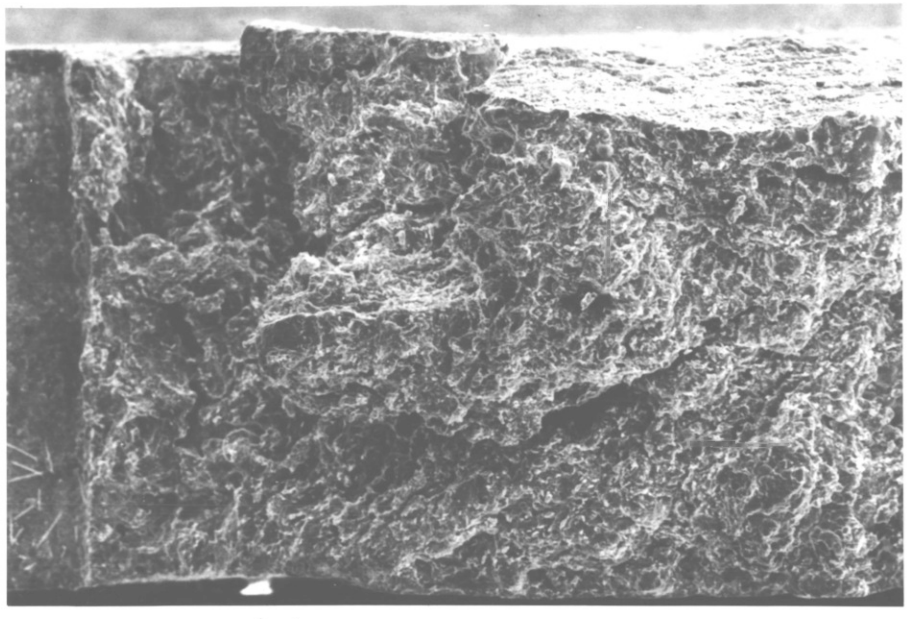


(a) Notch/pre-crack/R=0.9,x54

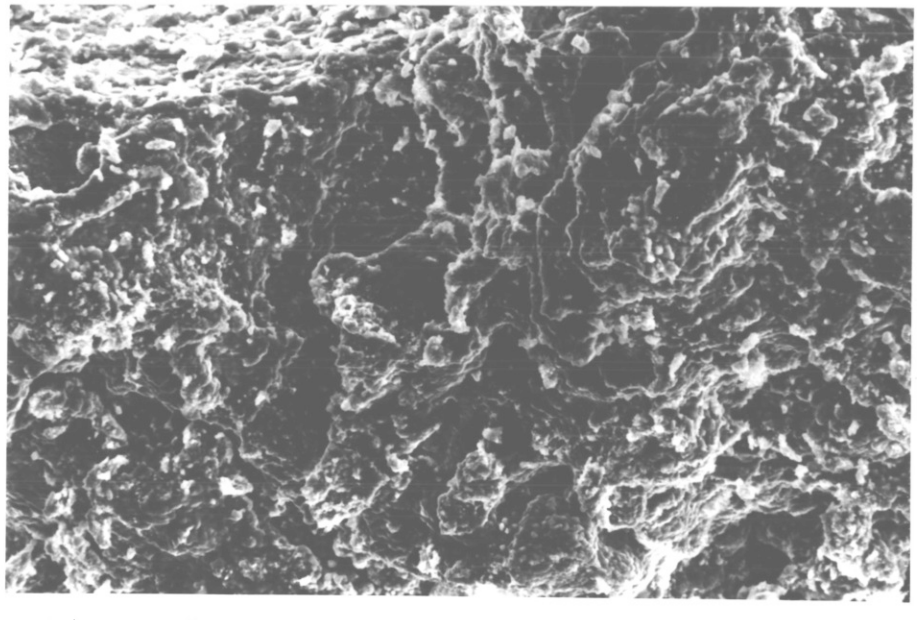


(b) Pre-crack/R=0.9,x300

Fig. 9.40 Fracture surface of a specimen tested at R=0.9 in the threshold region at 950°C.

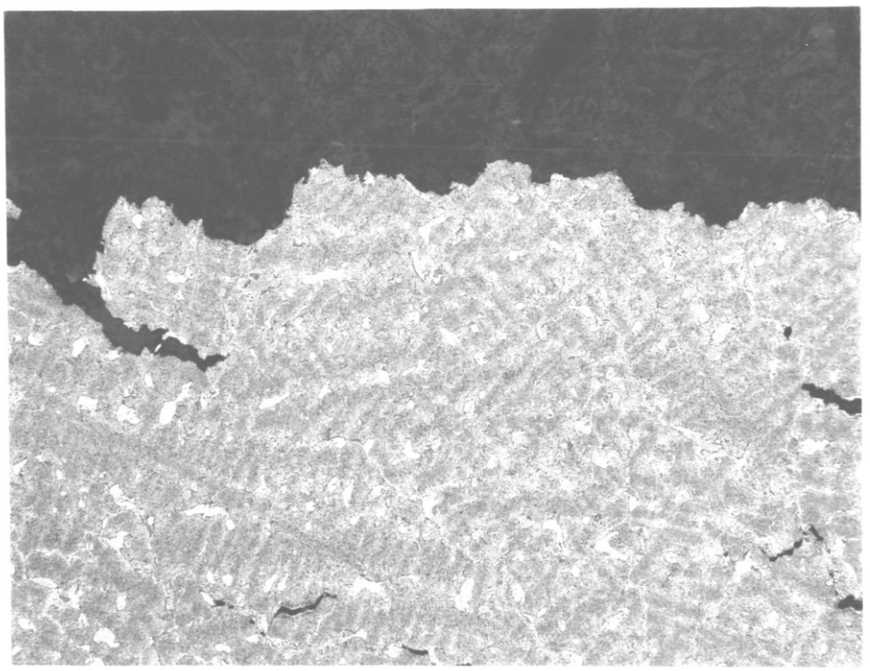


(a) Notch and R=1,x54

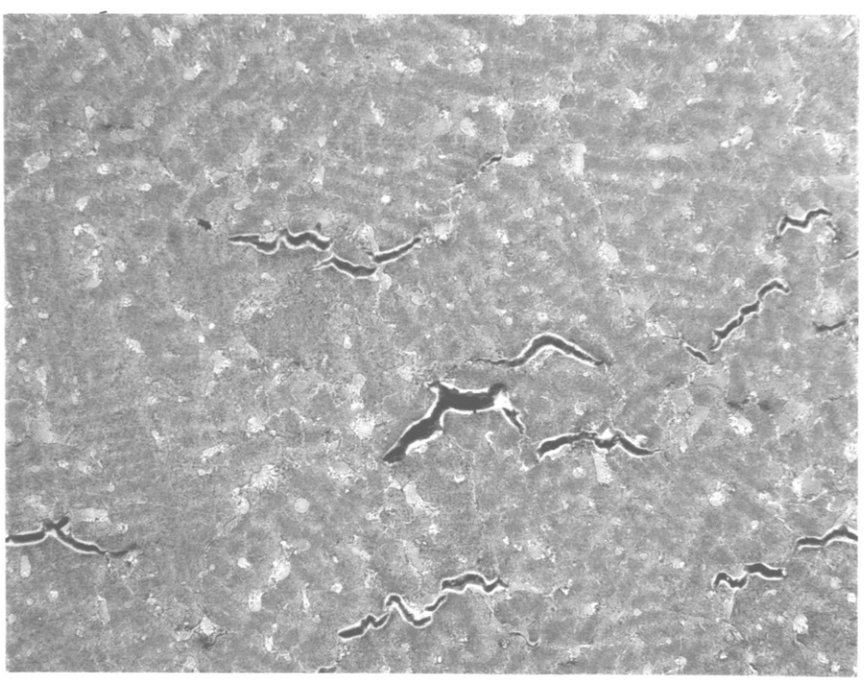


(b) R=1,x300

Fig. 9.41 Fracture surface of a specimen tested at R=1 and 950°C.

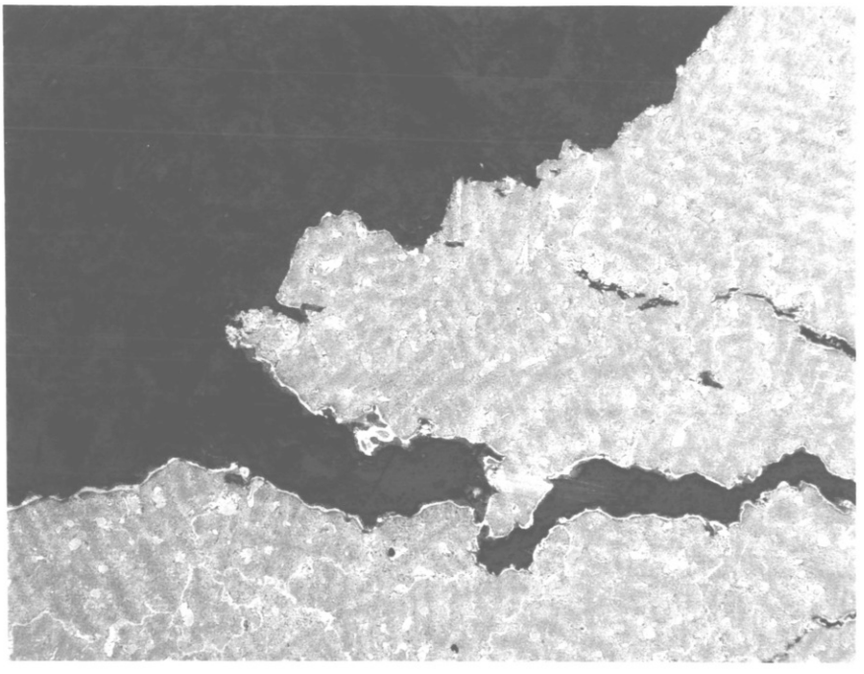


(a) Crack branching and damage accumulation in the vicinity of the main crack,x50

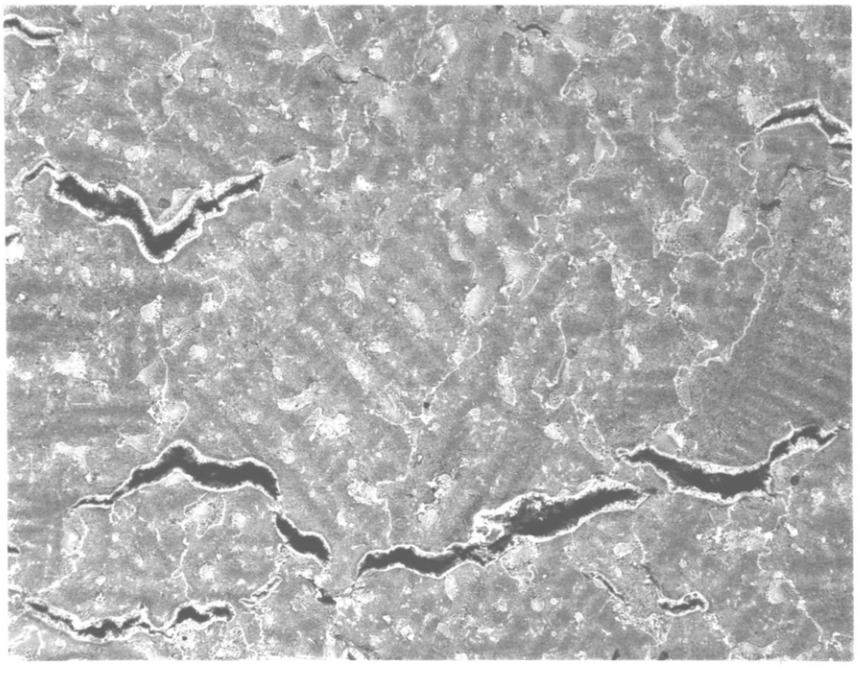


(b) Damage accumulation in the specimen gauge section remote from the main crack,x50.

Fig. 9.42 Optical micrographs of a specimen tested at R=0.9 in the threshold region at 950^{o}C.



(a) Crack branching and damage accumulation in the vicinity of the main crack,x50



(b) Damage accumulation in the specimen gauge section remote from the main crack,x50

Fig. 9.43 Optical micrographs of a specimen tested under static loading (R=1) at 950^{o}C

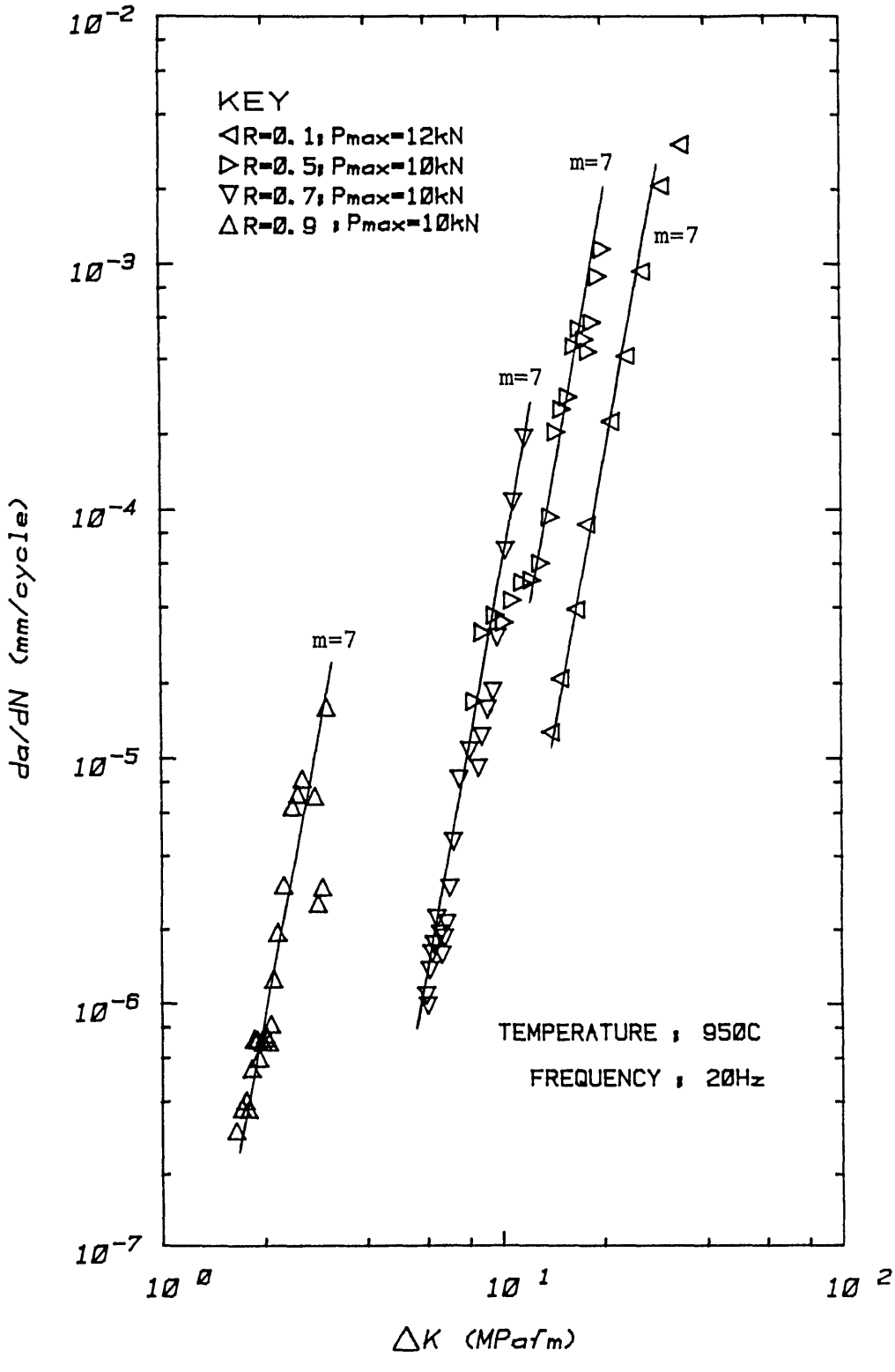


Fig. 9.44 Effect of R ratio on crack growth per cycle at 950°C

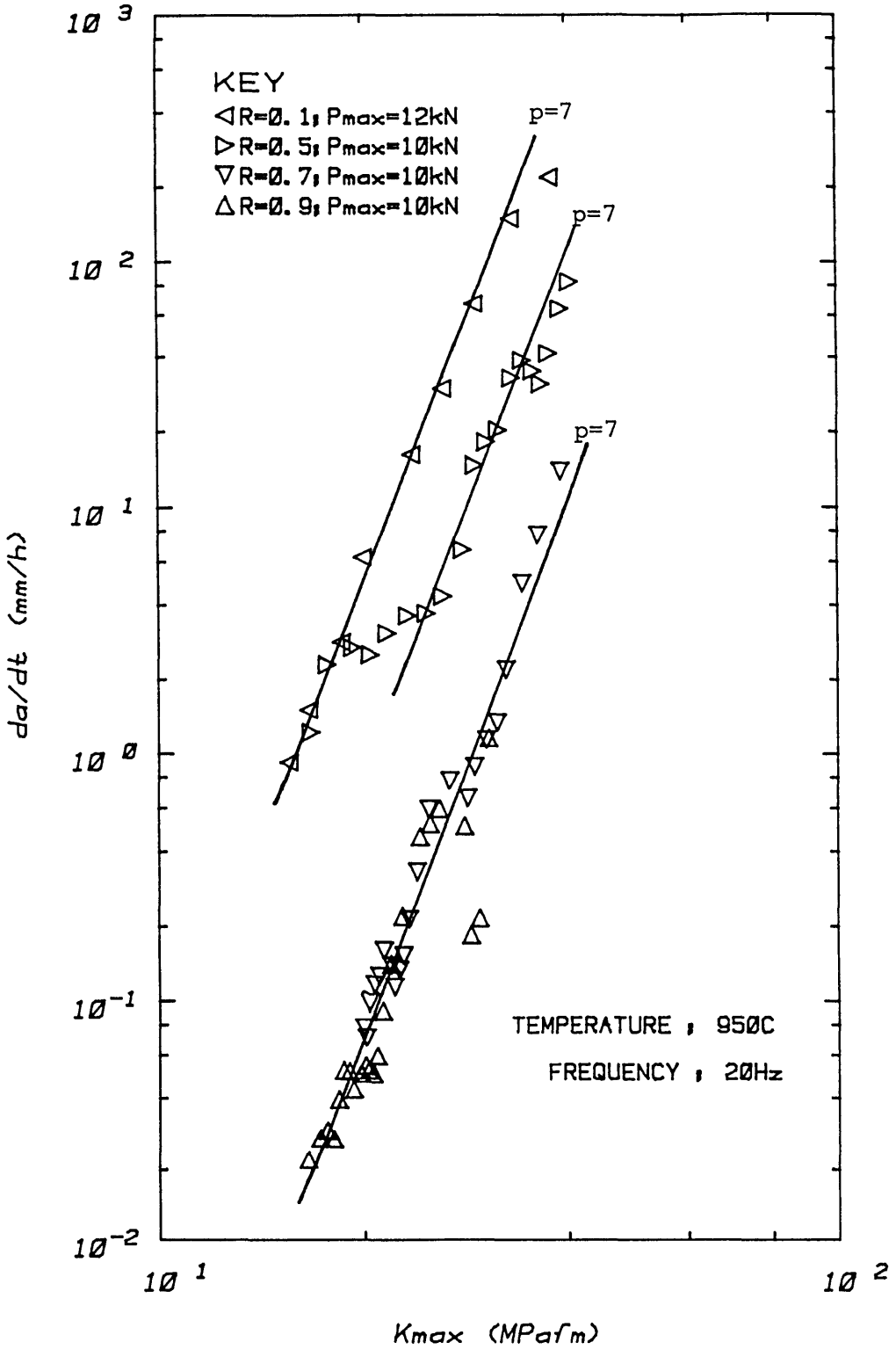


Fig. 9.45 Effect of R ratio on crack growth rate at 950°C

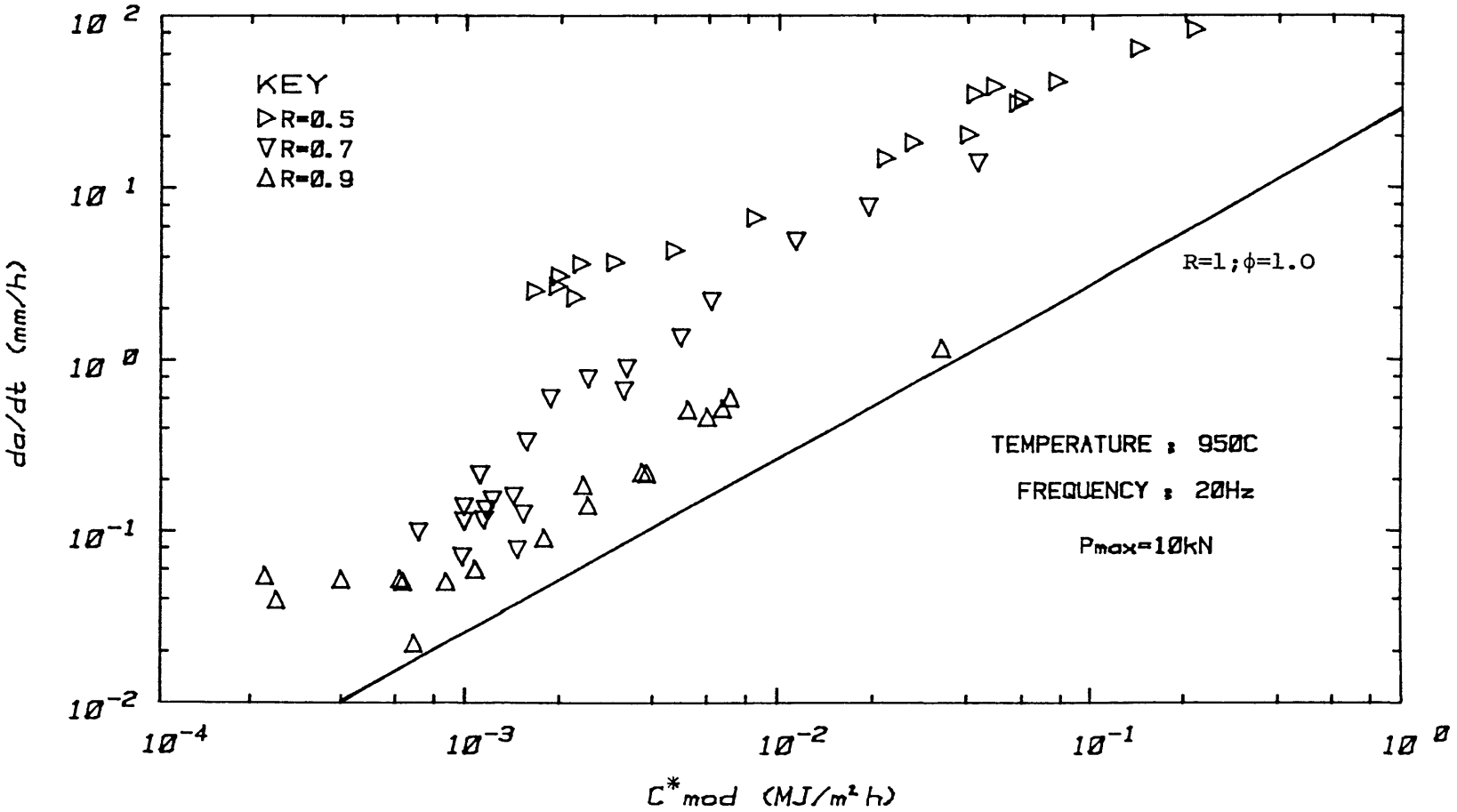


Fig. 9.46 Effect of R ratio on crack growth rate at 950°C

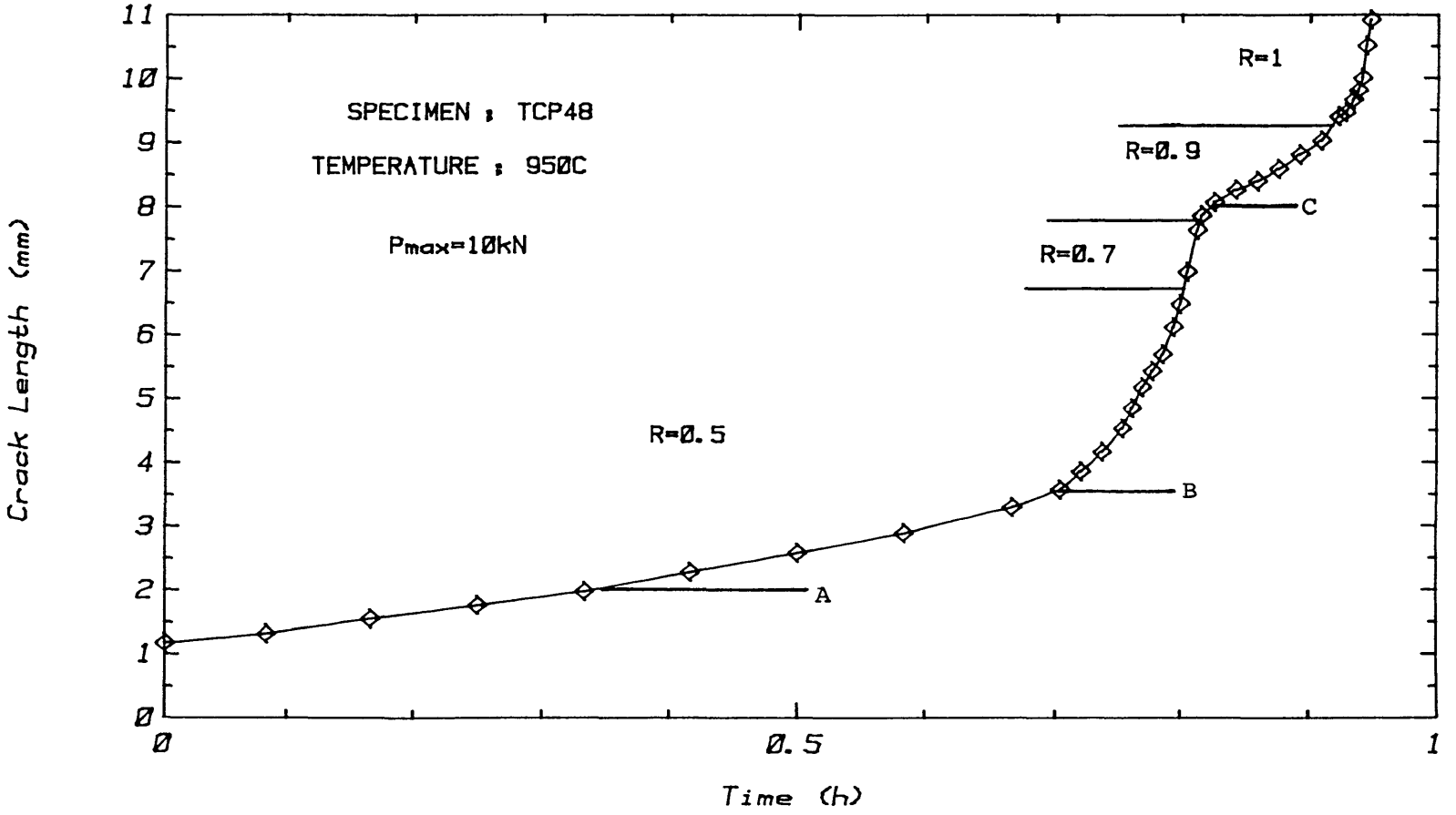


Fig. 9.47 Effect of changing the R ratio during a crack growth test at 950°C

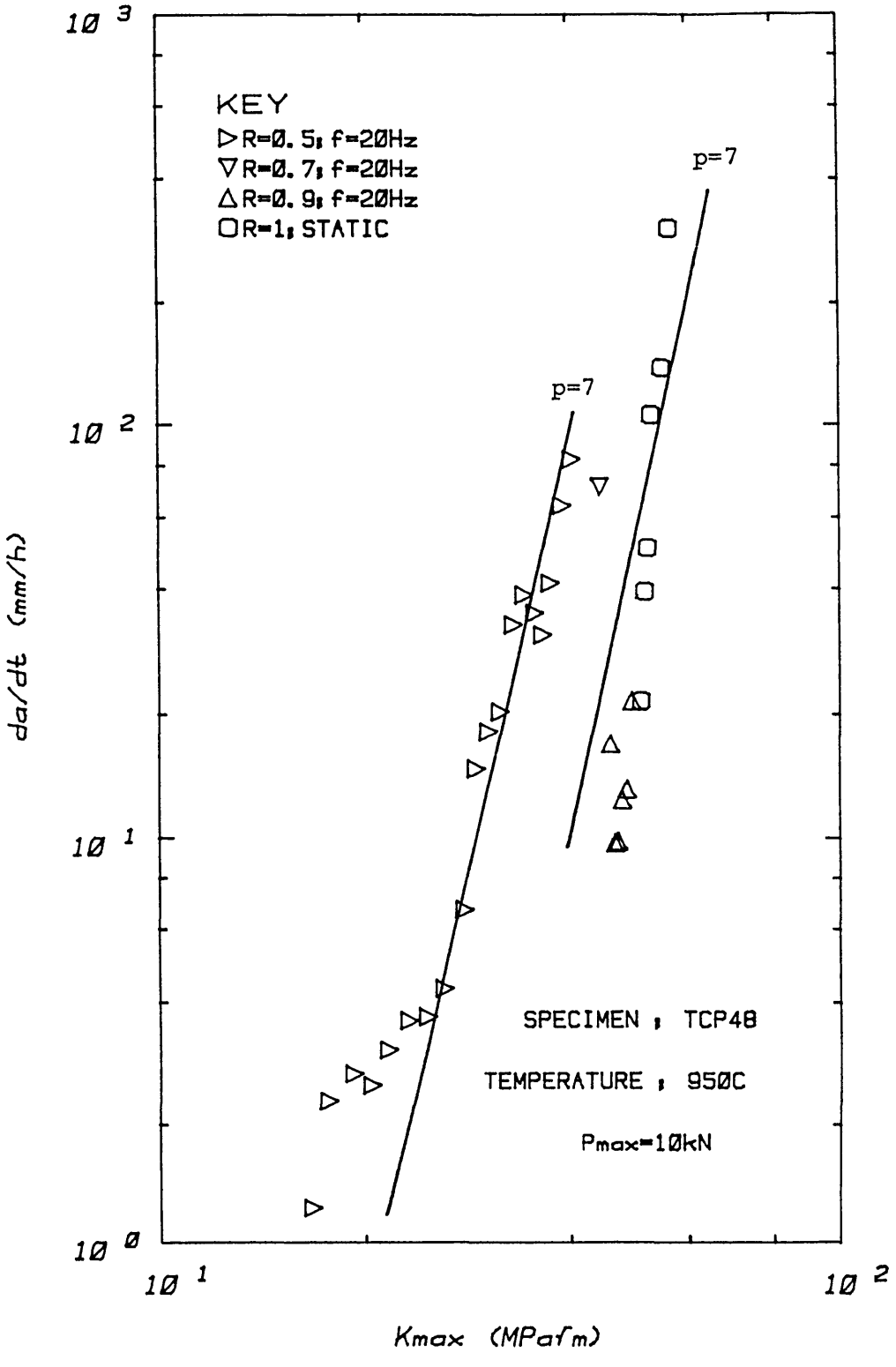


Fig. 9.48 Effect on crack growth rate of changing the R ratio during a test at 950°C

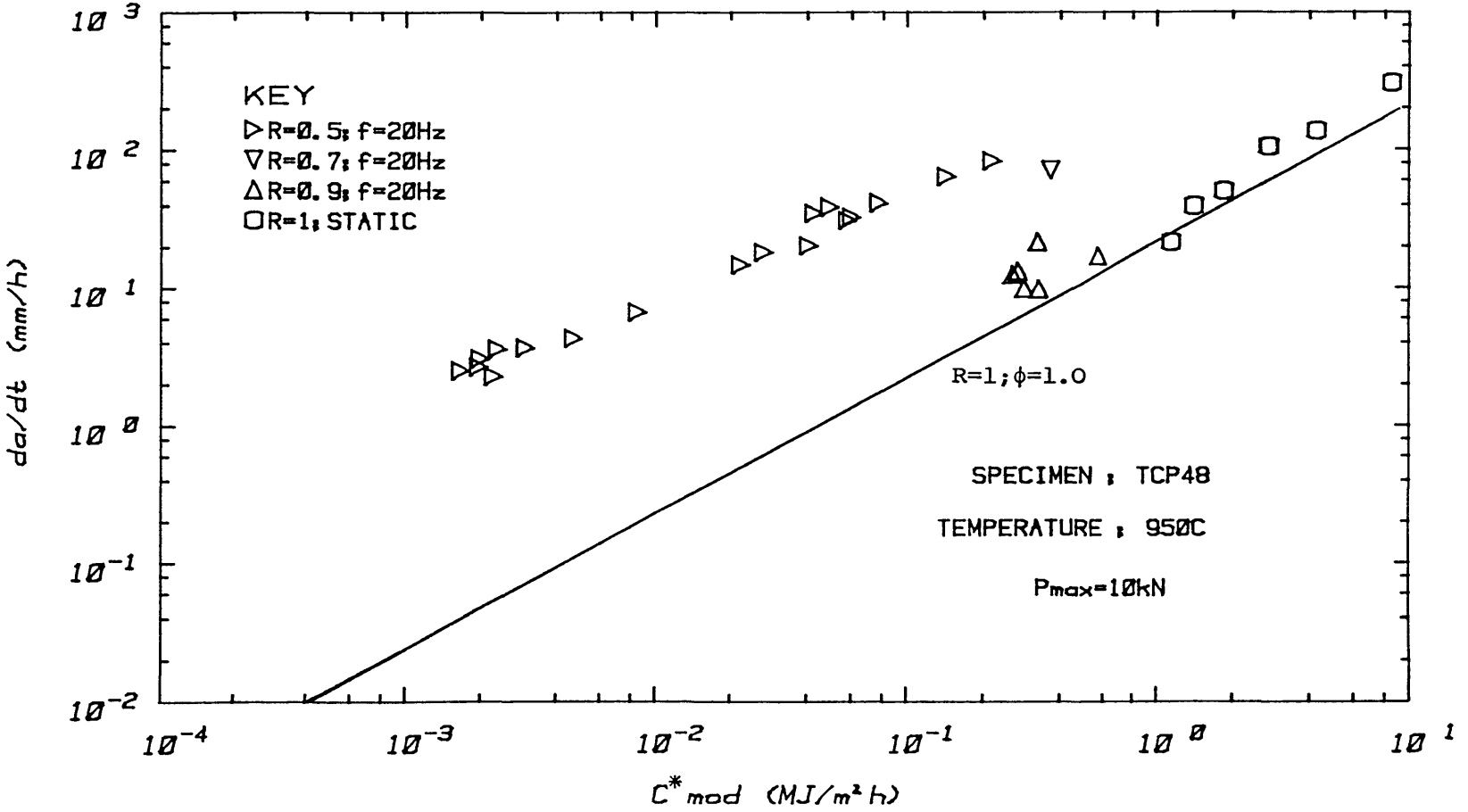


Fig. 9.49 Effect on crack growth rate of changing the R ratio during a test at 950°C

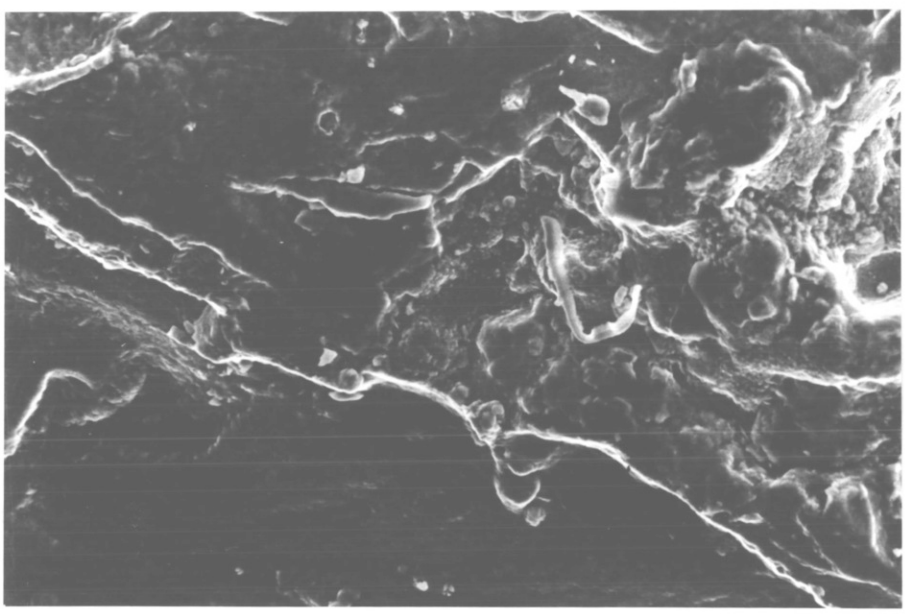
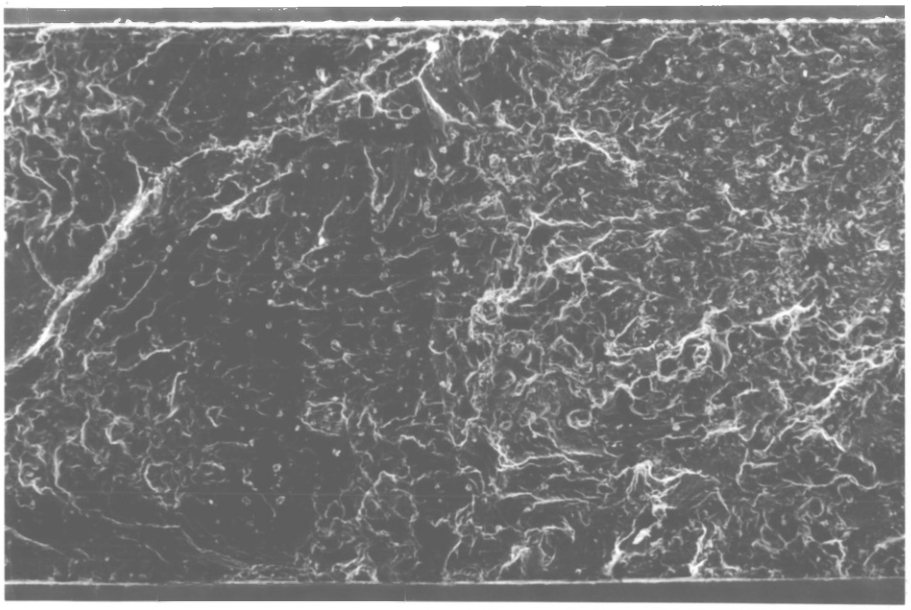
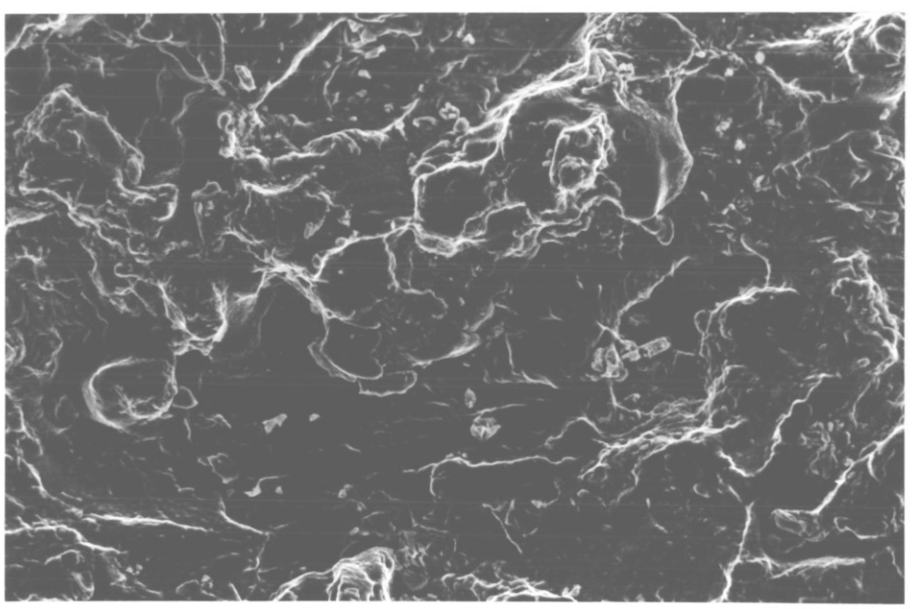


Fig. 9.50 Fracture surface of specimen TCP48 tested at 950°C. Crack length approx. 2mm corresponding to point A of figure 9.47; R=0.5,x300

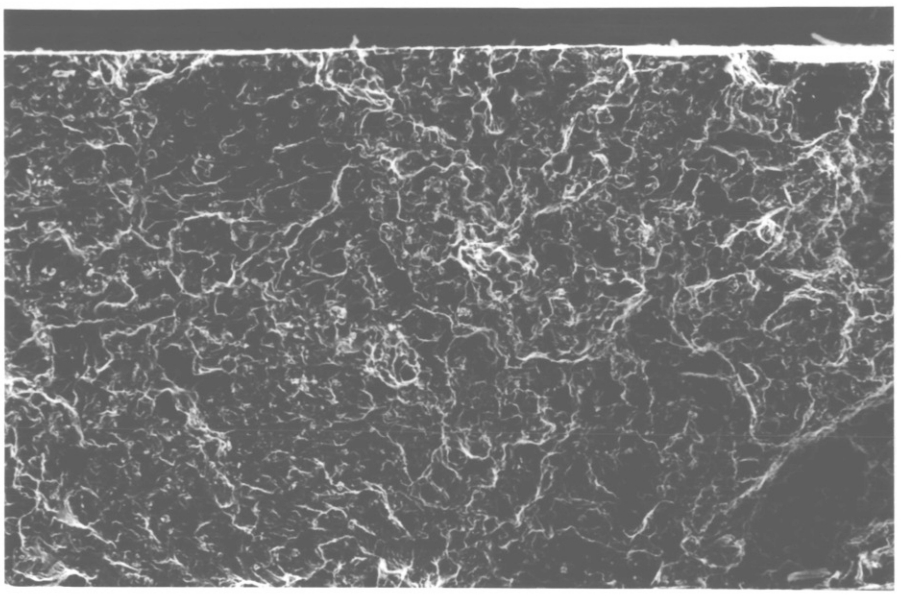


(a) x54

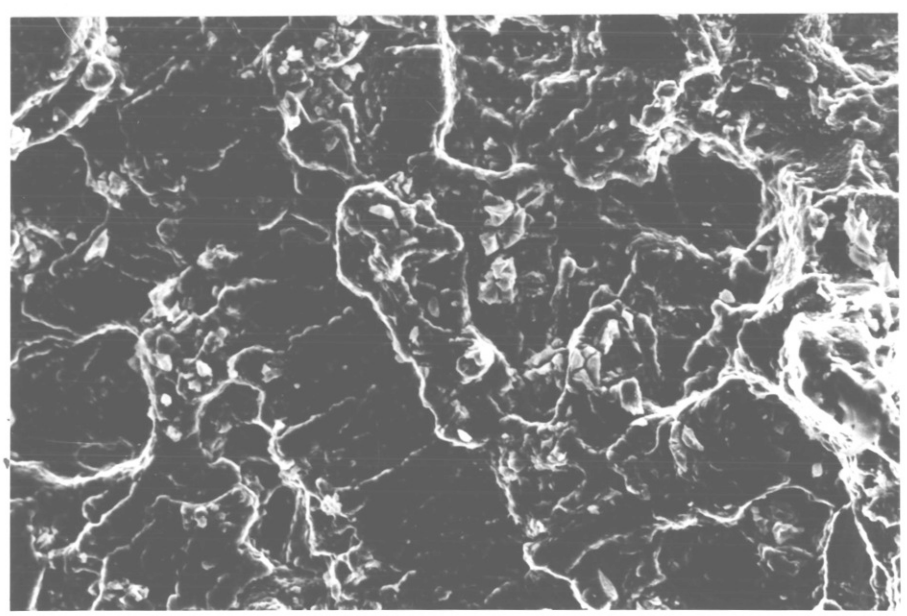


(b) x200

Fig.9.51 Fracture surface of specimen TCP48 tested at 950°C. Crack length approx. 3.5mm corresponding to point B of figure 9.47 ; R=0.5



(a) x54



(b) x300

Fig. 9.52 Fracture surface of specimen TCP48 tested at 950°C. Crack length approx. 8mm corresponding to point C of figure 9.47 ; transition R=0.5→0.7→0.9→1

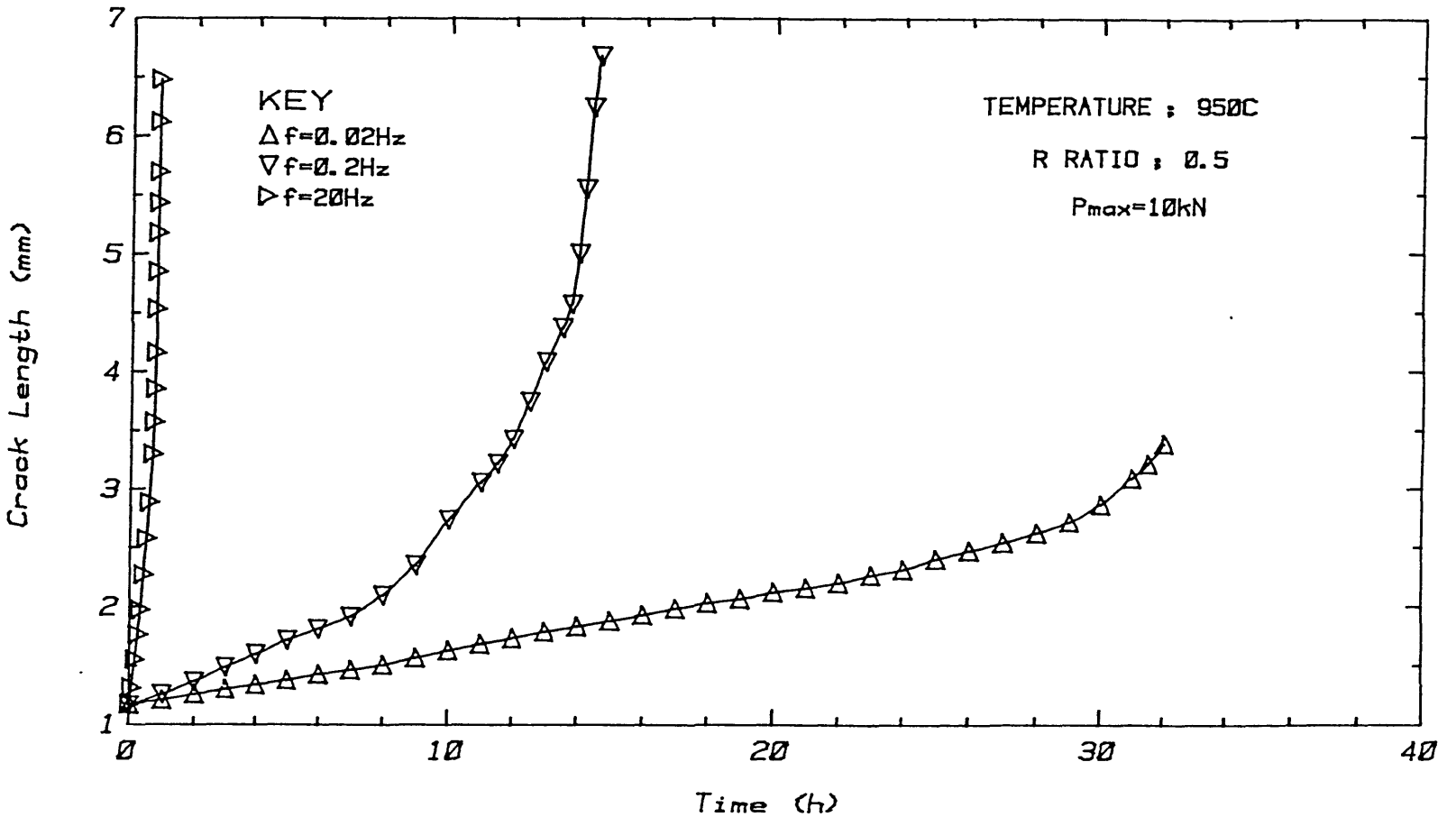


Fig. 9.53 Effect of frequency on crack growth at 950°C for R=0.5

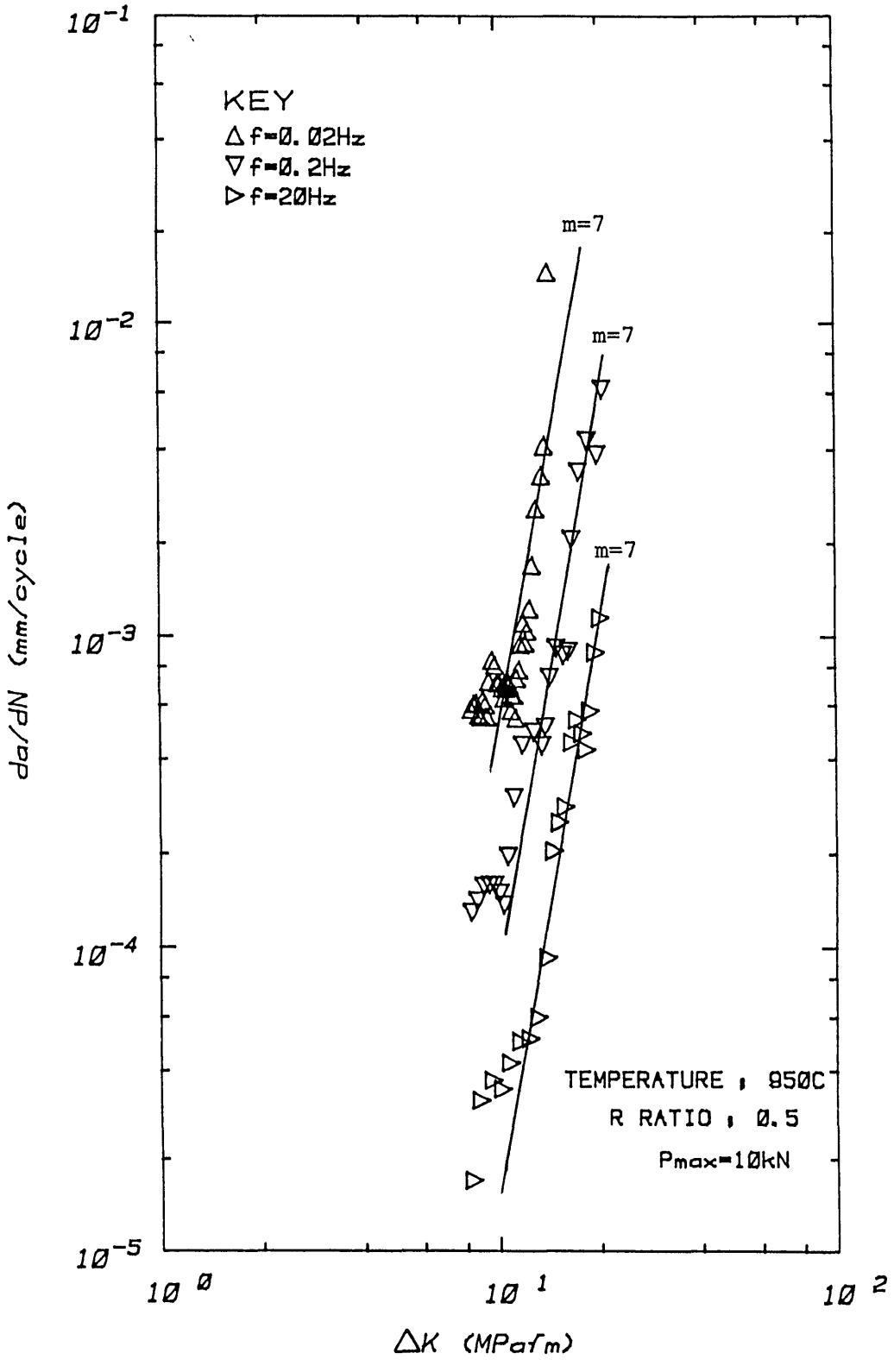


Fig. 9.54 Effect of frequency on crack growth per cycle at 950°C for R=0.5

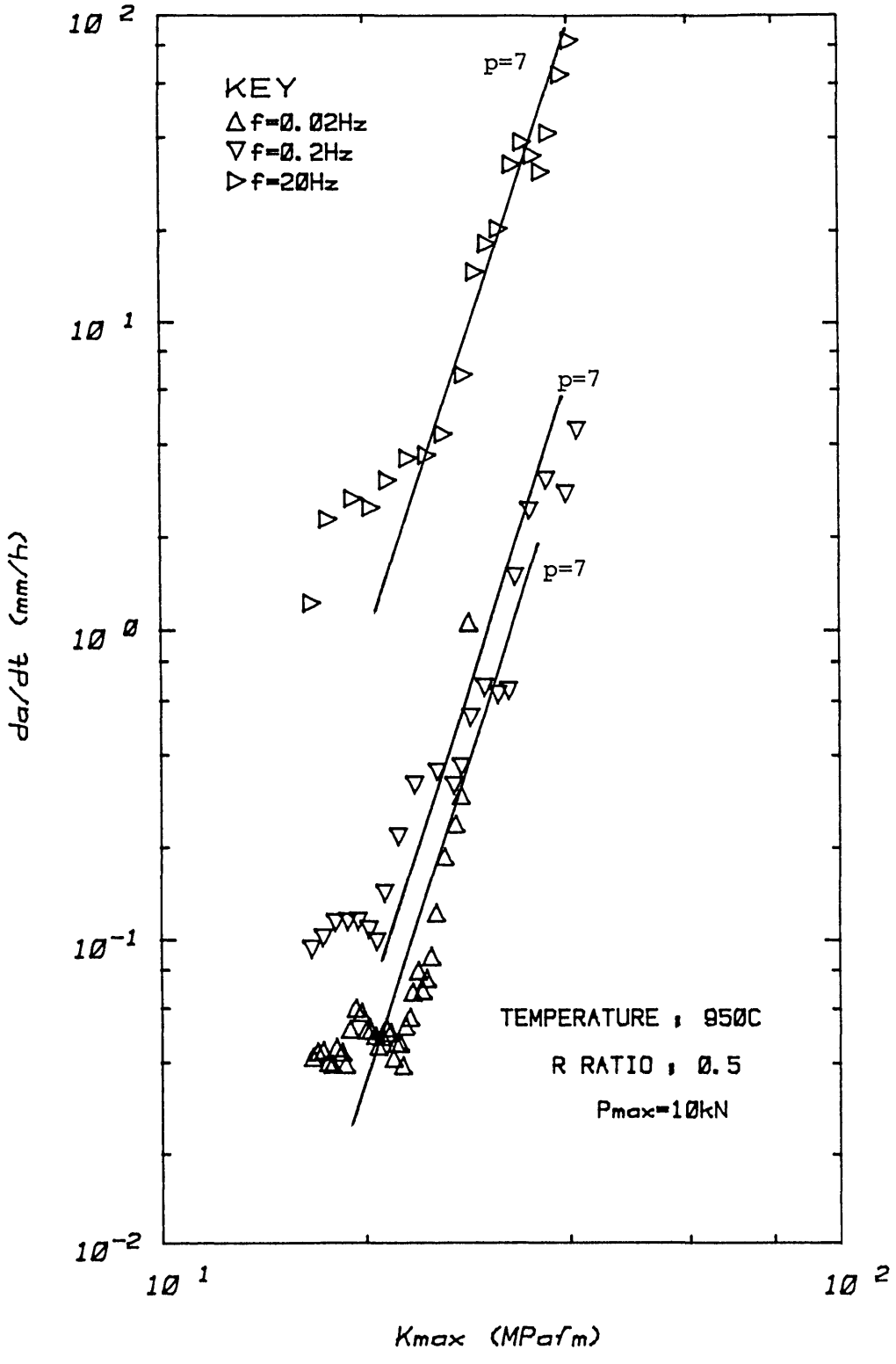


Fig. 9.55 Effect of frequency on crack growth rate at 950°C for R=0.5

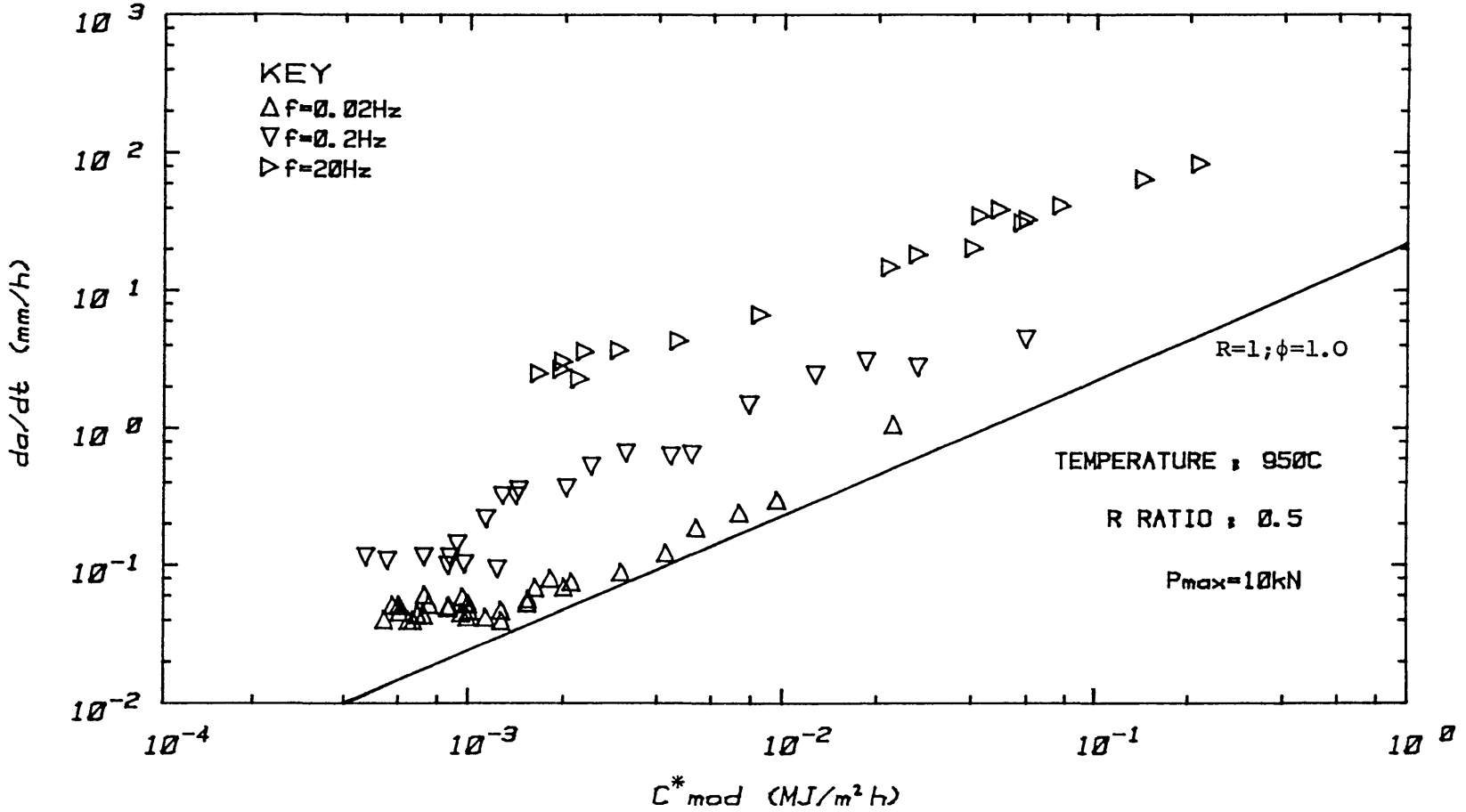


Fig. 9.56 Effect of frequency on crack growth rate at 950°C for R=0.5

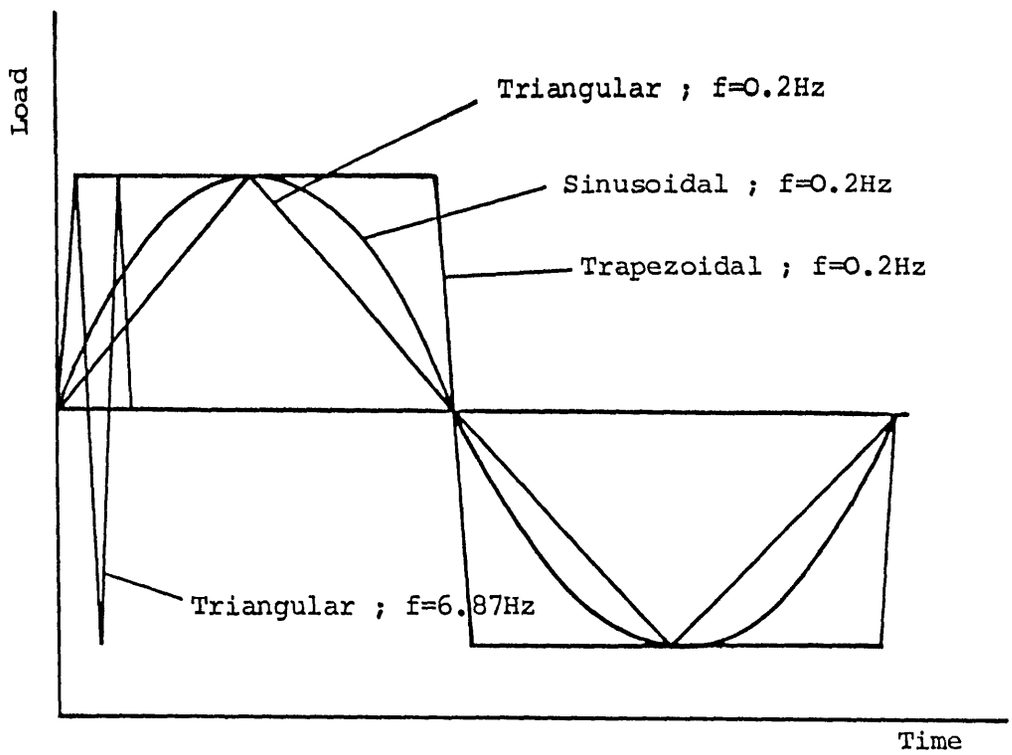


Fig. 9.57 Loading waveforms used to investigate the effect of loading waveform on crack growth at 950^{o}C for R=0.1

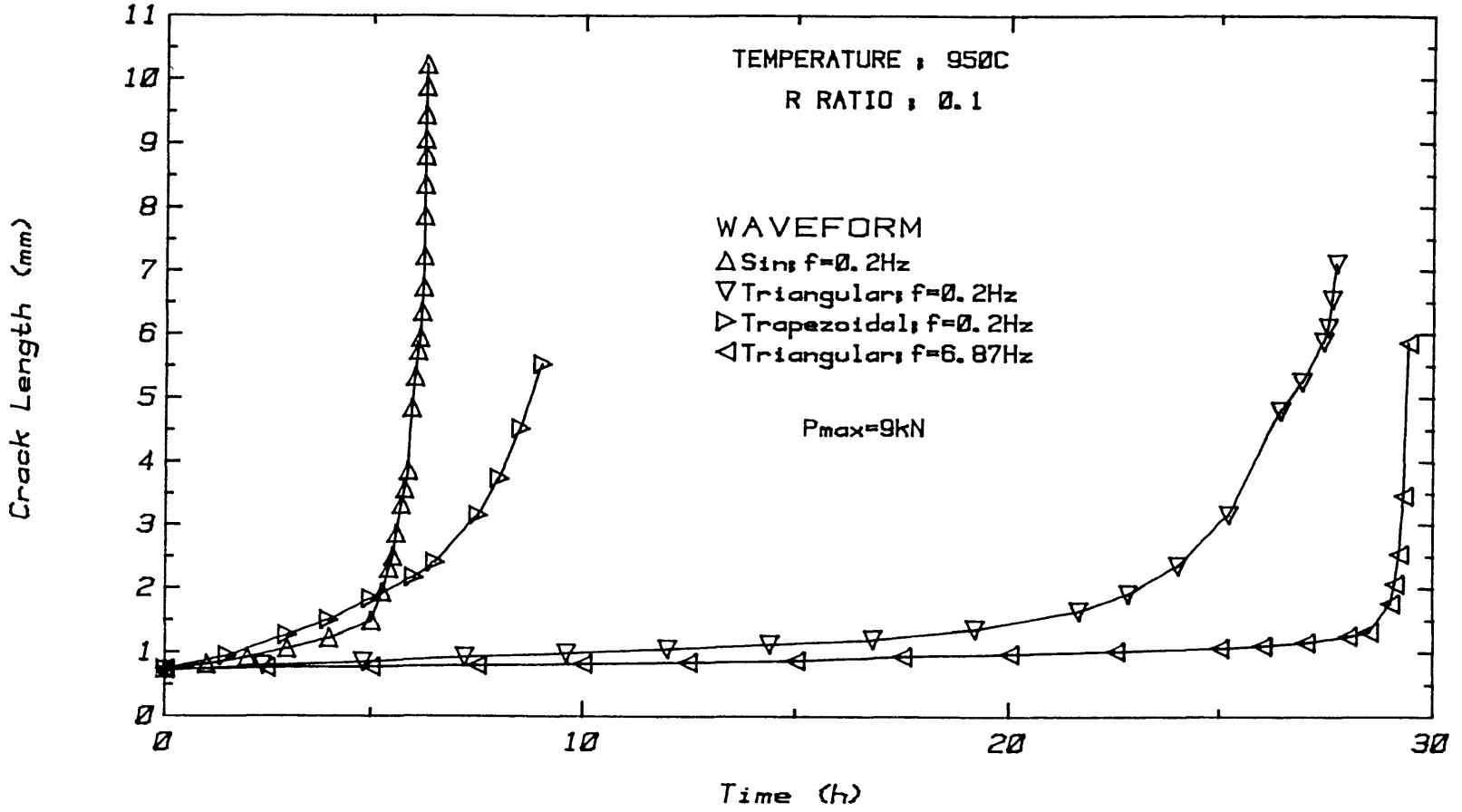


Fig. 9.58 Effect of loading waveform on crack growth at 950°C for R=0.1

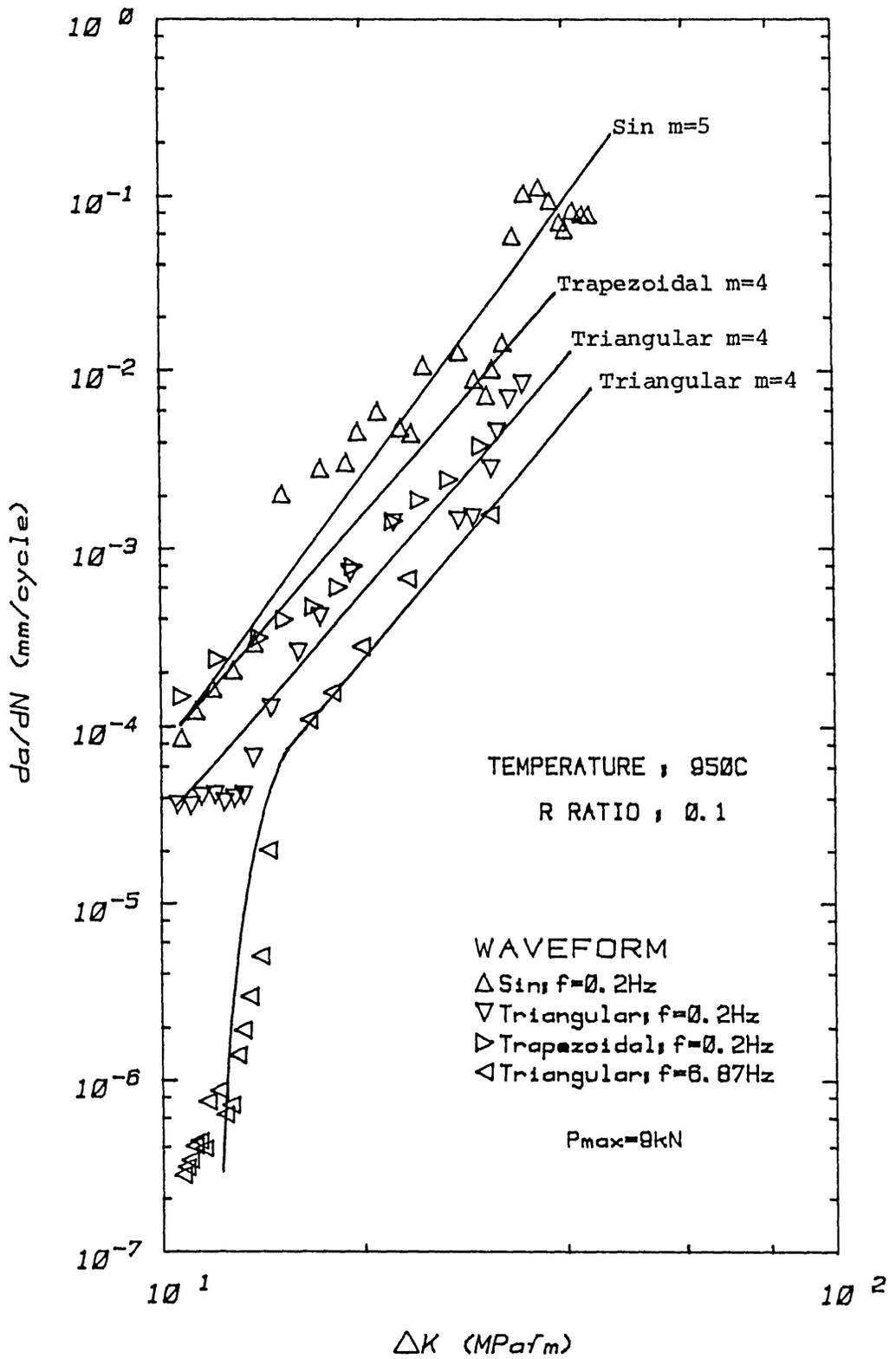


Fig. 9.59 Effect of loading waveform on crack growth per cycle at 950°C for R=0.1

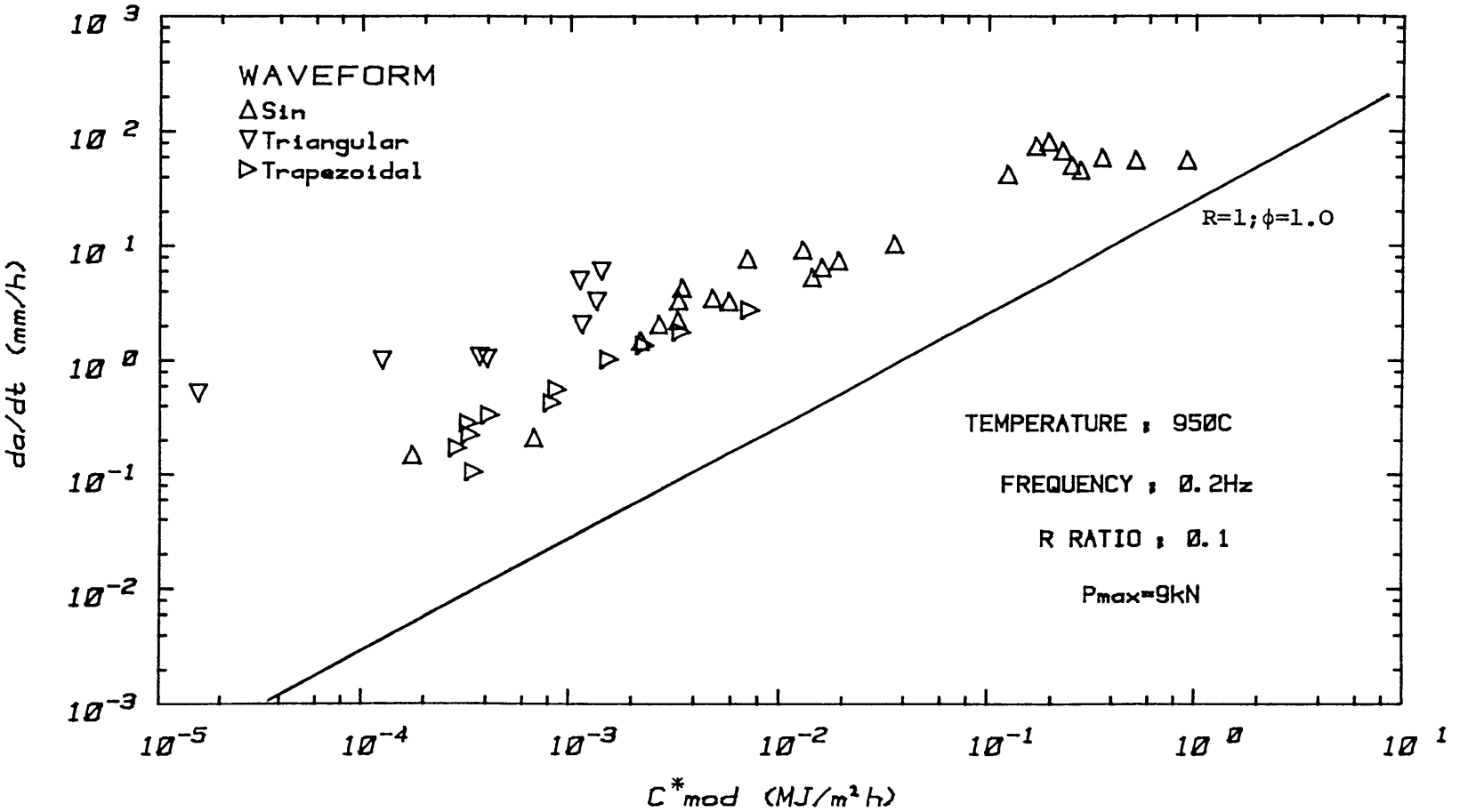


Fig. 9.60 Effect of loading waveform on crack growth rate at 950°C for R=0.1

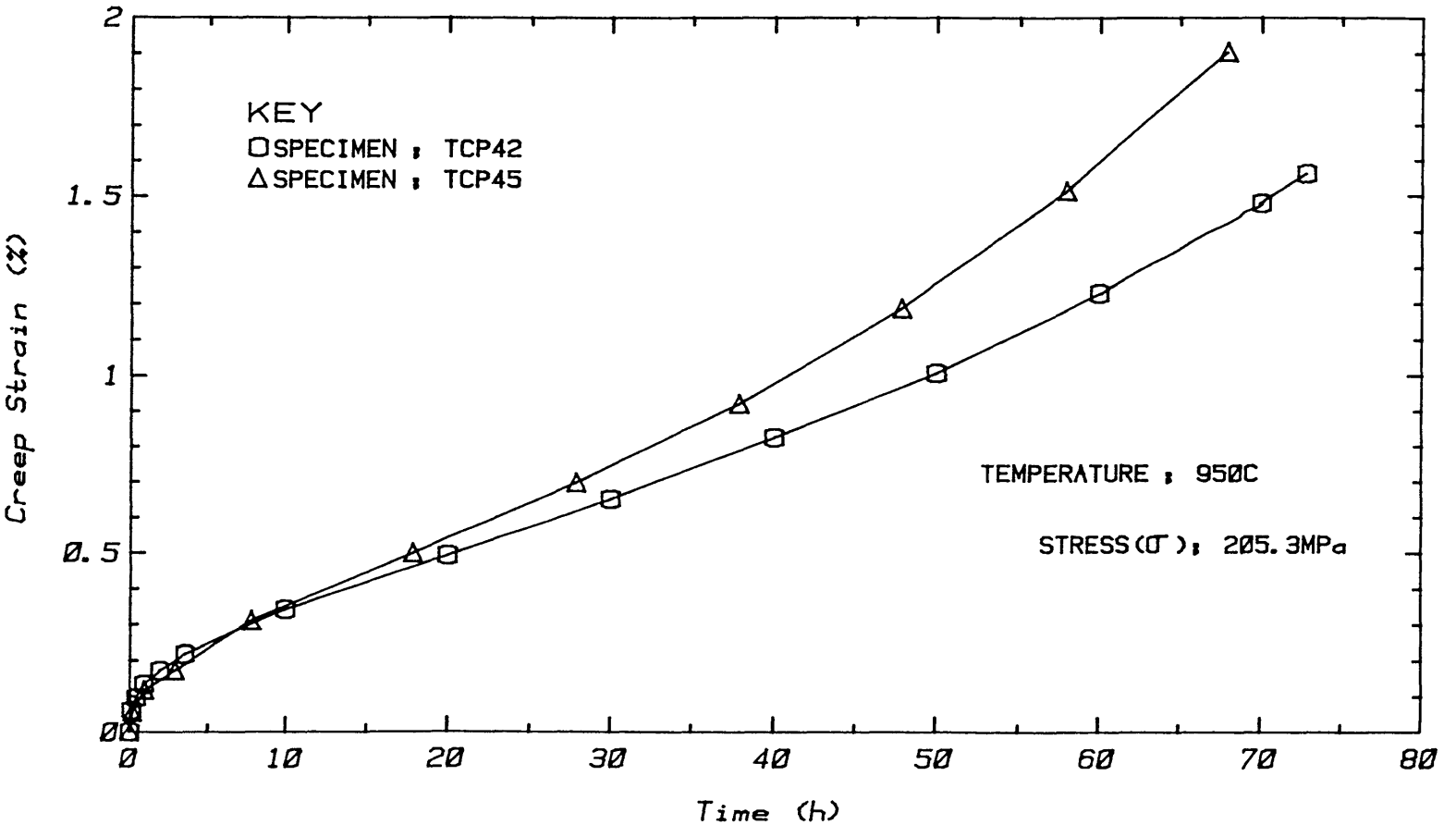


Fig. 9.61 Introducing creep damage into TCP crack growth specimens at 950°C

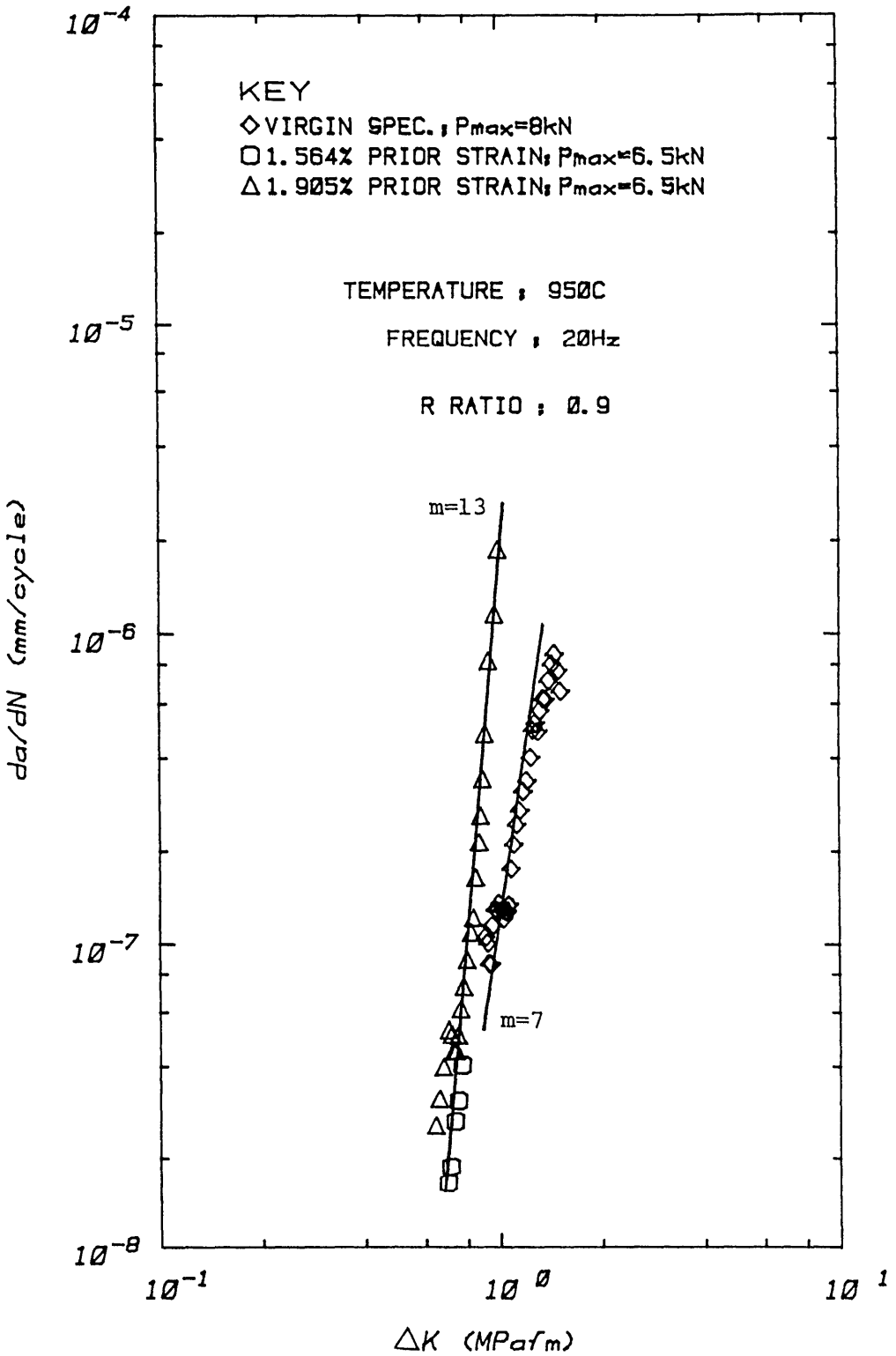


Fig. 9.62 Effect of prior creep damage on crack growth per cycle at 950°C for R=0.9

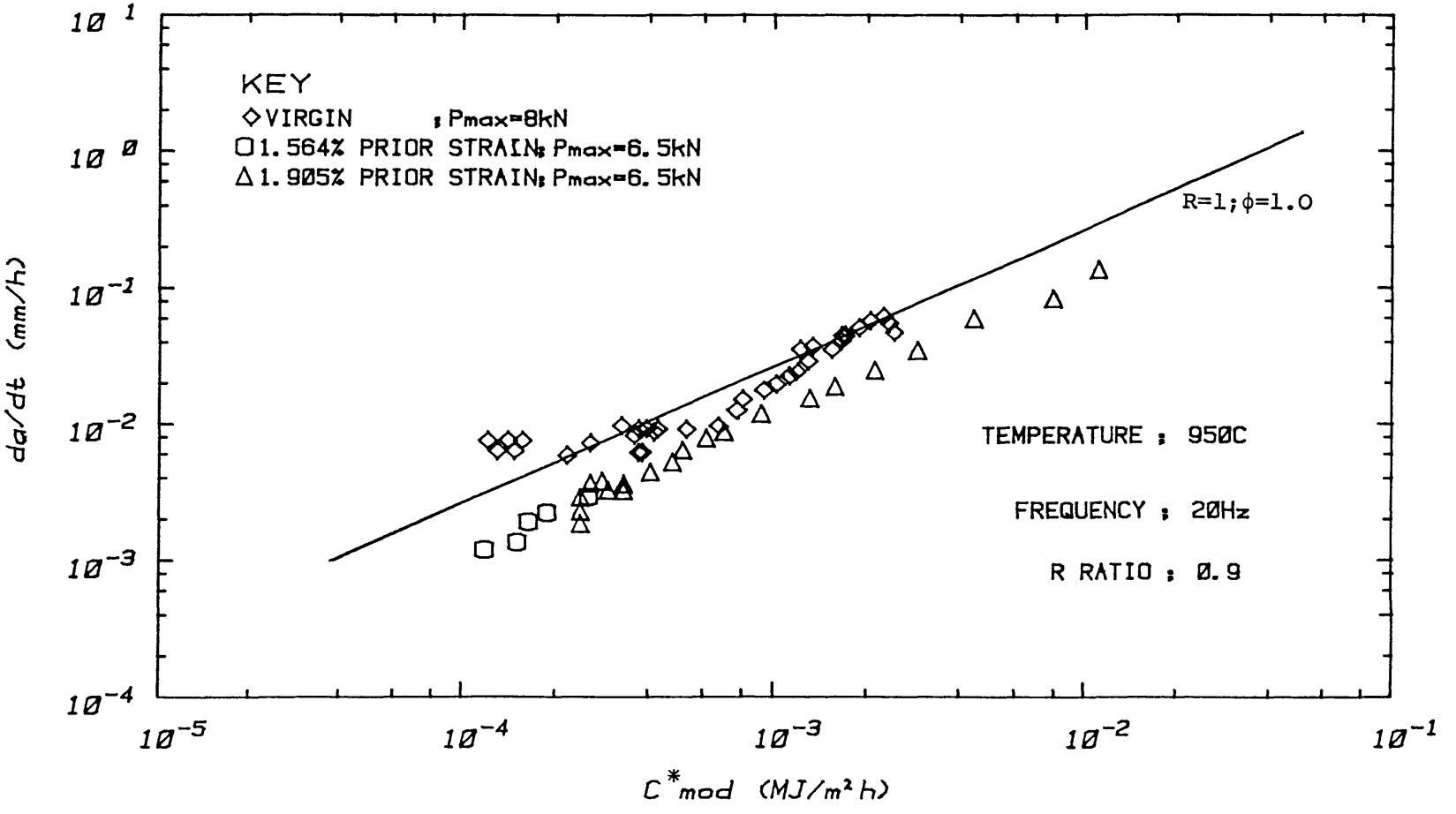
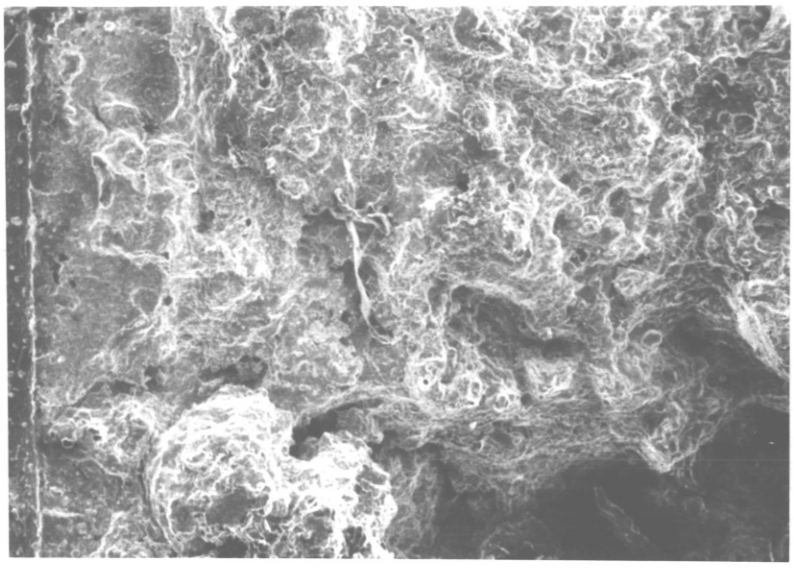
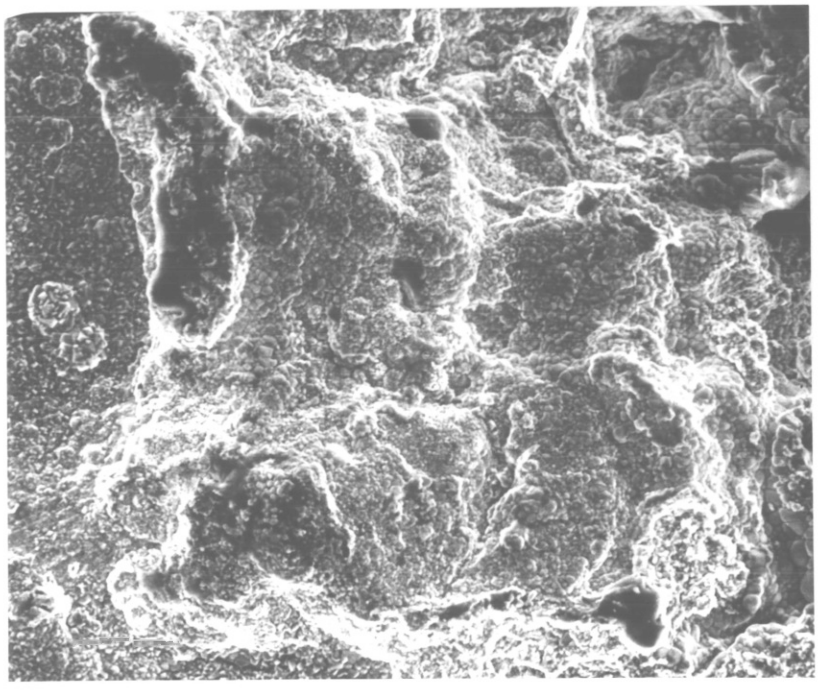


Fig. 9.63 Effect of prior creep damage on crack growth rates at 950°C for R=0.9

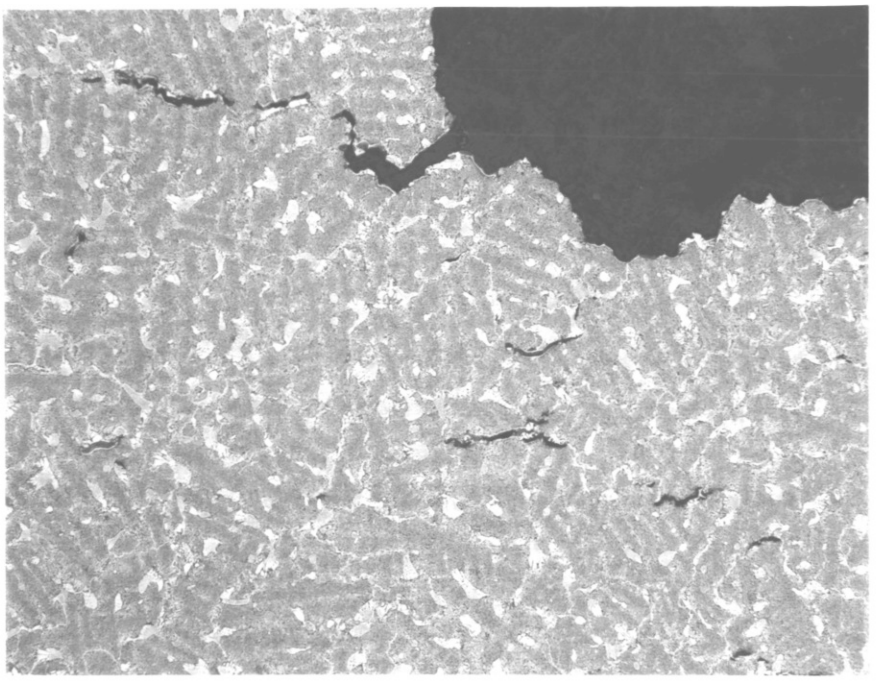


(a) x60

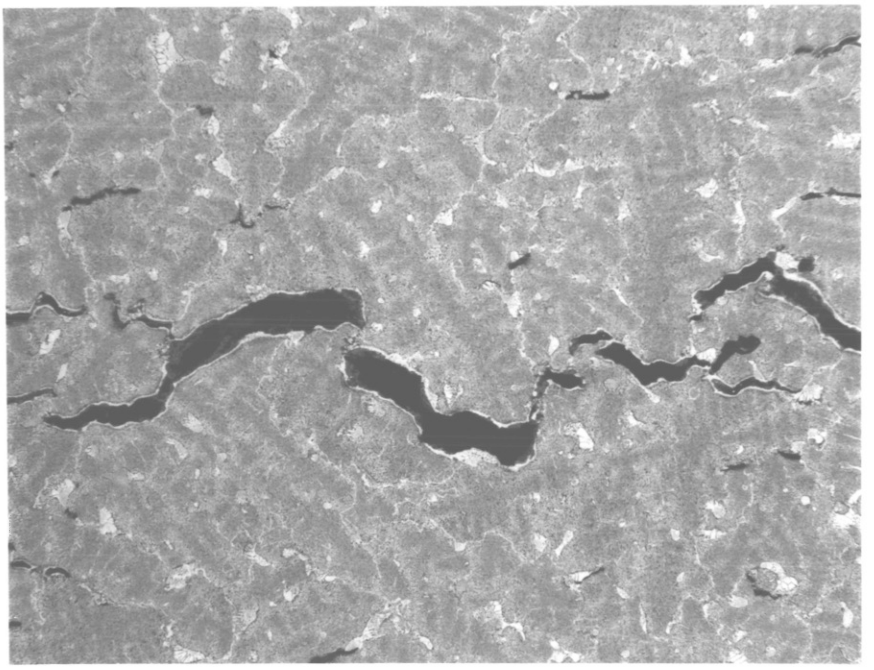


(b) x400

Fig. 9.64 Fracture surface of a creep damaged specimen tested at R=0.9 in the threshold region at 950^{o}C



(a) Crack branching and damage accumulation in the vicinity of the main crack,x50



(b) Damage accumulation in the specimen gauge section remote from the main crack,x50

Fig. 9.65 Optical micrographs of a creep damaged specimen tested at R=0.9 in the threshold region at 950^{o}C

CHAPTER 10

DISCUSSION

10.1 Crack Growth at 750°C

10.1.1 Crack Growth in the Threshold Region

A phenomenon requiring further discussion is the large discrepancy observed between crack growth behaviour at R ratios of 0.9 and 1 (figure 9.14). The effect is most marked for slower crack growth rates ($da/dt \simeq 10^{-3}mm/h$), and, although close similarities were observed in the cracking modes for the two R ratios (figures 9.16 and 9.17), the amount of deformation accompanying crack growth differs significantly. While crack growth under static loading was accompanied by significant deformation, relatively little deformation was evident for $R = 0.9$.

Differences in the crack growth behaviour for $R = 0.9$ and $R = 1$ may be caused by

(a) The cyclic element of loading at $R = 0.9$.
(b) Differences in crack growth behaviour for long and short cracks.

Several experimental studies have revealed that, for the same nominal driving force, the growth rates of short cracks are greater than (or equal to) the corresponding growth rates of long cracks (127, 128). A crack may be regarded as short (128) if it is

(a) Small in comparison to the material grain size.
(b) Small in comparison to the crack tip plastic zone.
(c) Physically short. (less than 0.5 - 1mm).

The initial crack length for the test carried out at $R = 0.9$ (0.51mm) is significantly shorter than that for the test carried out at $R = 1$ (4.00mm), and may be considered to be physically short. (definition c)

It is therefore of interest to consider the effect of initial crack length on the near threshold crack growth behaviour for $R = 0.9$. Crack growth rates are shown as a function of ΔK in figure 10.1 for crack growth tests carried out at 750°C for $R = 0.9$. Clearly, significantly higher ΔK values are required to propagate the crack of length 2.19mm compared with those required for a crack of length 0.51mm. Thus, for a given value of ΔK (or K_{max}), the shorter crack exhibits higher crack growth rates. It could be argued that this observation suggests that either

(a) shorter cracks exhibit higher growth rates for the same nominal driving force (ΔK or K_{max}) or

(b) that crack growth under these conditions may not be characterised in terms of the stress intensity factor, K.

In summary, the large discrepancies observed between crack growth behaviour at $R = 0.9$ and $R = 1$, for crack growth rates below 1mm/h, suggest that either K is not the correct parameter for characterising the crack growth or that enhanced growth rates for $R = 0.9$ may be caused by both the short initial crack length and the cyclic element of loading. The effect of the cyclic element of loading is demonstrated in figure 9.14 by the higher crack growth rates observed for $R = 0.7$ compared with those for $R = 0.9$ at the same value of K_{max}.

10.1.2 Effect of R Ratio

The effect of R ratio on the crack growth rate at 750°C was considered for sinusoidal loading at a frequency of 20Hz for $da/dN > 10^{-5}$mm/cycle. Fracture morphology ranged from predominantly transgranular (crystallographic) at $R = 0.5$ and 0.7 to predominantly intergranular at $R = 0.9$. Similar effects have been observed in crack growth testing of the cast nickel base superalloys IN738LC and 1N939

at 850°C (11).

Correlation of crack growth per cycle (da/dN) for $R = 0.5$ and $R = 0.7$ in terms of ΔK (figure 9.18) suggested that at these R ratios crack growth is occurring primarily as a result of the load range and is not significantly affected by the mean load level. Crack growth for $R = 0.5$ and $R = 0.7$ $(da/dN > 10^{-5}\ mm/cycle)$ occurs in a crystallographic transgranular manner over the entire range of ΔK considered. Several authors have observed a transition from crystallographic Stage I growth to 'structure insensitive' Stage II growth when the cyclic plastic zone size, Δr_p, becomes equal to the material grain size (7, 36, 50). This explains the tendency for large grained cast alloys to exhibit extensive Stage I cracking, as was observed in Mar M002 at 750°C. Assuming that the cyclic plastic zone size, Δr_p, is given by equation 4.11, then, taking the average grain size as 0.5mm, Stage I cracking is expected for $\Delta K < 90MPa\sqrt{m}$ (ie over the entire range of ΔK considered).

However, for $R = 0.9$, the fracture morphology becomes predominantly intergranular, resulting in increased crack growth per cycle (da/dN) for a given value of ΔK. Increased sensitivity of growth rate to R ratio at higher values of R has also been observed in the wrought nickel base superalloy Inconel 718 tested at 650°C (45).

Comparison of crack growth data obtained for $R = 0.5$, 0.7 and 0.9 with data obtained under static loading, on a C^* basis (figure 9.20), revealed reasonably good correlation between crack growth rates obtained under static loading and those obtained under cyclic loading for $R = 0.9$, particularly at higher crack growth rates. This suggests that the effect of R ratio on the crack growth behaviour at 750°C may be

attributed primarily to creep effects for $da/dN > 10^{-5}$ mm/cycle.

In summary, for $da/dN > 10^{-5}$ mm/cycle, crack growth is cycle dependent for $R = 0.5$ and 0.7 and predominantly time dependent for $R > 0.9$ for sinusoidal loading at a frequency of 20Hz. In addition, the test which involved changing the R ratio in the sequence 0.5, 0.7, 0.9, 1 demonstrated that cycle dependent loading has no significant effect on subsequent time dependent crack growth rates. It could be argued that fatigue dominated loading at R ratios of 0.5 and 0.7 does not cause significant intergranular damage and is unlikely to influence subsequent time dependent crack growth at R ratios of 0.9 and 1.

10.1.3 Effect of Frequency

A number of authors (11,23,26,29,40 - 42) have observed an increase in crack growth per cycle (da/dN) with a reduction in cyclic loading frequency (at a given value of ΔK) for nickel base superalloys tested at elevated temperatures in an air environment. The effect of frequency on the crack growth behaviour of Mar M002 was studied at 750°C for $R = 0.5$ and 0.9.

The results reported in figure 9.29 for $R = 0.5$ exhibit an interesting effect, which is worthy of further discussion. For $\Delta K < 25MPa\sqrt{m}$, da/dN values for the lower frequency (0.2Hz) are lower than those for the higher frequency (20Hz) at the same value of ΔK. The discrepancy between da/dN values for the two frequencies is greatest at lower values of ΔK. However, for $\Delta K > 25MPa\sqrt{m}$, da/dN values for the lower frequency appear to be of the same order as or, greater than, those expected for the higher frequency (assuming $da/dN \propto \Delta K^4$ describes the crack growth behaviour at 20Hz) for a given value of ΔK. In addition, displacement rates for the 0.2Hz test only become significant for $\Delta K > 25MPa\sqrt{m}$. The value

of ΔK, below which lower crack growths per cycle are observed for the lower frequency, is associated with a value of K_{max} which corresponds to the stress intensity ($50\ MPa\sqrt{m}$) at which creep crack growth becomes significant at this temperature ($(da/dt)_{creep} > 10^{-3}$mm/h).

It could be argued that for values of K_{max} below $50\ MPa\sqrt{m}$ significant creep crack growth may not occur (i.e. in the case of $R = 0.5$ for $\Delta K < 25\ MPa\sqrt{m}$). However, for $\Delta K < 25\ MPa\sqrt{m}$ sufficient time may be available at the lower frequency (0.2Hz) for creep deformation to blunt the crack tip, causing lower values of da/dN than for the higher frequency (where crack tip blunting does not occur) at a given value of ΔK. Similar retardation effects have been observed in the nickel base superalloys Udimet 700 and Inconel 718, at low frequencies or with hold times, when the stress intensities are less than those required to cause significant creep crack growth (33, 34, 35).

The effect of frequency on the crack growth at $R = 0.9$ is more typical of the type of effect observed in the majority of studies on crack growth in nickel base superalloys. Figure 9.32 shows, that for a given value of ΔK, the crack growth per cycle increases with decreasing frequency. In order to illustrate the frequency dependence of the crack growth behaviour crack growth rates at $\Delta K = 5\ MPa\sqrt{m}$ are shown as a function of frequency in figure 10.2. The fracture surfaces for 0.02Hz, 0.2Hz and 20Hz all exhibited close similarites to fracture surfaces observed under static loading, suggesting that crack growth may be creep dominated for these frequencies at $R = 0.9$. This argument is endorsed by the correlation of $\dot{a}$ values for all three frequencies in terms of C^*_{mod} (figure 9.34) showing good agreement with data obtained under static loading. It may be noted that for a given value of C^*_{mod} crack growth rates ($\dot{a}$) are slightly higher

for cyclic loading at $R = 0.9$, indicating a minor effect due to the load range. In addition, the effect of the load range on the crack growth behaviour increases with increasing frequency.

When time dependent processes control the crack growth mechanism, $\dot{a}$ should be constant for given loading conditions, and if

$$\frac{da}{dN} = \frac{1}{3600} \frac{\dot{a}}{f} \qquad (10.1)$$

where da/dN is in mm/cycle, f in Hz and $\dot{a}$ in mm/h, a slope of -1 should be obtained in figure 10.2. A slope of -1 shows good agreement with the experimental data, particularly at the lower frequencies. Crack growth/cycle at $20Hz$ is slightly higher than predicted from $\dot{a}$ = constant, suggesting that cyclic fatigue processes contribute to the crack growth at this frequency.

The high value of the slope of da/dN versus ΔK for the frequency of $20Hz$ (figure 9.32), compared with the slopes of $0.2Hz$ and $0.02Hz$, means that the form of figure 10.2 is dependent on the value of ΔK chosen. However, the form of figure 10.2 is consistent with the results presented in figures 9.33 and 9.34, which demonstrate that crack growth at $R = 0.9$ is essentially time dependent for frequencies of $0.02Hz$, $0.2Hz$ and $20Hz$.

In summary, the effect of frequency on the crack growth behaviour at $750^{\circ}C$ is dependent on both the R ratio and stress intensity (K_{max} or ΔK) at which the tests are carried out. Higher R ratios favour time dependent crack growth at higher loading frequencies, while the relative magnitudes of K_{max} and the stress intensity required for creep crack growth determine whether crack growth rates are enhanced or retarded at lower frequencies.

10.2 Crack Growth at 950°C

10.2.1 Crack Growth in the Threshold Region

Fractography of the specimen tested at $R = 0.1$ (figure 9.39) suggested that crack growth data obtained from this test could not be relied upon due to possible crack initiation away from the starter notch at point 1. However, crack growth data obtained at both $R = 0.7$ and $R = 0.9$ correlated very well with data obtained under static loading in terms of both K_{max} (figure 9.36) and C^*_{mod} (figure 9.38). Fracture surfaces of the specimens tested at $R = 0.7$ and 0.9 showed close similarities to the fracture surface of the specimen subjected to static loading, suggesting that time dependent crack growth in the threshold region at 950°C was dominated by creep (rather than environmental) effects.

The mechanisms responsible for crack growth in the threshold region at $R = 0.7$ and $R = 0.9$ showed close similarities to those responsible for crack growth under static loading and involved the build up of damage ahead of the crack tip. Mechanisms of crack growth involving damage accumulation ahead of the crack tip were discussed in Section 3.2., and have been observed during creep crack growth in the wrought nickel base superalloys Udimet 700 (27) and Nimonic PE16 (28). Crack growth by this type of mechanism has generally been found to exhibit limited environmental sensitivity.

It must be emphasised here that damage accumulation (in the form of grain boundary cracking) was not confined to a small creep zone near the crack tip but was also observed in specimen gauge sections away from the main crack (figures 9.42(b) and 9.43(b)). The accumulation of damage away from the main crack would be expected to influence the displacement rates measured during crack growth and result in experimental

C^* values, which are significantly higher than those predicted theoretically (figure 9.10). Discrepancies between experimental and theoretical C^* values are discussed in more detail in Section 10.4.

In summary, crack growth in the threshold region at 950°C for R ratios of 0.7 and 0.9 occurs by a relatively ductile mode of crack growth, involving significant damage accumulation throughout the specimen and bearing close similarities to crack growth under static loading at the same temperature. Crack growth rates for $R = 0.7$, 0.9 and 1 correlate very well with the parameter C^*_{mod} (see Section 9.2.2).

10.2.2 Effect of R Ratio

The effect of R ratio on crack growth rate at 950°C was considered for sinusoidal loading at a frequency of $20Hz$ for $da/dN > 10^{-6}\,mm/cycle$ Fracture morphology ranged from predominantly transgranular at $R = 0.1$, 0.5 and 0.7 to predominantly intergranular at $R = 0.9$.

In contrast to the threshold region (Section 10.2.1), in which crack growth at $R = 0.7$ occurs in a predominantly intergranular manner, when the crack growth test is started at a higher initial stress intensity (and greater crack length) the crack propagates in a predominantly transgranular manner at the same R ratio. It could be argued that, because the initial crack growth rate is relatively high, insufficient time is available for intergranular damage to accumulate ahead of the crack tip and allow crack propagation by the mechanism outlined in Section 10.2.1. For a given value of ΔK (or K_{max}) the mechanism involving intergranular crack growth gives rise to higher crack growths per cycle than the transgranular mechanism.

Crack growth rates for $R = 0.1$, 0.5, 0.7 and 0.9 are shown as a function of ΔK in figure 9.44. The trend is similar to that observed at 750°C, in that higher R ratios give rise to higher values of da/dN for a given value of ΔK. Once again the results agree qualitatively with results obtained from tests on other nickel base superalloys. (11,45). Displacement rates were not measured for the test at $R = 0.1$, but crack growth rates are shown as a function of C^*_{mod} in figure 9.46 for $R = 0.5$, 0.7 and 0.9. Correlation between crack growth rates obtained under static loading and those obtained under cyclic loading improved with increasing R ratio, indicating the increasing influence of time dependent creep effects at higher R ratios.

In summary, higher R ratios encourage an increase in the amount of intergranular fracture, leading to increases in da/dN for a given value of ΔK. At 950°C, crack growth in the threshold region (Section 10.2.1) occurs by an intergranular mode involving damage accumulation ahead of the crack for R ratios of 0.7 and 0.9 at 20Hz. However, when the crack growth tests are started at higher initial stress intensities, crack growth for $R = 0.7$ may occur in a predominantly transgranular manner. Thus, the effect of R ratio on the crack growth behaviour at 950°C and $20Hz$ can be significantly influenced by the initial stress intensity level. For a given ΔK, crack growths per cycle for R ratios of 0.5 and 0.7 are greater than for $R = 0.1$, suggesting that crack growth rates for $R > 0.5$ are influenced by time dependent creep effects (even for frequencies of $20Hz$) at 950°C.

10.2.3 Effect of Frequency

The effect of frequency on the crack growh behaviour was studied at 950°C for $R = 0.5$. Figure 9.54 shows, that for a given value of

ΔK, the crack growth per cycle increases with decreasing frequency. In addition, the crack path changes from predominantly transgranular at 20Hz to predominantly intergranular at $0.02Hz$. An increase in the amount of intergranular fracture, with a reduction in loading frequency, has been observed by several authors (11,23,26,40,42 - 44). In order to illustrate the frequency dependence of the crack growth behaviour, crack growth rates at $\Delta K = 12MPa\sqrt{m}$ are shown as a function of frequency in figure 10.3.

Crack growth at $0.02Hz$ for $R = 0.5$ is almost entirely time dependent and crack growth rates correlate well with those obtained under static loading in terms of the parameter C^*_{mod}. Cycle dependent fatigue processes have an increasing effect as the loading frequency is increased. Several authors have shown that crack growth is governed by time dependent processes at low frequencies and cycle dependent processes at high frequencies (40,43,44). The effect of frequency on the crack growth per cycle is shown schematically in figure 3.4. At high enough loading frequencies the crack growth per cycle is independent of frequency (ie cycle dependent), and depends only on ΔK. Purely cycle dependent crack growth was not observed at 950°C for $R = 0.5$ over the range of frequencies studied, and figure 9.51 shows that intergranular features are evident on the fracture surface of the specimen tested at 20Hz. The line of slope -1 in figure 10.3 represents purely time dependent crack growth. Increasing deviations from this line as the frequency is increased, indicate an increasing contribution from cycle dependent fatigue processes.

In summary, crack growth at 950°C for 0.5 is time dependent at a frequency of $0.02Hz$. Purely cycle dependent growth was not observed,

even for frequencies as high as 20Hz. Crack growth occurred by a combination of time dependent and cycle dependent processes for frequencies of 0.2 - 20Hz.

10.2.4 Effect of Waveform

The effect of loading waveform on the crack growth per cycle is shown in figures 9.59 and 9.60 for the waveforms shown in figure 9.57 at $R = 0.1$. For a given value of ΔK, da/dN values were lowest for the triangular waveform of frequency 6.87Hz, for which time dependent creep effects should be minimal. Decreasing the frequency of the triangular waveform to 0.2Hz leads to higher values of da/dN for the same value of ΔK (similar to the effect observed for sinusoidal loading at $R = 0.5$ in Section 10.2.3). Crack growths per cycle for the trapezoidal waveform were higher than those for both of the triangular waveforms at a given value of ΔK, indicating that the hold times in the trapezoidal waveform cause an increase in crack growth rate (loading and unloading rates for the trapezoidal waveform of 0.2Hz were the same as those for the 6.87Hz triangular waveform). A further increase in da/dN was observed for sinusoidal loading at 0.2Hz.

Equivalent steady loads for the sinusoidal, triangular and trapezoidal waveforms are shown in figure 9.8. The equivalent steady load under steady state creep conditions is highest for the trapezoidal waveform, followed by the sinusoidal and triangular waveforms. It could be argued that the loading rates for the 0.2Hz triangular and sinusoidal waveforms are low enough to allow creep effects to influence the crack growths per cycle. Creep effects should then be greater for the sinusoidal waveform, at a given ΔK, as the equivalent steady stress is higher for this waveform. Loading rates for the trapezoidal and 6.87Hz

triangular waveforms are identical so that higher values of da/dN for the trapezoidal waveform may be explained in terms of an increase in crack growth per cycle caused by the hold times of approximately 2.5s at maximum and minimum loads. Clavel and Pineau (42) carried out a similar study on the effect of waveform on the crack growth behaviour of Inconel 718 at 550°C. They found that crack growths per cycle were not significantly influenced by hold times, and were more sensitive to loading and unloading rates than the frequency per se.

In summary, crack growths per cycle in Mar M002 at 950°C were found to be sensitive to both loading and unloading rates and to the imposition of hold times at both maximum and minimum load.

10.2.5 Effect of Prior Creep Damage

The effect of 1.905% prior creep strain on the subsequent crack growth behaviour at 950°C for $R = 0.9$ at a frequency of $20Hz$ is shown in figures 9.62 and 9.63. Observations of the fracture surfaces of the virgin and pre-strained specimens indicate that crack propagation occurs by a more brittle mode in the damaged material. This is borne out by the higher value of m obtained for the damaged material in figure 9.62, and is consistent with crack propagation models which assume a critical strain or strain exhaustion criterion for crack advance (74 - 76).

Values of C^*_{mod} for the damaged material were greater than those for the virgin material at a given crack growth rate (figure 9.63). However, values of $\dot{\Delta}_o$, the uncracked displacement rate, were calculated assuming that there was no prior damage, according to equation 9.17.

$$\dot{\Delta}_o = \ell_e \frac{\dot{\varepsilon}_o}{\sigma_o^n} \left[\frac{Peq}{BW}\right]^n \qquad (10.2)$$

If the amount of prior damage corresponding to 1.905% pre strain is denoted by η, then the uncracked displacement allowing for this damage, $\dot{\Delta}_{o,\eta}$, is given by

$$\dot{\Delta}_{o,\eta} = \ell_e \frac{\dot{\varepsilon}_o}{\sigma_o^n} \left[\frac{Peq}{BW(1-\eta)}\right]^n \qquad (10.3)$$

so that

$$\frac{\dot{\Delta}_{o,\eta}}{\dot{\Delta}_o} = \frac{1}{(1-\eta)^n} \qquad (10.4)$$

If we assume the model of Kachanov and Rabotnov with $n = \gamma$ (appendix 5), then $\eta = \varepsilon/\varepsilon_f$, and taking $\varepsilon_f = 12\%$ for Mar M002 at 950°C, $\eta = 0.159$ represents the amount of prior damage, and

$$\frac{\dot{\Delta}_{o,\eta}}{\dot{\Delta}_o} = 3.35 \qquad (10.5)$$

If C^*_{mod} values for the damaged material are re-calculated using

$$C^*_{mod} = \frac{Peq}{BW(1-\eta)} \left(\dot{\Delta}_T - \dot{\Delta}_{o,\eta}\right). F \qquad (10.6)$$

then agreement between crack growth data (plotted in the form $\log da/dt$ versus $\log C^*_{mod}$) for the virgin and damaged material is very good (figure 10.4), although some divergence in the data is apparent at higher crack growth rates (when the value of η will have increased above 0.159).

Results of this study of the effect of prior creep damage on time dependent crack growth rates in Mar M002 at 950°C agree qualitatively with results obtained by Pilkington (129) using a low alloy steel tested at 550°C. He observed faster cracking rates at a given stress intensity value in the damaged material, while crack growth data for both

the virgin and damaged material could be correlated in terms of C^*.

In summary, 1.905% prior creep strain had a substantial effect on the crack growth behaviour of Mar M002 specimens subjected to cyclic loading of $R = 0.9$ and f = 20Hz at a temperature of 950°C. For a given value of ΔK, crack growth rates were significantly higher in the damaged material. This is attributed to grain boundary damage (caused by 1.905% prior creep strain) enhancing the intergranular crack growth mechanism which operates at 950°C for $R = 0.9$ and f = 20Hz. However, crack growth rates for both the virgin and damaged material could be correlated in terms of the parameter C^*_{mod}.

10.3 Comparison of Crack Growth Behaviour of Mar M002 at Temperatures of 750°C and 950°C

In order to facilitate comparison of the crack growth behaviour at the two temperatures, only time dependent crack growth was considered for each temperature. For a given value of C^*_{mod} this represents a lower bound for da/dt at each temperature. The influence of cycle dependent processes can significantly increase the value of da/dt at a given value of C^*_{mod}.

Time dependent crack growth rates for both 750°C and 950°C are shown as functions of C^*_{mod} in figures 10.5 and 10.6 respectively. The solid lines in each figure represent crack growth data obtained under static loading at that temperature. Nikbin et al (75) developed a model for time dependent creep crack growth, which yields an expression of the form (Section 5.2.1)

$$\frac{da}{dt} = (n+1)\frac{\dot{\varepsilon}_o}{\varepsilon_f^*}\left[\frac{C^*}{I_n \sigma_o \dot{\varepsilon}_o}\right]^{\frac{n}{(n+1)}} \cdot r_c^{\frac{1}{(n+1)}} \qquad (10.7)$$

where ε_f^* is the creep ductility appropriate to the state of stress at the crack tip. For plane stress conditions, the authors suggested that reduction of area, rather than uniaxial creep ductility, ε_f, should be used as a measure of creep ductility appropriate to the state of stress at a crack tip. The reduction of area measured for ductile materials is usually of the order $2\varepsilon_f$, while for brittle materials, the reduction of area is usually of the same order as ε_f. Uniaxial creep data for Mar M002 at temperatures of 750°C and 950°C, given in Sections 8.4.1 and 8.4.2, reveal that at 750°C $\varepsilon_f \simeq 4\%$, while at 950°C $\varepsilon_f \simeq 12\%$. It could be argued that the value of ε_f^* used at 750°C should be of the order ε_f, while it may be more appropriate to use $\varepsilon_f^* = 1.5\varepsilon_f$ at 950°C.

The value of n is taken as 7 for both temperatures, and

$$\frac{\dot{\varepsilon}_o}{\sigma_o^n} = 2.80 \times 10^{-25}\ h^{-1}(MPa)^{-7} \text{ at } 750^oC \qquad (10.8)$$

$$\frac{\dot{\varepsilon}_o}{\sigma_o^n} = 1.05 \times 10^{-20}\ h^{-1}(MPa)^{-7} \text{ at } 950^oC \qquad (10.9)$$

The average grain size, r_c, was taken to be 0.5mm, and the value of I_n was taken as 3.2 for plane stress loading with $n = 7$ (62,63).

Expressions obtained for crack growth rates are given below

$$\dot{a} = 23.8 \left[C^*\right]^{0.875} \text{ for } 750^oC \qquad (10.10)$$

$$\dot{a} = 19.7 \left[C^*\right]^{0.875} \text{ for } 950^oC \qquad (10.11)$$

where $\dot{a}$ is in mm/h and C^* is in MJ/m^2h. The above expressions are shown as broken lines in figures 10.5 and 10.6. Agreement between the model and experimental data is very good at both 750^oC and 950^oC. Further, the model is in qualitative agreement with experimental observations (figure 10.7) of higher creep crack growth rates at the lower temperature (750^oC) for a given value of C^*.

Creep crack growth rates for Mar M002, at temperatures of 750^oC and 950^oC, are compared with data obtained from a range of high temperature alloys (97) in figure 10.8. Sadananda and Shahinian (16) have suggested that C^* is the controlling parameter for crack growth occurring as a result of deformation controlled processes with little environmental contribution. This assumption appears reasonable and suggests that time dependent crack growth may occur by such a process in Mar M002 at 750^oC and 950^oC. However, the same authors (16) also

claim that a unique relationship, independent of material and temperature, may exist between $\dot{a}$ and C^*. The model, proposed by Nikbin et al (75), shows that the relationship between $\dot{a}$ and C^* is influenced by the values of ε_f^*, n, the constant $\dot{\varepsilon}_o/\sigma_o^n$ and the material grain size, r_c. The relationship between $\dot{a}$ and C^*, derived from the model, may be conveniently expressed in the form.

$$\dot{a} = \left[(n+1) \left\{ \frac{r_c \dot{\varepsilon}_o}{\sigma_o^n I_n^n} \right\}^{\frac{1}{(n+1)}} \cdot \frac{1}{\varepsilon_f^*} \right] \cdot C^{*\frac{n}{(n+1)}} \qquad (10.12)$$

Clearly, the relationship between $\dot{a}$ and C^* is dependent on the values of n and ε_f^*, appropriate to the material of interest, and to a lesser extent on the constant $\dot{\varepsilon}_o/\sigma_o^n$ and the grain size, r_c. Thus, although a unique relationship between $\dot{a}$ and C^* does not exist, materials with similar values of n and ε_f^* should exhibit similar relationships between $\dot{a}$ and C^* in situations in which environmental contributions to the crack growth processes are minimised.

Figure 10.8 shows that there is close agreement between creep crack growth data for Udimet 700 at 850°C and Mar M002 at both 750°C and 950°C. Creep ductilities and values of n for the two materials are similar and it has been shown (16) that Udimet 700 exhibits little environmental sensitivity at 850°C. It seems reasonable to argue, in view of the above evidence, that creep crack growth occurs by similar mechanisms in Mar M002 and Udimet 700 at the temperatures considered.

In summary, time dependent crack growth in Mar M002 at temperatures of 750°C and 950°C exhibits limited environment (air) sensitivity and may be correlated in terms of the paramter C^*.

10.4 Crack Growth Modelling

Theoretical modelling of high temperature crack growth is useful for two reasons.

(a) Successful modelling of the crack growth process may allow crack growth rates to be predicted for service applications not directly covered by laboratory experiments. For instance, if crack growth rates can be predicted for the TCP geometry in the current investigations, similar procedures may be adopted in order to predict crack growth in more complex geometries (eg aircraft engine blades)

(b) Discrepancies between actual and predicted behaviour may help to identify discrepancies between actual and theoretical crack growth mechanisms.

Time dependent crack growth in Mar M002 has been successfully correlated in terms of the parameter C^*_{mod} for temperatures of 750° and 950°C. However, figures 9.9 and 9.10 show that large discrepancies exist between theoretical and experimental estimates of C^*. The trend is for experimental values of C^* to be larger than theoretical values for a given crack growth rate. Discrepancies between experimental and theoretical values of C^* are most marked at higher crack growth rates. It could be argued that these discrepancies are caused by the theoretical values of C^* failing to take account of damage accumulation ahead of the crack tip. Damage accumulation has been allowed for in an approximate way by using the brittle fracture theories of Kachanov and Rabotnov, which were outlined in Appendix 5. Applications of the theory were restricted to the temperature of 950°C, because uniaxial creep data were available over a wider range of stresses at this temperature. (see Sections 8.4.1 and 8.4.2).

It was first assumed that C^* values were proportional to σ_{ref}^{n+1} (see Section 6.4.2.3). It was further assumed that the reference stress for damaged material, $\sigma_{ref,\eta}$ (where η is the amount of damage), could be related to the reference stress for virgin material, σ_{ref}, by the following expression

$$\sigma_{ref,\eta} = \frac{\sigma_{ref}}{(1 - \eta)} \tag{10.13}$$

C^* values in the damaged material, C^*_{dam}, could then be related to C^* values in the virgin material by

$$C^*_{dam} = C^*_{th} \cdot \left[\frac{\sigma_{ref,\eta}}{\sigma_{ref}}\right]^{n+1} \tag{10.14}$$

which can be rewritten as

$$C^*_{dam} = C^*_{th} \cdot \left[\frac{1}{1 - \eta}\right]^{n+1} \tag{10.15}$$

The damage rate, $\dot{\eta}$, in the uncracked ligament may than be related to σ_{ref} (using equation A5.6) by

$$\frac{\dot{\eta}}{\dot{\eta}_o} = \left[\frac{\sigma_{ref}}{\sigma_o}\right]^{\nu} \frac{1}{(1 - \eta)^{\gamma}} \tag{10.16}$$

or

$$\dot{\eta} = \dot{\eta}_o \left[\frac{\sigma_\infty}{\sigma_o (1 - a/w)}\right]^{\nu} \frac{1}{(1 - \eta)^{\gamma}} \tag{10.17}$$

where σ_∞ is the remote applied stress (P/Bw). Assuming that C^*_{dam} is the controlling parameter for crack growth in the damaged material then

$$\frac{da}{dt} = H\,(C^*_{dam})^{\phi} \tag{10.18}$$

and using

$$\eta = \int_0^t \dot{\eta}\, dt \qquad (10.19)$$

and substituting for dt in equation 10.19 from equation 10.18, the current value of the damage in the remaining ligament is given by

$$\eta = \int_{a_0}^{a} \left[\dot{\eta}_0 \left\{ \frac{\sigma_\infty}{\sigma_0} \right\}^{\nu} \frac{1}{(1-a/w)^{\nu}} \frac{1}{(1-\eta)^{\gamma}} / H.(C^*_{dam})^{\phi} \right] da \qquad (10.20)$$

where a_0 is the initial crack length and a is the current crack length. An expression may also be derived for the elapsed time,

$$t = \int_{a_0}^{a} \frac{dt}{da} \cdot da = \int_{a_0}^{a} \frac{da}{H(C^*_{dam})^{\phi}} \qquad (10.21)$$

Equations 10.20 and 10.21 were solved numerically.

Constants ν, γ, $\dot{\eta}_0$ and σ_0 were determined from the uniaxial creep data for Mar M002 at 950°C (Section 8.4.2) using the procedure outlined in Appendix 5. For Mar M002 at 950°C

$$\nu = \gamma = n = 7 \qquad (10.22)$$

$$\frac{\dot{\varepsilon}_0}{\sigma_0^{\,n}} = 1.05 \times 10^{-20}\ h^{-1}(MPa)^{-7} \qquad (10.23)$$

$$\frac{\dot{\eta}_0}{\sigma_0^{\,n}} = 8.75 \times 10^{-20}\ (MPa)^{-7} \qquad (10.24)$$

The value chosen for H was calculated on the assumption that the effective failure strain for the damaged material was reduced by a

factor $(1 - \eta)$. Using the model of Nikbin et al (75) and referring to equation 10.12

$$H = (n + 1) \left[\frac{A_c \dot{\varepsilon}_o}{\sigma_o^n I_n^n}\right]^{\frac{1}{n+1}} \frac{1}{\varepsilon_f^{*(1-\eta)}} \qquad (10.25)$$

The model was applied to the prediction of time dependent crack growth at 950°C for three different loadings.

1. Static loading ; $P = 5.783kN$ (figures 10.9, 10.10)
2. $R = 0.9$; $f = 20Hz$; $P_{max} = 8kN$ (figures 10.11, 10.12)
3. $R = 0.5$; $P = 0.02Hz$; $P_{max} = 10kN$ (figures 10.13, 10.14)

In all cases the values of C^*_{dam} are much closer to the experimental C^* values than the original theoretical values, C^*_{th} (figures 10.9, 10.11, 10.13). Predicted failure times are within a factor of 1.5 of actual failure times in all cases and in the latter two tests agreement between actual and predicted crack lengths is very good. Discrepancies in actual and predicted behaviour for the test carried out under static loading (figure 10.10) may be attributed to difficulty in modelling the very slow cracking rate observed during the first 300 hours of testing.

In summary, the model outlined here shows considerable promise as an approximate means of predicting time dependent crack growth in Mar M002 at 950°C. Predicted failure times were, in all cases, within a factor of 1.5 (generally conservative) of actual failure times. Failure caused by purely time dependent crack growth represents an upper bound on component life. Failure times may be significantly reduced when cycle dependent processes affect the crack growth behaviour, and at high enough loading frequencies component lifetimes may be determined simply by the number of loading cycles.

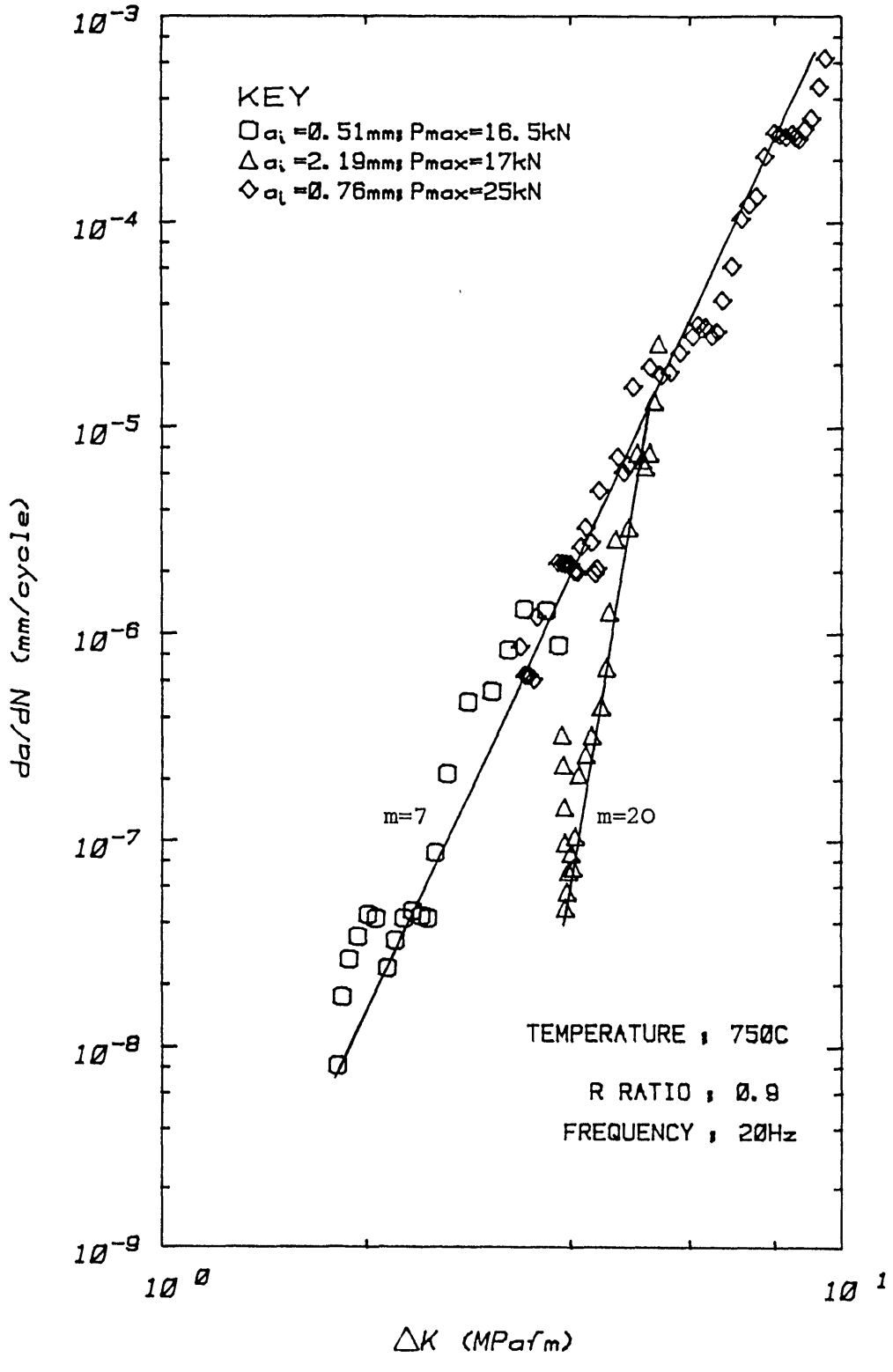


Fig. 10.1 Effect of initial crack length on crack growth in the threshold region at 750°C for R=0.9

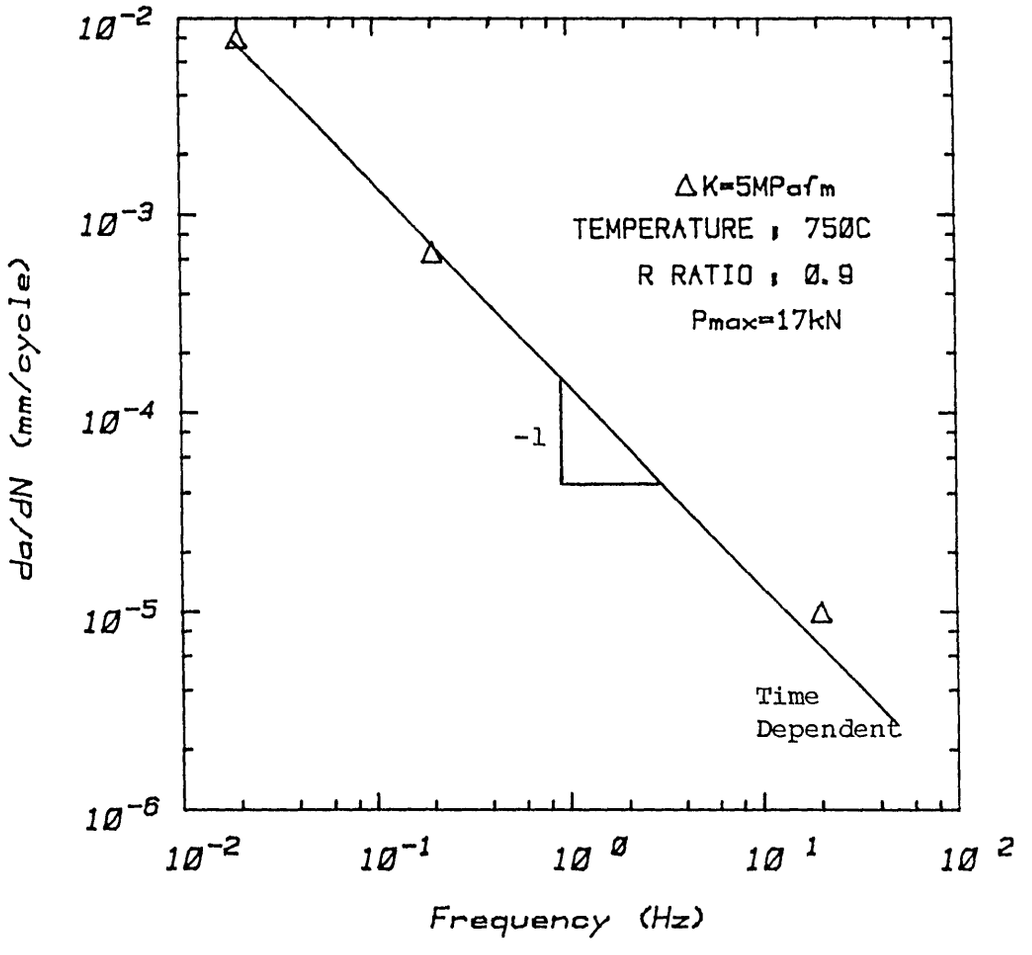


Fig. 10.2 Frequency dependence of crack growth per cycle at 750°C for R=0.9

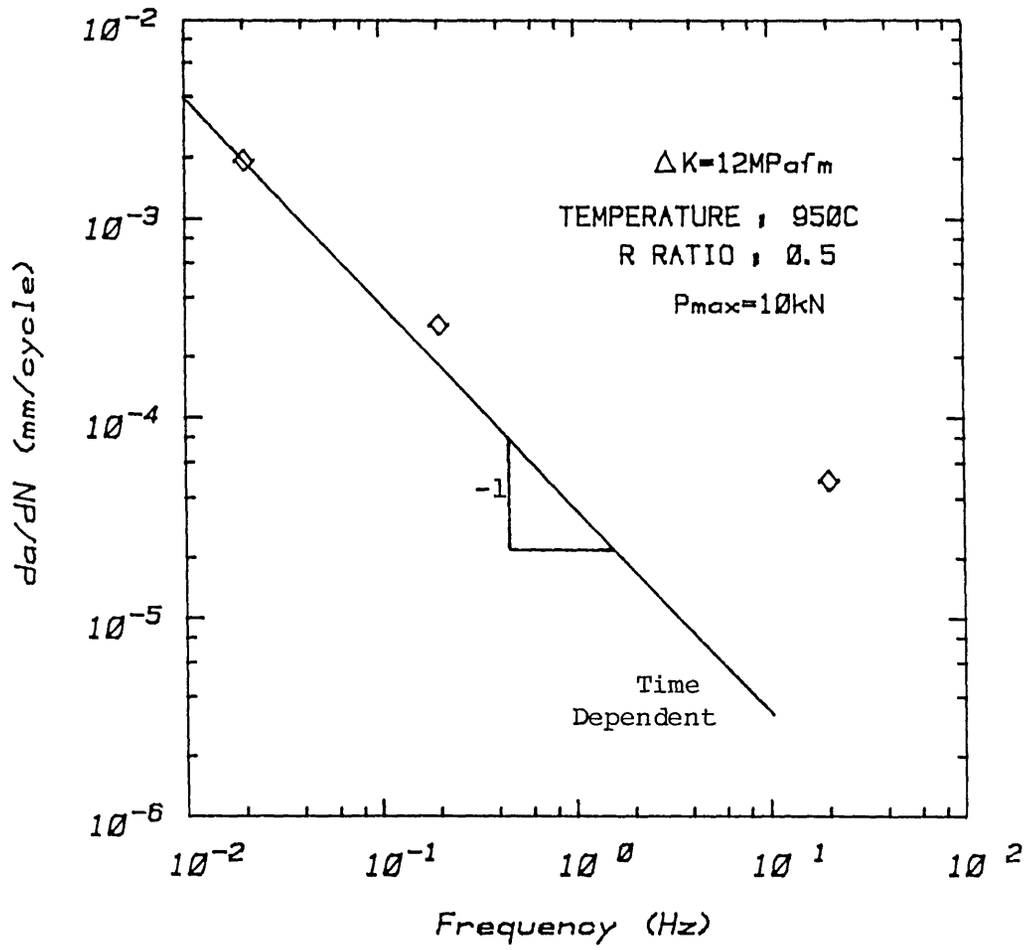


Fig. 10.3 Frequency dependence of crack growth per cycle at 950°C for R=0.5

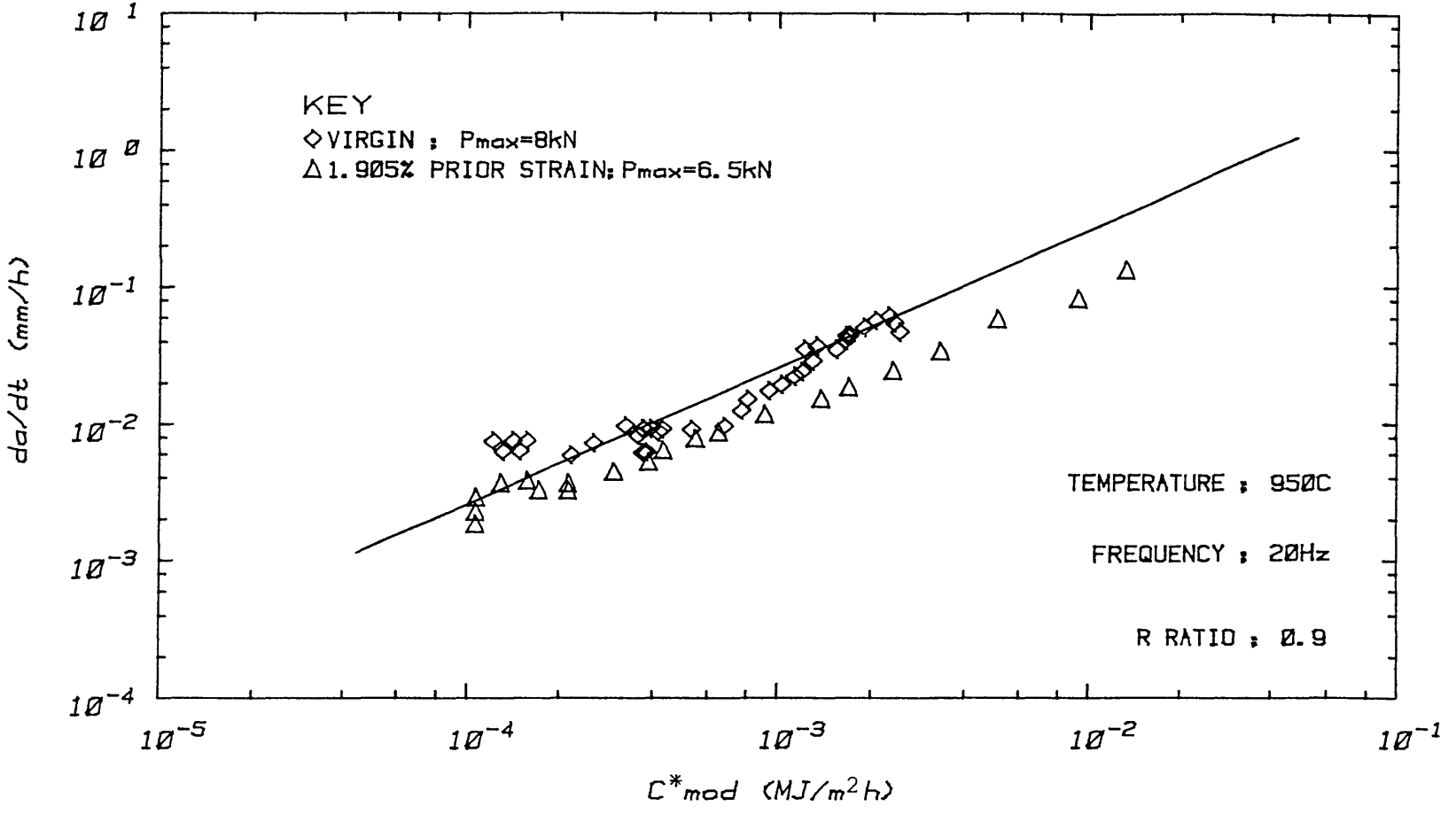


Fig. 10.4 Correlation of crack growth rates for virgin and damaged material in terms of C^*_{mod}

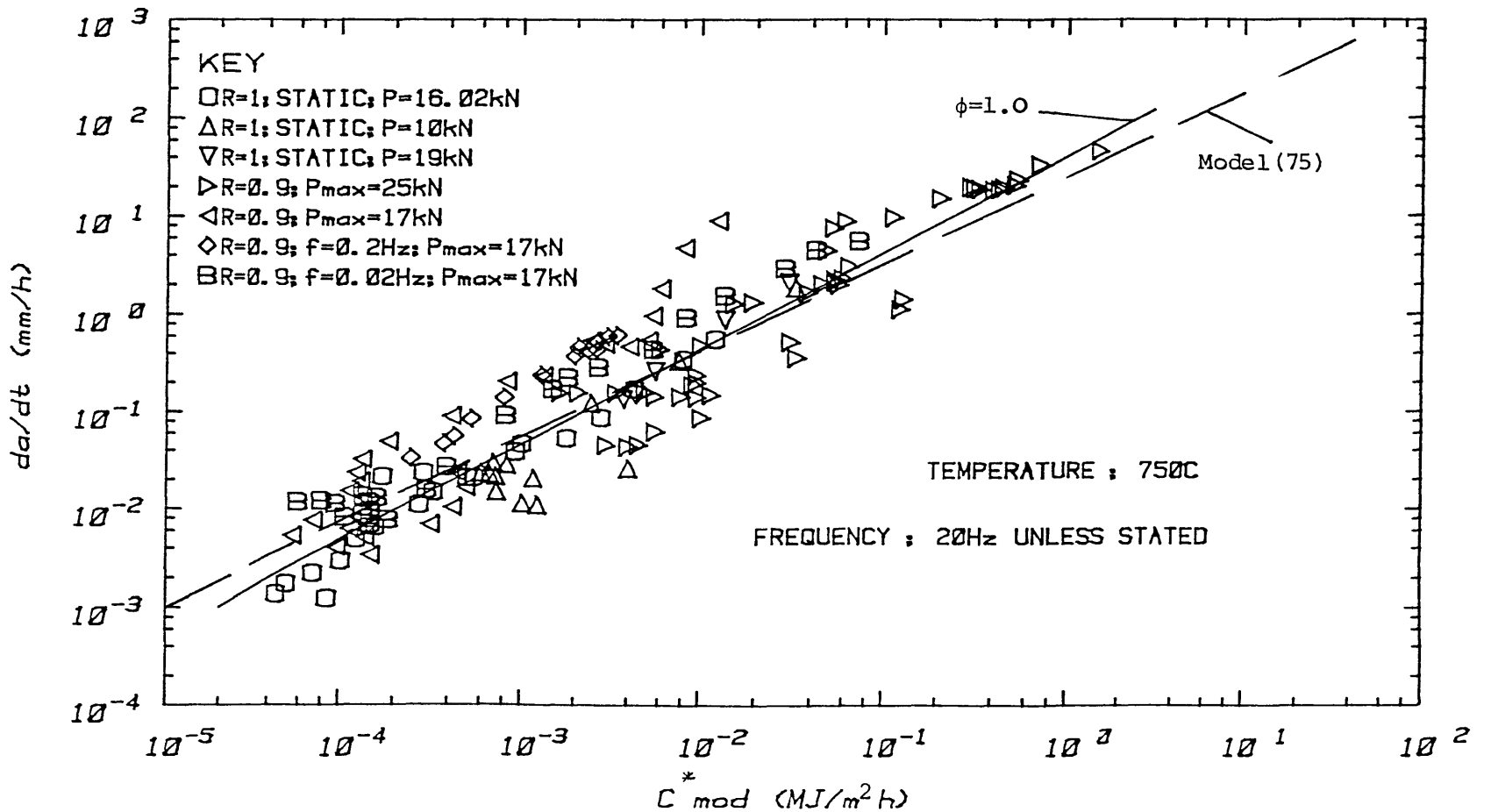


Fig. 10.5 Correlation of time dependent crack growth rates at 750°C with C^*_{mod}

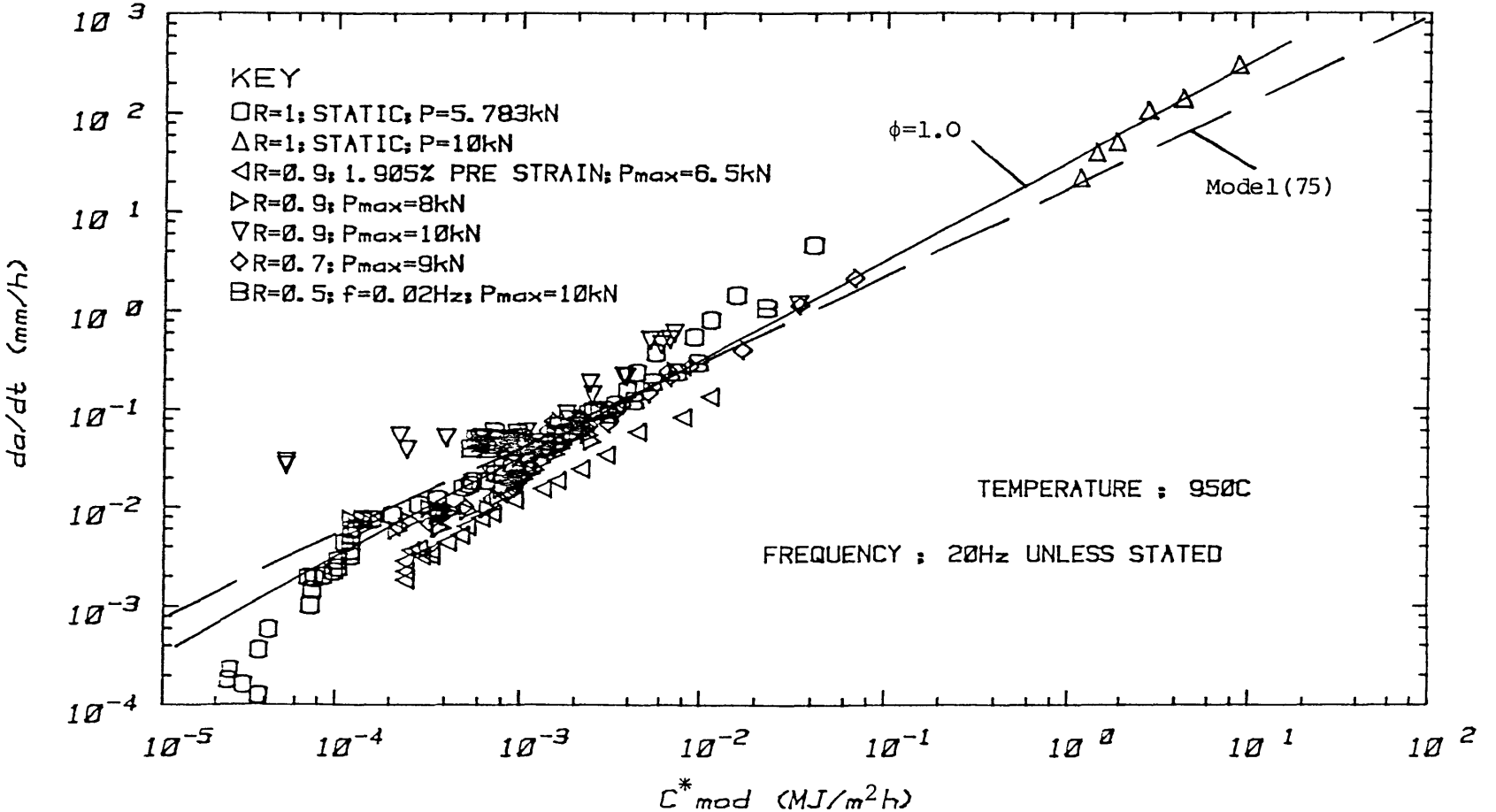


Fig. 10.6 Correlation of time dependent crack growth rates at 950°C with C^*_{mod}

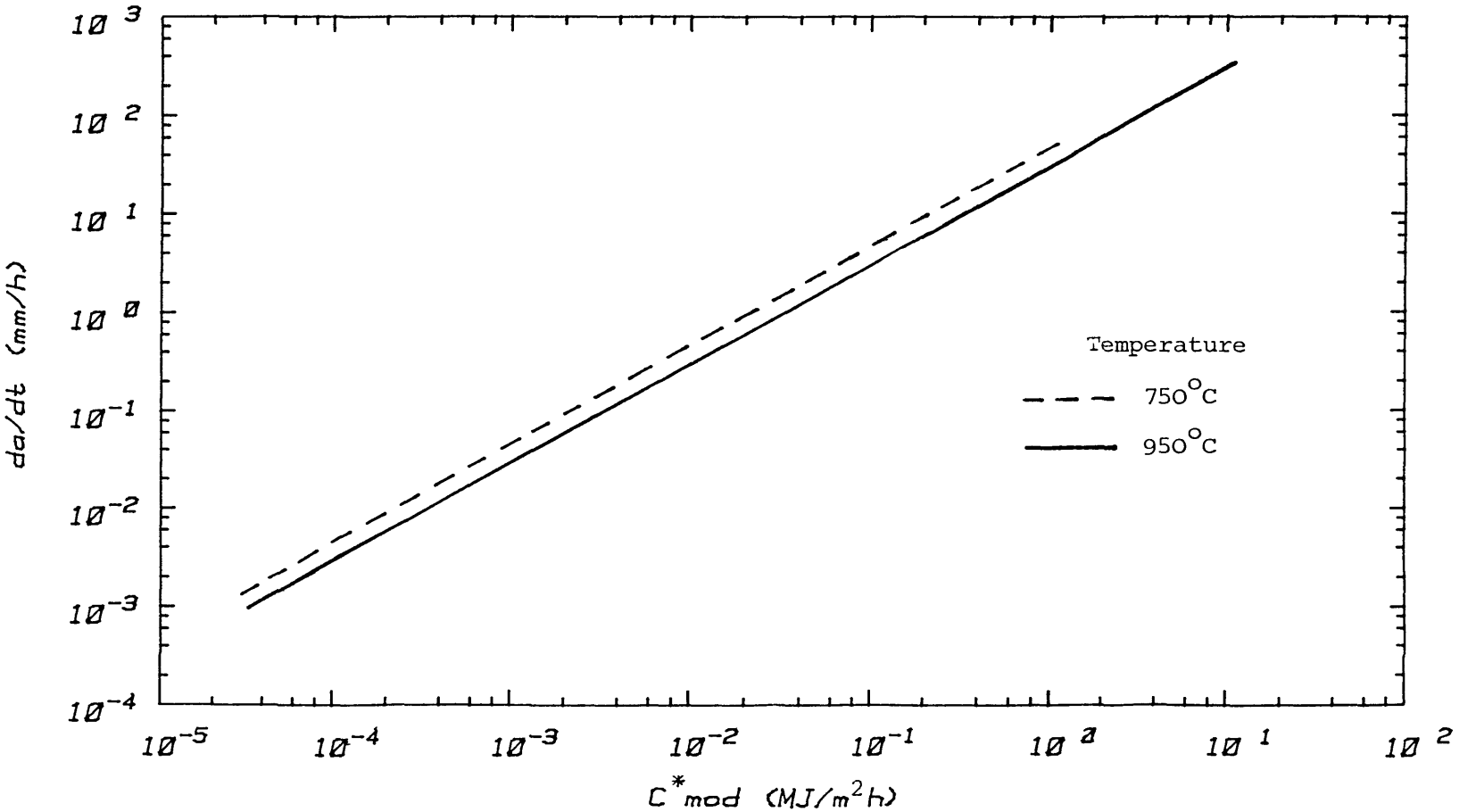


Fig. 10.7 Comparison of crack growth rates obtained for static loading at temperatures of 750°C and 950°C

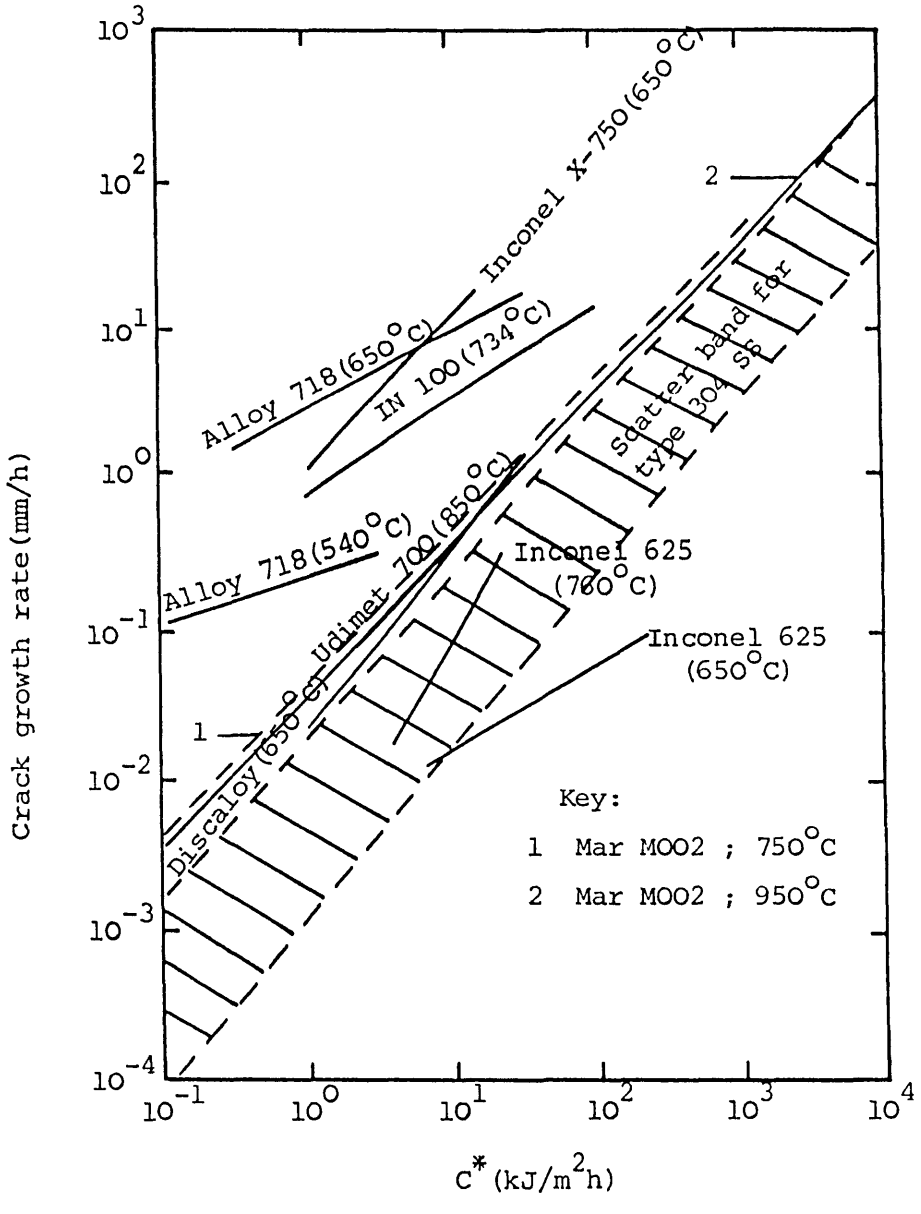


Fig. 10.8 Comparison of creep crack growth rates measured for Mar MOO2 at 750°C and 950°C with creep crack growth data obtained for a range of other high temperature alloys (97)

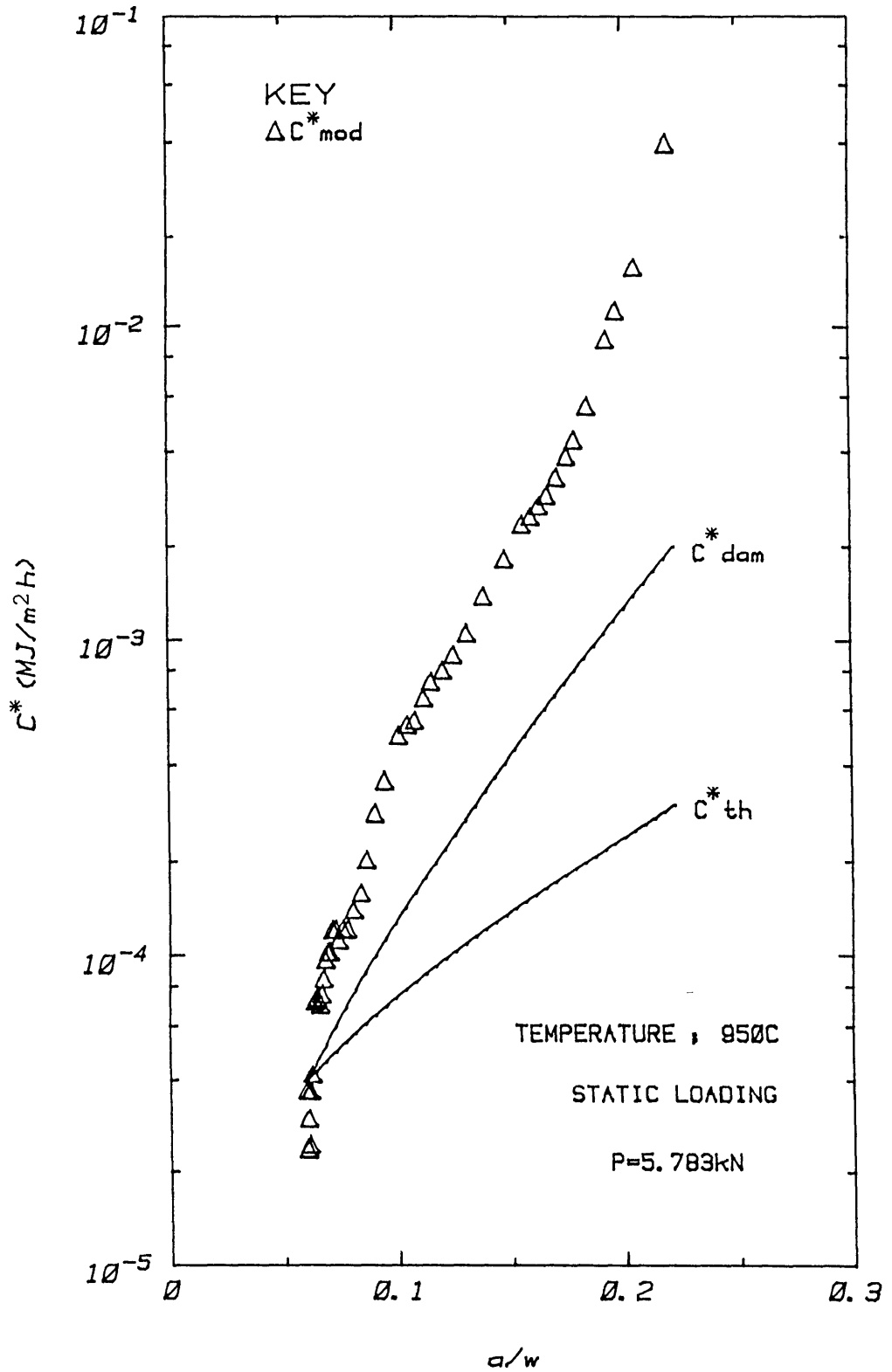


Fig. 10.9 Comparison of C^*_{dam} and C^*_{th} with experimentally measured C^* values ; static loading at 950°C

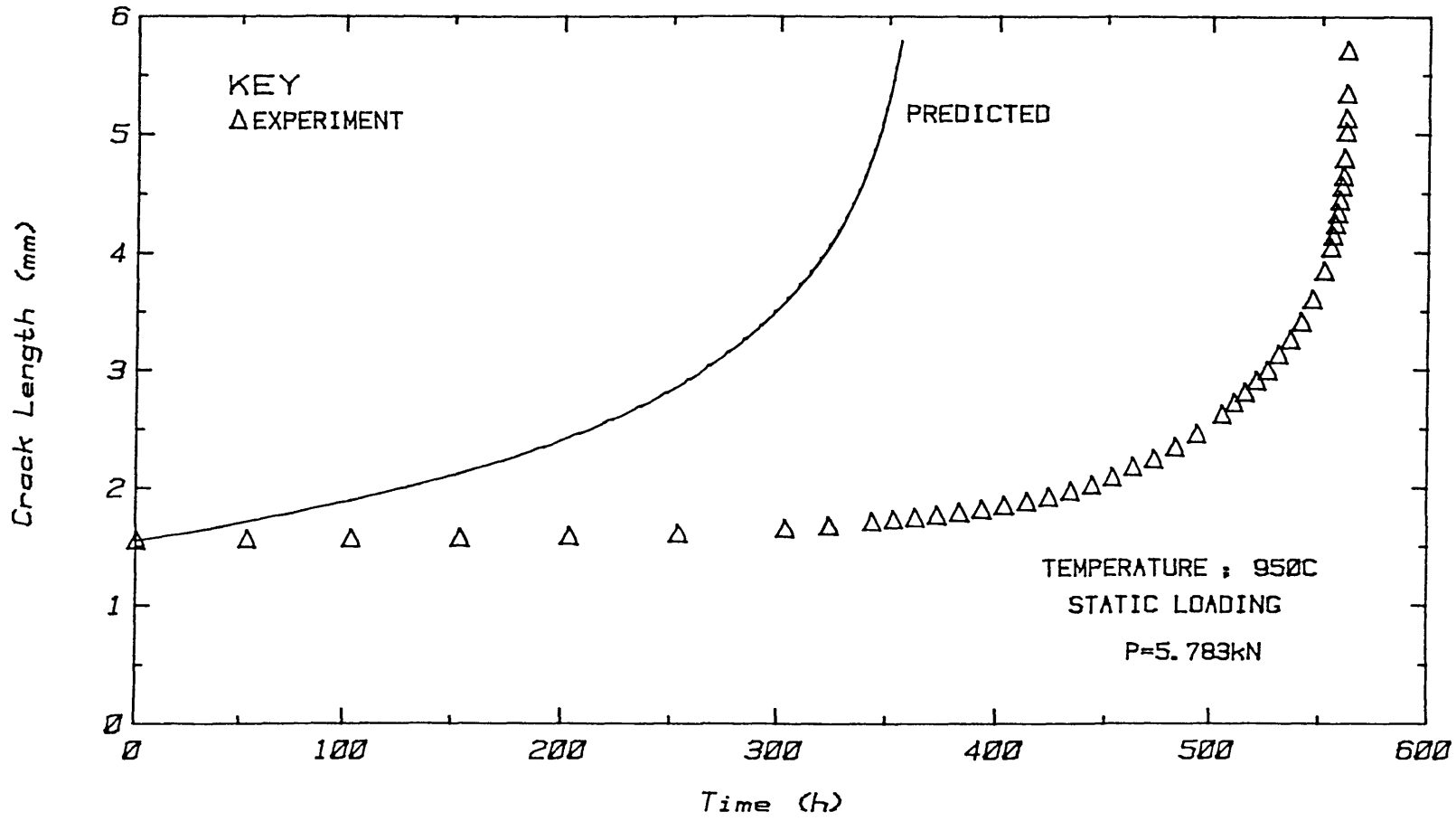


Fig. 10.10 Comparison of experimental and predicted crack growth behaviour for static loading at 950°C

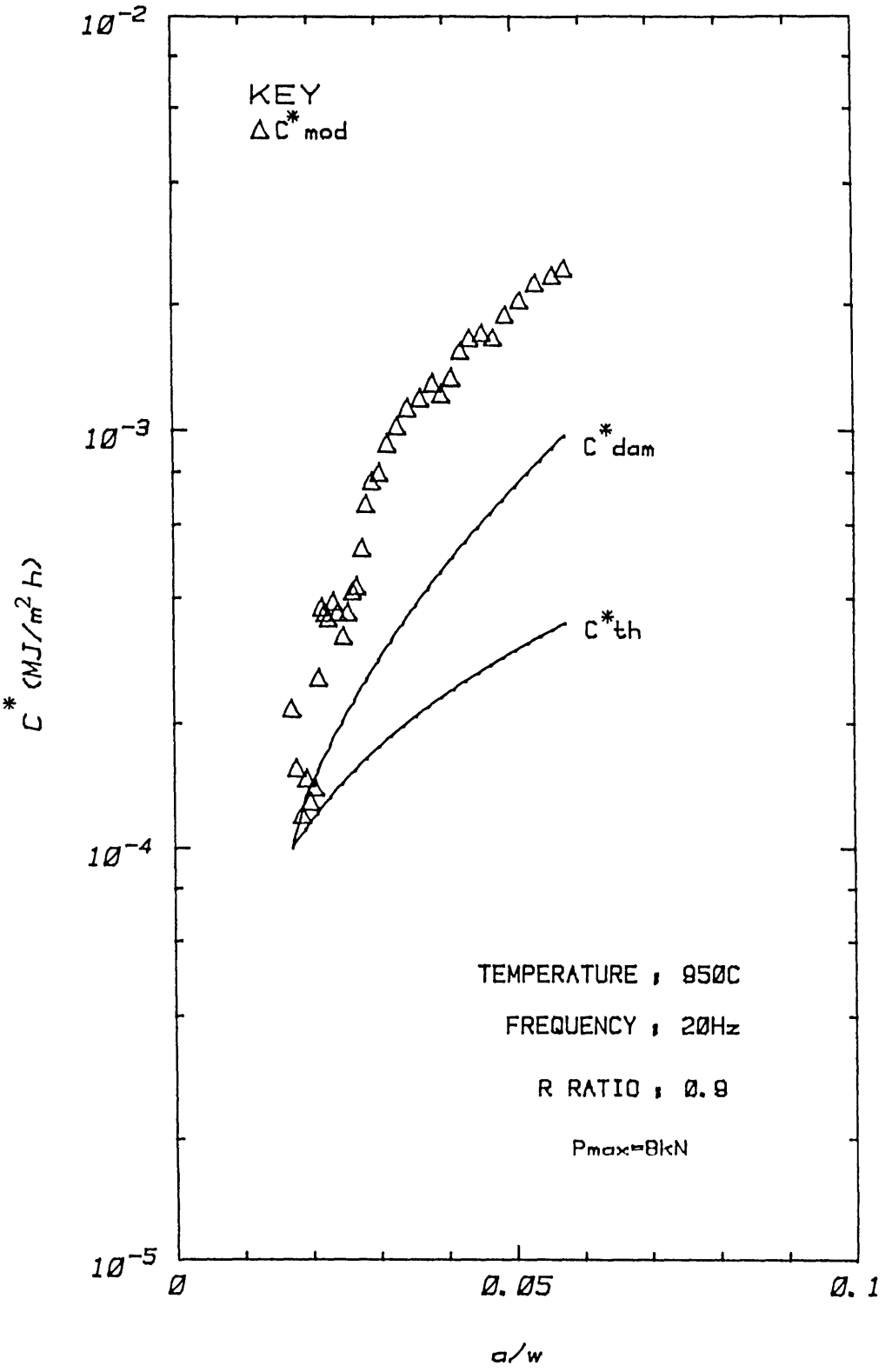


Fig. 10.11 Comparison of C^*_{dam} and C^*_{th} with experimentally measured C^* values ; R=0.9, f=20Hz at 950°C

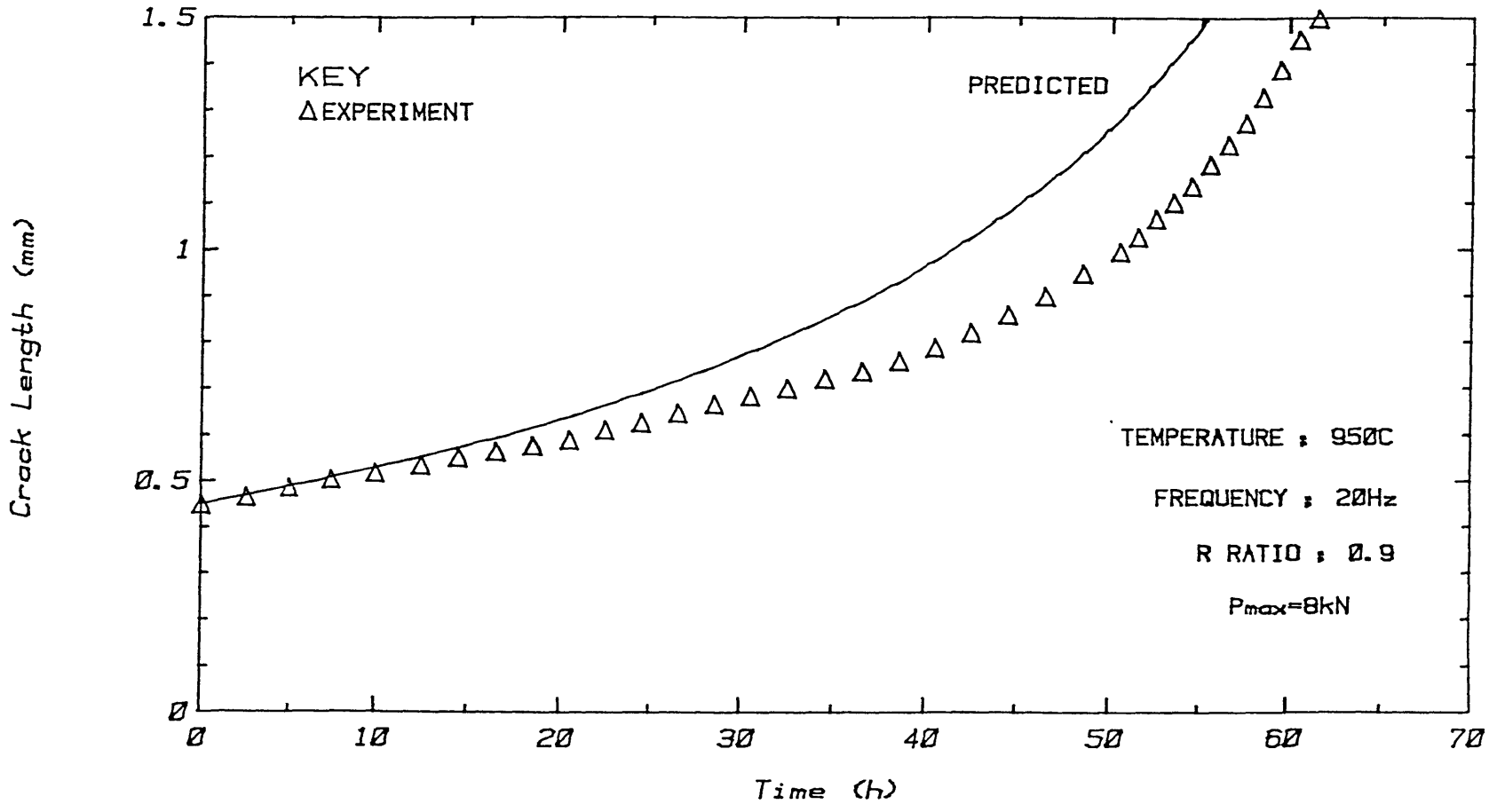


Fig. 10.12 Comparison of experimental and predicted crack growth behaviour for R=0.9,f=20Hz at 950°C

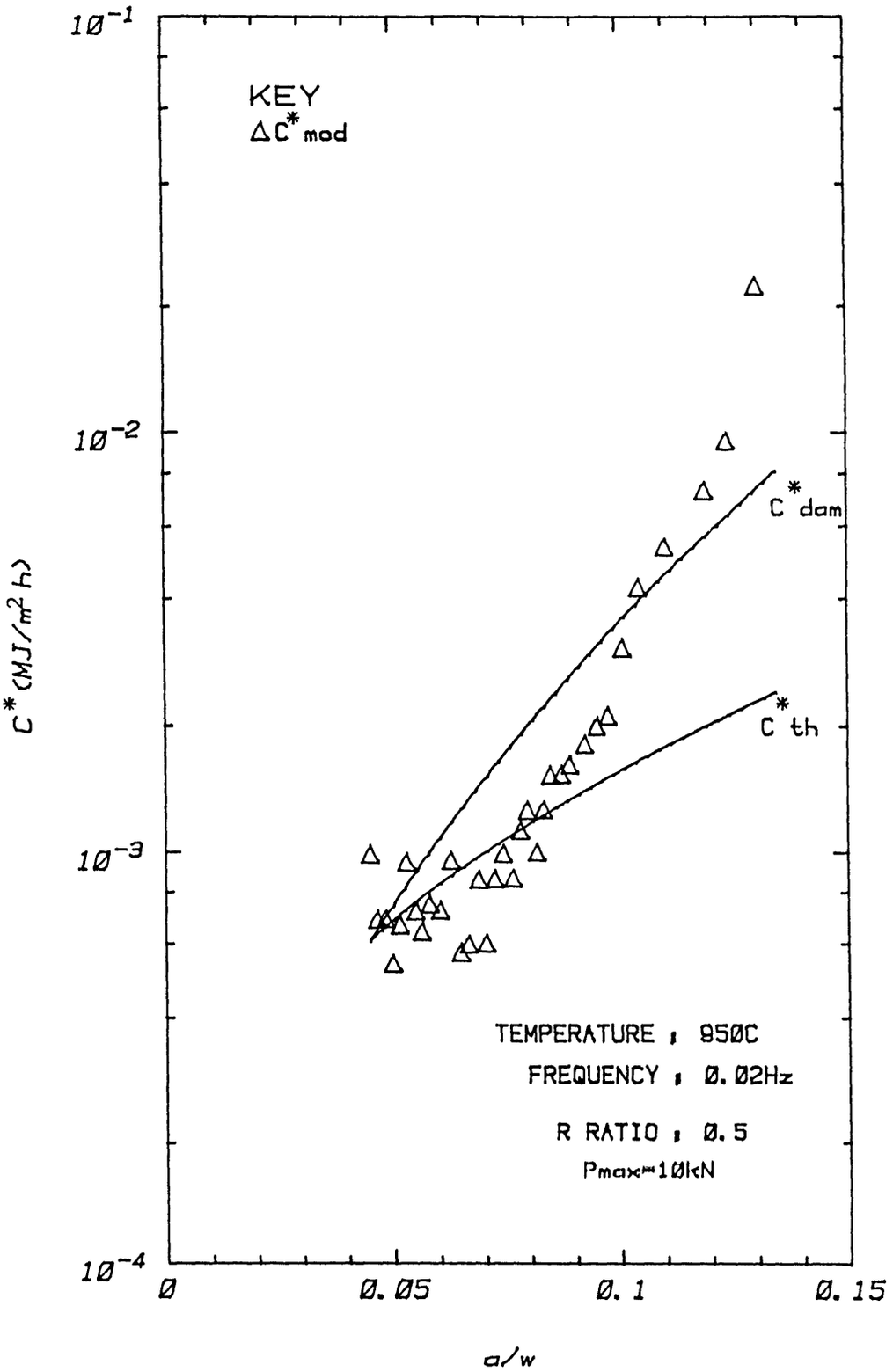


Fig. 10.13 Comparison of C^*_{dam} and C^*_{th} with experimentally measured C^* values ; R=0.5, f=20Hz at 950°C

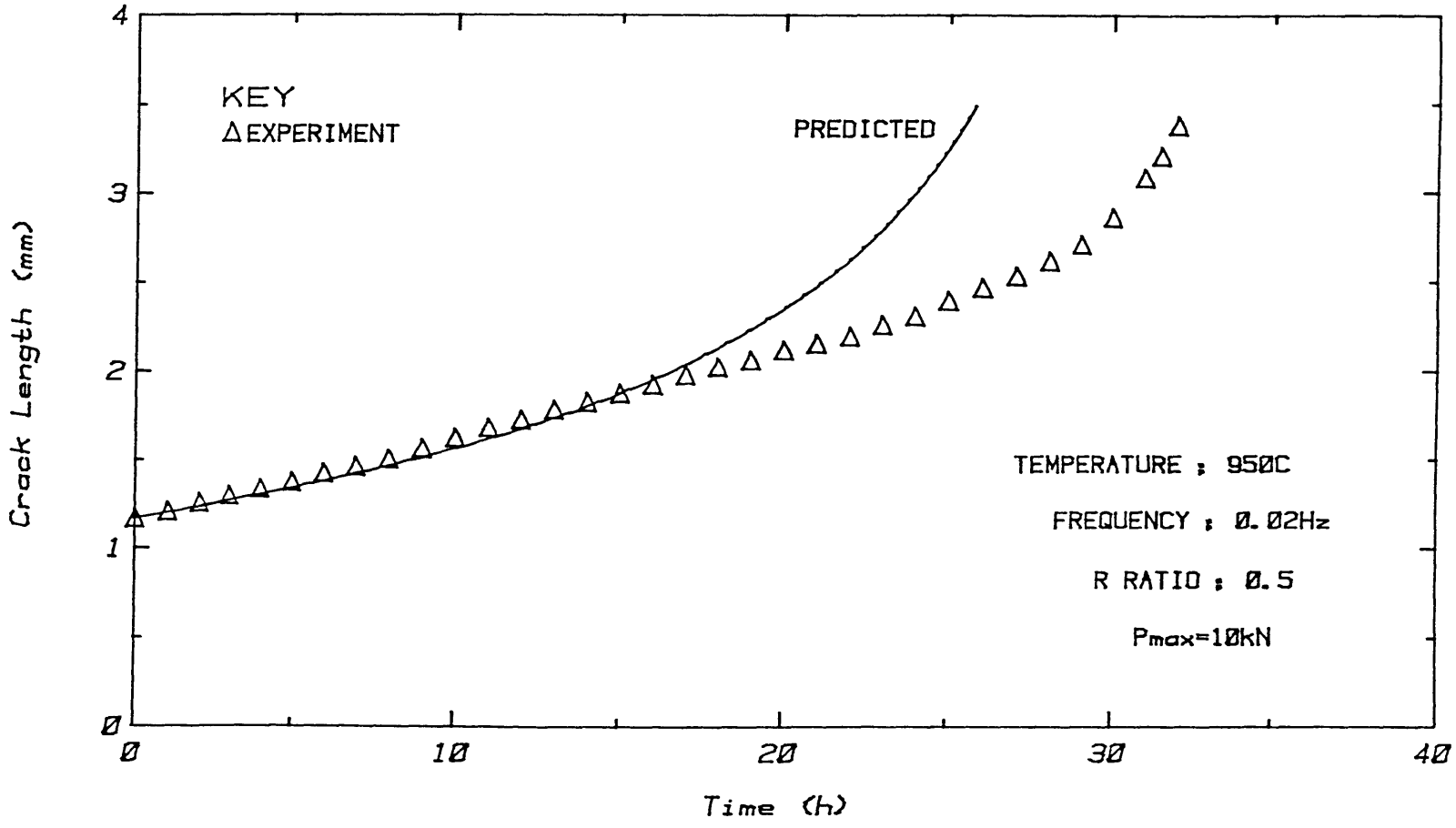


Fig. 10.14 Comparison of experimental and predicted crack growth behaviour for R=0.5, f=0.02Hz at 950°C

CONCLUSIONS

1. Material

The cast Mar M002, used throughout the current experimental programme is representative of the type of conventionally cast nickel base superalloy used for gas turbine blading in the aircraft industry, possessing similar microstructural features and material properties. In addition, heat treatments received by the TCP crack propagation specimens were designed in order to simulate those received by turbine blades during fabrication. The alloy microstructure is complex and contains a high volume fraction of carbide and γ' ($\sim$ 60%) phases precipitated in the γ matrix. Casting procedures resulted in large grain sizes in the range 0.2 - 3 mm.

2. Specimen Geometry

The TCP specimen, used throughout the experimental investigations, was designed in order to model crack propagation in the trailing edge section of nickel base superalloy gas turbine blades containing internal cooling holes. The thin (1.5 mm) central gauge section allows crack propagation to be studied in material of representative thickness and microstructure subjected to tensile loading.

3. Crack Length Measurement

(*i*) The d.c. potential drop (pd) technique was adopted for the measurement of crack length throughout the current experimental programme because of its suitability to the problem of monitoring small increases in crack length for short cracks at elevated temperatures.

(ii) Current supply positions for the TCP specimen were chosen as a compromise between providing a uniform current density in the gauge section and experimental convenience.

(iii) Two output voltages, designated V_c and V_{ref}, were monitored throughout each test via leads spot-welded to the specimen. Lead locations were chosen so that the crack pd, V_c, was sensitive to small changes in crack length while the reference pd, V_{ref}, was relatively insensitive to changes in crack length.

(iv) Finite element techniques were used to obtain a theoretical pd calibration for the specimen and to select suitable locations for the crack and reference pd leads. Thus a pd calibration in the form (V_c/V_{ref}) versus a/w, which is independent of material and temperature, was obtained for the TCP specimen. However, in the range $0 < a/w < 0.1$ the pd calibration was found to be highly sensitive to the positioning of the crack pd leads. An interpolation procedure has been developed, which allows an accurate pd calibration to be obtained for each TCP specimen from a knowledge of the precise location of the crack pd monitoring leads.

4. Fracture Mechanics Parameters

(i) A theoretical stress intensity factor, K, calibration for the TCP specimen was obtained from a linear elastic finite element analysis incorporating the differential stiffness method for evaluation of energy release rates due to crack extension.

(ii) The stress intensity factor calibration for the TCP specimen is of the same form as that for the centre crack plate (CCP)

geometry, differing only by a constant numerical factor (1.073) over the range $0 \leq a/w \leq 0.5$.

(iii) A theoretical C^*, C^*_{th}, calibration for the TCP specimen, based on an analogy between fully plastic power law hardening and secondary creep behaviour has been obtained by modifying fully plastic analytical J-integral solutions for the centre cracked plate (CCP) geometry.

(iv) Experimental C^*, C^*_{exp}, values were obtained via an approximate method based on limit analysis using experimentally measured load point displacement rates, $\dot{\Delta}_T$.

(v) Modified experimental C^*, C^*_{mod}, values were obtained via the approximate method based on limit analysis using displacement rates due to the crack alone, $\dot{\Delta}_c$, where $\dot{\Delta}_c = \dot{\Delta}_T - \dot{\Delta}_o$ and $\dot{\Delta}_o$ is the theoretical displacement rate which would be observed in an uncracked TCP specimen subjected to the same loading.

(vi) An equivalent steady load, P_{eq}, has been defined to allow C^* to be evaluated under cyclic loading conditions. Assuming that deformations are governed by a secondary creep law of the form, $\dot{\varepsilon} \alpha \sigma^n$, the equivalent steady load under cyclic loading is defined by $P_{eq} = \left[f \int_0^{1/f} P^n(t)\, dt \right]^{1/n}$ where $P = P(t)$ and f is the cyclic loading frequency.

(vii) Large discrepancies have been observed between theoretical and experimental estimates of C^* (C^*_{th} and C^*_{mod}). Experimental C^* values were generally larger than theoretical values and discrepancies increased during the course of a crack growth test. This

phenomenon was most marked in Mar M002 at 950°C where time dependent crack growth is accompanied by significant damage accumulation. Better agreement between theoretical and experimental C^* estimates was obtained by modifying theoretical C^* values to take account of damage accumulation ahead of the crack tip.

5. Experimental Results

An experimental test programme has been carried out in order to investigate high temperature crack growth in the cast nickel base superalloy Mar M002 at two temperatures, 750°C and 950°C, chosen to represent typical service temperatures experienced by cast turbine blades.

(a) Slow Crack Growth ($da/dt \simeq 10^{-3}$ mm/h)

(i) Slow crack growth in Mar M002 at 750°C can occur at significantly lower stress intensity, K_{max}, values for cyclic loading at 20Hz compared with those required for static loading. Characteristation of slow crack growth in terms of C^*_{mod} is only possible for static loading as deformations accompanying crack growth under cyclic loading at 20Hz were not large enough to permit C^*_{mod} to be evaluated.

(ii) Slow crack growth at 950°C for R ratios in the range 0.7 - 1 at cyclic frequencies of 20Hz occurs by means of a time dependent mechanism involving significant damage accumulation away from crack tip regions. Crack growth rates for R ratios in the range 0.7 - 1 were best correlated in terms of C^*_{mod}.

(b) Effect of R Ratio

(i) The effect of R ratio on cyclic crack growth in Mar M002 at 20Hz is qualitatively similar for temperatures of 750°C and 950°C. In general, higher crack growths per cycle at higher R ratios (for a given ΔK) are associated with an increase in the amount of intergranular fracture and can be explained in terms of creep effects at both temperatures.

(ii) Higher crack growths per cycle for higher R ratios at 750°C were only obtained if stress intensity levels were in excess of $50\ MPa\sqrt{m}$, the stress intensity required for significant creep crack growth ot occur at this temperature.

(iii) Crack growth at 950°C can occur by either a transgranular or intergranular mode for $R = 0.7$ at a frequency of 20Hz depending on the initial stress intensity level. Transgranular crack growth was observed for an initial ΔK of $8\ MPa\sqrt{m}$, while for an initial ΔK of $2MPa\sqrt{m}$ crack growth occurred by an intergranular mode.

(c) Effect of Frequency

(i) The effect of frequency on crack growth behaviour in Mar M002 depends on the temperature, R ratio and stress intensity (K_{max} or ΔK) level at which tests are carried out. In general, the higher crack growths per cycle (da/dN), observed for lower cyclic loading frequencies at a given ΔK, R ratio and temperature, can be explained by the increasing influence of time dependent creep effects at lower frequencies.

(*ii*) The effect of frequency on crack growth behaviour at 750°C has been studied for R ratios of 0.5 and 0.9. Time dependent creep effects enhance crack growths per cycle for $K > 50$ $MPa\sqrt{m}$ (the stress intensity factor required for significant creep crack growth) but for lower stress intensity levels creep effects at lower frequencies may cause crack tip blunting and consequent reduction in da/dN compared with higher frequencies. This effect was observed for frequencies of 0.2 and 20Hz at $R = 0.5$. For $R = 0.9$ crack growth was essentially time dependent for frequencies of 0.02 - 20Hz at $\Delta K = 5$ $MPa\sqrt{m}$

(*iii*) The effect of frequency on crack growth behaviour at 950°C has been studied for an R ratio of 0.5. Crack growth at 0.02Hz was essentially time dependent. Purely cycle dependent crack growth was not observed, even for frequencies as high as 20Hz. Crack growth occurred by a combination of time dependent and cycle dependent processes for frequencies in the range 0.2 - 20Hz.

(*d*) Effect of Waveform

The effect of loading waveform on crack growth behaviour in Mar M002 has been studied at a temperature of 950°C. Although the effect of waveform on crack growth is complex, parameters which have been found to be important in assessing the extent of any effect in Mar M002 are those which allow time dependent creep effects to influence the crack growth behaviour. Higher crack growths per cycle were observed with reductions in loading frequency, loading and unloading rates and with the imposition of hold times.

(e) Effect of Prior Creep Damage

The effect of 1.905% prior creep strain on subsequent crack growth behaviour has been studied in Mar M002 at a temperature of 950°C for $R = 0.9$ at a frequency of 20Hz. At a given stress intensity (ΔK or K_{max}) level, crack growth rates were found to be significantly higher in the damaged material. However, crack growth rates for the damaged material correlated well with those for the virgin material when plotted against C^*_{mod}.

(f) Correlation of Crack Growth Data

(i) Two parameters, K and C^*, have been used to correlate crack growth rates obtained from the current experimental programme. A modified experimental C^*, C^*_{mod}, has been shown to be the best parameter for correlating time dependent crack growth rates in Mar M002 at temperatures of 750°C and 950°C. Time dependent crack growth in Mar M002 was generally favoured by higher temperatures and R ratios and by lower loading frequencies. It is anticipated that purely cycle dependent crack growth data for Mar M002 would be best correlated in terms of the stress intensity factor range, ΔK.

(ii) Correlation of time dependent crack growth in Mar M002 with the parameter C^* at temperatures of 750°C and 950°C suggests that the alloy exhibits limited environmental (air) sensitivity at these temperatures.

6. Crack Growth Modelling

(i) A simple model has been developed in order to predict time dependent (creep dominated) crack growth in Mar M002 at 950^{o}C based on ductility exhaustion in a crack tip zone and allowing for damage accumulation in the uncracked ligament. Predicted failure times for the three tests considered were within a factor of 1.5 of actual failure times.

(ii) It should be recognised that time dependent crack growth represents an upper bound to the life of a cracked component. When cyclic processes influence crack growth behaviour, component lifetimes can be significantly reduced.

RECOMENDATIONS FOR FURTHER WORK

1. Determination of a theoretical C^* calibration for the TCP crack propagation specimen using non-linear finite element methods.

2. Conduct a parallel experimental programme in an inert environment to establish whether environmental effects influence crack growth behaviour in Mar MOO2 at temperatures of 750°C and 950°C.

3. Conduct crack growth tests using the TCP specimen at high frequencies and low R ratios for temperatures of 750°C and 950°C to ascertain whether purely cycle dependent crack growth occurs in Mar MOO2 at these temperatures.

4. Develop the model outlined in Section 10.4 to enable crack growth in Mar MOO2 to be predicted in both time and cycle dependent regimes.

5. Conduct crack growth tests using a range of specimen geometries to determine whether correlations obtained between crack growth rates and the fracture mechanics parameters K and C^* are independent of specimen geometry.

6. Conduct an investigation into the micromechanisms responsible for crack propagation in Mar MOO2 at 750°C and 950°C.

REFERENCES

1. DECKER, R.F., and SIMS, C.T. (1972), in The Superalloys, (eds. C.T. Sims and W.C. Hagel), Wiley-Interscience, New York, p.33.

2. STOLOFF, N. (1972). in The Superalloys, (eds. C.T. Sims and W.C. Hagel), Wiley-Interscience, New York, p.79.

3. FLOREEN, S. (1983). ASTM STP 803, p.I-708.

4. KOUL, A.K., and WALLACE, W. (1982). Met. Trans., Vol. 13A, p.673.

5. LARSON, J.M., and FLOREEN, S. (1977). Met. Trans., Vol. 8A, p.51.

6. MERRICK, H.F., and FLOREEN, S. (1978). Met. Trans., Vol. 9A, p.231.

7. RUNKLE, J.C., and PELLOUX, R.M. (1979). ASTM STP 675, p.501.

8. FLOREEN, S., and DAVIDSON, J.M. (1983). Met. Trans., Vol. 14A, p.895.

9. WOODFORD, D.A. (1981). Met. Trans., Vol. 12A, p.299.

10. GELL, M., LEVERANT, G.R., and WELLS, C.H. (1970), ASTM STP 467, p.113.

11. HOFFELNER, W., and SPEIDEL, M.O. (1981), in Advances in Fracture Research, Proc. 1CF5, Cannes, June 1981, p.2431.

12. FLOREEN, S. (1975). Met. Trans., Vol. 6A, p.1741.

13. PELLOUX, R.M., and HUANG, J.S. (1980), in Creep-Fatigue Environment Interactions, (eds. R.M. Pelloux and N.S. Stoloff). Proc. ASME Meeting, Milwaukee, September 1979, p.151.

14. SADANANDA, K. (1978). Met. Trans., Vol. 9A, p.635.

15. SADANANDA, K., and SHAHINIAN, P. (1977). Met. Trans., Vol. 8A, p.439.

16. SADANANDA, K., and SHAHINIAN, P. (1983). Met. Trans., Vol. 14A, p.1467.

17. MIN, B.K. (1979), in Mechanical Behaviour of Materials, Proc. ICM3, Cambridge, August 1979, Vol. I, p.151.

18. HULL, D., and RIMMER, C.E. (1959). Phil. Mag., Vol. 4, p.673.

19. CHUANG, T.J., and RICE, J.R. (1973). Acta. Met., Vol. 2, p.1625.

20. RAJ, R., and ASHBY, M.F. (1975). Acta. Met., Vol. 23, p.653.

21. NEEDLEMAN, A., and RICE, J.R. (1980),Acta. Met., Vol. 28, p.557.

22. PAVINICH, W., and RAJ, R. (1977), Met. Trans., Vol. 8A, p.1917.

23. FLOREEN, S., and KANE, R.H. (1980), Fat. Eng. Mat. and Structures, Vol. 2, p.401.

24. RAJ, R. (1982), Acta. Met., Vol. 30, p.1259.

25. COOK, R.H., and SKELTON, R.P. (1974). Int. Metall. Rev., Vol. 19, p.199.

26. GABRIELLI, F., and PELLOUX, R.M. (1982), Met. Trans., Vol. 13A, p.1083.

27. SADANANDA, K., and SHAHINIAN, P. (1980). Mat. Sci. and Eng., Vol. 43, p.159.

28. SADANANDA, K., and SHAHINIAN, P. (1982). Metals Tech., Vol. 9 p.18.

29. PEDRON, J.P., and PINEAU, A. (1982). Mat. Sci. and Eng., Vol. 56, p.143.

30. CHAKU, P.N., and McMAHON, C.J., JR. (1974), Met. Trans., Vol. 5, p.441.

31. SADANANDA, K., and SHAHINIAN, P. (1978), Met. Trans., Vol. 9A, p.79.

32. VINCENT, J.N., and REMY, L. (1981), in Fatigue Thresholds, Proc. Int. Conf., Stockholm, June 1981, p.441.

33. SADANANDA, K., and SHAHINIAN, P. (1981), Met. Trans., Vol. 12A, p.343.

34. SADANANDA, K., and SHAHINIAN, P. (1979), Eng. Fract. Mech., Vol. 11, p.73.

35. SCARLIN, R.B. (1979), ASTM STP 675, p.396.

36. GAYDA, J., and MINER, R.V. (1983). Int. J. Fatigue, Vol. 5, No. 3, p.135.

37. SHAHINIAN, P. (1978), Metals. Tech., Vol. 5, p.372.

38. MILLS, W.J., and JAMES, L.A. (1980). Fat. Eng. Mat. and Structures, Vol. 3, p.159.

39. LLOYD, G.J. (1983), in Fatigue at High Temperature, (ed. R.P. Skelton), Applied Science, London, p.187.

40. SCARLIN, R.B. (1977), in Fracture 1977, Proc. ICF4, Waterloo, June 1977, p.849.

41. CROMPTON, J.S., and MARTIN, J.W. (1984), Mat. Sci. and Eng., Vol. 64, p.37.

42. CLAVEL, M., and PINEAU, A. (1978), Met. Trans., Vol. 9A, p.471.

43. SOLOMON, H.D., and COFFIN, L.F.,JR. (1973), ASTM STP 520, p.112.

44. OHMURA, T., PELLOUX, R.M., and GRANT, N.J. (1973), Eng. Fract. Mech., Vol. 5, p.909.

45. SHAHINIAN, P., and SADANANDA, K. (1979). Trans. ASME, J. Eng. Mat. Tech., Vol. 101, p.224.

46. HICKS, M.A., and KING, J.E. (1983). Int. J. Fatigue, Vol. 5, No.2, p.67.

47. MIN, B.K., and RAJ, R. (1979), ASTM STP 675, p.569.

48. SHAHINIAN, P., and SADANANDA, K. (1980), in Proc. Int. Conf. on Eng. Aspects of Creep, Sheffield, September 1980, Paper C239/80.

49. PEDRON, J.P., and PINEAU, A. (1981), in Advances in Fracture Research, Proc. ICF5, Cannes, June 1981, p.2385.

50. KING, J.E. (1981), Fat. Eng. Mat. and Structures, Vol. 4, No. 4, p.311.

51. ASHBY, M.F., and TOMKINS, B. (1979), in Mechanical Behaviour of Materials, Proc. 1CM3, Cambridge, August 1979, Vol. I, p.47.

52. BURT, H., DENNISON, J.P., ELLIOTT, I.C., and WILSHIRE, B. (1982), Mat. Sci. and Eng., Vol. 53, p.245.

53. DENNISON, J.P., HOLMES, P.D., and WILSHIRE, B. (1978). Mat. Sci. and Eng., Vol. 33, p.35.

54. BURT, H., ELLIOTT, I.C., and WILSHIRE, B. (1981), Metal Sci., Vol. 15, p.421.

55. DAVIDSON, J.M., and TIEN, J.K. (1981), Met. Trans., Vol. 12A, p.865.

56. IRWIN, G.R. (1957), Trans. ASME, J. Appl. Mech., Vol. 24, p.361.

57. KNOTT, J.F., (1973), Fundamentals of Fracture Mechanics, Butterworths, London.

58. RICE, J.R. (1973), in Proc. 3rd. Int. Conf. Fracture, Munich, Part 2, p.1-441.

59. RICE, J.R. (1967), ASTM STP 415, p.247.

60. RICE, J.R. (1968), Trans. ASME, J. Appl. Mech., Vol. 35, p.379.

61. RICE, J.R., and ROSENGREN, G.F. (1968), J. Mech. Phys. Solids, Vol. 16, p.1.

62. HUTCHINSON, J.W. (1968), J. Mech. Phys. Solids, Vol. 16, p.13.

63. HUTCHINSON, J.W. (1968), J. Mech. Phys. Solids, Vol. 16, p.337.

64. McCLINTOCK, F.A. (1977), in Fundamental Aspects of Structural Alloy Design (eds. R.I. Jaffee and B.A. Wilcox), Plenum Press, p.147.

65. GOLDMAN, N.L., and HUTCHINSON, J.W. (1975), Int. J. Solids Structures, Vol. 11, p.575.

66. LANDES, J.D., and BEGLEY, J.A. (1974), Westinghouse Scientific Paper, 74-1E7-FESGT-P1.

67. NIKBIN, K.M., WEBSTER, G.A., and TURNER, C.E. (1976), ASTM STP 601, p.47.

68. RIEDEL, H., and RICE, J.R. (1980), ASTM STP 700, p.112.

69. WILKINSON, D.S., and BINER, S.B (1984), The Application of Fracture Mechanics to Creep Crack Growth in Pressure Vessel Steels, DSS File No. 053U-23440-0-9199, McMaster University, Ontario, Canada.

70. RIEDEL, H. (1981), J. Mech. Phys. Solids, Vol. 29, p.35.

71. HUI, C.Y., and RIEDEL, H. (1979), Brown University, Materials Research Report No. MRL E-117.

72. RIEDEL, H., and WAGNER, W. (1981), in Advances in Fracture Research, Proc. ICF5, Cannes, June 1981.

73. BARNBY, J.T. (1975), Eng. Fract. Mech., Vol. 7, p.299.

74, FLOREEN, S., and KANE, R.H. (1976), Met. Trans., Vol. 7A, p.1157.

75. NIKBIN, K.M., SMITH, D.J., and WEBSTER, G.A. (1983), in Advances in Life Prediction Methods at Elevated Temperatures, Proc. ASME Conf., Albany, New York, April 1983.

76. NIKBIN, K.M., SMITH, D.J., and WEBSTER, G.A. (1985), Proc. Royal Soc., to be published.

77. KUBO, S., OHJI, K., and OGURA, K. (1979), Eng. Fract. Mech., Vol. 11, p.315.

78. VITEK, V. (1977), Int. J. Fracture, Vol. 13, No.1, p.39.

79. MILLER, D.A., and PILKINGTON, R. (1980), Met. Trans., Vol. 11A, p.177.

80. WILKINSON, D.S. (1981), in Creep and Fracture of Engineering Materials and Structures, Proc. Conf., Swansea, March 1981, p.315.

81. HUTCHINSON, J.W. (1983), Acta Met., Vol. 31, p.1079.

82. BASSANI, J.L. (1981), in Creep and Fracture of Engineering Materials and Structures, Proc. Conf., Swansea, March 1981, p.329.

83. DIMELFI, R.J., and NIX, W.D. (1977), Int. J. Fracture, Vol. 13, No. 3, p.341.

84. SADANANDA, K., and SHAHINIAN, P. (1981), Metal Sci., Vol. 15, p.425.

85. ELLISON, E.G., and HARPER, M.P. (1978), J. Strain Anal., Vol. 13, No. 1, p.35.

86. WILKINSON, D.S., and VITEK, V. (1982), Acta Met., Vol. 30, p.1723.

87. PARIS, P.C., and ERDOGAN, F. (1963), Trans. ASME, J. Basic Eng., Vol. 85, p.528.

88. JASKE, C.E. (1983), Fat. Eng. Mat. and Structures, Vol. 5, No. 2, p.159.

89. RIEDEL, H. (1981), presented at the ASTM Symposium on Elastic-Plastic Fracture Mechanics, Philadelphia.

90. SAXENA, A. (1981), Fat. Eng. Mat. and Structures, Vol. 3, p.247.

91. SAXENA, A., WILLIAMS, R.S., and SHIH, T.T. (1981), ASTM STP 743, p.86.

92. SAXENA, A. (1983), in Advances in Life Predition Methods at Elevated Temperatures, Proc. ASME Conf., Albany, New York, April 1983.

93. KACHANOV, L.M. (1958), Izv. Akad. Nauk. USSR, Otd. Tekh. Nauk., No. 8, p.26 (in Russian).

94. RABOTNOV, Y.N. (1969), Creep Problems in Structural Members, (Ed. F.A. Leckie), North-Holland, Amsterdam.

95. WEBSTER, G.A. (1983), in Engineering Approaches to High Temperature Design, (eds. B. Wilshire and D.R.J. Owen), Pineridge Press, Swansea, p.1.

96. KOTERAZAWA, R., and MORI, T. (1977), Trans. ASME, J. Eng. Mat. Tech., Vol. 99, p.298.

97. SADANANDA, K., and SHAHINIAN, P. (1981), Eng. Fract. Mech., Vol. 15, No. 3-4, p.327.

98. SADANANDA, K., and SHAHINIAN, P. (1981), presented at the ASTM Symposium on Elastic-Plastic Fracture Mechanics, Philadelphia.

99. FU, L.S. (1980), Eng. Fract. Mech., Vol. 13, p.307.

100. VAN LEEUWEN, H.P. (1977), Eng. Fract. Mech., Vol. 9, p.951.

101. NIKBIN, K.M., WEBSTER, G.A., and TURNER, C.E. (1977), in Fracture 1977, Proc. ICF4, Waterloo, June 1977, Vol. 2, p.627.

102. OHJI, K., OGURA, K., KUBO, S., and KATADA, Y. (1980) in Proc. Int. Conf. Eng. Aspects of Creep, Sheffield, September 1980, Paper C240/80.

103. WILLIAMS, J.A., and PRICE, A.T. (1975), Trans. ASME, J.Eng. Mat. Tech., Vol. 97, p.214.

104. SCARLIN, R.B. (1976), Met. Trans., Vol. 7A, p.1535.

105. JAMES, L.A. (1974), Trans. ASME, J. Eng. Mat. Tech., Vol. 96, p.249.

106. SADANANDA, K., and SHAHINIAN, P. (1980), ASTM STP 700, p.152.

107. TAIRA, S., OHTANI, R., and KOMATSU, T. (1979), Trans. ASME, J. Eng. Mat. Tech., Vol. 101, p.162.

108. OHTANI, R. (1980), in Proc. Int. Conf. Eng. Aspects of Creep, Sheffield, September 1980, Paper C226/80.

109. KOTERAZAWA, R., and MORI, T. (1980), in Proc. Int. Conf. Eng. Aspects of Creep, Sheffield, September 1980, Paper C238/80.

110. ROOKE, D.P., and CARTWRIGHT, D.J. (1976), Compendium of Stress Intensity Factors, HMSO, London.

111. TADA, H., PARIS, P.C., and IRWIN, G.R. (1973), The Stress Analysis of Cracks Handbook, Del Research, Hellertown, Pa.

112. ILLYUSHIN, A.A. (1946), Prikadnaia Matematika i Mekhanka Vol. 10, p.347.

113. HARPER, M.P., and ELLISON, E.G. (1977), J. Strain Anal., Vol. 12, No. 3, p.167.

114. SMITH, D.J., and WEBSTER, G.A. (1983), ASTM STP 803, P.1-654.

115. HAIGH, J.R., and RICHARDS, C.E. (1974), CEGB, CERL Memo No. RD/L/M461.

116. MERKLE, J.G., and CORTEN, H.T. (1974), Trans. ASME, J. Press. Vess. Tech., Vol. 96, p.286.

117. RICE, J.R., PARIS, P.C., and MERKLE, J.G. (1973), ASTM STP 536., p.231.

118. SHIH, C.F., and HUTCHINSON, J.W. (1976), Trans. ASME, J. Eng. Mat. Tech., Vol. 98, p.289.

119. KUMAR, V., GERMAN, M.D., and SHIH, C.F. (1981), An Engineering Approach for Elastic-Plastic Fracture Analysis, EPRI Report NP-1931.

120. SAXENA, A. (1980), ASTM STP 700, p.131.

121. WEBSTER, G.A. (1981), in Measurement of High Temperature Mechanical Properties of Materials, (eds. M.S. Loveday, M.F. Day and B.F. Dyson), HMSO, London.

122. HICKS, M.A., and PICKARD, A.C. (1982), Int. J. Fracture, Vol. 20, p.91.

123. SMITH, D.J. (1983), PhD Thesis, University of London.

124. SAXENA, A. (1980). Eng. Fract. Mech., Vol. 13, p.741.

125. HUANG, J.S., and PELLOUX, R.M. (1980), Met. Trans., Vol. 11A, p.899.

126. HE, M.Y., and HUTCHINSON, J.W. (1983), ASTM STP 803, p1-277.

127. McCARVER, J.F., and RITCHIE, R. O. (1982), Mat. Sci. and Eng., Vol. 55, p.63.

128. RITCHIE, R.O., and SURESH, S. (1982), in Proc. 55th Meeting of AGARD Structural and Materials Panel on the Behaviour of Short Cracks in Airframe Components, Toronto, September 1982.

129. PILKINGTON, R. (1980), in Proc. Int. Conf. Eng. Aspects of Creep, Sheffield, September 1980, Paper C206/80.